UNIVERSITY OF CALIFORNIA SAN DIEGO

Numerical simulation and spectral modal analysis of nonlinear dynamics and acoustics in turbulent jets

A dissertation submitted in partial satisfaction of the
requirements for the degree
Doctor of Philosophy

in

Engineering Sciences (Mechanical Engineering)

by

Akhil Nekkanti

Committee in charge:

Professor Oliver T. Schmidt, Chair
Professor Stefan Llewellyn Smith
Professor Antonio L. Sanchez
Professor Sutanu Sarkar
Professor Qiang Zhu

2023

The dissertation of Akhil Nekkanti is approved, and it is acceptable in quality and form for publication on microfilm and electronically.

University of California San Diego

2023

DEDICATION

To my parents, Mohan and Rajini, for their unconditional love and support.

TABLE OF CONTENTS

LIST OF FIGURES

LIST OF TABLES

ACKNOWLEDGEMENTS

Firstly, I would like to express my gratitude to Prof. Oliver T. Schmidt for his unwavering guidance and support throughout my Ph.D. journey. I deeply appreciate the significant amount of time he invested in me, which has played a crucial role in my growth as a researcher. He not only gave me the freedom to explore new research ideas but also steered me toward relevant problems. His enthusiasm for developing new techniques and making them as rigorous as possible is inspiring, and I hope to have imbibed this quality from him. I am grateful for his openness in allowing me to express disagreements and say no. Overall, I have gained valuable insights into research and technical writing from him.

Next, I would also like to acknowledge the support of my dissertation committee members: Prof. Sarkar, Prof. Sanchez, Prof. Llewellyn Smith, and Prof. Zhu. I am particularly thankful to Prof. Sarkar and Prof. Sanchez, who provided valuable mentorship during different stages of my PhD journey. I express my gratitude to the UCSD MAE personnel and the HPCMP support for resolving many administrative and technical issues over the last five years.

To all members of the Computational Modeling and Flow Physics Lab, Tianyi, Edward, Brandon, and Cong, it was a pleasure working with you guys. Tianyi, our brainstorming sessions on numerical techniques were very informative. My fellow jet noise researcher, Brandon, our discussions were always productive. I would also like to acknowledge a number of collaborators for their insights and help along the way: Igor Maia, Peter Jordan, Liam Heidt, and Tim Colonius.

During my stay in San Diego, I have been fortunate to make great friends who have supported me along the way: Ayush, Sheel, Arijit, Roshan, Sparsh, Siddharth, Shruti, Yash, Pranav, Mrudula, Aashi, Snigdha, Alex. They have made my time, especially during the pandemic, memorable and fun. I would like to express my heartfelt gratitude to Ayush, Sheel, and Arijit for always being there when I needed them. Ayush, my roommate, has been a constant source of brotherhood, empathy, and a positive influence on me. Sheel has been a close companion in many endeavors, providing invaluable feedback on my work. Arijit has been an encouraging comrade,

engaging in insightful and illuminating discussions from which I have learned a great deal. I also cherish the memories of our board game nights and debates with Roshan, Sparsh, and Siddharth.

I also extend my thanks to my other friends, Sanyam, Tejaswi, Rajesh, Harish, Jagadish, Sumanth, Faisal, and Mahesh, who provided their support from afar. I am also grateful to my professors at IIT Ropar, particularly Prof. Rakesh Kumar Maurya and Prof. Himanshu Tyagi, who instilled in me an interest in conducting research.

Finally, I would like to express my heartfelt gratitude to my parents, Mohan and Rajini, to whom I dedicate this thesis. Their unwavering love, support, and sacrifices have made this journey possible. I am immensely grateful to them for instilling in me the values of education and pursuit of excellence, and for believing in me and encouraging me every step of the way.

I acknowledge the technical help and support of my co-authors. I also thank them for allowing me to use the following manuscripts for my dissertation.

Chapter 2 is a reprint of the material in the article: A. Nekkanti, and O. T. Schmidt. "Frequency–time analysis, low-rank reconstruction and denoising of turbulent flows using SPOD", Journal of Fluid Mechanics, 926, A26 (2021). The dissertation author was the primary investigator and author of this work.

Chapter 3 is a reprint of the material in the article: A. Nekkanti, and O. T. Schmidt. "Gappy spectral proper orthogonal decomposition", Journal of Computational Physics, 478, 111950 (2023). The dissertation author was the primary investigator and author of this work.

Chapter 4 is a reprint of the material in the article: A. Nekkanti, and O. T. Schmidt. "Modal analysis of acoustic directivity in turbulent jets", AIAA Journal, 59.1, 228-239 (2021). The dissertation author was the primary investigator and author of this work.

Parts of chapter 5, with modifications, appear in two conference proceedings titled: 1) A. Nekkanti, O. T. Schmidt, I. Maia, P. Jordan, L. Heidt, & T. Colonius. "Bispectral mode decomposition of axisymmetrically and non-axisymmetrically forced turbulent jets", *AIAA Aviation 2023 Forum*; 2) A. Nekkanti, I. Maia, P. Jordan, L. Heidt, T. Colonius, & O. T. Schmidt. "Triadic non-

linear interactions and acoustics of forced versus unforced turbulent jets", *Twelfth International Symposium on Turbulence and Shear Flow Phenomena (TSFP), 2022*. The dissertation author is the primary investigator and author of this work.

Chapter 6 is being prepared for publication titled: A. Nekkanti, and O. T. Schmidt. "Non-linear energy transfer during vortex-pairing of initially-laminar jets". The dissertation author was the primary investigator and author of this work.

VITA

2017	Bachelor of Technology with Honors, Mechanical Engineering, Indian Institute of Technology Ropar, India
2018	Master of Science in Engineering Sciences (Mechanical Engineering), University of California San Diego, CA, USA
2023	Doctor of Philosophy in Engineering Sciences (Mechanical Engineering), University of California San Diego, CA, USA

PUBLICATIONS

JOURNAL PUBLICATIONS

A. Nekkanti, I. Maia, P. Jordan, L. Heidt, T. Colonius & O. T. Schmidt,. "Triadic interactions and mean flow distortions of axisymmetrically and non-axisymmetrically forced turbulent jets". in preperation

A. Nekkanti, & O. T. Schmidt, "Nonlinear energy transfer during vortex-pairing in initially-lamianar jets". in preperation

A. Nekkanti, S. Nidhan, O. T. Schmidt, & S. Sarkar, "Large-scale streaks in a turbulent bluff body wake". arXiv preprint arXiv:2304.08679, 2023

A. Nekkanti & O. T. Schmidt. "Gappy spectral proper orthogonal decomposition". *Journal of Computational Physics*, 478:111950, 2023.

A. Nekkanti & O. T. Schmidt. "Frequency–time analysis, low-rank reconstruction and denoising of turbulent flows using SPOD", *Journal of Fluid Mechanics*, 926:A26, 2021.

A. Nekkanti & O. T. Schmidt. "Modal analysis of acoustic directivity in turbulent jets", *AIAA Journal*, 59(1), 2021.

A. Nekkanti, A. L. Sanchez, & F. A. Williams. "Explanations of influences of differential diffusion on flame-temperature variations in usual and inverse jet flames", *Combustion and Flame*, 200, 2019.

R. K. Maurya & **N. Akhil**. "Comparative study of the simulation ability of various recent hydrogen combustion mechanisms in HCCI engines using stochastic reactor model", *International Journal of Hydrogen Energy*, 42(16), 2017.

R. K. Maurya & **N. Akhil**. "Development of a new reduced hydrogen combustion mechanism with NOx and parametric study of hydrogen HCCI combustion using stochastic reactor model", *Energy Conversion and Management*, 132, 2017.

R. K. Maurya & **N. Akhil**. "Numerical investigation of ethanol fuelled HCCI engine using stochastic reactor model. Part 2: Parametric study of performance and emissions characteristics using new reduced ethanol oxidation mechanism", *Energy Conversion and Management*, 121, 2016.

R. K. Maurya & **N. Akhil**. "Numerical investigation of ethanol fuelled HCCI engine using stochastic reactor model. Part 1: Development of a new reduced ethanol oxidation mechanism", *Energy Conversion and Management*, 118, 2016.

CONFERENCE PROCEEDINGS

A. Nekkanti, O. T. Schmidt, I. Maia, P. Jordan, L. Heidt, & T. Colonius. "Bispectral mode decomposition of axisymmetrically and non-axisymmetrically forced turbulent jets", *AIAA Aviation 2023 Forum*.

A. Nekkanti, I. Maia, P. Jordan, L. Heidt, T. Colonius, & O. T. Schmidt. "Triadic nonlinear interactions and acoustics of forced versus unforced turbulent jets", *Twelfth International Symposium on Turbulence and Shear Flow Phenomena (TSFP), 2022*.

O. T. Schmidt & **A. Nekkanti**. "Gappy spectral proper orthogonal decomposition for reconstruction of turbulent flow data", *Twelfth International Symposium on Turbulence and Shear Flow Phenomena (TSFP), 2022*.

L. Heidt, T. Colonius, **A. Nekkanti**, O. T. Schmdit, I. Maia, & P. Jordan. "Analysis of forced subsonic jets using spectral proper orthogonal decomposition and resolvent analysis", *AIAA Aviation 2021 Forum*.

I. Maia, P. Jordan, L. Heidt, T. Colonius, **A. Nekkanti**, & O. T. Schmidt. "Nonlinear dynamics of forced wavepackets in turbulent jets", *AIAA Aviation 2021 Forum*.

A. Nekkanti & O. T. Schmidt. "Modal analysis of the directivity of acoustic emissions from wavepackets in turbulent jets", *AIAA Scitech 2020 Forum*.

R. K. Maurya & **N. Akhil**. "Experimental Investigation on Effect of Compression Ratio, Injection Pressure and Engine Load on Cyclic Variations in Diesel Engine Using Wavelets", *SAE Technical Paper*, No. 2018-01-5007.

ABSTRACT OF THE DISSERTATION

Numerical simulation and spectral modal analysis of nonlinear dynamics and acoustics in turbulent jets

by

Akhil Nekkanti

Doctor of Philosophy in Engineering Sciences (Mechanical Engineering)

University of California San Diego, 2023

Professor Oliver T. Schmidt, Chair

Turbulent jets are canonical flows that occur when fluid emerges from an orifice into the surrounding environment, such as the jet from aircraft engines. As the fluid emerges from the nozzle, it forms an unstable shear layer that grows very rapidly, forming large-scale coherent structures, which are the main sources of aft-angle jet noise. The mechanism behind the generation of jet noise is still not fully understood. Further insights into characteristics of coherent structures can aid our understanding of turbulence, and in modeling and controlling various mechanisms. The main foci of this work are: (i) performing high-fidelity numerical simulations of turbulent jets and extracting physical insights from coherent flow structures, and (ii) developing techniques

that extract these flow structures from the large dataset generated by these simulations.

In recent years, spectral proper orthogonal decomposition (SPOD) has emerged as a major tool for extracting coherent structures. In the first part, we extend SPOD for low-rank reconstruction, denoising, prewhitenening, frequency–time analysis, and gappy-data reconstruction. Two approaches for flow-field reconstruction are proposed, a frequency-domain approach, and a time-domain approach. A SPOD-based denoising strategy is also presented, which achieves significant noise reduction while facilitating drastic data compression. A convolution-based strategy is proposed for frequency-time analysis that characterizes the intermittency of spatially coherent flow structures. When applied to the turbulent jet data, SPOD-based frequency–time analysis reveals that the intermittent occurrence of large-scale coherent structures is directly associated with high-energy events. Lastly, a new algorithm, gappy-SPOD, is developed that leverages the space-time correlation of SPOD modes to estimate missing data. Even for highly chaotic flows with up to 20% missing data, our method facilitates that structures associated with different time scales are well-estimated in the missing regions. For the cases considered here, it outperforms established techniques such as gappy-POD and Kriging.

In the second part, we investigate the nonlinear dynamics and controllability of coherent structures by actuating them. Large-eddy simulations (LES) of two unforced and four forced jets at $Re = 50,000$ and $M_j = 0.4$ were performed. The two unforced jets include an initially laminar and a turbulent jet. All four forced jets are turbulent and are forced at the azimuthal wavenumbers $m = 0$, $m = \pm 1$, $m = \pm 2$, and $m = \pm 6$. The unforced and forced jets were validated with companion experiments. Compared to the turbulent jet, the initially laminar jet develops later but at a faster rate, which is a result of the vortex pairing in the shear layer. The emphasis of the analysis is on characterizing the vortex pairing and the associated nonlinear energy transfer. Here, for the first time, we evaluate the spectral energy budget based on the leading modes of the SPOD. Our analysis reveals that energy flows from the fundamental to its subharmonic, resulting in the growth of the subharmonic. These results provide evidence for a previously

suggested parametric resonance mechanism. In the forced jets, we examine the effect of forcing using a recently proposed method, bispectral mode decomposition (BMD), which extracts flow structures associated with nonlinear triadic interactions. We use BMD to construct a cascade of triads and find that the most dominant triads arise due to fundamental self-interaction and second-harmonic-fundamental difference interaction. Furthermore, our analysis of the far-field in the unforced and $m = 0$-forced jets sheds light on the crucial role of difference-interactions in the generation of jet noise.

Chapter 1

Introduction

1.1 Motivation: Jet noise

Jets are one of the canonical flows that have been of significant interest to fluid dynamics researchers. They belong to the class of free shear flows that arise when a fluid emerges from a nozzle into the ambient surroundings. A circular jet transitions from laminar to turbulent at a Reynolds number of approximately 2000. The Reynolds number is a non-dimensional number defined as the ratio of the inertial forces to the viscous forces, $Re = \rho UD/\mu$, where ρ is the density, U is the velocity, D is the diameter, and μ is the dynamic viscosity. Turbulent jets have a wide range of practical applications, from industrial processes such as mixing and cooling to environmental phenomena like ocean currents and atmospheric turbulence. Understanding the complex dynamics of turbulent jets is therefore essential in a variety of fields, including engineering, physics, and atmospheric science. Many of the jets encountered in nature are turbulent. One such example is a jet emanating from aircraft engines. The reduction of jet noise is an important objective for the aviation community, as excessive noise can cause temporary or permanent hearing loss. The primary motivation for studying turbulent jets, other than scientific curiosity, is to identify the mechanisms behind the generation of jet noise.

Lighthill's eighth power law states that turbulence-generated sound intensity is directly proportional to the eighth power of airspeed (Lighthill, 1954). One way to reduce jet noise is by decreasing jet exit velocity, which can be achieved by increasing the bypass ratio of turbofan jet engines. Commercial turbofan jet engines have already increased their bypass ratio, but there are design limitations to further increase it. To address this issue, passive and active strategies have been developed to modify the flow. Passive strategies involve nozzle shape modifications such as chevrons and tabs, while active strategies involve adding mass or energy to excite flow instabilities or generate new flow structures. However, these control devices are often designed empirically and lack a mechanistic understanding that limits their scalability and improvement. In order to develop effective control strategies for jet noise, it is crucial to have a thorough understanding of the mechanisms that generate it. As noted by Jordan and Colonius (2013), there are still gaps in our understanding of jet noise that need to be filled in order to complete the "jigsaw puzzle" of this complex phenomenon. This dissertation aims to contribute to this effort by identifying and characterizing the sources and mechanisms of jet noise.

1.2 Sources of jet-noise: Large-scale coherent structures

Jet-noise can be categorized as near-field or far-field noise (Bowes et al., 2009), with the former referring to noise in the aircraft's vicinity and the latter to long-range noise beyond the airfield perimeter. Historically, attention has been focused on far-field noise due to its significant environmental impact during various flight conditions. Jordan and Colonius (2013) define the far-field region as a zone far from the vortical, turbulent motions where the wave equation can be approximated through linearization, and the wave field can be described as spherical waves originating from a point. Now, there is overwhelming evidence that far-field noise originates from the near-field of the jet, with the large-scale coherent structures in the shear layer being primarily responsible for jet noise production (Crow and Champagne, 1971).

The general process for jets appears to follow this sequence: The high-speed jet generates a shear layer in the immediate vicinity of the orifice. This shear layer is unstable and grows quickly, creating ring vortices that further pair up downstream and result in mixing and entrainment (List, 1982, Moore, 1977). The large-scale vortices that exhibit a *puff*-like structures are the sources of jet noise (Crow and Champagne, 1971). The pioneering works by Crow and Champagne (1971) and Brown and Roshko (1974) were the earliest to report the presence of large-scale coherent structures in turbulent jets and shear layers, respectively. Mollo-Christensen (1967) described them as intermittent spatial structures, or wavepackets, present in the mixing layer. These wavepackets were identified as the main source of aft-angle noise Jordan and Colonius (2013). The acoustic radiation of wavepackets is highly directive and concentrated in the downstream direction. The directive emission shows an exponential decay at high polar angles θ_p, or low jet inlet angle $\phi_j = 2\pi - \theta_p$, correspondingly. This pattern was termed *superdirective* radiation by Crighton and Huerre (1990). Cavalieri et al. (2012) have shown that the axisymmetric mode of the subsonic jets exhibits super-directivity. Tam et al. (2008) suggest that the jet noise in the downstream direction is associated with the large scales, whereas, in the sideline directions, it is associated with small-scale turbulence.

Wavepackets and their role in the generation of jet noise have been studied extensively using various methods of linear stability analysis and other perturbation formulations. Global stability analyses (Nichols and Lele, 2011, Schmidt et al., 2016), solutions to the parabolized stability equations (Gudmundsson and Colonius, 2011, Rodriguez et al., 2013, Rodríguez et al., 2013, Sinha et al., 2014) and the one-way Navier-Stokes equations (Rigas et al., 2017) have consistently identified Kelvin-Helmholtz (KH) instability waves and associated them with downstream radiation patterns. Numerical evidence for upstream travelling acoustic wave patterns in global modes has been presented by Nichols and Lele (2011) and Schmidt et al. (2017b). Similarly, multi-directive radiation patterns that include sideline and upstream radiation have been identified using resolvent analysis (Jeun and Nichols, 2018a, Jeun et al., 2016). The validity of

classical linear stability theory and resolvent analysis applied to mean flows has been confirmed by comparison with empirical modes obtained from high-fidelity simulation data using spectral proper orthogonal decomposition (Schmidt et al., 2018, Towne et al., 2018) and conditional space-time proper orthogonal decomposition (Schmidt and Schmid, 2019). According to the two-source modeling paradigm (Tam et al., 2008), jet noise in the sideline direction is associated with scales of dimensions much smaller than the jet diameter, referred to as small-scale turbulence by the authors. In accordance with the observation of upstream radiation patterns in modal solutions, as described above, Papamoschou (2018) showed that stochastic wavepacket models predict far-field noise at both low and high angles. Hence, even in subsonic and ideally expanded jets where mechanisms leading to upstream propagation of energy may be absent (Edgington-Mitchell, 2019), these results underpin the notion that large-scale coherent structures significantly contribute to the sideline and upstream radiation.

In recent years, there has been an upsurge in studies investigating the coherent structures present in turbulent jets, such as those conducted by Schmidt et al. (2018), Tissot et al. (2017a), Towne et al. (2018), **?**. Three prominent structures have been identified and extracted from these studies: KH-wavepackets, Orr-wavepackets, and streaks. The discovery of KH-wavepackets dates back to the works of Brown and Roshko (1974) and Winant and Browand (1974). These structures are reminiscent of convective instability, where a growing wave becomes neutral and decays eventually (Crighton and Gaster, 1976). Through resolvent analysis, researchers (Jeun et al., 2016, Schmidt et al., 2018) have demonstrated that KH wavepackets are initiated in the initial shear layer and are the most amplified structures from the nozzle's exit to the end of the potential core, i.e., $0 \leqslant x \leqslant 6$. In contrast, Orr-wavepackets and streaks correspond to non-modal instability waves. Orr-wavepackets are tilted structures that make an acute angle with the direction of the mean flow (Schmidt et al., 2018, Tissot et al., 2017a). They originate from the Orr mechanism, in which vortical structures are initially tilted opposite to the mean shear and are then aligned with the mean flow upon advection. As the tilt angle decreases from an obtuse angle to 90°, there is

algebraic energy growth of the fluctuations, followed by an energy decay when the angle is further reduced to $< 90^{\circ}$ (Jiménez, 2018, Lesshafft et al., 2019). Lastly, streaks are elongated regions of streamwise velocity and are formed due to the lift-up mechanism. Streamwise vortices eject high-speed fluid from the core of the jet and sweep low-speed fluid from the radially outward regions, resulting in the formation of streaks. The transient analyses of Jiménez-González and Brancher (2017) and Nogueira et al. (2019) reveal that the perturbations in the form of streamwise vortices will undergo the largest growth and evolve into streamwise elongated streaks.

In this thesis, turbulent jets at different Mach numbers are investigated to identify the most energetic patterns of acoustic radiation to the far-field. Radiation patterns to specific jet inlet angles are isolated and the source regions of these beams are traced back to the hydrodynamic-near field. Essentially, the goal is to identify the location of the source of acoustic radiation in different directions. Our findings have two main implications: (i) KH-wavepackets are the most significant sources of jet noise, and (ii) the sources of sideline and downstream radiation are closely connected.

1.3 Modal decompositon techniques

Turbulent flows are characterized by randomness. These flows exhibit an order within the randomness, consisting of coherent structures. These coherent structures play a vital role in our understanding of turbulence that helps in modeling and control of various mechanisms, for example, mitigating jet noise. The role of these structures at different scales becomes even more significant in flows at higher Reynolds numbers. The extraction of coherent structures and the curse of dimensionality (see, e.g., Meneveau et al., 1992) in the analysis of large turbulent flow data has led to the development of a number of modal decomposition techniques (Holmes et al., 2012).

The primary uses of modal decomposition techniques are to identify the essential features

of the flow and to represent the data in a lower-dimensional space. Most of these techniques seek modes that lie in the span of the snapshots that constitute the time-resolved data, and adhere to certain mathematical properties that define the decomposition. Arguably the most widely used technique is the proper orthogonal decomposition (POD), introduced by Lumley (1967, 1970). A specific flavor of POD, the computationally inexpensive method of snapshots (Aubry, 1991, Sirovich, 1987), decomposes the flow field into spatial modes and temporal coefficients. Its modes optimally represent the data in terms of its variance, or energy, and are coherent in space and at zero time lag. The POD is useful because it can capture a significant portion of energy in a small number of modes, and these modes are orthogonal to each other. Consequently, the POD has been widely used in model reduction, such as POD-based Galerkin models (Aubry et al., 1988, Noack et al., 2003, Rowley and Dawson, 2017). However, the information contained in each POD mode is a combination of different time scales, which makes it harder to interpret the underlying physics of the problem.

Another popular method is dynamic mode decomposition (DMD, Schmid, 2010), which is rooted in Koopman theory (Rowley et al., 2009) and assumes an evolution operator that maps the flow field from one snapshot to its next. The DMD modes are characterized by a single frequency and linear amplification rate. DMD decomposes the flow field into spatial modes and temporal coefficients, similar to POD, but unlike POD, it operates on the snapshots of the data and does not require the modes to be orthogonal to each other. DMD seeks modes that have a coherent spatiotemporal structure and evolve in time at a fixed frequency, which makes it particularly useful for studying systems that exhibit periodic or quasi-periodic behavior. The technique has been applied to a wide range of problems in fluid mechanics, such as turbulence (Schmid, 2010, Towne et al., 2018), flow control (Dawson et al., 2016, Proctor et al., 2016, Rowley et al., 2009), stratified flows (Nidhan et al., 2019, Ohh and Spedding, 2022), and reactive flows Schmid (2011). We refer to the review by Schmid (2022) for details on dynamic mode decomposition and its variants.

Spectral proper orthogonal decomposition (SPOD) is the frequency-domain variant of POD and computes modes as estimates of the eigenvectors of the cross-spectral density (CSD) matrix. At each frequency, SPOD yields a set of orthogonal modes, ranked by energy. The mathematical framework underlying SPOD was first outlined by Lumley (1967, 1970). Early implementations of SPOD include Arndt et al. (1997), Citriniti and George (2000), Delville (1994), Glauser and George (1992), Glauser et al. (1987), Picard and Delville (2000) and Gordeyev and Thomas (2000). For statistically stationary flows, Towne et al. (2018) have demonstrated that SPOD combines the advantages of POD, namely optimality and orthogonality, and DMD, namely temporal monochromaticity. SPOD also decouples the different time -scales of the flow which is helpful for understanding the flow dynamics and deriving non-empirical models. A number of studies showed that the dominant dynamics is often accurately captured by only a few modes (Citriniti and George, 2000, Glauser et al., 1987, Jung et al., 2004, Nidhan et al., 2020, 2022, Schmidt et al., 2018, Towne et al., 2018). Experimentally, Glauser et al. (1987), Citriniti and George (2000) and Jung et al. (2004) showed that a large fraction of the kinetic energy is contained in the first three SPOD modes. Recently, Schmidt et al. (2018) applied SPOD to high-fidelity simulation data of turbulent jets in the subsonic, transonic, and supersonic regimes. The authors give a detailed account of the Kelvin-Helmholtz and the Orr-type instability mechanisms that dominate the initial shear-layer and the region downstream of the potential core, respectively. SPOD has also been used to analyze a number of turbulent flows, including jets (Arndt et al., 1997, Gamard et al., 2004, Jung et al., 2004, Pickering et al., 2020, Schmidt et al., 2018), the wake behind a disk (Ghate et al., 2020, Johansson and George, 2006a, Johansson et al., 2002, Nidhan et al., 2020), pipe flows (Hellström et al., 2015, 2016, Hellström and Smits, 2014, 2017), and channel flows (Muralidhar et al., 2019). Recently it has also been extended for frequency-time analysis, gappy data reconstruction, and low-order modelling (Chu and Schmidt, 2021). In this work, we will show how SPOD can be extended for different applications. We will also employ SPOD to extract the dominant dynamics of the flow.

Another technique of interest is bispectral mode decomposition (BMD). In this dissertation, we excite the jets harmonically, which results in peaks at the forcing frequency and its harmonics. We employ BMD to characterize the nonlinear triadic interactions that are triggered by the forcing. Bispectral mode decomposition, proposed by Schmidt (2020), extracts the flow structures that are generated through triadic interactions. It identifies the most dominant triads in the flow by maximizing the spatially-integrated bispectrum. Furthermore, it picks out the spatial regions of nonlinear interactions between the coherent structures. BMD has been used to characterize triadic interactions in various flow configurations, such as laminar-turbulent transition on a flat plate (Goparaju and Gaitonde, 2022), forced jets (Maia et al., 2021a, Nekkanti et al., 2022), swirling flows (Moczarski et al., 2022), bluff body wakes (Nekkanti et al., 2023), and the wake of an airfoil (Patel and Yeh, 2023). Later in this work, we will also generalize this to the convective term in the Navier-Stokes equations to identify the direction of non-linear energy transfer.

The techniques discussed so far are inherently data-driven, i.e., they are based on optimizing second or third-order statistics. On the other hand, modal decomposition techniques, such as global linear stability analysis (Nichols and Lele, 2011) and resolvent analysis (McKeon and Sharma, 2010), take into account the linearized form of the governing equations. Global linear stability analysis converts the linearized equations of motion (initial-value problem) into an eigenvalue problem with respect to the base flow. The solution to this eigenvalue problem provides information on the spectrum of the linearized Navier-Stokes operator as $t \rightarrow \infty$. The resolvent operator, also based on the linearized equations, serves as a transfer function between the nonlinear forces and the corresponding responses. There exists a connection between SPOD and resolvent analysis. Towne et al. (2018) have shown that the SPOD modes and resolvent response modes are identical if the resolvent forcing modes are uncorrelated. For a comprehensive summary of various modal techniques, we refer the reader to the reviews by Taira et al. (2017) and Rowley and Dawson (2017).

1.4 Contribution and outline

The contributions of this thesis are divided into two parts. The first part focuses on the development of modal decomposition techniques, and the second part investigates the flow physics of turbulent jets. A summary of the contributions to these two aspects is listed below, which also serves as an outline for the remainder of the thesis.

1.4.1 Development of modal decomposition techniques for turbulent flows

In chapter 2 (Nekkanti and Schmidt, 2021a), we extend SPOD to four different applications: low-rank reconstruction, denoising, frequency–time analysis, and prewhitening. These are demonstrated on large-eddy simulation data of a turbulent jet. We propose two approaches, a frequency-domain and a time-domain approach, for low-rank reconstruction. The former is accomplished by a using direct inversion of the SPOD algorithm whereas the latter is based on the projection of the time series data onto the modes. We further present a SPOD-based denoising strategy that is based on hard thresholding of the SPOD eigenvalues. The proposed strategy achieves significant noise reduction while facilitating drastic data compression. Finally, a convolution-based strategy is proposed to compute the time-continuous expansion coefficients, which yields a spectrogram that characterizes the temporal evolution of spatially coherent flow structures. In contrast to standard methods of frequency–time analysis such as wavelet transform, this method characterizes the intermittency of the spatially coherent flow structures.

Chapter 3 (Nekkanti and Schmidt, 2023), focuses on the development of a new algorithm to reconstruct gaps or missing data in the flow field. Experimental measurements often suffer from gaps or other types of undesired artifacts. To reconstruct flow data in the compromised or missing regions, a data completion method based on spectral proper orthogonal decomposition is developed. The algorithm leverages the temporal correlation of the SPOD modes with preceding and succeeding snapshots, and their spatial correlation with the surrounding data at the same

time instant. For each gap, the algorithm first computes the SPOD of the remaining, unaffected data. In the next step, the compromised data are projected onto the basis of the SPOD modes. This corresponds to a local inversion of the SPOD problem and yields expansion coefficients that permit the reconstruction in the affected regions. This local reconstruction is successively applied to each gap. After all gaps are filled in, the procedure is repeated in an iterative manner until convergence. This method is demonstrated on two examples: direct numerical simulation of laminar flow around a cylinder and time-resolved PIV data of turbulent cavity flow obtained by Zhang et al. (2019). Randomly added gaps that correspond to 1%, 5%, and 20% of data loss are considered. Even for 20% data corruption and in the presence of measurement noise in the experimental data, the algorithm recovers 97% and 80% of the original data in the corrupted regions of the simulation and PIV data, respectively. Our method outperforms other established methods such as gappy POD and Kriging.

1.4.2 Investigating the flow physics of turbulent jets

In chapter 4 (Nekkanti and Schmidt, 2021b), we investigate the directivity of three large-eddy simulations of turbulent jets at Mach 0.7, 0.9, and 1.5. The most energetic patterns of acoustic radiation are extracted using the far-field pressure 2-norm. Specialization of the norm to the far field is accomplished through localized spatial weighting. Radiation patterns to specific jet inlet angles are isolated by further restricting the spatial weighting to small rectangular regions in the far field. We find that the most energetic radiation pattern for all cases and relevant frequencies is a single superdirective acoustic beam in the downstream direction. The source region of these beams is traced back to the end of the potential core for low frequencies and the shear-layer region for higher frequencies. In the sideline direction, to low jet angles, the acoustic patterns consist of beams that propagate upstream or perpendicular to the jet axis. The sideline radiation patterns originate from the same source locations as the dominant superdirective beams. We also find that the sideline radiation is directly linked to directive downstream radiation. Up until now, it has

been suggested by Tam et al. (2008) that the downstream radiation arises from the large-scale structures, whereas the sideline radiation is caused by the fine-scale structures. In contrast to this, our findings reveal that the large-scale coherent structures are the sources of both the sideline and downstream radiation.

In chapter 5 (Nekkanti et al., 2022), we perform large-eddy simulations of a turbulent unforced jet at $Re = 50,000$ and $M_j = 0.4$, and jets forced at azimuthal wavenumbers $m = 0$, $m = \pm 1$, $m = \pm 2$ and $m = \pm 6$. We validate the LES with the companion experiments at the Institut Pprime. The objective of this study is to characterize the nonlinear interactions that are initiated by the forcing. To achieve this, we used the bispectral mode decomposition (BMD) technique, which is tailored to extract flow structures associated with triadic interactions. The analysis reveals that triadic interactions in both forced and unforced jets are most prevalent in a well-defined region near and downstream of the closure of the potential core. Axisymmetric forcing generates peaks at the forcing frequency and its harmonics in the $m = 0$ component only, whereas non-axisymmetric forcing generates peaks at different azimuthal wavenumbers. The latter aspect is investigated using cross-BMD. Forcing the jet at $m = \pm 1$, the only odd-m forcing case considered, creates a cascade of triads that generates peaks at the forcing frequency and its odd harmonics at odd azimuthal wavenumbers and even harmonics at even azimuthal wavenumbers. Forcing the jet at $m = \pm m_f$ azimuthal wavenumbers produces peaks at the odd harmonics in the odd integer multiples of m_f and at even harmonic frequencies in the even integer multiples of m_f. A BMD analysis of far-field pressure sheds light on the previously reported observation that difference-interactions are more efficient radiators of jet noise than the sum-interactions.

In chapter 6, we perform large-eddy simulations of a turbulent and initially-laminar jet. Compared to the turbulent jet, the initially-laminar jet develops later but at a faster rate, resulting in a shorter potential core length and a hump in the RMS velocity along the centerline. We find that this is due to a stronger vortex-pariing in the shear-layer of the initially-laminar

jets. Here, our focus is on characterizing the vortex-pairing and the associated energy transfer. During this process, two sets of vortex pairing occur (*i*) two vortices of $St = 1.76$ pair to form an $St = 0.88$ vortex, and (*ii*) two $St = 0.88$ vortices pair to form an $St = 0.44$ vortex. Using local stability theory, we identify the fundamental as the most unstable frequency, which is $St = 1.76$. Next we compute the spectral energy budget, based on the leading modes of the spectral proper orthogonal decomposition, which reveals that energy is transferred from the fundamental to its subharmonic, resulting in the growth of the subharmonic. This transfer was found to be caused by the most dominant triads of (St_1, St_2, St_3) = (1.76,-0.88,0.88) and (0.88,-0.44,0.44). Our results are consistent with previous work by Monkewitz (1988), which demonstrated that the transfer was due to a resonance mechanism between the fundamental and subharmonic frequencies.

Part I

Development of modal decomposition techniques for turbulent flows

Chapter 2

Extension of SPOD for different applications: Low-rank reconstruction, denoising, frequency-time analysis, and prewhitening

2.1 Introduction

In the past, SPOD has been used to analyze a number of turbulent flows, including jets (Arndt et al., 1997, Gamard et al., 2002, 2004, Gordeyev and Thomas, 2000, 2002, Iqbal and Thomas, 2007, Jung et al., 2004, Nekkanti and Schmidt, 2021b, Pickering et al., 2020, Schmidt et al., 2018, Tinney et al., 2008a,b), the wake behind a disk (Ghate et al., 2020, Johansson and George, 2006a,b, Johansson et al., 2002, Nidhan et al., 2020, Tutkun et al., 2008), pipe flows (Hellström et al., 2015, 2016, Hellström and Smits, 2014, 2017), and channel flows (Muralidhar et al., 2019). Several studies have shown that a significant amount of energy is captured by the first few modes at each frequency. For jets and disk wakes, Glauser et al. (1987), Citriniti and

George (2000), Jung et al. (2004), Johansson and George (2006b), Tinney et al. (2008b) have shown that the leading mode and first three modes capture at least 40%, and 80% of the total energy, respectively. The above studies have on common that SPOD modes and eigenvalues are interpreted directly as physical structures and energies. The applications shown in this work, however, require a full or partial reconstruction of the data in the time domain (often after a manipulation of the expansion coefficients in the frequency domain). Partial reconstructions of the flow field from SPOD were previously shown by Citriniti and George (2000), Tinney et al. (2008b), and more recently, by Ghate et al. (2020). We demonstrate low-rank reconstruction using two approaches. One is by inverting the SPOD algorithm, which was previously employed by Citriniti and George (2000) in a similar manner, and for which we present an alternative means of computation based on convolution in the time domain. The other one is by taking an oblique projection of the data on the SPOD modes. The advantages and disadvantages of both approaches for different applications are discussed.

The first of these applications is denoising. Most experimental flow field data exhibit measurement noise that hampers the physical analysis. The computation of spatial derivatives required for quantities like the vorticity or strain rate, for example, leads to particularly large errors. Another difficulty is that physically relevant small-scale structures may be concealed by the noise. The most wide-spread experimental technique for multi-dimensional flow field measurement is particle image velocimetry (PIV). Common techniques to remove noise from PIV data include spatial filtering (Discetti et al., 2013), temporal filtering based on Fourier truncation, and POD-based techniques (Brindise and Vlachos, 2017, Raiola et al., 2015). Spatial filters are typically based on Gaussian smoothing (Discetti et al., 2013). Different temporal filters such as median filters (Son and Kihm, 2001), Hampel filters (Fore et al., 2005), Wiener filters (Vétel et al., 2011), and band-pass filters (Sciacchitano and Scarano, 2014) have been used for denoising PIV data. A comparison of different spatial and temporal filters is presented, for example, in Vétel et al. (2011). As an alternative to these standard techniques, POD reconstruction has been used as

a means of denoising through mode truncation. Low-dimensional reconstructions from standard POD have been applied for this purpose to flows past a backward-facing step (Kostas et al., 2005), arterial flows (Brindise et al., 2017, Charonko et al., 2010), turbulent wakes (Raiola et al., 2015), and vortex rings (Brindise and Vlachos, 2017, Stewart and Vlachos, 2012). In this contribution, we demonstrate the use of SPOD for denoising on surrogate data obtained by imposing high levels of additive Gaussian noise on simulation data. We demonstrate that SPOD-based denoising combines certain advantages of temporal filters and standard POD-based denoising.

Due to their chaotic nature, turbulent flows are characterized by high levels of intermittency. A common tool for the analysis of intermittent behaviour is frequency-time analysis, that is, the representation of the frequency content of a time signal as a function of time. This representation is particularly well-suited to identify events such as short-time interval of high or low energy, and identify their wave characteristics, i.e., frequencies or wavenumbers. Frequency-time analysis can be performed using several different signal-processing tools such as wavelet transforms (WT) (Farge, 1992), the short-time Fourier transform (STFT) (Cohen, 1995), the S-transform (Stockwell et al., 1996), the Hilbert-Huang transform (Huang et al., 1998), and the Wigner-Ville distribution (Boashash, 1988). Short-time Fourier and wavelet transforms are arguably the most widely used techniques in fluid mechanics. Frequency-time diagrams obtained from these methods are generally referred to as spectrograms, or as scalograms for wavelet transforms. STFT performs Fourier transforms on consecutive short segments of a time signal. It has been used, for example, in the analysis of blood flows (Izatt et al., 1997, Zhang et al., 2003), magnetohydrodynamics (Bale et al., 2005), aerodynamics (Samimy et al., 2007a), and physical oceanography (Brown et al., 1989). The wavelet transform is based on the convolution of the time signal with a compact waveform, the so-called mother wavelet, that is scaled to represent different frequencies. Typical applications of the WT are found in atmospheric science (Gu and Philander, 1995), oceanography (Meyers et al., 1993), and, most importantly for the present work, turbulence research (Farge, 1992). In the latter context, they have been used to extract coherent structures (Farge et al., 2001, 1999), and

analyze their intermittency (Camussi, 2002, Camussi and Guj, 1997, Onorato et al., 2000). All methods mentioned above are signal-processing techniques that are applied to one-dimensional data. Here, we expand on the ideas of Schmidt et al. (2017a) and Towne and Liu (2019), and analyse the intermittency of the entire flow field. The underlying idea is that the global dynamics of the entire flow field can be described in terms of a limited set of statistically prevalent, most energetic coherent flow structures. For statistically stationary flows, such structures are distilled by the SPOD, and their temporal dynamics are described by the SPOD expansion coefficients. Since SPOD is a frequency-domain technique, this idea leverages the fact that each SPOD mode is associated with a single frequency. Based on the two reconstruction techniques mentioned above, we apply analyze and compare two variants of SPOD-based frequency-time analysis. The frequency-domain approach relies on direct inversion of the SPOD algorithm and was previously demonstrated by Towne and Liu (2019). This approach, however, becomes computationally intractable even for moderate-sized, two-dimensional data. We show that this problem can be avoided by the convolution-based approach introduced herein.

Prewhitening is post-processing technique for trend detection that is commonly used in the atmospheric and geophysical sciences. It was first proposed by von Storch (1995). Prewhitening was used, for example, for the detection of trends in temperature and precipitation data (Zhang et al., 2001), rainfall (Lacombe et al., 2012), teleconnections (Rodionov, 2006), and hydrological flows (Khaliq et al., 2009, Serinaldi and Kilsby, 2015). Technically, prewhitening is achieved by a filtering operation that results in a flat power spectrum to remove serial correlations. We show two different SPOD-based ways to achieve this goal in the frequency domain.

The remainder of this paper is organized as follows. § 2.2 describes the two techniques for SPOD-based flow field reconstruction. In § 2.2.2.2, we demonstrate these techniques on numerical data of a turbulent jet. The four different applications, SPOD-based low-dimensional reconstruction, denoising, frequency-time analysis, and prewhitenening are demonstrated in § 2.3, § 2.4, § 2.5, and § 2.6, respectively. § 2.7 summarizes this work.

2.2 Methodology

2.2.1 Spectral proper orthogonal decomposition (SPOD)

In the following, we provide an outline of a specific procedure of computing the SPOD based on Welch's method (Welch, 1967) and emphasize aspects that are important in the context of data reconstruction. Refer to the work of Towne et al. (2018) for details of the derivation and mathematical properties and Schmidt and Colonius (2020) for a practical introduction to the method.

Given a fluctuating flow field $\mathbf{q}_i = \mathbf{q}(t_i)$, where $i = 1, \cdots, n_t$, that is obtained by subtracting the temporal mean $\bar{\mathbf{q}}$ from each snapshot of the data, we start by constructing a snapshot matrix

$$\mathbf{Q} = [\mathbf{q}_1, \mathbf{q}_2, \cdots, \mathbf{q}_{n_t}]. \tag{2.1}$$

Note that multi-dimensional data is cast into the form of a vector $\mathbf{q}_i$ of length n, corresponding to the number of variables times the number of grid points. The instantaneous energy of each time instant, or snapshot, is expressed in terms of a spatial inner product

$$\|\mathbf{q}\|_x^2 = \langle \mathbf{q}, \mathbf{q} \rangle_x = \int_\Omega \mathbf{q}^*(x',t)\mathbf{W}(x')\mathbf{q}(x',t)dx', \tag{2.2}$$

where $\mathbf{W}$ is a positive-definite Hermitian matrix that accounts for the component-wise weights, Ω the spatial domain of interest, and $(.)^*$ denotes the complex conjugate. The common form of space-only POD is obtained as the eigendecomposition of $\mathbf{QQ}^*\mathbf{W}$ and yields modes that are optimal in terms of equation (2.2). SPOD, however, specializes POD to statistically stationary processes and seeks modes that are optimal in terms of the space-time inner product

$$\|\mathbf{q}\|_{x,t}^2 = \langle \mathbf{q}, \mathbf{q} \rangle_{x,t} = \int_{-\infty}^{\infty} \int_\Omega \mathbf{q}^*(x',t)\mathbf{W}(x')\mathbf{q}(x',t)\mathrm{d}x'\mathrm{d}t. \tag{2.3}$$

For statistically stationary data, it is natural to proceed in the frequency domain and solve the POD eigenvalue problem for Fourier transformed two-point space-time correlation matrix, that is, the cross-spectral density matrix. To estimate the CSD, the data is segmented into n_{blk} overlapping blocks with n_{fft} snapshots in each of them.

$$\mathbf{Q}^{(k)} = \left[\mathbf{q}_1^{(k)}, \mathbf{q}_2^{(k)}, \cdots, \mathbf{q}_{n_{\text{fft}}}^{(k)}\right] \tag{2.4}$$

If the blocks overlap by n_{ovlp} snapshots, the j-th column in the k-th block is given by

$$\mathbf{q}_j^{(k)} = \mathbf{q}_{j+(k-1)(n_{\text{fft}}-n_{\text{ovlp}})+1}. \tag{2.5}$$

Each block is considered as a statistically independent realization of the flow under the ergodic hypothesis. The motive behind the segmentation of data is to increase the number of ensemble members. In practice, a windowing function is applied to each block to reduce spectral leakage. In this study, we use the symmetric hamming window

$$w(i+1) = 0.54 - 0.46\cos\left(\frac{2\pi i}{n_{\text{fft}}-1}\right) \quad \text{for} \quad i = 0, 1, \cdots, n_{\text{fft}}-1. \tag{2.6}$$

Following best practices established by Harris (1978), we only apply windowing for overlapping blocks to avoid excessive loss of information at the boundaries, i.e, if $n_{\text{ovlp}} \neq 0$. Subsequently, the weighted temporal discrete Fourier transform,

$$\hat{\mathbf{q}}_j^{(k)} = \mathcal{F}\left\{w(j)\mathbf{q}_j^{(k)}\right\}, \tag{2.7}$$

is performed on each windowed block to obtain the Fourier-transformed data matrix,

$$\hat{\mathbf{Q}}^{(k)} = \left[\hat{\mathbf{q}}_1^{(k)}, \hat{\mathbf{q}}_2^{(k)}, ..., \hat{\mathbf{q}}_{n_{\text{fft}}}^{(k)}\right], \tag{2.8}$$

where $\hat{\mathbf{q}}_i^{(k)}$ denotes the k-th Fourier realization at the i-th discrete frequency. Next, we reorganize the data by frequency. The matrix containing all realizations of the Fourier transform at the l-th frequency reads

$$\hat{\mathbf{Q}}_l = \left[\hat{\mathbf{q}}_l^{(1)}, \hat{\mathbf{q}}_l^{(2)}, \ldots \hat{\mathbf{q}}_l^{(n_{\mathrm{blk}})}\right]. \tag{2.9}$$

From this form, the SPOD modes, $\boldsymbol{\Phi}$, and associated energies, λ, can be computed as the eigenvectors and eigenvalues of the CSD matrix $\mathbf{S}_l = \hat{\mathbf{Q}}_l \hat{\mathbf{Q}}_l^*$. In practice, the number of spatial degrees of freedom, n, is often much larger than number of realizations. In that case, it is more economical to solve the analogous eigenvalue problem

$$\frac{1}{n_{\mathrm{blk}}} \hat{\mathbf{Q}}_l^* \mathbf{W} \hat{\mathbf{Q}}_l \boldsymbol{\Psi}_l = \boldsymbol{\Psi}_l \boldsymbol{\Lambda}_l \tag{2.10}$$

for the coefficients ψ that expand the SPOD modes in terms of the Fourier realizations. In terms of the column matrix $\boldsymbol{\Psi}_l = [\psi_l^{(1)}, \psi_l^{(2)}, \cdots \psi_l^{(n_{\mathrm{blk}})}]$, the SPOD modes at the l-th frequency are recovered as

$$\boldsymbol{\Phi}_l = \frac{1}{\sqrt{n_{\mathrm{blk}}}} \hat{\mathbf{Q}}_l \boldsymbol{\Psi}_l \boldsymbol{\Lambda}_l^{-1/2}. \tag{2.11}$$

The matrices $\boldsymbol{\Lambda}_l = \mathrm{diag}(\lambda_l^{(1)}, \lambda_l^{(2)}, \cdots, \lambda_l^{(n_{\mathrm{blk}})})$, where by convention $\lambda_l^{(1)} \geqslant \lambda_l^{(2)} \geqslant \cdots \geqslant \lambda_l^{(n_{\mathrm{blk}})}$, and $\boldsymbol{\Phi}_l = [\phi_l^{(1)}, \phi_l^{(2)}, \cdots, \phi_l^{(n_{\mathrm{blk}})}]$ contain the SPOD energies and modes, respectively. By construction, the SPOD modes are orthogonal in the space-time inner product, equation (2.3). At any given frequency, the modes are also orthogonal in the spatial inner product, equation (2.2).

2.2.2 Data reconstruction

In §2.2.2.1, we show how the data can be reconstructed in the frequency-domain, that is, the inversion of the SPOD. An alternative approach based on (oblique) projection in the time domain is presented in §2.2.2.2. Whether one approach or the other is preferred depends on the

specific application. Detailed discussions for each application under consideration in this work can be found in §2.2.2.2. We will use the term *frequency-domain* if the expansion coefficients are computed using the inversion of the SPOD problem, equation (2.13), and *time-domain* if oblique projection, equation (2.19), is used.

2.2.2.1 Reconstruction in the Frequency Domain

The common feature of the different applications of the SPOD considered in this study is that they require truncation or re-weighting of the SPOD basis. In practice, this is achieved by modifying the expansion coefficients. The original realizations of the Fourier transform at each frequency can be reconstructed as

$$\hat{\mathbf{Q}}_l = \mathbf{\Phi}_l \mathbf{A}_l, \tag{2.12}$$

where $\mathbf{A}_l$ is the matrix of expansion coefficients,

$$\mathbf{A}_l = \sqrt{n_{\text{blk}}} \mathbf{\Lambda}_l^{1/2} \mathbf{\Psi}_l^* = \mathbf{\Phi}_l^* \mathbf{W} \hat{\mathbf{Q}}_l. \tag{2.13}$$

Equation (2.13) shows that the expansion coefficients can either be saved during the computation of the SPOD or be recovered later by projecting the Fourier realizations onto the modes. In the following, we omit the frequency index l with the understanding that the SPOD eigenvalue problem is solved at each frequency separately. From equation (2.12), it can be inferred that each column of the matrix

$$\mathbf{A} = \begin{bmatrix} a_{11} & a_{12} & \cdots & a_{1n_{\text{blk}}} \\ a_{21} & a_{22} & \cdots & a_{2n_{\text{blk}}} \\ \vdots & \vdots & \ddots & \vdots \\ a_{n_{\text{blk}}1} & a_{n_{\text{blk}}2} & \cdots & a_{n_{\text{blk}}n_{\text{blk}}} \end{bmatrix}, \tag{2.14}$$

contains the expansion coefficients that allow for the reconstruction of a specific Fourier realization from the SPOD modes. *Vice versa*, the coefficients contained in each row of $\mathbf{A}$ can be used to

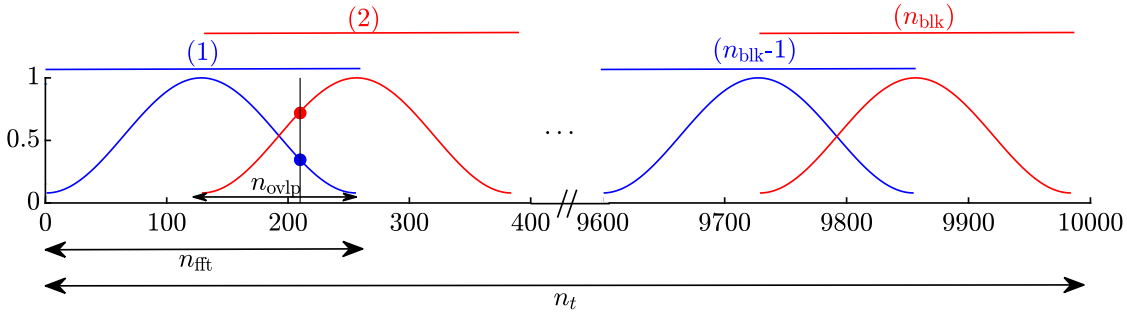

Figure 2.1: Schematic representation of overlapping blocks, Hamming window, and the SPOD parameters such as n_t, n_{fft}, n_{ovlp} and n_{blk}. The left, and right blocks are denoted using blue, and red lines, respectively. The vertical line corresponds to the snapshot number 210, and the blue and red circles indicate the corresponding value of the window function.

expand a specific SPOD mode in terms of the Fourier realizations. This can most easily be seen by rewriting equation (2.12) as $\boldsymbol{\Phi}_l = \frac{1}{n_{\mathrm{blk}}} \hat{\mathbf{Q}}_l \mathbf{A}_l^* \boldsymbol{\Lambda}_l^{-1}$. The Fourier-transformed data of the k-th block can be reconstructed as

$$\hat{\mathbf{Q}}^{(k)} = \left[\left(\sum_i a_{ik} \boldsymbol{\phi}^{(i)} \right)_{l=1}, \left(\sum_i a_{ik} \boldsymbol{\phi}^{(i)} \right)_{l=2}, \cdots, \left(\sum_i a_{ik} \boldsymbol{\phi}^{(i)} \right)_{l=n_{\mathrm{fft}}} \right]. \tag{2.15}$$

The original data in the k-th blocks $\mathbf{Q}^{(k)}$ can now be recovered using the inverse (weighted) Fourier transform,

$$\mathbf{q}_j^{(k)} = \frac{1}{w(j)} \mathcal{F}^{-1} \left\{ \hat{\mathbf{q}}_j^{(k)} \right\}. \tag{2.16}$$

Reconstructing the time series from the reconstructed data segments concludes the inversion of the SPOD.

A schematic of the windowing and blocking strategy is shown in figure 2.1. The use of overlapping blocks leads to an ambiguity in the reconstruction as the i-th snapshot can either be obtained from the k-th block as $\mathbf{q}_j^{(k)}$, or from the $(k+1)$-th block as $\mathbf{q}_{j+n_{\mathrm{ovlp}}-n_{\mathrm{fft}}}^{(k+1)}$. Different possibilities to remove this ambiguity are described in appendix 2.A. Based on this discussion, snapshots are reconstructed as averages of two reconstructions from overlapping blocks, weighted

by the relative value of their windowing function. Partial reconstructions in the frequency-domain are readily achieved by zeroing the expansion coefficients of specific modes prior to applying the inverse Fourier transform.

2.2.2.2 Reconstruction in the Time Domain

As an alternative to the reconstruction in the frequency domain, we present in the following a projection-based approach in the time domain. This approach is computationally efficient, and has the advantage that it can be applied to new data that was not used to compute the SPOD and to individual snapshots. However, the time-domain reconstruction does not leverage the orthogonality of the SPOD modes in the space-time inner product. Instead, it is based on an oblique projection of the data onto the modal basis. We start by representing the data as a linear combination of the SPOD modes as

$$\mathbf{Q} \approx \tilde{\mathbf{\Phi}}\tilde{\mathbf{A}}. \tag{2.17}$$

The matrix $\tilde{\mathbf{\Phi}}$ contains the basis of SPOD modes at all frequencies. Arranging the basis vectors by frequency first, we write

$$\tilde{\mathbf{\Phi}} = \left[\boldsymbol{\phi}_1^{(1)}, \boldsymbol{\phi}_1^{(2)}, \cdots, \boldsymbol{\phi}_1^{(n_{\mathrm{blk}})}, \boldsymbol{\phi}_2^{(1)}, \boldsymbol{\phi}_2^{(2)}, \cdots, \boldsymbol{\phi}_2^{(n_{\mathrm{blk}})}, \cdots, \boldsymbol{\phi}_{n_{\mathrm{fft}}}^{(1)}, \boldsymbol{\phi}_{n_{\mathrm{fft}}}^{(2)}, \cdots, \boldsymbol{\phi}_{n_{\mathrm{fft}}}^{(n_{\mathrm{blk}})}\right]. \tag{2.18}$$

Assuming that $\tilde{\mathbf{\Phi}}$ has full column rank, the matrix of expansion coefficient is obtained from the weighted oblique projection

$$\tilde{\mathbf{A}} = \left(\tilde{\mathbf{\Phi}}^* \mathbf{W} \tilde{\mathbf{\Phi}}\right)^{-1} \tilde{\mathbf{\Phi}}^* \mathbf{W} \mathbf{Q}. \tag{2.19}$$

The oblique projection is required as SPOD modes at different frequencies are not orthogonal in the purely spatial inner product, $\langle \cdot, \cdot \rangle_x$, defined in equation (2.2). We furthermore use a weighted oblique projection based on the weight matrix $\mathbf{W}$ to guarantee compatibility with this inner

product. Using the oblique projection, a single snapshot $\mathbf{q} = \mathbf{q}(\mathbf{x},t)$ is represented in the SPOD basis as

$$\tilde{\mathbf{q}} = \tilde{\mathbf{\Phi}}\left(\tilde{\mathbf{\Phi}}^*\mathbf{W}\tilde{\mathbf{\Phi}}\right)^{-1}\tilde{\mathbf{\Phi}}^*\mathbf{W}\mathbf{q}, \tag{2.20}$$

and the entire data is recovered as

$$\tilde{\mathbf{Q}} = \tilde{\mathbf{\Phi}}\tilde{\mathbf{A}}. \tag{2.21}$$

In the case where $\tilde{\mathbf{\Phi}}$ is rank deficient or ill-conditioned, $\tilde{\mathbf{\Phi}}^*\mathbf{W}\tilde{\mathbf{\Phi}}$ is not invertible. For a generally rank-r matrix, we perform the symmetric eigenvalue decomposition,

$$\tilde{\mathbf{\Phi}}^*\mathbf{W}\tilde{\mathbf{\Phi}} = \mathbf{U}\mathbf{D}\mathbf{U}^*, \quad \text{with} \quad \mathbf{U} = \left[\mathbf{U}_1\ \mathbf{U}_2\right],\ \mathbf{D} = \begin{bmatrix} \mathbf{D}_1 & \mathbf{0} \\ \mathbf{0} & \mathbf{0} \end{bmatrix}, \tag{2.22}$$

where $\mathbf{D}_1 = \mathrm{diag}(d_1, d_2, \cdots, d_r)$ with $d_1 \geqslant d_2 \geqslant \cdots \geqslant d_r > 0$ is the diagonal matrix of (numerically) non-zero eigenvalues and $\mathbf{U}_1$ is the corresponding matrix of orthonormal eigenvectors. In some applications, we desire a more aggressive truncation to rank $k < r$. For full-rank reconstructions, we use a truncation threshold of $\frac{d_k}{d_1} = 10^{-6}$ in this work. Denoted by

$$\tilde{\mathbf{A}}_{\{k\}} = \mathbf{U}_{\{k\}}\mathbf{D}_{\{k\}}^{-1}\mathbf{U}_{\{k\}}^*\tilde{\mathbf{\Phi}}^*\mathbf{W}\mathbf{Q} \tag{2.23}$$

is the rank-k approximation of $\tilde{\mathbf{A}}$, where $\mathbf{D}_{\{k\}} = \mathrm{diag}(d_1, d_2, \cdots, d_k)$ and $\mathbf{U}_{\{k\}} = [\mathbf{u}_1, \mathbf{u}_2, \cdots, \mathbf{u}_k]$. In the truncated basis, $\mathbf{U}_{\{k\}}\mathbf{D}_{\{k\}}^{-1}\mathbf{U}_{\{k\}}^*$ approximates $\left(\tilde{\mathbf{\Phi}}^*\mathbf{W}\tilde{\mathbf{\Phi}}\right)^{-1}$. In the following, we demonstrate how the above and other truncation and partial reconstruction strategies can be used to achieve a number of objectives in the processing of flow data.

Applications of SPOD: Low-rank reconstruction, denoising, frequency-time analysis, and prewhitening

In this section, four different uses of SPOD-based applications are introduced and demonstrated on the example of a turbulent jet. The theoretical background of each applications is presented in the context of the jet. In particular, low-dimensional reconstruction is discussed in §2.3, denoising in §2.4, frequency-time analysis in §2.5, and prewhitening in §2.6 respectively.

We consider the LES data of an isothermal subsonic turbulent jet, the Reynolds number, Mach number and temperature ratio are defined as $Re = \rho_j U_j D/\mu_j = 0.45 \times 10^6$, $M_j = U_j/c_j = 0.4$ and $T_j/T_\infty = 1.0$, respectively, where ρ is the density, U velocity, D nozzle diameter, μ dynamic viscosity, c speed of sound, and T temperature. The subscripts j and ∞ refer to the jet inlet and free-stream conditions, respectively. We use the large-eddy simulation data computed by Brès and Lele (2019). The simulation was performed using the compressible flow solver 'Charles' (Brès et al., 2017) on an unstructured grid using a finite-volume method. The reader is referred to Brès et al. (2018, 2019) for further details on the numerical method. The LES database consists of 10,000 snapshots sampled at an interval of $\Delta t c_\infty/D = 0.2$ acoustic time units. Data interpolated on a cylindrical grid spanning $x, r \in [0,30] \times [0,6]$ is used in this analysis. The flow is non-dimensionalized by the nozzle exit values, namely, velocity by U_j, pressure by $\rho_j U_j^2$, length by the nozzle diameter D, and time by D/U_j. Frequencies are reported in terms of the Strouhal number $St = fD/U_j$. For simplicity, and without loss of generality, we perform our analysis only on the pressure field in what follows. Refer to Freund and Colonius (2009) for analysis on different energy norms and POD modes of a jet. We further exploit the rotational symmetry of the jet and consider individual azimuthal Fourier components. The helical ($m = 1$) component provides an example of complex data.

To determine the spectral estimation parameters for the SPOD, we follow the guidelines provided in Schmidt and Colonius (2020) and Schmidt et al. (2018), which, in turn, follow

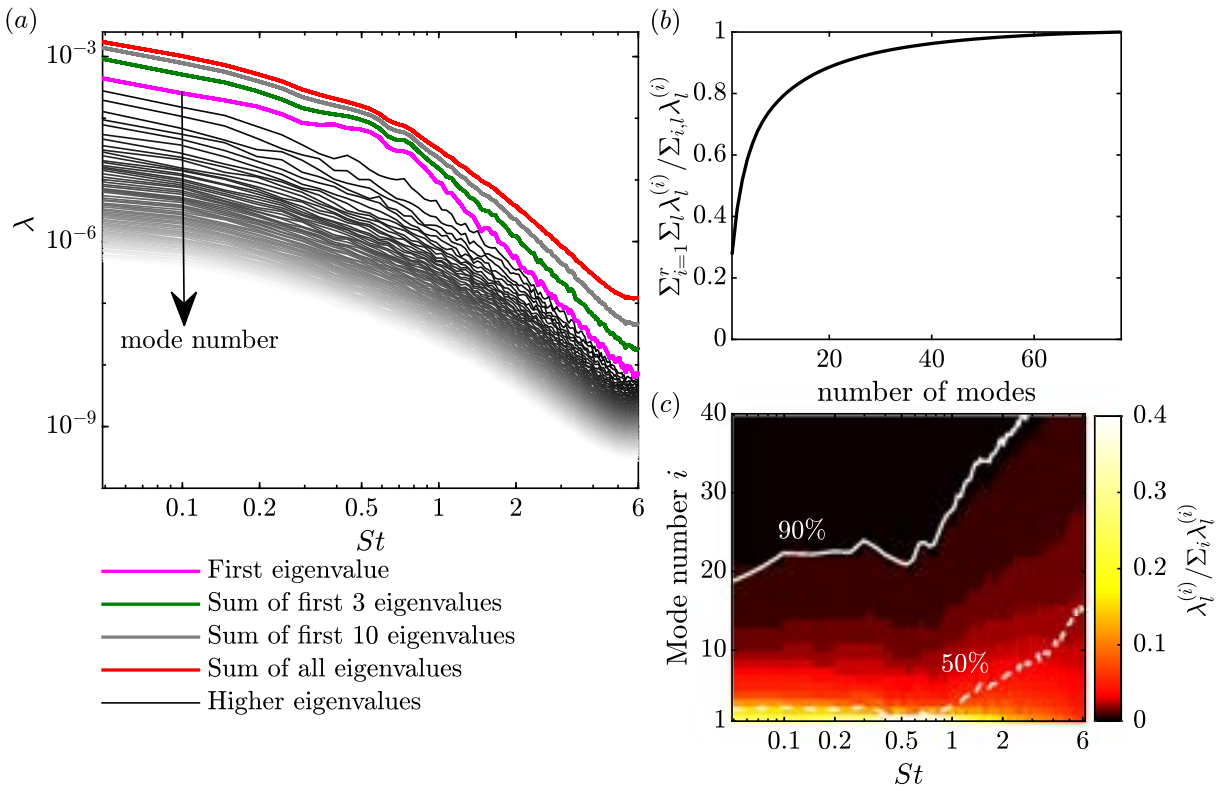

Figure 2.2: SPOD spectra of the turbulent jet for $m = 1$. All eigenvalues (gray lines) and the sum of all eigenvalues (red line), corresponding to the integral PSD, are shown. The normalized cumulative energy content and the percentage of energy accounted by each mode as a function of frequency are shown in (*b*) and (*c*), respectively. The solid and dashed white lines indicate the number of modes required to retain 90% and 50% energy at each frequency.

standard practice in spectral estimation. The SPOD is computed for blocks containing $n_{\text{fft}} = 256$ snapshots with 50% overlap, resulting in a total number of $n_{\text{blk}} = 77$ blocks. A 50% overlap is used to minimize the variance of the spectral estimate (Welch, 1967).

Since SPOD yields one set of eigenpairs per frequency, we may investigate the contributions of different frequencies independently. The SPOD eigenvalues are represented in the form of a spectrum, reminiscent to a power spectrum, in figure 2.2(a). Gray lines of decreasing intensity connect eigenvalues of constant mode number and decreasing mode energy. The first, most energetic mode is shown in magenta. The red line represents the sum of all eigenvalues and corresponds to the power spectral density (PSD) integrated over the physical domain. This line of the integral total energy can be compared to truncated sums of eigenvalues, that is, the energy contained in reconstructions of different ranks. As the eigenvalues are sorted by energy, the lines corresponding to the truncated sums of the leading 3 and 10 eigenvalues fall between the leading-eigenvalue spectrum and the total energy curve. Figure 2.2(b) shows the normalized cumulative energy content, independent of frequency. The first and the leading 10 modes contain 30% and 80% of the total energy, respectively. Figure 2.2(c) shows the percentage of energy accounted for by each mode as a function of frequency. At low frequencies, the first few modes contain a high percentage of energy, whereas the energy is more dispersed at higher frequencies. The solid and dashed white lines indicate the number of modes required to retain 50% and 90% of the total energy at each frequency.

The first and second modes at two representative frequencies are shown in figure 2.3. The frequency $St = 0.5$ corresponds to the maximum difference between first and second eigenvalues. The leading mode at this frequency shows a Kelvin-Helmholtz wavepacket (Gudmundsson and Colonius, 2011, Schmidt et al., 2018, Suzuki and Colonius, 2006) in the shear layer of the jet. A similar, but a more compact wavepacket structure is observed at $St = 1.0$. The suboptimal mode at both frequencies exhibit a multi-lobed wavepacket structure, whose amplitude peaks in near the end of the potential core at $x \approx 6$. The reader is referred to Schmidt et al. (2018) and Tissot

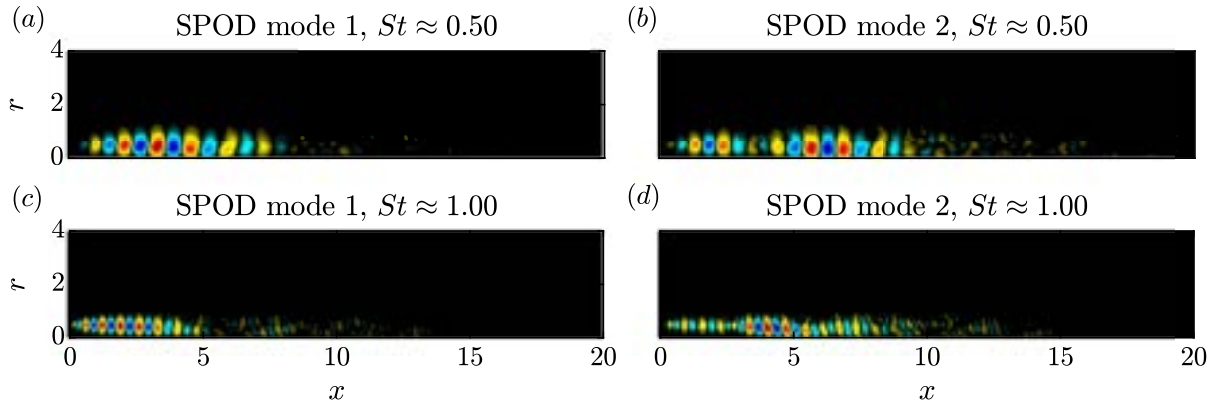

Figure 2.3: SPOD modes at $St = 0.5$ (a,b) and at $St = 1.0$ (c,d). The leading modes are shown in (a,c) and the suboptimal modes are shown in (b,d).

et al. (2017a) for a physical discussion of this observation and the link to non-modal instability. In the present context, our preliminary interest is in the desirable mathematical property of the SPOD that guarantee that the modes optimally represent the turbulent flow field in terms of the space-time inner product, equation (2.3). In the following, different uses of low-dimensional reconstructions that use SPOD modes as basis vectors are introduced and discussed.

2.3 Low-dimensional flow field reconstruction

Since SPOD seeks an optimal series expansion for each frequency, the choice of what eigenpairs to include in a low-dimensional reconstruction is not obvious. Here we first discuss the most elementary way of truncation based on the frequency-wise optimality property, that is, a certain number of modes is retained at each frequency. We refer to this as a $n_{\text{modes}} \times n_{\text{freq}}$-mode reconstruction, where n_{modes} is the number of modes retained at each frequency, and $n_{\text{freq}} = \frac{n_{\text{fft}}}{2} + 1$ is the number of positive frequencies, including zero. If all modes are linearly independent, the overall rank of the reconstructions is then given by the total number of basis vectors, $n_{\text{modes}} n_{\text{freq}}$.

Following the discussion in §2.2, we present two means of obtaining an SPOD-based low-dimensional reconstruction:

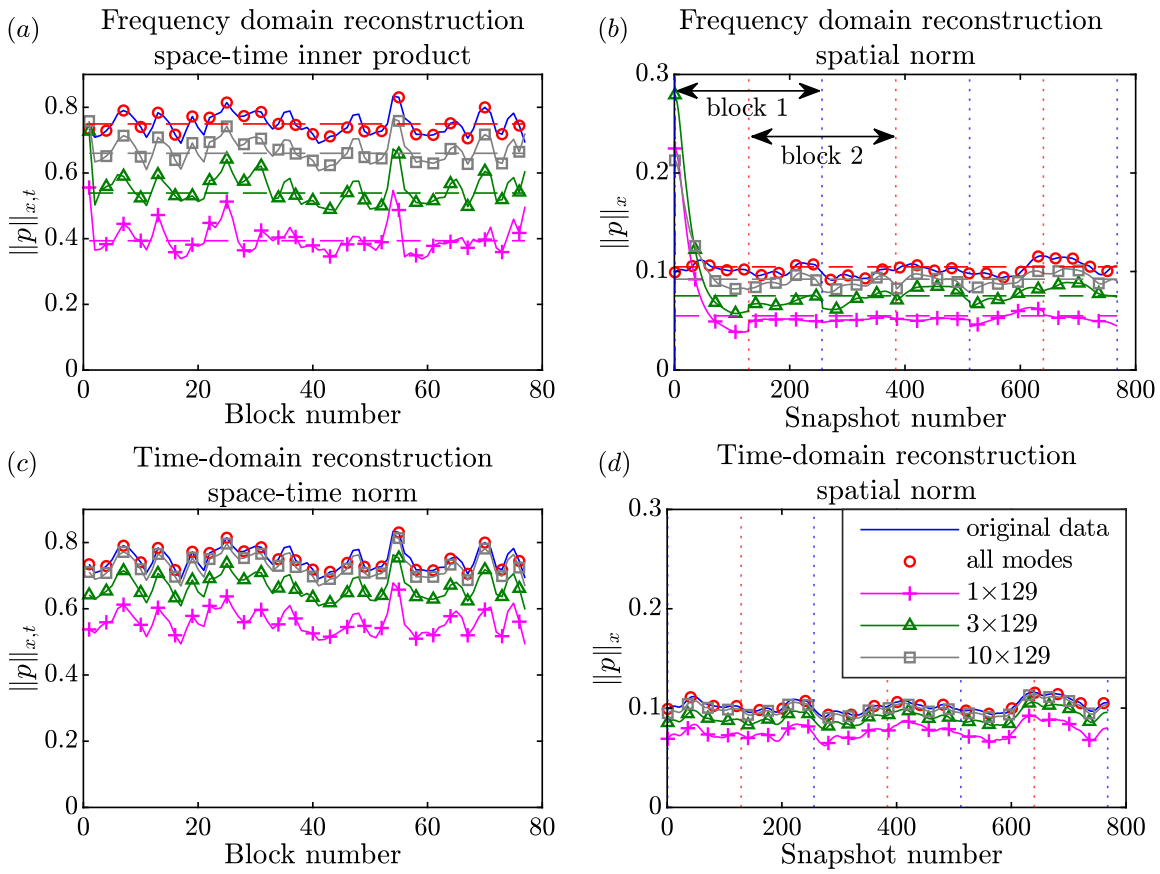

Figure 2.4: Low-dimensional reconstruction of the jet data: frequency-domain reconstruction (*a*,*b*), and time-domain reconstruction on the (*c*,*d*) in terms of the space-time norm (*a*,*c*) and the spatial norm (*b*,*d*). The original data (blue lines), shown for reference, is compared to the full reconstructions using all modes, and reconstructions using 10×129, 3×129, and 1×129 modes. Summed SPOD mode energies are shown as dashed lines. Vertical dotted blue and red lines in (*b*,*d*) indicate the left and right blocks in the reconstruction (see figure 2.1).

1. in the frequency domain (see §2.2.2.1) using equation (2.16), and

2. in the time domain (see §2.2.2.2) using equation (2.23).

The frequency-domain approach directly follows from the mathematical definition of the SPOD, and was previously used by Citriniti and George (2000), Johansson and George (2006b), Jung et al. (2004), Tinney et al. (2008a). The time-domain approach can be viewed as the most general approach that can be applied to any given modal basis. It is not specific to SPOD, but commonly used for low-order modeling.

In the following, we first compare different low-dimensional reconstructions in terms of their block-wise and snapshot-wise energy in figure 2.4. It follows from equation (2.3), that the energy of a single block is

$$\|\mathbf{q}\|_{x,t}^2 = \left\langle \mathbf{q}, \mathbf{q} \right\rangle_{x,t} = \int_{\Delta T} \int_{\Omega} \mathbf{q}^*(x',t)\mathbf{W}(x')\mathbf{q}(x',t)\mathrm{d}x'\mathrm{d}t, \tag{2.24}$$

where $\Delta T = [t_{1+(k-1)(n_{\mathrm{fft}}-n_{\mathrm{ovlp}})}, t_{n_{\mathrm{fft}}+(k-1)(n_{\mathrm{fft}}-n_{\mathrm{ovlp}})}]$ is the time interval of the k-th block. The spatial norm (2.2) measures the energy present in each snapshot. Both the block-wise and snapshot-wise pressure norms are computed for both reconstruction approaches. The evolution of the space-time norm is shown for the entire database in figure 2.4(a,c). For the spatial norm, we focus on the first 768 snapshots in figure 2.4(b,d). This segment corresponds to 5 blocks and exhibits dynamics that are representative of the rest of the data.

Low-dimensional reconstructions using 1×129, 3×129, 10×129 modes and the reconstruction using all modes are presented in figure 2.4. The dimension of the modal bases directly reflects their ability to capture the pressure norms of the data. The full-dimensional reconstructions in the frequency and time domain recover the data completely. Notably, the dynamics in space-time norm are accurately captured, even by the 1×129-mode reconstruction. For a fixed number of modes, the time domain approach captures more energy and provides a better approximation of the data than the frequency domain approach. Take as an example the 10×129 basis: the time-domain reconstruction accurately approximates for the full data (figure 2.4(c,d)), which is notably under-predicted by frequency-domain reconstruction (figure 2.4(a,b)). This difference can be understood by considering the SPOD energy content of the reconstruction. The dashed lines in figure 2.4(a,b) denotes this energy, which is given by the sum of first n_{modes} eigenvalues over all frequencies. As expected, the space-time and spatial norm of the different reconstructions fluctuate about the sum of the eigenvalues. Higher energies are obtained by the time-domain reconstruction in figure 2.4(c,d) as the modal expansion coefficients obtained via

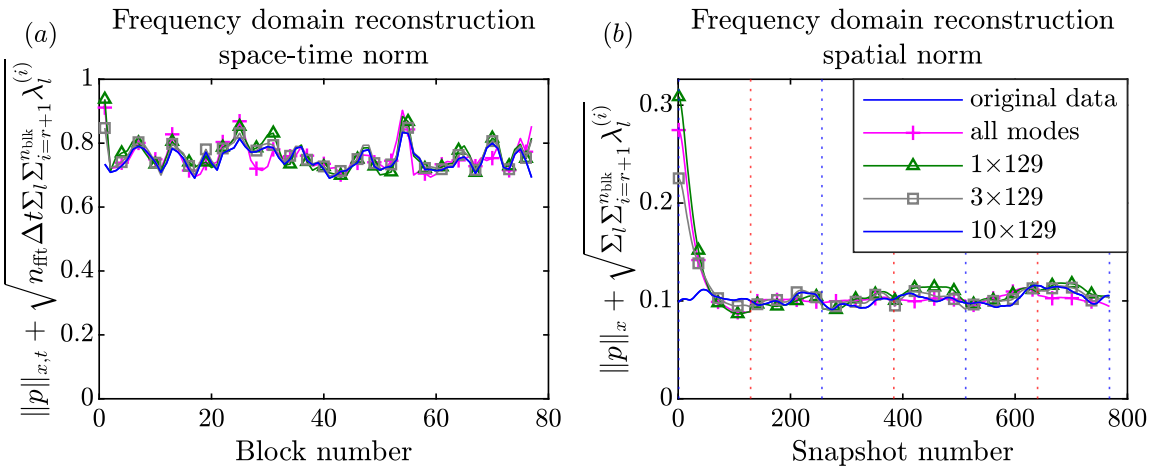

Figure 2.5: Low-dimensional reconstruction in the frequency-domain with truncation correction: (*a*) space-time norm; (*b*) spatial norm. Parts (*a*) and (*b*) correspond to figure 2.4(*a*) and (*b*), respectively, but with a correction for the truncated modes. The correction is facilitated by adding the energies of the truncated modes (given by their SPOD eigenvalues).

oblique projection are not bound to specific frequencies. In what follows, we will see again and again that this flexibility of the expansion coefficients of the time-domain approach leads to an overall better reconstruction. This additional degree of freedom can be leveraged to obtain an accurate reconstruction of the flow dynamics. It is, in fact, the optimality property of the oblique projection, equation (2.23), that guarantees that the time-domain approach yields the best possible approximation in a least-square sense. For example, the 1×129 time-domain reconstruction seen in figure 2.4(*d*) is sufficient to capture the dynamics of the original data accurately. From figure 2.4(*b*), it can be seen that the frequency-domain reconstruction significantly over-predicts the pressure norm during the first 32 snapshots. This effect only occurs for the two out-most blocks, which do not posses neighbouring blocks in one direction. In appendix 2.A (figure 2.A.2), we show by comparison with rectangular window that this error is a result of the Hamming window. The presence of the windowing-effect in the first and last blocks is equally reflected in the space-time norm, see figure 2.4(*a*).

Figure 2.5 demonstrates that the frequency-domain approach accurately recovers the mode energies given by the SPOD eigenvalues. By adding the residual energy contained in the truncated

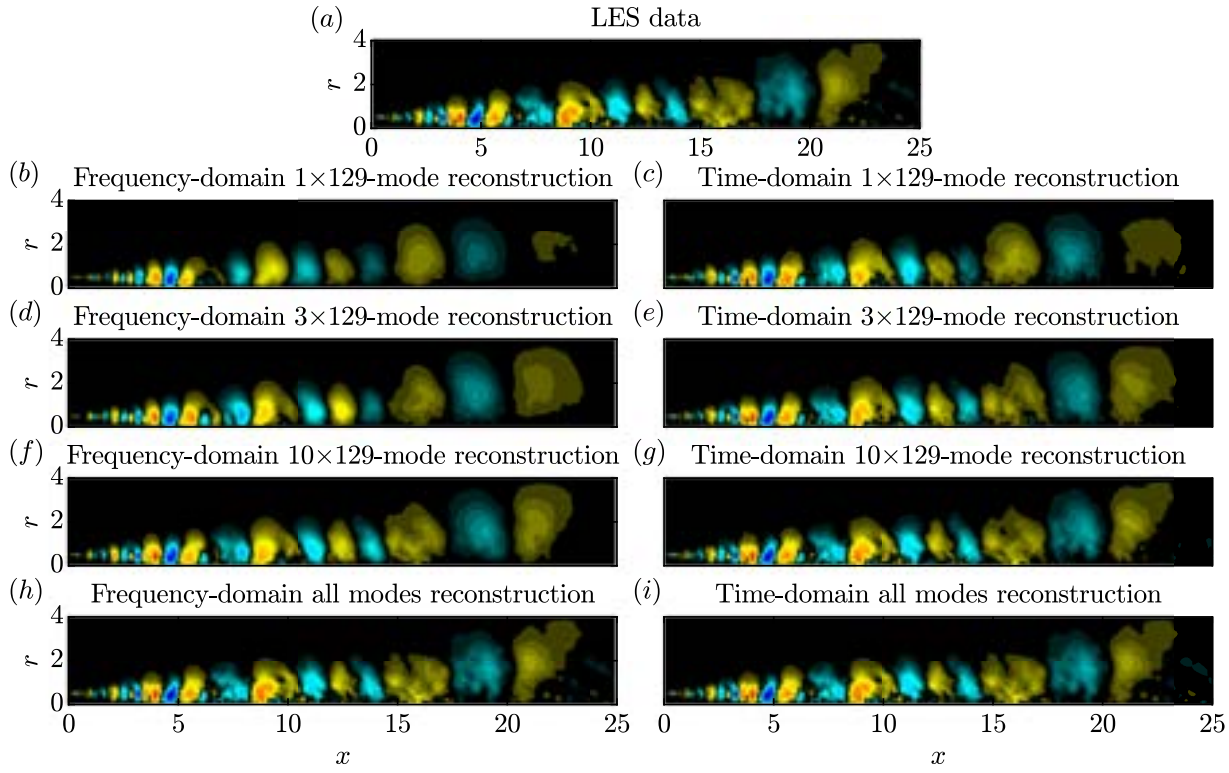

Figure 2.6: Instantaneous pressure field: (*a*) original flow field is shown; (*b*,*d*,*f*,*h*) reconstructions in the frequency domain; (*c*,*e*,*g*,*i*) reconstructions in the time domain. Flow fields reconstructed using 1×129 modes, 3×129 modes, 10×129 modes, and all modes are shown in (*b*,*c*), (*d*,*e*), (*f*,*g*), and (*h*,*i*), respectively. Contours in (*a*-*i*) are reported on the same color axis.

eigenvalues, both the space-time norm (figure 2.5(*a*)) and the spatial norm (figure 2.5(*b*)) can be collapsed to the total energy. The remaining differences are largely due to the windowing effect.

Figure 2.6 compares a single time instant of the original data in (*a*) with reconstructions of increasing fidelity in the frequency (left) and the time domain (right). Both the 1×129-mode reconstructions shown in figure 2.6(*b*,*c*) capture the dominant wavepackets. However, the frequency-domain reconstruction lacks the detail of the time-domain reconstruction. The higher accuracy of the time-domain reconstruction can be explained by its less stringent nature. As the leading SPOD modes often represent a spatially highly confined structure, other structures associated with the same frequency cannot be represented by the frequency-domain reconstruction. The KH-type wavepacket seen in figure 2.3(*c*) is a good example of such a confined structure. This

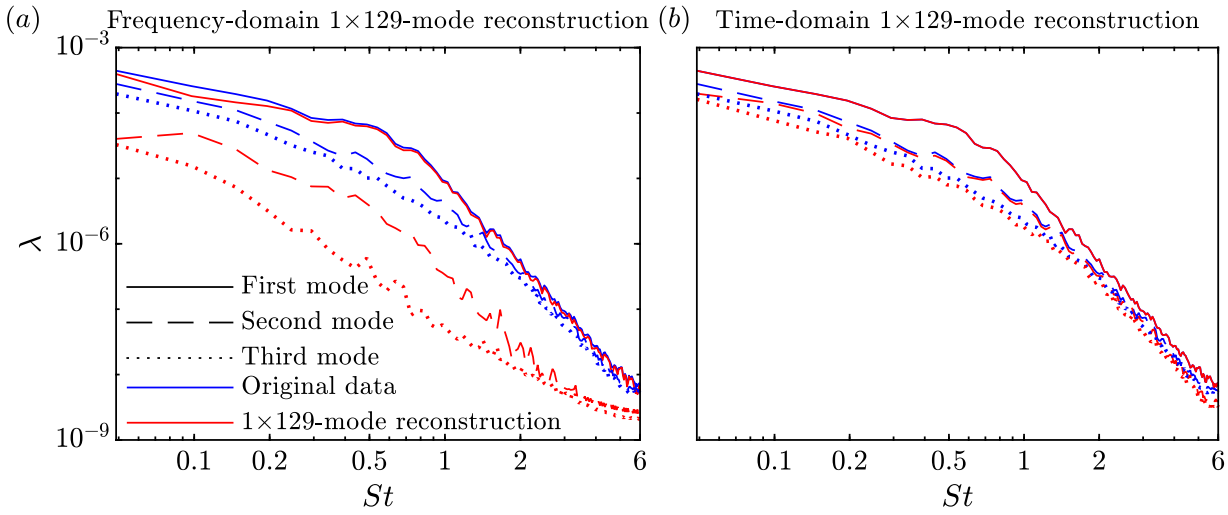

Figure 2.7: Comparison between SPOD eigenvalue spectra of the original data (blue lines) and 1×129-mode reconstructions (red lines): (*a*) frequency-domain; (*b*) time-domain. Solid, dashed, and dotted lines denote the first, second, and third modes, respectively.

difference between the approaches also explains the better reconstruction of the integral energy in the time domain, as previously observed in figure 2.4. The higher-dimensional versions for both approaches shown in figure 2.6(*d*-*g*) yield increasingly more detailed and accurate reconstructions. Both approaches yield reconstructions that are indistinguishable from the original data when all modes are used (see figure 2.6(*h*,*i*)).

We infer from figures 2.4 to 2.6 that reconstruction in the time-domain provides a better estimate of the flow field than the frequency-domain version. To understand this observation, figure 2.7 reports the SPOD eigenspectra of the 1×129-mode reconstructions and compares them to those of the full data. Only the leading three eigenvalues are shown for clarity. The leading eigenvalue of the frequency-domain reconstruction in figure 2.7(*a*) approximately follows the full data with some discrepancies at lower frequencies. No such discrepancies are observed for the time-domain reconstruction in figure 2.7(*b*); in fact, the leading eigenvalue spectra are indistinguishable. Contrast this observation with the expectation that a $1\times n_{\text{freq}}$ frequency-domain reconstruction should exactly reproduce the leading-mode eigenspectrum, and that all higher-eigenvalue spectra are expected to be zero. In the context of figure 2.A.3 in appendix 2.A, we

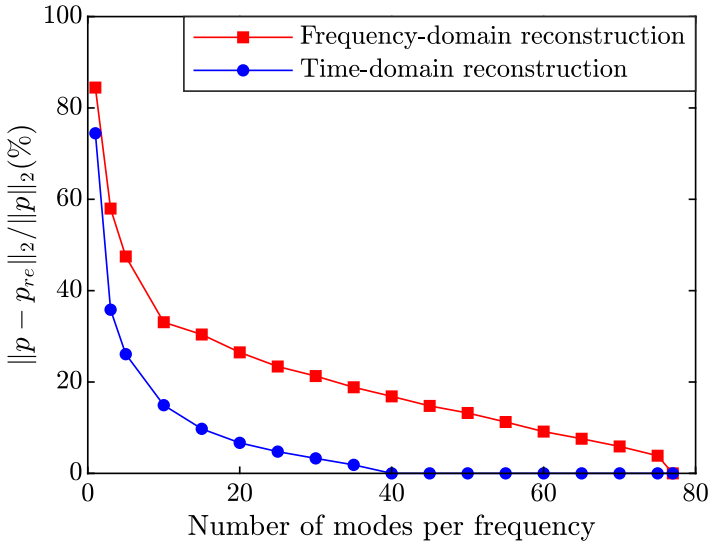

Figure 2.8: Two-norm error of the pressure field reconstructed with different rank approximation: (red lines with squares) reconstruction in the frequency domain; (blue lines with circles) reconstruction in the time domain.

show that this is an effect of windowing that is not observed when using a rectangular window. The time-domain reconstruction, on the other hand, accurately approximates the first, and, to some degree, the leading suboptimal eigenvalue spectra. This again demonstrates the higher accuracy of the time-domain reconstruction that results from the higher flexibility of the expansion.

To quantify the accuracy of the two approaches, figure 2.8 compares their 2-norm errors as a function of the number of basis vectors (modes). For both the methods, the error reduces significantly as the number of modes retained per frequency increases from one to ten. For a fixed number of modes, the time-domain reconstruction is consistently more accurate. Recall that this is guaranteed by the optimality property of the oblique projection. It is, in fact, observed that the error of the time-domain reconstruction approaches machine precision for 40 or more modes per frequency. For the frequency-domain approach this only occurs for the full reconstruction using all modes.

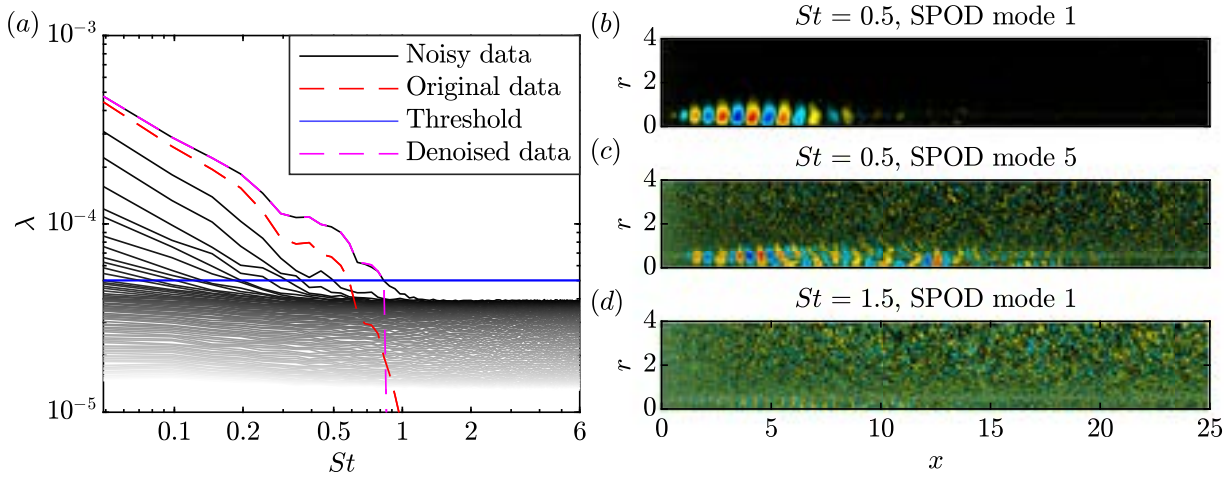

Figure 2.9: SPOD of data subjected to additive Gaussian white noise: (*a*) SPOD spectrum (black lines), leading SPOD eigenvalue of the original data (red dashed line), threshold of 5×10^{-5} (blue line), and the leading SPOD eigenvalue of the denoised data (magenta dashed line); (*b*) leading SPOD mode at $St = 0.5$; (*c*) fifth SPOD mode at $St = 0.5$; (*d*) leading SPOD mode at $St = 1.5$.

2.4 Denoising

After using SPOD truncation for low-dimensional approximation above, we now explore its potential for denoising. We will show that additive noise is captured by certain parts of the spectrum, and that truncation of these parts leads to efficient denoising. This strategy is most efficiently implemented in the frequency domain. The local-in-time optimality of the time-domain approach is a hindrance in this context as it tends to reconstruct the noise. On the contrary, the one-to-one correspondence between modes and frequencies of the frequency domain approach leads to efficient denoising.

As the arguably most common type of noise occurring in experimental environments, we demonstrate denoising on additive Gaussian white noise. In particular, we add Gaussian white noise that has a standard deviation equal to the spatial mean of the standard deviation along the lipline ($r = 0.5$) of the pressure data. This scenario mimics, for example, heavily contaminated particle image velocimetry data in which the variance of the noise is of the same order as the variance of the physical phenomena of interest. The SPOD eigenvalue spectrum of this noisy data

is shown in figure 2.9(a). Most noticeably, the addition of noise has introduced a noise floor at $\lambda \approx 4 \cdot 10^{-5}$, effectively cutting off the spectrum at $St \approx 1.5$. Information above this frequency lies below the noise floor and is not directly accessible. The leading eigenvalue of the original data (red dashed line) is shown for comparison. It lies well below the leading eigenvalue of the noisy data, which is elevated due to the energy contained in the added noise. To illustrate the ability of SPOD to differentiate between spatially correlated, physical structures and noise, examples of modes that are above and below the noise floor are compared in figure 2.9(b-d). The leading mode at $St = 0.5$ (figure 2.9(b)) clearly reveals the K-H wavepacket and is indistinguishable from the corresponding mode of the original data shown in figure 2.3(a) above. The fifth mode at $St = 0.5$ (figure 2.9(c)) and the leading mode at $St = 1.5$ (figure 2.9(d)), on the contrary, are heavily contaminated by noise. The noise floor in the SPOD spectrum is found to be a very good indicator of this distinction. We hence propose a denoising-strategy based on hard-thresholding of the spectrum. In this example, we pick a threshold of 5×10^{-5} (blue line), slightly above the noise floor. To address the effect of the truncation on the SPOD spectrum, we report the leading SPOD eigenvalue of the denoised data (magenta dashed line) in the same figure. It coincides with the leading eigenvalue of the noisy data up to the point where it intersects with the threshold limit, beyond which it falls off sharply, giving it the characteristics of a low-pass filter. A closer analysis of the truncated and original spectra reveals that the denoised field contains only 2.6% energy of the noisy field, but that it contains 92.7% energy of the original flow field. Another positive side effect is that only 74 out of 9933 modes ($n_{\text{freq}} \times n_{\text{blk}}$) have been retained, resulting in a space saving of 99.26%. These significant space savings are an advantage over standard denoising strategies based on low-pass filtering.

A representative instantaneous snapshots of the original data is compared to its noisy and denoised counterparts, and to the result of standard low-pass filtering in figure 2.10. The standard low-pass filter uses the cut-off frequency of $St = 0.8$ of the SPOD approach (inferred from figure 2.9) in the truncation of the long-time Fourier transform. A higher threshold, and its associated

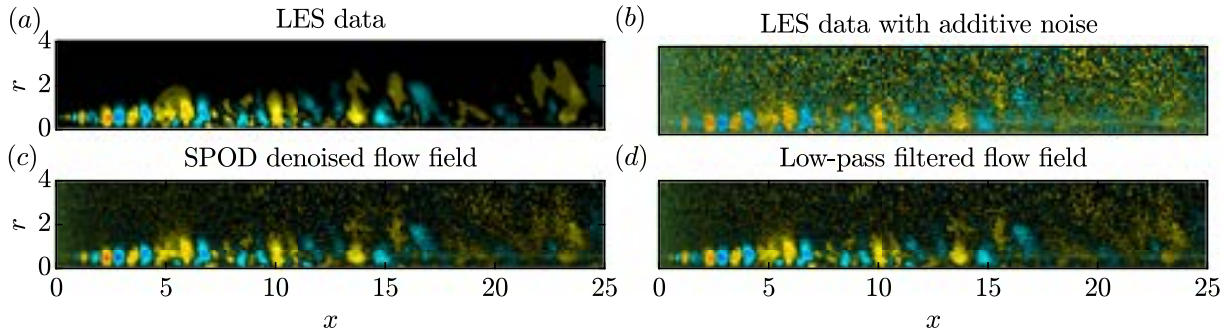

Figure 2.10: Comparison of noisy and denoised instantaneous pressure fields: (*a*) original; (*b*) data with additive Gaussian white noise; (*c*) SPOD-based denoised flow field; (*d*) low-pass filtered flow field. Denoising is achieved by rejecting all SPOD eigenpairs with $\lambda < 5 \times 10^{-5}$. This hard threshold is indicated in figure 2.9.

cut-off frequency, was found to lead to more aggressive filtering that can partially remove relevant flow structures. A threshold below the noise floor, on the other hand, leads to unsatisfactory noise rejection. In practice, a good trade-off between noise rejection and preservation of physically relevant flow structures is achieved by using the SPOD spectrum as a gauge to choose a threshold slightly above the noise floor. A comparison of the denoised data in figure 2.10(*c*,*d*) with the noisy data in figure 2.10(*b*) shows that significant noise reduction was achieved in all parts of the domain using both strategies. The resulting denoised flow fields clearly reveal the flow structures present in the original data. By visual inspection of the filtered pressure fields shown in figures 2.10(*c*) and 2.10(*d*), the SPOD-based strategy appears somewhat more efficient at removing the noise.

For a more quantitative assessment, we compare the denoised flow fields in terms of two quantities. First, their signal-to-noise ratio (SNR) along the lipline, and second, the relative error between the denoised snapshots and the original data. The SNR is defined as

$$\mathrm{SNR} = \frac{P_{\mathrm{signal}}}{P_{\mathrm{noise}}} = \frac{\sigma^2_{\mathrm{signal}}}{\sigma^2_{\mathrm{noise}}}, \tag{2.25}$$

where P is power and σ standard deviation. We further define the integral (over the physical

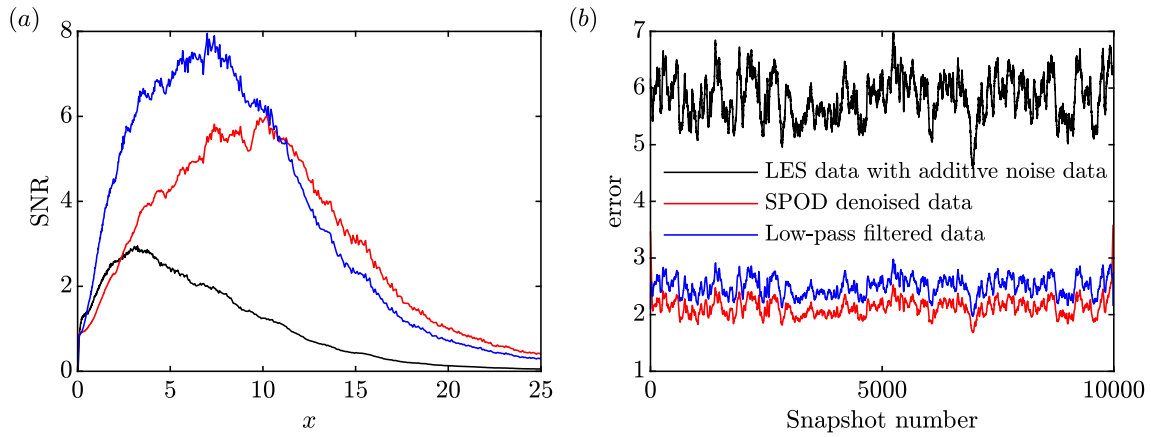

Figure 2.11: Comparison of the two denoising strategies: (*a*) signal to noise ratio (SNR) along the lipline ($r = 0.5$) for the noise added flow field (black line), SPOD-based denoised flow field (red lines), and the low-pass filtered flow field (blue line); (*b*) error of the noisy data, SPOD-based denoised data, and the low-pass filtered data. The amplitude of the additive noise was adjusted such that the average SNR along the lipline is one.

domain) error as

$$\text{error} = \frac{\|\mathbf{q} - \check{\mathbf{q}}\|_x}{\|\mathbf{q}\|_x}, \tag{2.26}$$

where $\mathbf{q}$ and $\check{\mathbf{q}}$ are the original and the denoised flow fields, respectively. Figure 2.11(*a*) compares the SNR along the lipline at $r = 0.5$ for the noisy and the denoised flow fields. Both methods are able to increase the signal-to-noise ratio over large parts of the domain. The low-pass filter performs better for $x \lesssim 10$, and the SPOD-based filter beyond that point. For $x \lesssim 2.5$, the SPOD-filtered pressure field exhibits a marginally lower SNR than the unfiltered data. We find that this is the results of the aggressive truncation of high-frequency components by the SPOD-based filter. A result that is almost identical to that of the low-pass filter can be achieved by lowering the λ-threshold (a similar value for both methods is used here for consistency). Figure 2.11(*b*) compares the time traces of the errors of the noisy and the two denoised flow fields. The error of the noisy data serves as a reference, and it is observed that both methods significantly reduce this error. The SPOD-based approach performs consistently better than the low-pass filter. This result is consistent with the visual observation of the denoised fields in figure 2.10(*c*,*d*). Note that

the threshold is an adjustable parameter in both methods. In practice, we find that by adjusting this parameter qualitatively very similar results can be obtained by both methods. This, however, leaves the SPOD-based approach with the advantage of significant data reduction.

2.5 Frequency-time analysis

Intermittency, that is the occurrence of flow events at irregular intervals, is an inherent feature of any turbulent flow. A common approach for the characterization of intermittent behaviour is frequency-time analysis. Arguably the most widespread tools of frequency-time analysis are wavelet transforms and short-time Fourier transform. Their outcomes are scalograms and spectrograms, respectively, that indicate the presence of certain scales (WT) or frequency components (STFT) at certain times. Both methods are signal-processing techniques that are applied to 1-D time series, and therefore only quantify intermittency locally. As an alternative to this local perspective, we demonstrate how SPOD expansion coefficients can be used to study intermittency of the spatially coherent flow structures represented by the modes. Below, frequency-time analyses based on both time-domain and frequency-domain reconstructions are introduced and compared.

2.5.1 Time-domain approach

We first consider the time-domain approach, in which the expansion coefficients obtained via oblique projection readily describe the temporal behaviour of each mode. The amplitudes of the expansion coefficients computed from equation (2.19), $|\sum_{j=1}^{n_{\text{modes}}} \tilde{a}^{(j)}(f_l,t)|$, hence yield the desired frequency-time representation for the leading n_{modes}. The expansion coefficients are calculated using the full basis, i.e, $\tilde{\phi}$ in equation (2.18) consists of all modes at all frequencies. Subsequently, we only consider the expansion coefficients of the leading n_{modes} modes at each frequency. An alternative approach is to perform the oblique projection using a reduced basis

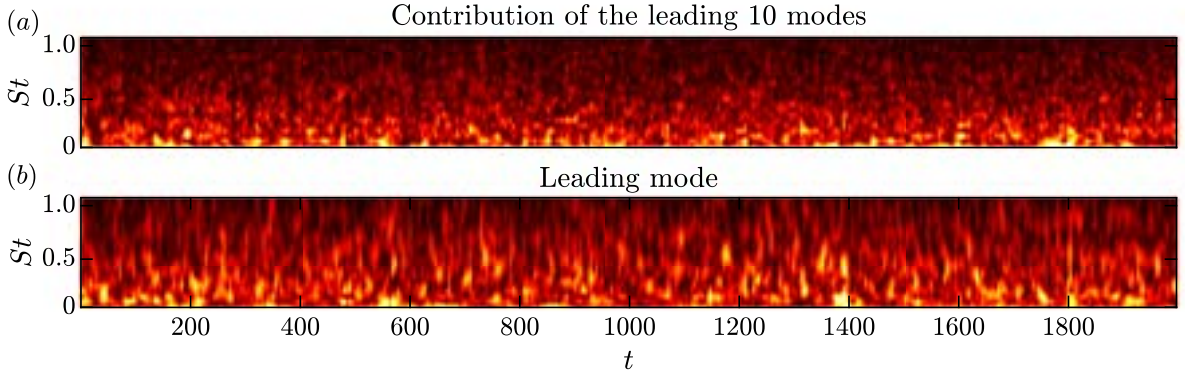

Figure 2.12: SPOD-based frequency-time diagrams obtained using the time-domain approach: (*a*) first 10 modes at each frequency; (*b*) leading mode at each frequency. The SPOD of the pressure field is considered.

that consists of only the leading n_{modes} modes at each frequency. We find that the first approach is preferable in the context of frequency-time analysis and is explained in the appendix 2.B (see figure 2.B.1). The frequency-time diagrams for $n_{\text{modes}} = 10$, and 1, are shown in figure 2.12(*a*), and (*b*), respectively. The leading 10 modes correspond approximately to 80% of the total energy as shown in figure 2.2(*b*). Most of the energy is concentrated at low frequencies, $St \lesssim 0.2$, as expected from the eigenvalue spectrum in figure 2.2. The eigenvalue spectrum provides a statistical representation of the structures that are coherent in space and time, whereas the frequency-time diagrams provide a temporal information of these structures. Bright yellow spots indicate high similarity of the instantaneous flow field with the leading mode in (*b*). These regions also correspond to high energy events as we will show in figure 2.14.

2.5.2 Convolution-based approach

A direct way of using SPOD for frequency-time analyses is in terms of the SPOD expansion coefficients. Since each block is associated with a finite time interval, this approach requires the computation of the SPOD using an overlap of $n_{\text{ovlp}} = n_{\text{fft}} - 1$ to obtain time-resolved coefficients (Towne and Liu, 2019). This approach assumes that the value of the expansion coefficient obtained from a finite time segment (block) represents the instantaneous frequency

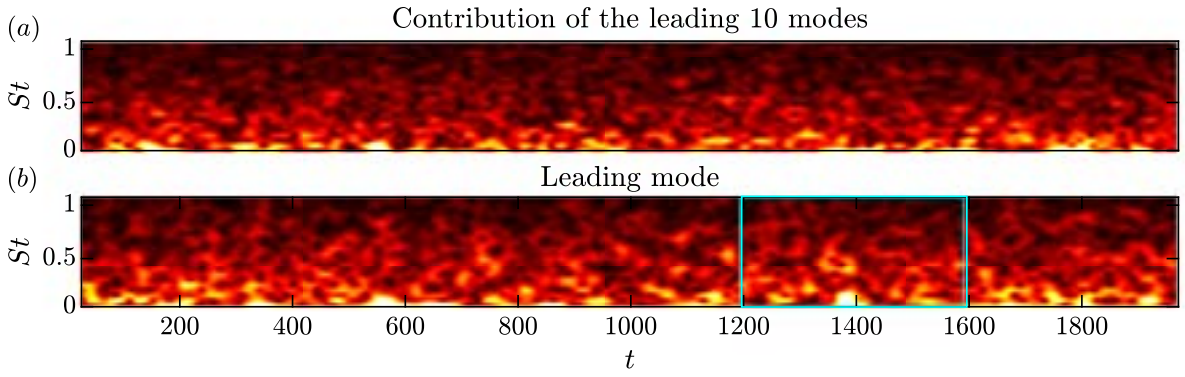

Figure 2.13: SPOD-based frequency-time diagrams obtained using the convolution approach: (*a*) first 10 modes at each frequency; (*b*) leading mode at each frequency. The SPOD of the pressure field is considered. The cyan box in (*b*) is centered around the global maximum of the instantaneous energy at $t = 1380$, analysed in figures 2.14 and 2.15(*c*,*d*) below.

content at the center of the time segment. A limitation of this approach is its high memory requirement (3.6 TB for the present example). As an alternative, we propose a computationally tractable way of calculating time-continuous expansion coefficients based on the convolution theorem. Applying the convolution theorem to the inverse SPOD problem yields

$$\mathbf{a}_l^{(i)}(t) = \left((\phi_l^{(i)} e^{-i2\pi f_l t}) \circledast \mathbf{q} \right)(t) = \int_{\Delta T} \int_{\Omega} \left(\phi_l^{(i)}(x) \right)^* \mathbf{W}(x) \mathbf{q}(x, t+\tau) w(\tau) e^{-i2\pi f_l \tau} \mathrm{d}x \mathrm{d}\tau, \quad (2.27)$$

where $\circledast$ indicates the convolution between the time evolving SPOD mode and the data, that takes into the account the windowing function, $w(\tau)$, and the weight matrix $\mathbf{W}$. In practise this convolution is computed by expanding the SPOD mode in time as $\phi_l^{(i)} e^{-i2\pi f_l t}$ and convolving it over the data one snapshot at a time. In this step, we leverage the orthogonality property of the SPOD mode in the space-time inner product, which allows us to compute the expansion coefficient one at a time. If the SPOD was computed using an overlap of n_{fft}-1, then the expansion coefficients, $\mathbf{a}_l^{(i)}$, obtained from equation (2.27) and equation (2.13) are mathematically identical. Here, the underlying idea is to apply the continuously-discrete convolution integral to the SPOD mode computed with a significantly lower overlap to make it computationally feasible. We confirmed that the frequency-time diagrams of the expansion coefficients obtained using equation

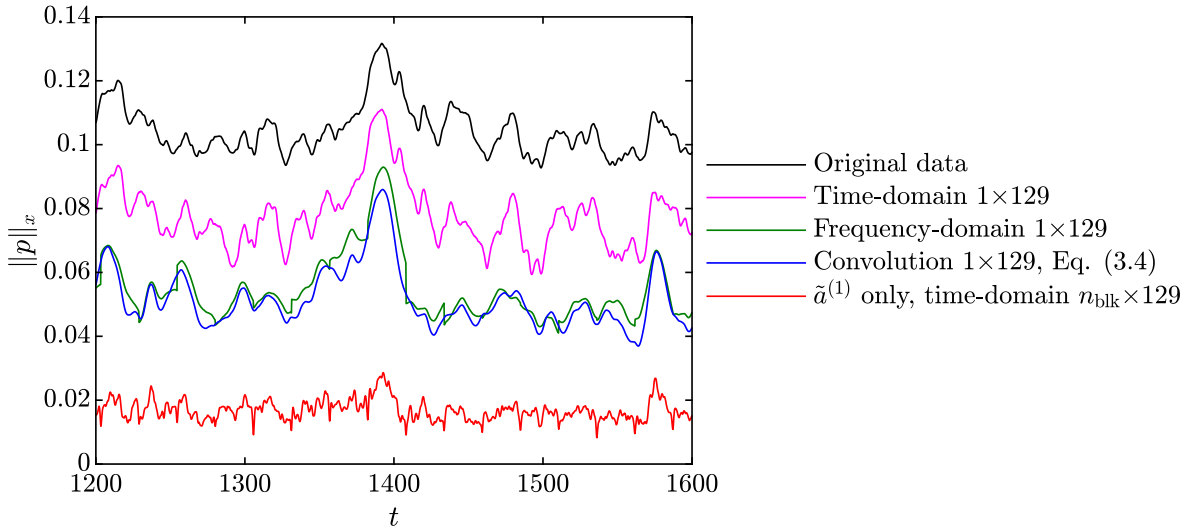

Figure 2.14: Temporal evolution of the pressure 2-norm in the vicinity of its global maximum at $t = 1380$. The convolution approach, based on equation (2.27), is compared to the time- and frequency-domain approaches, previously shown in figure 2.4(*b*,*d*). The 1×129-mode reconstructions are shown.

(2.27) for an overlap of 50% are virtually indistinguishable to those obtained from equation (2.13) for an $n_{\mathrm{ovlp}} = n_{\mathrm{fft}} - 1$ (shown in the appendix 2.C, figure 2.C.1). This is to be expected since the convergence of the SPOD modes does not improve significantly for overlap over 50%. In practice, the convolution integral in equation (2.27) is most efficiently computed using the FFT.

Frequency-time diagrams of the expansion coefficients for the convolution approach are shown in figure 2.13. Figure 2.13(*a*), and (*b*) show the contribution of the leading 10 modes, and the leading mode, respectively. These frequency-time diagrams appear less detailed compared to the frequency-time diagrams of the time-domain approach. In the context of figure 2.15, however, we will show that figures 2.12 and 2.13 basically contain the same information. For now, it is sufficient to note that the convolution and time-domain approaches detect the same trends. Take as an example, the high energy events occurring at low frequency in the time ranges, $550 \lesssim t \lesssim 590$ and $1370 \lesssim t \lesssim 1400$, in the spectrograms of figure 2.12(*b*) and 2.13(*b*).

2.5.3 Comparison of methods and interpretation of results

Next, we investigate if the high similarity between the instantaneous flow field and the modes indicates high energy. Figure 2.14 shows the temporal evolution of the pressure 2-norm for the original data, low-dimensional 1×129-mode reconstructions using the time-domain, frequency-domain and the convolution approaches. The pressure 2-norm of the data is highly underpredicted by the time-domain approach that uses a full basis ($n_{\mathrm{blk}}\times129$), but is able to capture the major trends of the original data. The time-domain reconstruction performed using a modal basis of 1×129 is also shown for comparison. This accurately follows the spatial norm of the original data, except for an offset, similar to figure 2.4(d). The frequency-domain curve also shows a similar trend. In addition, the spatial norm of the 1×129-mode reconstruction using the convolution approach is shown. It follows the trend of the original data and attains its global maximum at the same time instant. Minor differences between the convolution (time-continuous) and frequency-domain (50% overlap) approaches are expected, see appendix 2.C. All curves in figure 2.14 peak at the time of maximum instantaneous energy, previously indicated in figure 2.13(b). This indicates that a high similarity between the instantaneous flow field and the leading mode implies high overall energy. We highlight that this finding is not self-evident as the leading SPOD mode represents the most energetic flow structure in a purely *statistical* sense. The important physical insight hence is that the intermittent occurrence of large-scale coherent structures is directly associated with high-energy events.

To understand the qualitative differences of the frequency-time diagrams in figure 2.12 and 2.13, we now look at the expansion coefficients of the two approaches. Figure 2.15 compares the expansion coefficient of the leading mode, obtained by the time-domain and convolution approaches. As an example, the expansion coefficient at $St\approx0.50$ is shown in figure 2.15(a). It is centered around its global maximum, in the time interval $1000\leqslant t\leqslant1300$. We observe that the time traces of the expansion coefficients obtained from the two approaches show similar trends. In particular, the local peaks occur at similar locations, with both curves exhibiting the

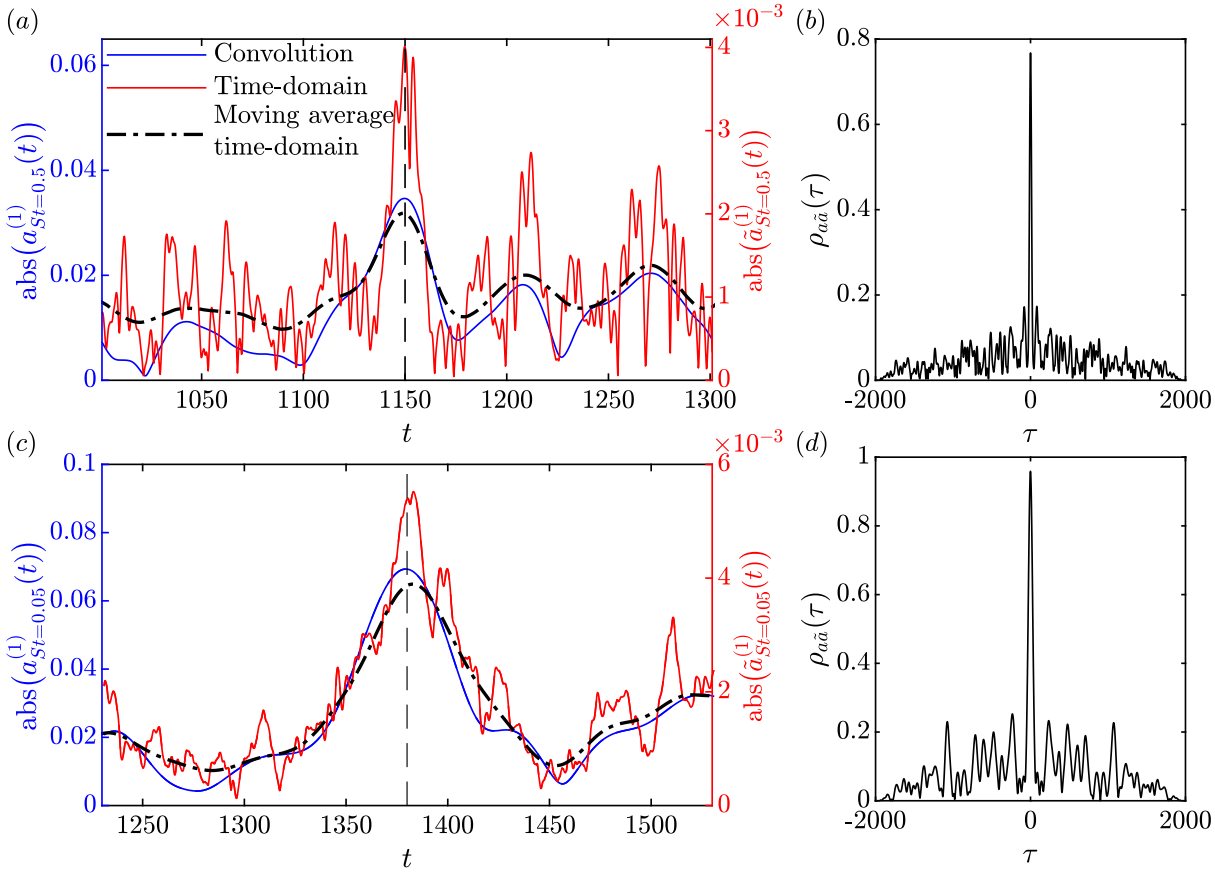

Figure 2.15: Oblique projection and convolution-based expansion coefficients of the leading mode at $St = 0.5$ (top) and $St = 0.05$ (bottom): (*a*,*c*) time traces in the vicinity of their global maximum (black dashed line); (*b*,*d*) cross-correlation of the expansion coefficients obtained using the two different approaches. The black dash-dotted line denotes the weighted moving mean of the time-domain expansion coefficient. The moving mean uses as weights the same Hamming windowing function as the SPOD.

global maximum at $t = 1150$ (black dashed line). Compared to the time-domain approach, the convolution curve is smoother and resembles a moving average of the time-domain curve (black dash-doted line). For optimal comparison with the convolution approach, the moving average is computed by weighting the time-domain curve by the Hamming window in equation (2.6) and averaging it 256 points. To further quantify the relation between the expansion coefficients of the two approaches, we show the cross-correlation coefficient in figure 2.15(b). The cross-correlation coefficient confirms the observation that the expansion coefficients obtained from the two approaches are similar, by demonstrating a cross-correlation coefficient of 0.77 at 0-time lag ($\tau = 0$). We have confirmed that this correspondence holds in general. In figure 2.15(c) and 2.15(d), for example, the same trends are observed for the expansion coefficients at the lower frequency of $St = 0.05$ over the time interval previously shown in figure 2.14 above. From figure 2.15, we infer that the intermittency of the coherent structures can be captured using both approaches.

After establishing the correspondence between the time-domain and convolution approaches, we now compare the spectral characteristics of the two approaches. The PSDs of the expansion coefficients associated with the leading mode at $St = 0.2$, 0.5, and 1.0, for the time and convolution-domain approaches are shown in figure 2.16 (a). As expected the PSDs peak at the frequency of the corresponding mode for both approaches. The expansion coefficients computed in the convolution approach exhibit a much narrower peak than those in the time-domain approach. Note that, we cannot expect a sharp spectral peak even for the convolution approach due to spectral leakage and the modulation of the wave amplitude as seen in figure 2.15. Figure 2.16(c) compares the PSDs of the leading mode and the 10 leading modes at $St = 0.5$, which underlines the dominance of the leading mode at this particular frequency. The expansion coefficients are presented in terms of the spectral energy content in figure 2.16(b) and (d). As the expansion coefficients are uncorrelated, and their expected value is the equal to SPOD modal

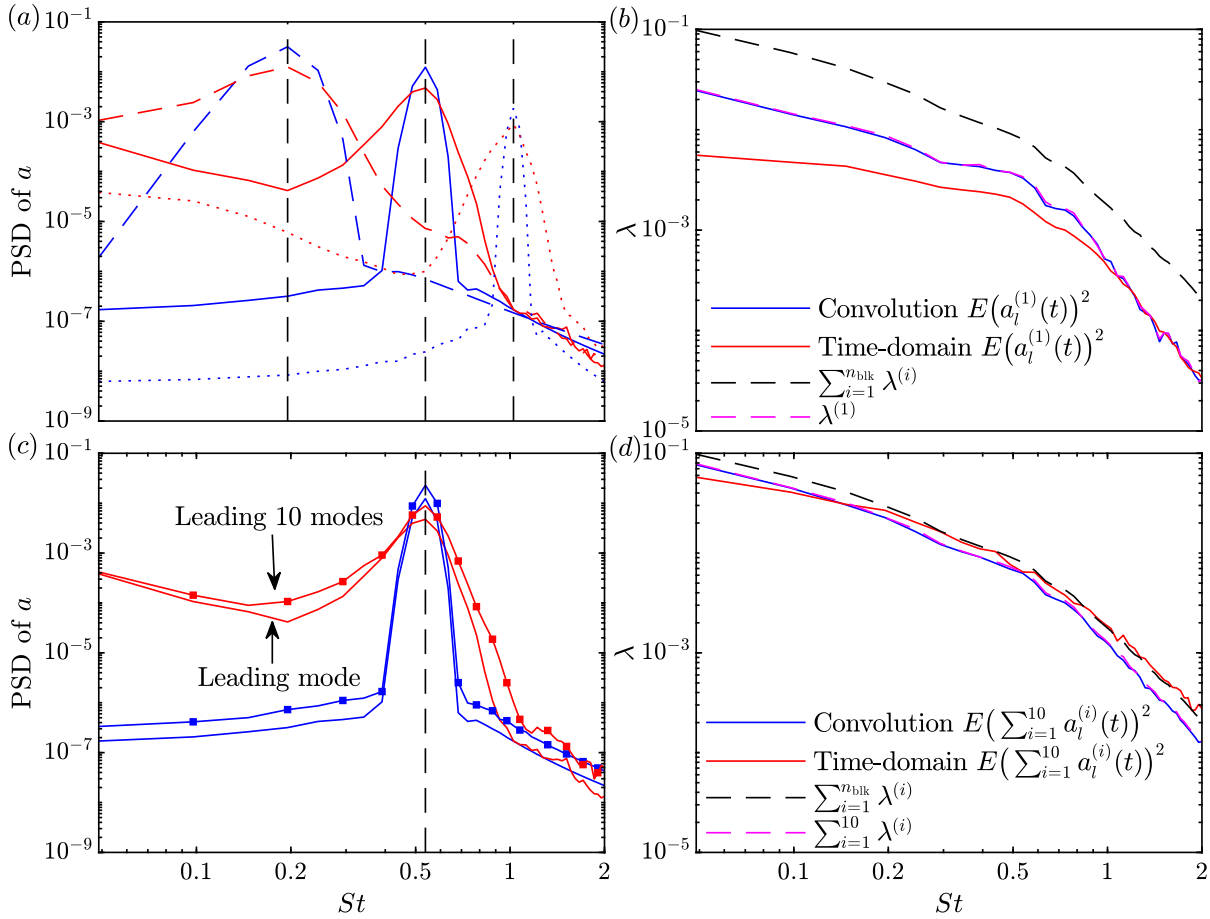

Figure 2.16: Spectral analysis of the expansion coefficients for the time-domain and convolution approaches: (*a*) PSD of the individual expansion coefficients of the leading SPOD mode at $St = 0.2$, 0.5 and 1.0; (*b*) expected values of the expansion coefficients of the leading mode; (*c*) PSD of the expansion coefficients of the leading mode and sum of the first 10 leading modes (line with squares) at $St = 0.5$; (*d*) expected value of the expansion coefficients for the sum of the first 10 modes. In (*b*) and (*d*), the leading, sum of leading 10, and sum of all eigenvalues are shown for comparison.

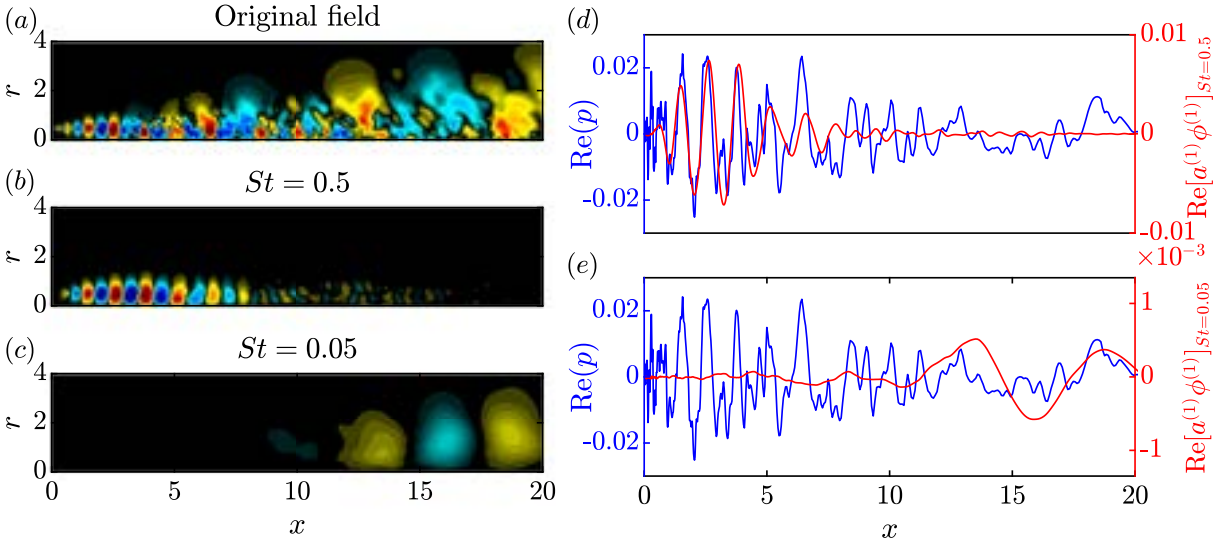

Figure 2.17: Contributions of individual modes to the reconstructed flow field: (a) instantaneous pressure field; (b) contribution of $\phi^{(1)}$ for St=0.5, and (c) for St=0.05; (d,e) comparison of the real part of the pressure field along the lipline ($r = 0.5$) for St=0.5 and St=0.05, respectively. The instantaneous flow field at t =1150 (see figure 2.15) is shown. Contours in (a,b,c) are reported on the same color axis.

energy,

$$E\left\{\mathbf{a}_f^{(i)}\mathbf{a}_f^{(j)}\right\} = \lambda_f^{(i)}\delta_{ij}, \tag{2.28}$$

it is expected that the convolution approach accurately approximates the eigenvalue spectrum. The blue and magenta lines are almost coincident in figure 2.16(b,d), thus confirming this conjecture. For the time-domain approach, the expected value for the sum of first 10 modes approximates the total integral PSD for all but the low frequencies $St \geqslant 0.2$ in figure 2.16(d). On considering only the first eigenvalue, the time-domain approach under predicts the eigenvalue spectrum for $St \leqslant 1.0$, (figure 2.16(b)). Note that, this observation does not contradict the observations made in context of figure 2.4, as the expansion coefficients are obtained from a full basis here, but from a smaller basis in figure 2.4(d).

After examining the properties of the expansion coefficients, we focus on the spatial composition of the reconstructed flow field in terms of contributions from individual modes in

figure 2.17. The time instant of high energy, previously marked in figure 2.15, is chosen as an example. The contribution of the leading SPOD modes at two representative frequencies, $St = 0.5$, and 0.05, to the original flow field is shown in figure 2.17. Figure 2.17(b) and (c) show the modes weighted by their expansion coefficient, $a^{(1)}\phi^{(1)}$ at the corresponding time instant and these two frequencies. Close to the nozzle exit the LES flow field clearly exhibits a KH-type instability wave. The leading mode at $St = 0.5$, closely resembles this structure. Similarly, the dominant wave pattern with a large wavelength (≈ 5) observed in the flow field, is represented by the mode at $St = 0.05$ in a location downstream of the potential core ($12 \lesssim x \lesssim 20$). The real part of the pressure field along the lipline ($r = 0.5$) is compared with the contributions of the leading modes at $St = 0.5$, and $St = 0.05$ in figure 2.17(d), and (e), respectively. It can be seen that the phases of the pressure field and the mode at $St = 0.5$ are aligned in the region where the mode attains its maximum. Weaker but similar kind of phase alignment is also observed for low frequency, $St = 0.05$, despite the disturbed nature of the wavepacket in the region, $12 \lesssim x \lesssim 20$. For the flow field at the current time instant, this also explains that the contribution of the leading mode at $St = 0.05$ is lower than $St = 0.5$, where the KH wavepacket dominates the flow field. These observations confirm that the maximum in the frequency-time diagrams indicate close resemblance of the instantaneous flow field with the corresponding SPOD modes. Since the SPOD modes are the most energetic structures it is not surprising that the maxima in the frequency-time diagrams indicate the intervals of high energy. Furthermore, as the leading SPOD modes are spatially coherent and contain the most energy at each frequency, we infer that SPOD-based frequency-time analysis can be used to gauge the intermittency of large-scale coherent structures. Here, for brevity, only the convolution approach is shown, but we note that these conclusions also hold for the time-domain approach.

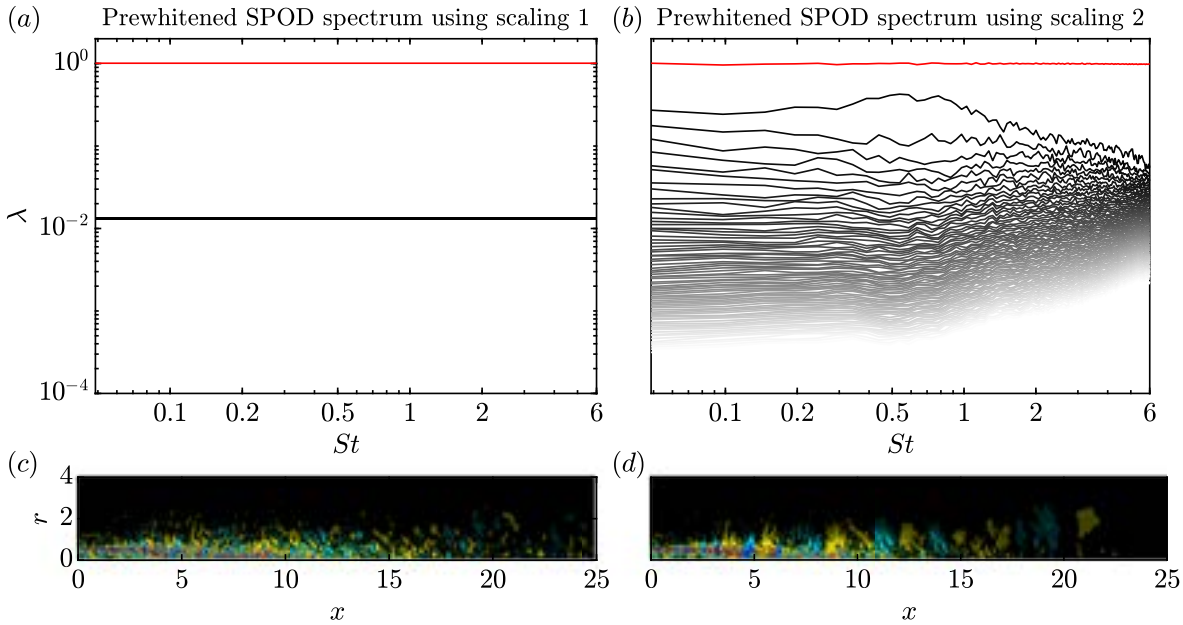

Figure 2.18: SPOD-based prewhitening: (a,b) rescaled SPOD spectra; (c,d), instantaneous pressure fields using definitions (2.30) and (2.31), respectively. Red lines indicate the sum of all eigenvalues, that is, the integrated PSD. All lines in (a) collapse due to the scaling. The original SPOD eigenvalue spectrum can be seen in figure 2.2(a).

2.6 Prewhitening

As mentioned in §2.1, prewhitening is a filtering operation that results in a flat power spectrum, and is commonly used for trend detection in atmospheric and geophysical applications. The goal hence is to use SPOD to scale the data to have the same energy at all frequencies. We propose to achieve this goal by re-scaling the expansion coefficients of the reconstruction in the frequency-domain. The frequency-domain is chosen for the same reasons as for denoising in §2.4. We leverage the fact that expansion coefficients are uncorrelated, and that their expected value is the equal to SPOD modal energy,

$$E\left\{\mathbf{a}_f^{(i)}\mathbf{a}_f^{(j)}\right\} = \lambda_f^{(i)}\delta_{ij}. \tag{2.29}$$

We propose two different scalings,

$$\frac{\sqrt{\sum_f \sum_i \lambda_f^{(i)}}}{\sqrt{\lambda_f^{(i)}}} \mathbf{a}_f^{(i)} \qquad \text{(scaling 1), and} \tag{2.30}$$

$$\frac{1}{\sqrt{\sum_i \lambda_f^{(i)}}} \mathbf{a}_f^{(i)} \qquad \text{(scaling 2)} \tag{2.31}$$

to scale the integral mode energy, that is, the sum of all eigenvalues, to one at each frequency. Both methods achieve this goal, but result in different relative scalings of individual SPOD modes. Figure 2.18(a) and 2.18(b) show the effect of the two scalings on the SPOD eigenvalue spectrum. The reconstructed flow fields obtained from the expansion coefficients scaled using equations (2.30) and (2.31) are shown in 2.18(c) and 2.18(d), respectively. Note that equation (2.30) collapses all eigenvalues in figure 2.18(a) to the same value. Scaling 2, on the contrary, preserves both the mode hierarchy and the relative energy content. In comparison to the original flow field shown in figure 2.6(a), prewhitening emphasizes high-frequency structures in the shear-layer, whereas it de-emphasizes the highly energetic large-scale structures associated with low frequencies downstream of the potential core. This portrayal of the flow field might appear unfamiliar; we emphasize that the objective of prewhitening is not physical interpretation, but pattern identification. Here, for example, the prewhitened pressure fields bring to light the trapped acoustic modes in the potential core. These modes have only recently been described in detail (Schmidt et al., 2017b, Towne et al., 2017). Previously, they remained largely unnoticed in the analysis of jet data because of their low energy content. An important difference between SPOD-based prewhitening and classical local, point-wise prewhitening techniques is that the SPOD-based approach preserves the spatial coherence of the flow structures identified by the SPOD modes.

2.7 Summary and Conclusions

Different applications of SPOD including low-rank reconstruction, denoising, prewhitening, and frequency-time analysis are demonstrated on the example of LES data of a turbulent jet. A fundamental building block for these applications is the capability to reconstruct the original data from the SPOD. In the frequency domain, this can be accomplished by inverting the SPOD problem (see, e.g., Citriniti and George, 2000). We demonstrate that this inversion can be computed either directly in the frequency-domain, or using a convolution-based strategy. The latter approach becomes a necessity in the context of frequency-time analysis, where the corresponding SPOD problem becomes intractable. As an alternative to frequency-domain reconstruction, we introduce a time-domain approach that is based on the oblique projection of the data onto the SPOD modes. A reduced-order model based on SPOD that uses oblique projection was recently devised by **?**.

Here, we show the complete recovery of the data using all modes and compare to low-dimensional reconstructions. The low-dimensional reconstructions from both approaches accurately capture the integral energy of the segmented data (in the space-time norm). However, the time-varying dynamics (in the purely spatial norm) are only captured by the low-dimensional reconstructions in the time-domain. For a fixed number of modes, the time-domain approach captures more of the energy (in both norms). On the downside, the association of the SPOD modes with a single frequency is lost. Instantaneous pressure fields reconstructed in the frequency-domain, on the contrary, preserve this monochromatic property of the SPOD modes, but may lack the finer details of the flow field reconstructions in the time-domain. The main advantage of the frequency-domain approach is that it conserves the orthogonality property and the frequency-mode correspondence of the SPOD. The main advantage of the time-domain approach is its optimality in reconstructing the instantaneous flow field with the least possible number of modes.

After establishing the advantages and disadvantages of both approaches, we demonstrate

SPOD-based denoising as an application of the frequency-domain approach. As expected, noise is mainly captured by higher SPOD modes at low frequencies and all modes at high frequencies. As a best practice, we propose a hard threshold above the noise floor that is identified from the SPOD eigenvalue spectrum. Significant noise reduction is achieved. At the same time, a substantial amount of energy of the original flow field is retained. Compared to a standard low-pass filter, SPOD-based denoising has the additional advantage of drastic space savings.

Finally, we demonstrate how SPOD-based frequency-time analysis can be used to analyse the intermittency of turbulent flows. Established means of frequency-time analysis such as wavelets transforms are signal-processing techniques that are applied to 1-D time signals. The alternative, SPOD-based approach demonstrated here, provides a global perspective in which spectrograms characterize the temporal evolution of the spatially coherent flow structures represented by the SPOD modes. The SPOD-based frequency-time analysis requires the computation of time-varying expansion coefficients at each time instant, and is computationally intractable in the frequency-domain. This problem is mitigated by the convolution-based strategy, which is mathematically equivalent in the limit of the intractable continuously-discrete (in time) SPOD problem. This convolution-based approach is compared to the projection-based approach in the time domain. The expansion coefficients calculated from both methods show similar trends. We further demonstrate that a moving average of the spectrogram obtained via oblique projection resembles the spectrogram obtained from the convolution approach. For consistency, the moving time average is directly based on the SPOD windowing. The main advantage of the frequency-domain, and therefore the convolution approach, is that it retains the orthogonality property and mode-frequency correspondence of the SPOD. The frequency-time analysis of the jet data confirms the highly intermittent nature of this turbulent flow. In accordance with the SPOD eigenvalue spectrum, it is found that most of the energy is concentrated at low frequencies, $St \lesssim 0.2$. A comparison of the total flow energy as a function of time with the spectrograms shows that high energy events are directly linked to the presence of flow structures resembling

the leading SPOD modes. We highlight that this behaviour is not necessarily expected as the SPOD modes represent the most energetic structures only in a *statistical* sense. From previous work (Schmidt et al., 2018), it is well-known that SPOD modes often isolate certain, prevailing physical phenomena. SPOD-based frequency-time analysis hence provides additional physical insight by indicating time intervals during which a particular mechanism is active.

Based on the results, we recommend the use of the time-domain approach for low-rank reconstruction of individual snapshots, and the frequency-domain approach for denoising and frequency-time analysis. For the latter application the proposed convolution strategy facilitates efficient computation of the time-continuous expansion coefficients. A Matlab code for the convolution-based frequency-time analysis is freely available online.

Acknowledgements

We gratefully acknowledge support from Office of Naval Research grant N00014-20-1-2311. The authors would like to thank the anonymous reviewers for their insightful comments. In particular, we thank the first reviewer for the suggestion regarding time-continuity. This chapter is a reprint of the material in the article: A. Nekkanti, and O. T. Schmidt. "Frequency–time analysis, low-rank reconstruction and denoising of turbulent flows using SPOD", Journal of Fluid Mechanics, 926, A26 (2021). The dissertation author was the primary investigator and author of this work.

Appendix

2.A Effect of different parameters on the flow field reconstruction

Segmentation of the data is a crucial step in spectral estimation. Following the original work by Welch (1967), we use an overlap of 50% between blocks to minimize the variance of the

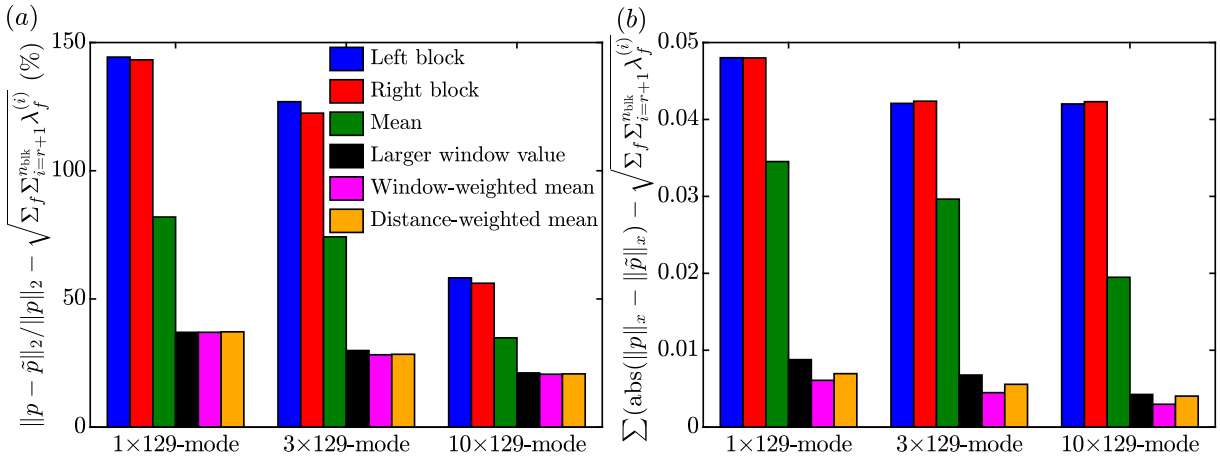

Figure 2.A.1: Errors of different ways to compute the frequency-domain reconstruction for 1×129, 3×129 and 10×129 modes: (*a*) 2-norm; (*b*) spatial norm (equation (2.2)). Analogous to figure 2.5, the residual energy of the truncated modes is subtracted for comparison.

spectral estimate, see §2.2.2.2 above. The use of overlapping segments, however, results in an ambiguity for the reconstruction, which we may compute as:

1. the left (previous) block,
2. the right (following) block,
3. the average of the left and right reconstructions,
4. either the left or right reconstruction based on the higher windowing weight,
5. the average of the left and right reconstructions weighted by the relative value of hamming window,
6. the average of the left and right reconstructions weighted by the relative distance to the centers of the overlapping blocks.

Figure 2.A.1 compares the errors of low-dimensional reconstructions using 1×129, 3×129, and 10×129 modes for all the six possibilities. It is found that the reconstruction based on the window-weighted average of the left and right reconstructions produces the smallest error. Based

on this finding, this option is used for the frequency-domain reconstruction throughout the paper. Using the window-weighted average approach, the i-th snapshot is reconstructed as,

$$\mathbf{q}_i \approx \frac{\mathbf{q}_j^{(k)} w(j) + \mathbf{q}_{j-n_{\mathrm{ovlp}}}^{(k+1)} w\big(|j - n_{\mathrm{ovlp}}|\big)}{w(j) + w\big(|j - n_{\mathrm{ovlp}}|\big)}, \tag{2.32}$$

where $j = i - (k-1)(n_{\mathrm{fft}} - n_{\mathrm{ovlp}})$, $i \in [1, n_t]$, $j \in [1, n_{\mathrm{fft}}]$ and $k \in [1, n_{\mathrm{blk}}]$. From figure 2.4 (in particular 2.4(b)), it becomes apparent that these distinctions only matter for truncated series reconstructions; full-dimensional reconstructions are generally accurate.

The sudden jumps in the local energy of the reconstruction observed in figure 2.4 are a windowing effect. We demonstrate this by comparison with reconstruction using rectangular windows and no overlap in figure 2.A.2. The low-dimensional reconstructions using 1×129, 3×129, and 10×129 modes, and all modes are shown. Many observations made in the context of figure 2.4, also hold here: the dimension of the modal bases is directly proportional to its ability to capture the pressure norm of the data, and for a fixed number of modes, the time-domain results in a better approximation of the data than the frequency-domain approach. The most notable difference can be seen between figure 2.A.2(b) and 2.4(b). The windowing effect in the frequency-domain reconstructions is absent if the rectangular window is used. Note in particular the difference during the first few snapshots and near the locations of switching from one block to another (vertical dotted black lines). Despite this advantage in the context of frequency-domain reconstructions for small n_{modes}, rectangular windowing is generally not recommended because of spectral leakage (Schmidt and Colonius, 2020).

Analogous to figure 2.7, we report in figure 2.A.3 the SPOD eigenspectra of the 1×129-mode frequency and time-domain reconstructions for a rectangular window and $n_{\mathrm{ovlp}} = 0$. The SPOD eigenvalue spectra of the full data is also shown for comparison. Only the leading three eigenvalues are shown for clarity. The leading eigenvalue of the frequency-domain and time-domain reconstructions are indistinguishable from the leading eigenvalues of the full data. For the

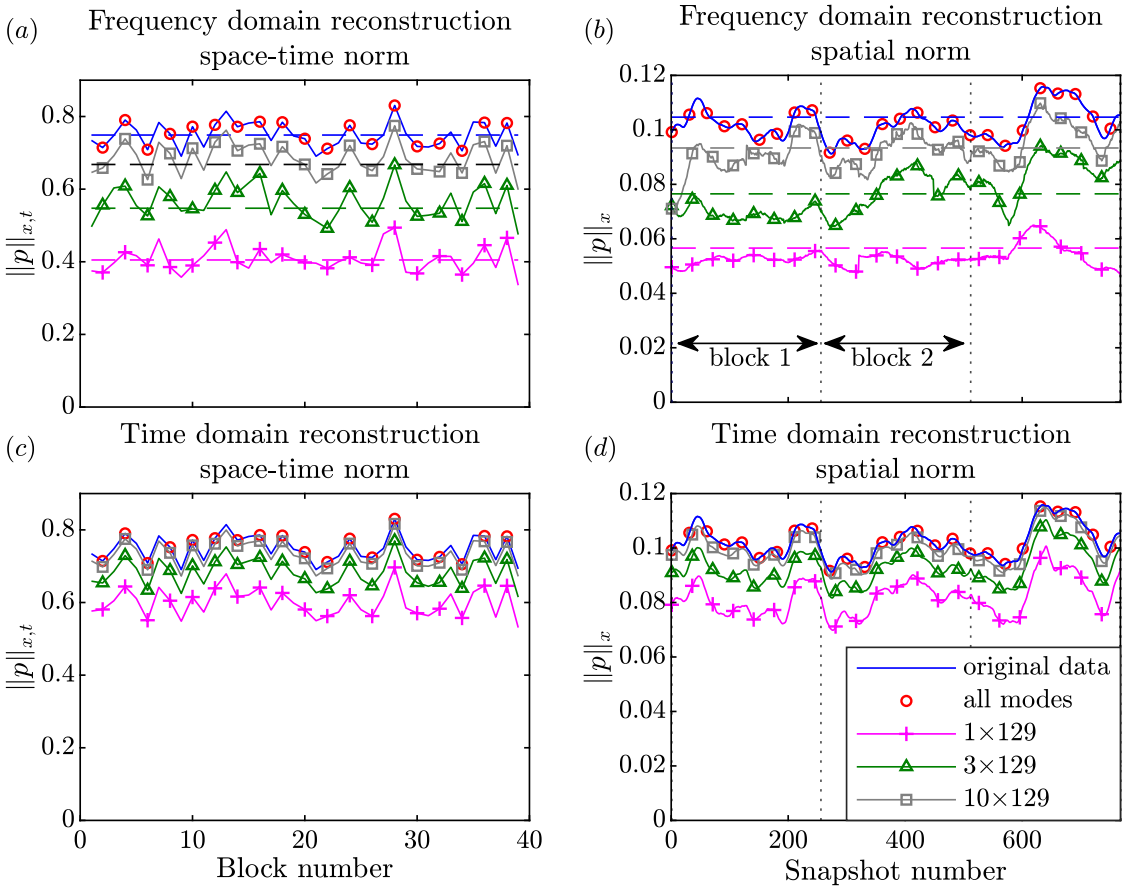

Figure 2.A.2: Low-dimensional reconstruction using a rectangular window: frequency-domain reconstruction (a,b), and time-domain reconstruction on the (c,d) in terms of the space-time norm (a,c) and the spatial norm (b,d). The original data (blue lines) is compared to the full reconstructions using all modes, and reconstructions using 10×129, 3×129, and 1×129 modes. Summed SPOD mode energies are shown as dashed lines. Vertical dotted black lines in (b,d) indicate the non-overlapping blocks. This figure is identical to figure 2.4, but for a rectangular window and no overlap.

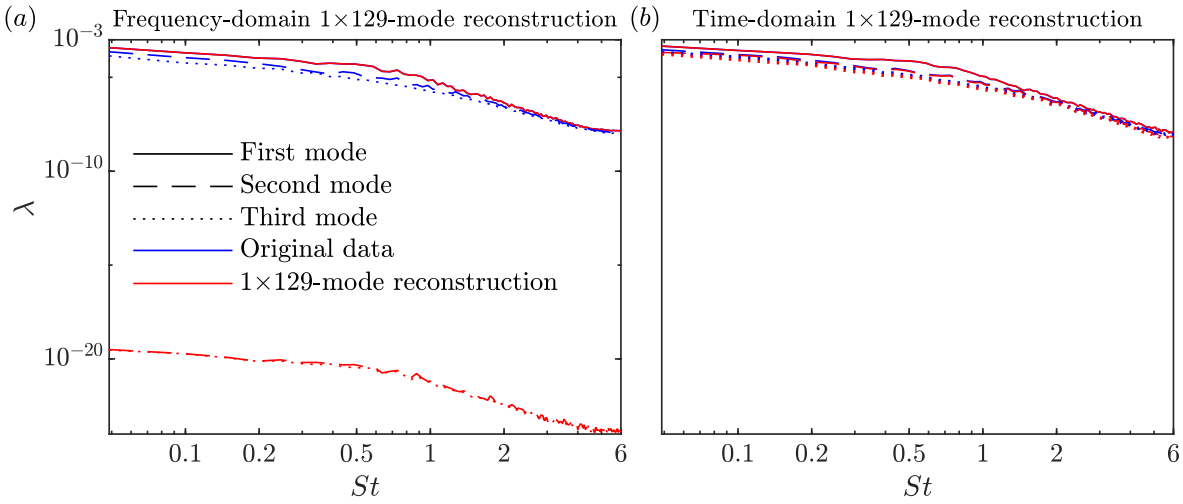

Figure 2.A.3: Comparison between SPOD eigenvalue spectra of the original data (blue lines) and 1×129-mode reconstructions (red lines): (*a*) frequency-domain; (*b*) time-domain. Solid, dashed, and dotted lines denote the first, second, and third modes, respectively. This figure is identical to figure 2.7, but for a rectangular window and no overlap.

frequency-domain reconstruction, the higher eigenvalue spectra are zero to machine precision, as expected. This indicates that the windowing-effect causes the elevation of the higher eigenvalue spectra in figure 2.7(*a*). The time-domain reconstruction, on the other hand, is able to predict the higher eigenvalues as explained in the context of 2.7(*b*). This implies that the time-domain reconstruction is much less sensitive to the choice of windowing function.

2.B Projection-based frequency-time analysis: effect of choice of basis and correspondence to convolution-based approach

Oblique projection-based frequency time analysis is dependent on the choice of modal basis. The two obvious choices of bases for the projection are

1. $n_{\text{modes}}\times129$ modes, i.e., only those SPOD modes used in the analysis,

$$\tilde{\boldsymbol{\Phi}} = \left[\boldsymbol{\phi}_1^{(1)}, \boldsymbol{\phi}_2^{(1)}, \cdots, \boldsymbol{\phi}_{n_{\text{fft}}}^{(1)}\right], \quad \text{or}$$

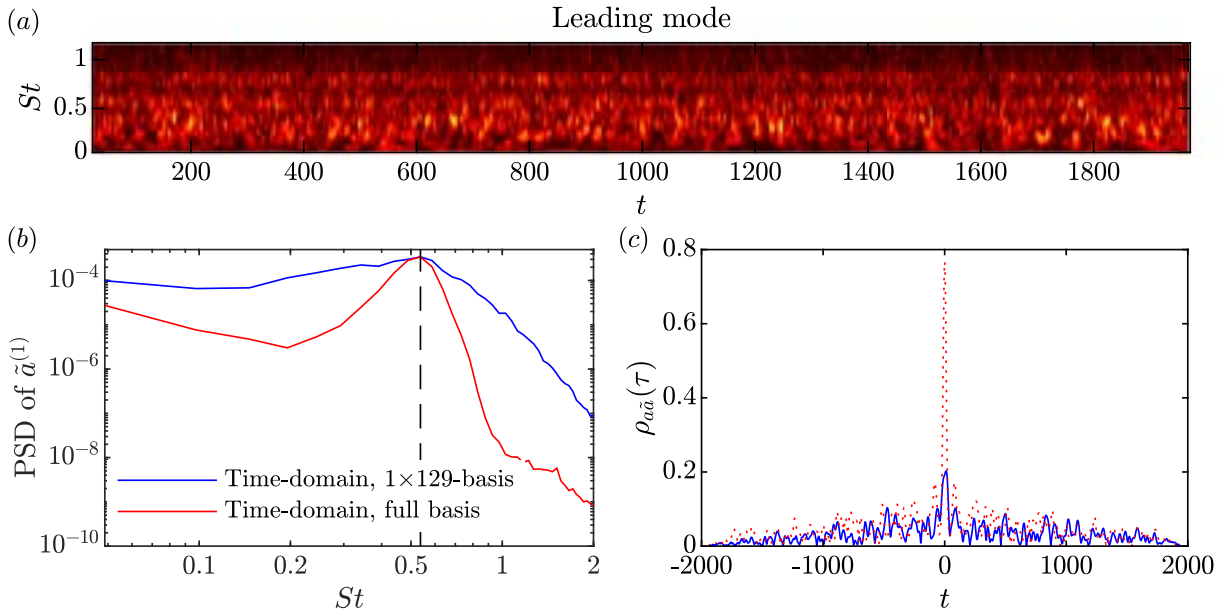

Figure 2.B.1: SPOD-based frequency-time analysis obtained using the time-domain approach with 1×129-modal basis: (*a*) frequency-time diagram of the leading mode at each frequency; (*b*) PSD of the individual expansion coefficients of the leading SPOD mode at $St = 0.5$ for the time-domain approach with the 1×129 basis (blue line) and $n_{\text{blk}}\times129$ basis (red line); (*c*) cross-correlation of the expansion coefficient in the time-domain approach using the 1×129 basis (blue line) and the $n_{\text{blk}}\times129$ basis (red dotted line) with the convolution approach.

2. $n_{\mathrm{blk}} \times 129$ modes, i.e., all available SPOD modes,

$$\tilde{\boldsymbol{\Phi}} = \left[\boldsymbol{\phi}_1^{(1)}, \boldsymbol{\phi}_1^{(2)}, \cdots, \boldsymbol{\phi}_1^{(n_{\mathrm{blk}})}, \boldsymbol{\phi}_2^{(1)}, \boldsymbol{\phi}_2^{(2)}, \cdots, \boldsymbol{\phi}_2^{(n_{\mathrm{blk}})}, \cdots, \boldsymbol{\phi}_{n_{\mathrm{fft}}}^{(1)}, \boldsymbol{\phi}_{n_{\mathrm{fft}}}^{(2)}, \cdots, \boldsymbol{\phi}_{n_{\mathrm{fft}}}^{(n_{\mathrm{blk}})}\right].$$

Due to the non-orthogonality of these modes in the spatial norm, these two choices will result in different outcomes. Shown in figure 2.B.1(a) is the frequency-time diagram for n_{modes}=1, that is a 1×129-mode basis containing only the leading mode at each frequency. A fundamentally different behaviour from that in figure 2.12 is observed. The diagram exhibits a banded structure, and, in contrast to the reference diagram based on all SPOD modes, the majority of maxima is not found in the low-frequency regime, $St \lesssim 0.2$. To understand this difference, the PSD of the expansion coefficient associated with the leading mode at $St = 0.5$ is shown in figure 2.B.1(b). The expansion coefficient computed with the 1×129-modal basis exhibits a much broader peak than the one computed with full basis. This behaviour indicates a loss of the mode-frequency correspondence for the heavily truncated basis. Next, both approaches are compared by taking the convolution-based expansion coefficient as the reference. The cross-correlation of the expansion coefficients from both approaches with the reference signal from the convolution approach are shown in figure 2.B.1(c). The expansion coefficient computed using the 1×129-modal basis exhibits a much lower correlation with the reference. We conclude from this analysis that the time-domain approach should be conducted using all SPOD modes, as it yields a more accurate description of the intermittency of the coherent structure represented by the SPOD modes.

In figure 2.15, we demonstrated that the expansion coefficients computed from a moving average of the time-domain approach resemble those from the convolution approach. For further evidence, we show in figure 2.B.2 the frequency-time diagrams obtained by taking the moving mean, at each frequency, of the time-domain diagram previously shown in figure 2.12. The outcome should be compared to the frequency-time diagrams obtained using the convolution approach, i.e., figure 2.13. It is observed that the frequency-time diagrams are qualitatively very

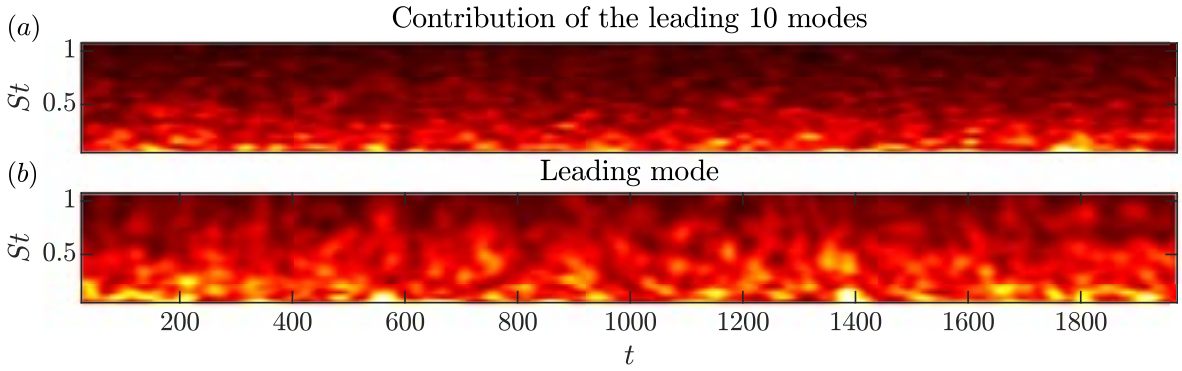

Figure 2.B.2: SPOD-based frequency-time diagrams obtained using the moving mean of the time-domain oblique projection based approach: (*a*) first 10 modes at each frequency; (*b*) leading mode at each frequency. The moving mean uses as weights the same Hamming windowing function as the SPOD.

similar. The effect of taking the moving average is mainly visible at higher frequencies, where it leads to minor loss of detail. For qualitative flow analysis, we hence conclude that the moving average of the time-domain approach can well be used to approximate the computationally much more involved convolution approach.

2.C Frequency-domain approach based frequency-time analysis: effect of overlap and correspondence to convolution-based approach

Figure 2.C.1 demonstrates the similarity between the frequency-time diagrams obtained using the convolution method and the frequency-domain approach. For the convolution method, equation (2.27), a basis of precomputed SPOD modes with 50% overlap was used. To obtain time-continuous expansion coefficients using the frequency-domain approach, we require $n_{\text{ovlp}} = n_{\text{fft}} - 1$. As this is computationally intractable, the data (only here) was reduced to every third grid point in the streamwise and radial directions. The time traces of the individual expansion coefficients for $St = 0.05$ and 1.0 are reported in 2.C.1(*c*,*d*).

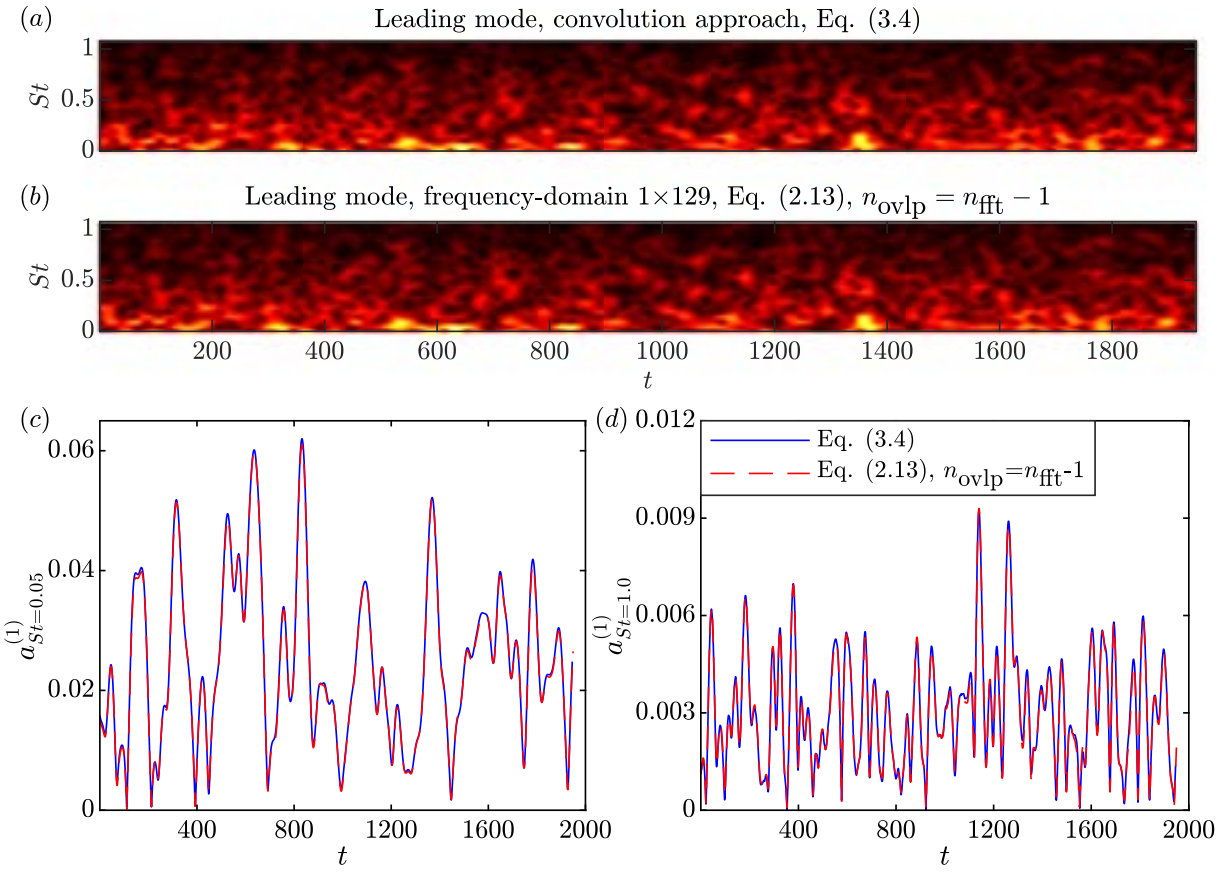

Figure 2.C.1: Comparison between two strategies for SPOD-based frequency-time analysis: frequency-time diagrams for (*a*) the convolution approach (SPOD modes precomputed with 50%, overlap), and (*b*) the frequency-domain approach using $n_{\mathrm{ovlp}} = n_{\mathrm{fft}} - 1$; expansion coefficients for (*c*) $St = 0.05$, and (*d*) $St = 1.0$.

Chapter 3

Gappy spectral proper orthogonal decomposition for reconstruction of missing flow data

3.1 Introduction

Gappy data reconstruction techniques find wide use in the completion of partially missing or otherwise compromised experimental data. The focus of this work is the estimation of missing regions in long time series of spatially resolved, generally turbulent, statistically stationary flow data. One of the most widely used experimental technique to acquire such data for turbulence research (Westerweel et al., 2013) and geophysical flows (Doron et al., 2001), but also in the automotive (Beaudoin and Aider, 2008, Conan et al., 2011) and aerospace industries (Willert, 1997), is particle image velocimetry (PIV, see e.g. Adrian and Westerweel (2011), Raffel et al. (1998)). Missing or corrupted regions in PIV measurements have many sources. Among them are shadowing, that is, the partial obstruction of the laser sheet, reflections from objects, and the inaccessibility of certain regions for the imaging system (Hart, 2000, Huang et al., 1997,

Sciacchitano et al., 2012, Westerweel, 1994). Corrupted regions also arise from irregular seeding or the absence of a sufficient number of tracer particles, for example, in recirculation zones. Whereas the latter sources of errors are specific to PIV, other measurement techniques suffer from similar problems. Atmospheric data obtained via satellite imagery, for example, often suffer from partial obstruction due to cloud coverage (Alvera-Azcárate et al., 2005).

Standard mathematical techniques for approximating missing data include basic interpolation and least-square estimation. Techniques devised specifically for the task of gappy data reconstruction include optimal interpolation (Kaplan et al., 1998, Reynolds and Smith, 1994, Smith et al., 1996) and Kriging (Oliver and Webster, 1990, Stein, 1999). Kriging, the more popular method, uses a local or global interpolant that is evaluated at the missing points based on local weighted averaging. An advantage of Kriging is that it is inherently capable of extrapolation, i.e, it can reconstruct spatial gaps that are persistent in time. The use of proper orthogonal decomposition (POD) in conjunction with least-squares estimation for data reconstruction was proposed by Everson and Sirovich (1995). This original 'gappy POD' algorithm was later extended by Venturi and Karniadakis (2004) and shown to outperform Kriging for the reconstruction of flow data with up to 50% of gappyness. A computational efficient algorithm that does not require the repeated solutions of least-squares problems was introduced by Gunes et al. (2006). Since its introduction, gappy POD has been applied to various flows such as the flow past an airfoil (Bui-Thanh et al., 2004, Willcox, 2006), cavity flow (Murray and Ukeiley, 2007), boundary layers (Gunes and Rist, 2007, Raben et al., 2012), gas turbine combustors (Saini et al., 2016), and arterial blood flow Yakhot et al. (2007). It has also become an essential component of several model reduction strategies that use POD modes as their basis (Benner et al., 2015, Chaturantabut and Sorensen, 2010). Another application is efficient sensor placement (Willcox, 2006, Yildirim et al., 2009). In the ocean sciences, gappy POD was independently developed under the name of data interpolating empirical orthogonal functions (DINEOF) by Beckers and Rixen (2003) and was used to, for example, fill in observational sea surface temperature (Alvera-Azcárate et al.,

2005, Beckers et al., 2006), Southern Oscillation Index (Kondrashov and Ghil, 2006), and surface chlorophyll concentration data (Alvera-Azcárate et al., 2007, Taylor et al., 2013).

In this work, we propose an algorithm based on frequency-domain, or spectral proper orthogonal decomposition (SPOD), for gappy data reconstruction. Even though the mathematical foundations of SPOD were first laid out by Lumley (1970), the method was rarely used, with a few notable exceptions like the work of Glauser et al. (1987), before its first application to very large numerical data by Schmidt et al. (2018). In the same year, Towne et al. (2018) established relationships to hydrodynamic stability theory and other modal decompositions. The proposed 'gappy SPOD' algorithm is fundamentally different from those of Everson and Sirovich (1995) and Venturi and Karniadakis (2004), both algorithmically and in that it leverages both spatial and temporal coherence. Note that space-only POD modes are only correlated at zero time lag, and hence do not possess the latter property (Towne et al., 2018).

The chapter is structured as follows. A brief overview of SPOD and SPOD-based reconstruction is given in §3.2. §3.3 describes the gappy SPOD algorithm. In §§3.4.1 and 3.4.2, we demonstrate the algorithm on numerical simulation data of laminar cylinder flow and PIV data of turbulent cavity flow, respectively. §3.5 compares the performance of the proposed gappy SPOD algorithm to established gappy POD and Kriging methods. The performance for cases involving sequences of missing snapshots and data that contains additive gaussian white noise are analysed in §3.6, and §3.7, respectively. Finally, §3.8 summarizes this work. Parameter studies on the effect of the spectral estimation parameters, as well as data length and SPOD convergence are presented in 3.A, and 3.B, respectively.

3.2 Methodology

3.2.1 Spectral Proper Orthogonal Decomposition

SPOD extracts monochromatic modes that optimally capture, depending on the choice of norm, the flow's energy. These modes are computed as the eigenvectors of the cross-spectral density matrix. We use a specific SPOD algorithm that estimates the cross-spectral density matrix based on Welch's approach (Welch, 1967). The implementation of this approach entails partitioning the entire time series into smaller segments that are interpreted as independent realizations of the flow. Next, we briefly introduce the notation used in this work. For a detailed mathematical derivation and the algorithmic implementation, the reader may refer to, for example, Towne et al. (2018) or Schmidt and Colonius (2020).

We denote by

$$\mathbf{q}_i = \mathbf{q}(t_i), \qquad i = 1, 2, \cdots, n_t, \tag{3.1}$$

the ensemble of n_t snapshots of the statistically stationary flow field with its mean removed. The first step of the standard Welch approach is to segment the data into n_{blk} overlapping blocks, each containing n_{fft} snapshots. If the blocks overlap by n_{ovlp} snapshots, then the j-th column in the k-th block is given by $\mathbf{q}_j^{(k)} = \mathbf{q}_{j+(k-1)(n_{\text{fft}}-n_{\text{ovlp}})+1}$, where $k = 1, 2, \cdots, n_{\text{blk}}$, and $j = 1, 2, \cdots, n_{\text{fft}}$. Next, we compute a windowed temporal discrete Fourier transform and arrange all the Fourier realizations of the l-th frequency, $\hat{\mathbf{q}}_l^{(j)}$, into a matrix,

$$\hat{\mathbf{Q}}_l = \left[\hat{\mathbf{q}}_l^{(1)}, \hat{\mathbf{q}}_l^{(2)}, \cdots, \hat{\mathbf{q}}_l^{(n_{\text{blk}})}\right]. \tag{3.2}$$

The SPOD modes, $\mathbf{\Phi}_l$, and eigenvalues, $\mathbf{\Lambda}_l$, are finally obtained as the eigenpairs of the weighted CSD matrix $\mathbf{S}_l = \frac{1}{n_{\text{blk}}} \hat{\mathbf{Q}}_l \hat{\mathbf{Q}}_l^* \mathbf{W}$, where $\mathbf{W}$ is a positive-definite Hermitian matrix that accounts for the component-wise and numerical quadrature weights. For data with more spatial degrees of

freedom than the number of snapshots, we solve the smaller eigenvalue problem,

$$\frac{1}{n_{\text{blk}}}\hat{\mathbf{Q}}_l^*\mathbf{W}\hat{\mathbf{Q}}_l\boldsymbol{\Psi}_l = \boldsymbol{\Psi}_l\boldsymbol{\Lambda}_l, \tag{3.3}$$

for the (unscaled) expansion coefficients, $\boldsymbol{\Psi}_l$. The SPOD modes at the l-th frequency are recovered as

$$\boldsymbol{\Phi}_l = \frac{1}{\sqrt{n_{\text{blk}}}}\hat{\mathbf{Q}}_l\boldsymbol{\Psi}_l\boldsymbol{\Lambda}_l^{-1/2}. \tag{3.4}$$

The column vectors of $\boldsymbol{\Phi}_l = [\boldsymbol{\phi}_l^{(1)}, \boldsymbol{\phi}_l^{(2)}, \cdots, \boldsymbol{\phi}_l^{(n_{\text{blk}})}]$ are the SPOD modes and the diagonal entries of $\boldsymbol{\Lambda}_l = \text{diag}(\lambda_l^{(1)}, \lambda_l^{(2)}, \cdots, \lambda_l^{(n_{\text{blk}})})$ contain the mode energies. An important property of the SPOD modes is their orthogonality in their weighted inner product, $\left\langle \boldsymbol{\phi}_l^{(i)}, \boldsymbol{\phi}_l^{(j)} \right\rangle = \boldsymbol{\phi}_l^{(i)}\mathbf{W}\boldsymbol{\phi}_l^{(j)} = \delta_{ij}$, at each frequency. The associated norm is denoted by $\|\cdot\|_2$.

3.2.2 Data reconstruction

The reconstruction of the original data is based on the inversion of the SPOD problem, comprehensively discussed in Nekkanti and Schmidt (2021a). The Fourier realizations at each frequency are reconstructed from the SPOD modes as $\hat{\mathbf{Q}}_l = \boldsymbol{\Phi}_l\mathbf{A}_l$. Here, $\mathbf{A}_l$ is the matrix of the (scaled) expansion coefficients computed as

$$\mathbf{A}_l = \sqrt{n_{\text{blk}}}\boldsymbol{\Lambda}_l^{1/2}\boldsymbol{\Psi}_l^*, \quad \text{or} \tag{3.5}$$

$$\mathbf{A}_l = \boldsymbol{\Phi}_l^*\mathbf{W}\hat{\mathbf{Q}}_l. \tag{3.6}$$

The expansion coefficients can be saved during the computation of SPOD using equation (3.5) or recovered later by projecting the Fourier realizations onto the modes using equation (3.6). Using the expansion coefficients a_{ik} contained in $\mathbf{A}$ at any given frequency, the k-th block can be

reconstructed as

$$\mathbf{Q}^{(k)} = \mathcal{F}^{-1}\left[\left(\sum_i a_{ik}\boldsymbol{\phi}^{(i)}\right)_{l=1}, \left(\sum_i a_{ik}\boldsymbol{\phi}^{(i)}\right)_{l=2}, \cdots, \left(\sum_i a_{ik}\boldsymbol{\phi}^{(i)}\right)_{l=n_{\mathrm{fft}}}\right], \tag{3.7}$$

where $\mathcal{F}^{-1}$ is the inverse windowed Fourier transform. Finally, the time series is reconstructed from the data segments by computing the average of the reconstructions from overlapping blocks, weighted by the relative value of their windowing function (Nekkanti and Schmidt, 2021a).

3.3 Algorithm

The gappy SPOD algorithm consists of three loops: in the local loop, a single gap is converged by repeated reconstruction with continuously updated local expansion coefficients; in the inner loop, this process is repeated for all gaps; in the outer loop, the global convergence of the inner loops is assessed.

Algorithm: Gappy SPOD

1. Segment the time series into overlapping blocks and compute the temporal Fourier transform of each block (if not computed in the previous iteration).

2. Proceed to the n-th gap and choose all the realizations of the Fourier transform that are *not* affected by this gap.

3. Compute the SPOD from all the Fourier realizations that are not affected by this gap (equations (3.3) and (3.4)) and store the corresponding expansion coefficients (equation (3.5)). (For denoising, apply mode truncation; see 3.7.)

4. Compute the SPOD expansion coefficients for blocks *affected* by the n-th gap by projecting their Fourier transforms onto the SPOD basis (equation (3.6)).

5. Reconstruct the affected blocks by inverting the SPOD (equation (3.7)) from the expansion coefficients computed in (iii) and (iv); replace the regions affected by the n-th gap.

6. (local loop) Go to (iv) to update the expansion coefficients now that the data is reconstructed in the affected regions until the convergence criterion based on the change of reconstruction of the n-th gap is met.

7. (inner loop) Set $n \leftarrow n+1$ and go to (i) until all gaps are reconstructed.

8. (outer loop) Set $n = 1$ and go to (i); repeat until convergence criterion based on change of reconstruction between outer loop iterations is met.

The metrics used to gauge the error, as compared to the true solution, and the convergence for the local and outer loops, as compared to the previous iteration within the respective loop, are defined next.

3.3.1 Error and Convergence metrics

Define G as the index set corresponding to all gappy snapshots and $G_n \subset G$ as the subset of indices corresponding to the n-th gap. The following error and convergence metrics are used to evaluate the efficacy of our method:

$$e_i = \frac{\left\| \mathbf{q}_i^g - \tilde{\mathbf{q}}_i^g \right\|_2^2}{\left\| \mathbf{q}_i^g \right\|_2^2} \quad \text{(relative error of } i\text{-th snapshot)}, \tag{3.8}$$

$$e_n = \sum_{i \in G_n} e_i \quad \text{(relative error of } n\text{-th gap)}, \tag{3.9}$$

$$E = \sum_{i \in G} e_i \quad \text{(global relative error)}, \tag{3.10}$$

$$c_n = \sum_{i \in G_n} \frac{\left\| \tilde{\mathbf{q}}_i^{g^{[j-1]}} - \tilde{\mathbf{q}}_i^{g^{[j]}} \right\|_2^2}{\left\| \tilde{\mathbf{q}}_i^{g^{[j-1]}} \right\|_2^2} \quad \text{(convergence of } n\text{-th gap)}. \tag{3.11}$$

Here, $\mathbf{q}^g$ and $\tilde{\mathbf{q}}^g$ are, respectively, the original and reconstructed data in the gappy regions only, and superscript $[j]$ the iteration index. The calculation of the relative errors, equations (3.9) and (3.10), requires knowledge of the original data, $\mathbf{q}$. For demonstration purposes only, artificial gaps were introduced in this study, and hence the relative errors can be computed. The convergence metric defined in equation (3.11) does not require the true data and can be evaluated even for gappy datasets. Throughout this paper, the thresholds used for convergence criteria are $tol = 10^{-8}$. We will demonstrate later that this tolerance is very conservative in that the error has long converged before the criterion is met for our examples.

3.3.2 Computational complexity

The computational cost of gappy SPOD is dominated by the matrix multiplications in the local loops, i.e, step (vi) of the algorithm in §3.3. Welch's algorithm outlined in §2 segments the dataset of size into n_{blk} blocks. Here m is the product of the spatial degrees of freedom and the number of variables. For flow data with a high spatial resolution, as the two cases considered here, we can typically assume that $m \gg n_{\text{fft}}, n_{\text{blk}}$. The SPOD in step (iii) requires the formation of the cross-spectral density matrix, its eigenvalue decomposition, and the computation of the SPOD modes at each frequency. The time complexities of these operations are (mn_{blk}^2), (n_{blk}^3), and (mn_{blk}^2), respectively. The total time complexity of step (iii) is hence $(mn_{\text{fft}}n_{\text{blk}}^2)$. The time complexities of steps (iv) and (v) are $(mn_{\text{fft}}n_{\text{blk}}n_{\text{blk,gaps}})$, and $(mn_{\text{fft}}n_{\text{blk,gaps}}\log(n_{\text{blk,gaps}}))$, respectively, where $n_{\text{blk,gaps}}$ is the number of blocks that contain gaps. The number of local loops required for the convergence of each gap is an *a priori* unknown number n_{local}. As each inner loop converges all gaps, which amounts to a time complexity of $(mn_{\text{gaps}}n_{\text{fft}}n_{\text{blk}}(n_{\text{blk}} + n_{\text{local}}n_{\text{blk,gaps}}))$. In practice, we find that $n_{\text{local}}n_{\text{blk,gaps}} \gg n_{\text{blk}}$ and the estimate simplifies to $(mn_{\text{gaps}}n_{\text{fft}}n_{\text{blk}}n_{\text{local}}n_{\text{blk,gaps}})$. Finally, if the algorithm requires n_{outer} outer loops for convergence, then its total time complexity is $(mn_{\text{out}}n_{\text{local}}n_{\text{gaps}}n_{\text{fft}}n_{\text{blk}}n_{\text{blk,gaps}})$.

Table 3.4.1: Parameters example databases and spectral estimation parameters.

Case	Variables	Re	n_x	n_y	n_z	n_t	Δt	n_{fft}	n_{ovlp}	n_{blk}
Cylinder DNS	u,v	500	250	125	1	4096	0.06	256	128	31
Cavity PIV	u,v	3.3×10^5	150	55	1	16000	6.25×10^{-5}s	256	128	124

3.4 Results

We demonstrate the reconstruction of missing data using the gappy SPOD reconstruction method on two examples. The parameters of these example datasets are given in table 1. The first example is direct numerical simulation (DNS) data of the canonical laminar flow past a cylinder. This flow is a popular benchmark case that we will use to compare with established methods such as gappy POD (Everson and Sirovich, 1995, Venturi and Karniadakis, 2004) and Kriging (Oliver and Webster, 1990). The second example is the experimental data of a high Reynolds number flow over an open cavity obtained from time-resolved particle image velocimetry (PIV) measurements (Zhang et al., 2017, 2020). This data exemplifies realistic turbulent flow data and is subject to measurement noise.

3.4.1 Example 1: Cylinder flow at Re=500

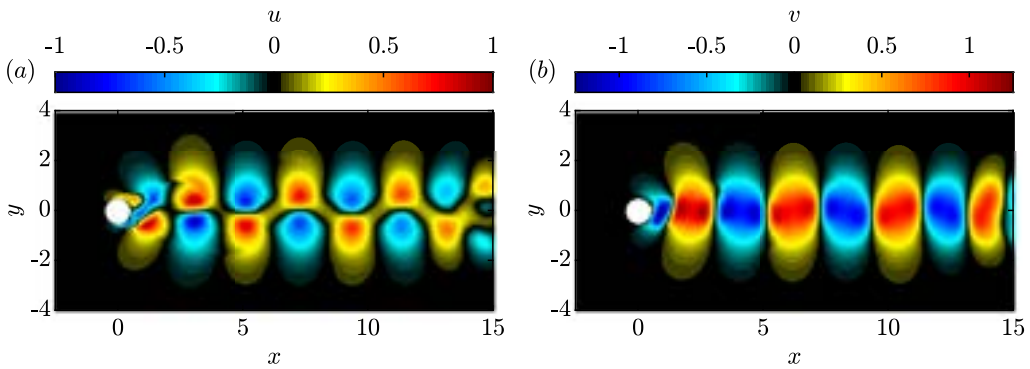

Figure 3.4.1: Instantaneous fluctuating flow field for flow around a cylinder at $Re = 500$: (a) streamwise velocity, u; (b) transverse velocity, v.

As a first example, we consider the flow around a cylinder at a Reynolds number $Re =$

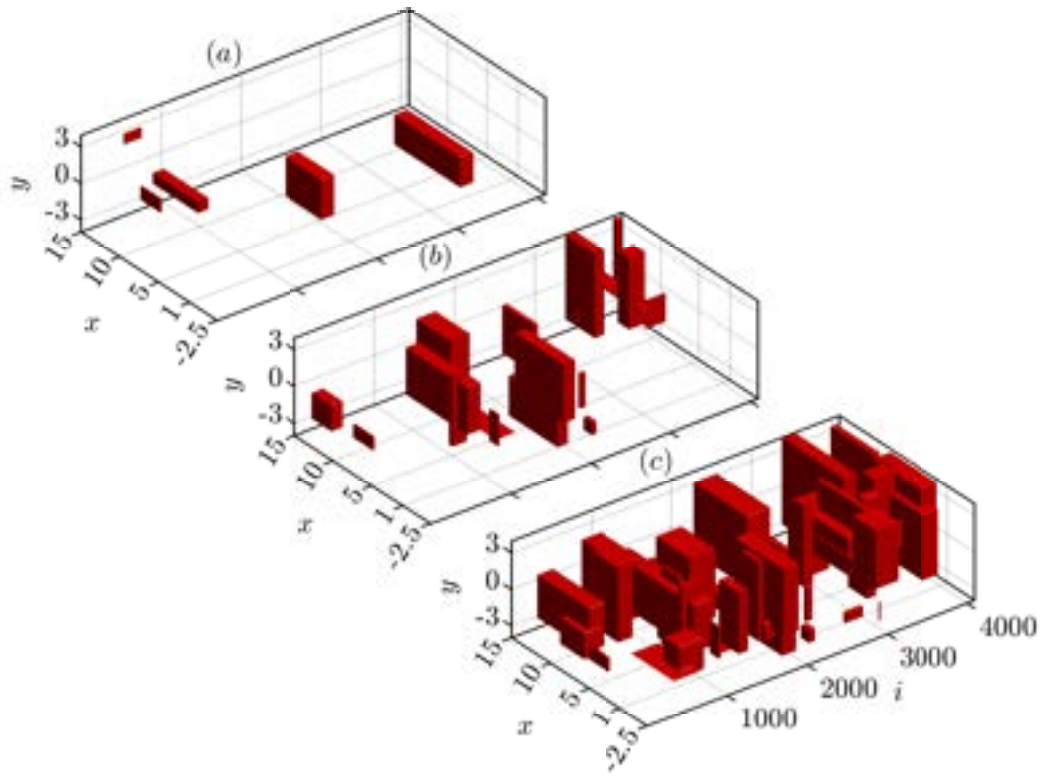

Figure 3.4.2: Randomly generated gaps in the flow past a cylinder: (a) 1% gappyness; (b) 5% gappyness; (c) 20% gappyness. Red blocks indicate gaps. The streamwise (x-y) plane is plotted aganist the snapshot index, i.

$\rho U_\infty D/\mu = 500$, where ρ is the density, U_∞ the incoming flow velocity, μ the dynamic viscosity, and D the diameter of the cylinder. The coordinates are non-dimensionalized by D and velocities by U_∞, respectively. This data was obtained by solving the two-dimensional incompressible Navier-Stokes equations for the velocity field $\mathbf{q} = [u, v]^T$ using the immersed-boundary solver by Goza and Colonius (2017). The data was acquired after all transients have subsided. Instantaneous flow fields of the streamwise velocity, u, and transverse velocity, v, are shown in figure 3.4.1.

The gappy SPOD reconstruction is demonstrated in three scenarios with 1%, 5%, and 20% of missing data. Missing regions, or gaps, are artificially introduced to the data after the mean is removed. The gaps are randomly seeded in space and time. Similarly, the spatial and temporal extent of the gaps is randomly sampled. Figure 3.4.2 shows the spatio-temporal distribution of the gaps for all three levels of gappyness. The gaps are allowed to extend over the entire field-of-view

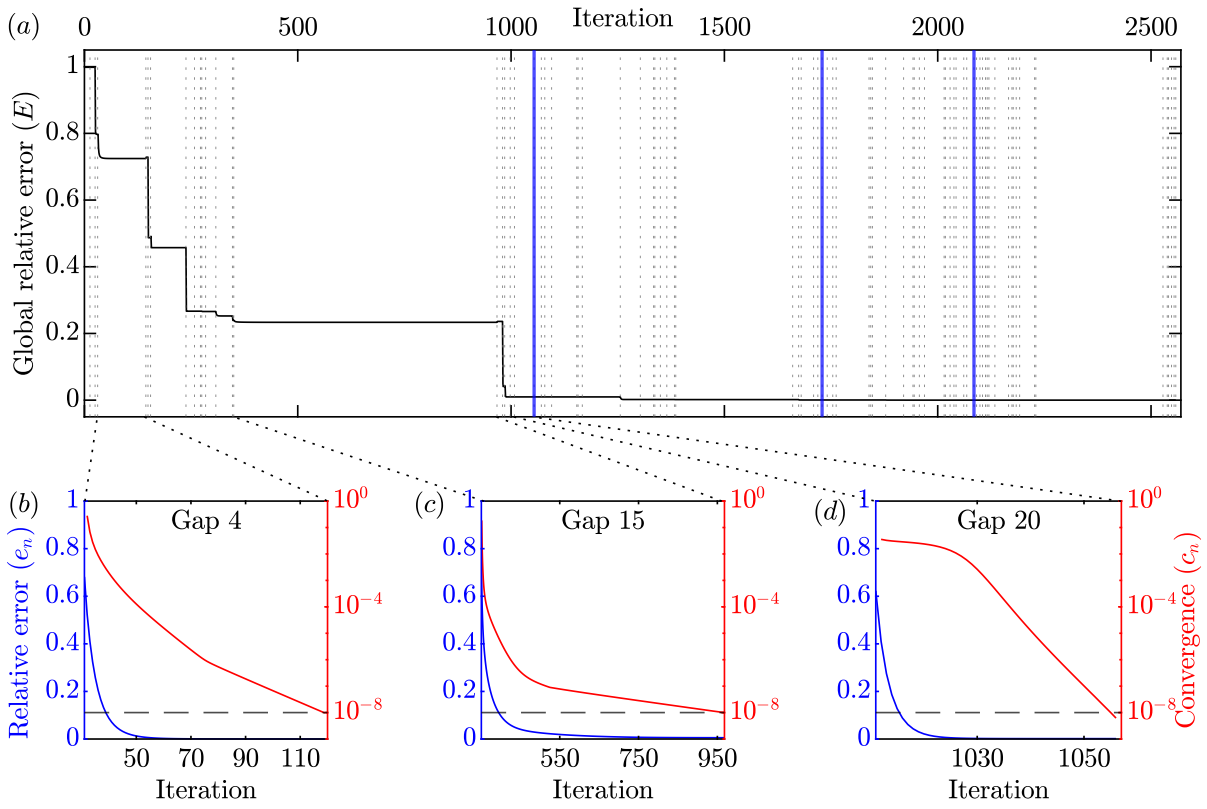

Figure 3.4.3: Errors and convergence for 5% gappyness, see figure 3.4.2(*b*). The global relative error is shown in (*a*). Inner (gap-wise) iterations are denoted by grey dotted lines and outer iterations (sweeps over all gaps) as blue solid lines. Panels (*b-d*) show the gap-wise error and convergence for three randomly selected gaps within the first outer loop.

and up to 300 snapshots. The gappy-SPOD algorithm reconstructs the data by filling gaps in sequential order. Here, we number the gaps according to their first occurrence in time and have verified that the final error upon convergence is insensitive to the order by which the algorithm handles the gaps. Figure 3.4.2(*c*) shows the extreme example of 20% gappyness in which every block contains missing data. Following best practices for SPOD (Schmidt and Colonius, 2020), the data is segmented into 31 blocks with 256 snapshots and 50% overlap. The effect of the parameter n_{fft} is investigated in 3.A. Additionally, in 3.6, we explore a case with 5% missing data and entire snapshots, or short sequences of snapshots, missing from the data.

We start by exploring the 5% gappyness case, previously shown in figure 2(*b*). This case consists of $n_{\text{gaps}} = 20$ randomly seeded and sized gaps. Figure 3.4.3 illustrates the local and

global error s and the convergence of the algorithm. By 'local', we refer to the gap-wise iteration, that is, steps (iv)-(vi) of the algorithm in §3.3, and by 'global' to the outer iteration loop over steps (i)-(viii). Figure 3.4.3(a) shows the evolution of the global relative error as defined in equation (3.10) as all gaps are converged to $c_n \leqslant tol = 1 \times 10^{-8}$ within each of the four outer loops. The gap-wise convergence, c_n, is defined by equation (3.11). The four outer loops required to achieve global convergence are marked by the thick blue lines. Each of these outer iterations comprises n_{gaps} inner loops, indicated by the grey dotted lines. The global relative error is normalized according to equation (3.10), and hence starts with one. The error non-strictly monotonically decreases as the gaps are sequentially filled in. This is a desirable property, but we note that the algorithm does not guarantee it. The amount by which each inner loop can reduce the global relative error is dependent on the spatial location and temporal extent of the corresponding gap. This explains the sharp drops at the beginning of some local iteration loops. At the end of the first outer loop, the global relative error is already reduced to 1.3%, and its final value after four outer loops is 7.7×10^{-5}. Notably, a large fraction of the reconstruction error reduction is accomplished by the first outer loop. A quantitative comparison with other methods such as the gappy-POD method by Venturi and Karniadakis (2004) is provided in section §3.5.

Panels 3.4.3(b-d) show the local relative errors and convergence for three representative gaps during the first outer loop. The local relative error for all gaps decreases monotonically from one to very small values of order 10^{-3}. After the final outer iteration loop, the local relative errors are of order 10^{-5}. The tolerance of $tol = 1 \times 10^{-8}$, as indicated by blacked dash lines, guarantees that the relative errors are all well converged.

Figures 3.4.4 and 3.4.5 compare the reconstructed, gappy, and original data for 5% of missing data. Figure 3.4.4 shows the streamwise velocity fluctuations, u, and figure 3.4.5 the transverse component, v. The same four time instances are shown in the four columns of both figures. The first column corresponds to the time instant of the largest instantaneous reconstruction error. The other three are randomly selected. Visual inspection of the reconstructed and original

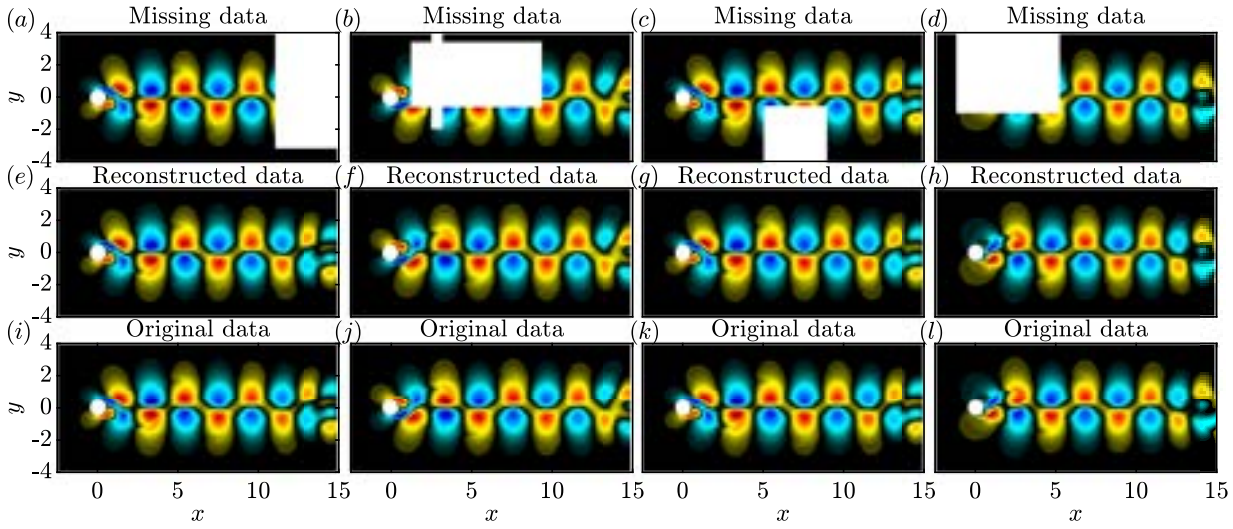

Figure 3.4.4: Reconstruction for 5% gappyness at four time instances: (*a-d*) gappy data; (*e-h*) reconstructed data; (*i-l*) original data. False colors of the streamwise velocity fluctuations, *u*, are on the same scale in all plots.

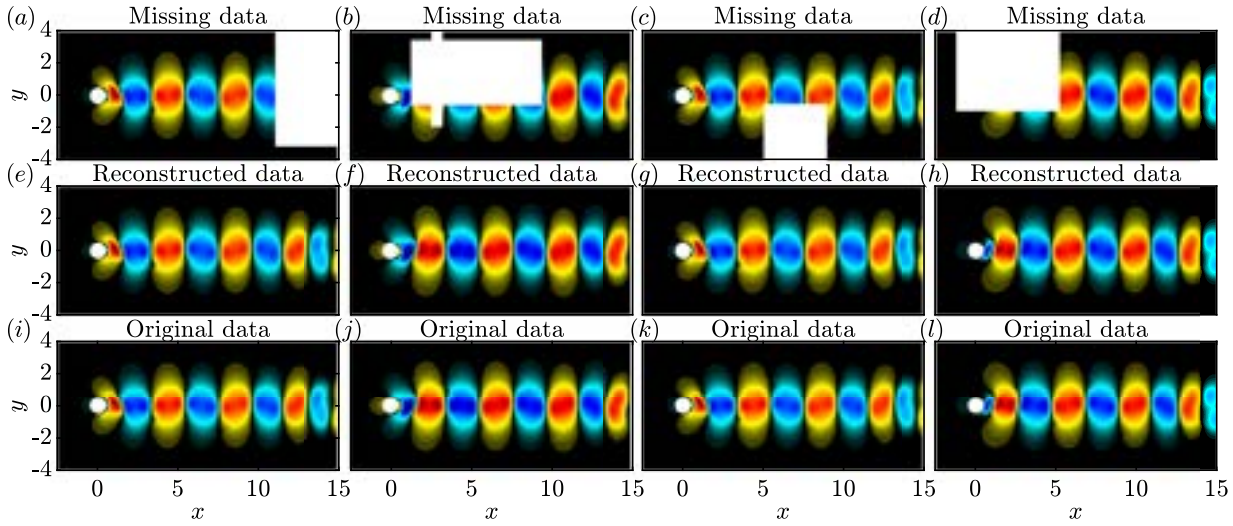

Figure 3.4.5: Same as figure 3.4.4 but for the transverse velocity fluctuations.

data indicates that the gappy SPOD algorithm is able to accurately reconstruct the flow structures

,

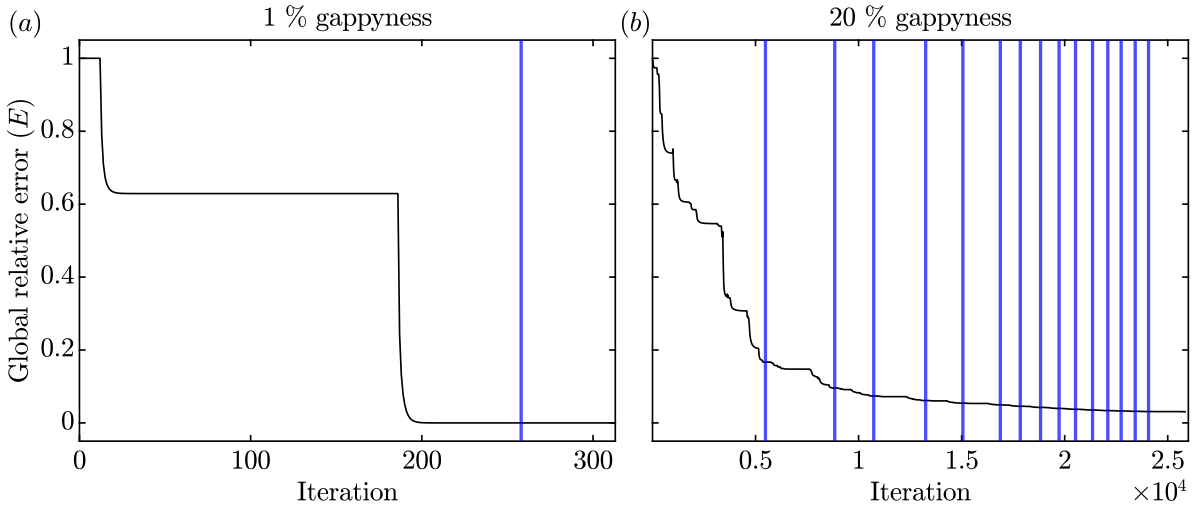

Figure 3.4.6: Global relative error of the gappy SPOD algorithm: (a) 1% gappyness; (b) 20% gappyness. The blue solid lines indicate the outer iterations.

We next study the performance of the algorithm for the more moderate case with 1% and the more extreme case with 20% of missing data. Figure 3.4.6 shows the global relative errors for these two cases. As in figure 3.4.3(a), outer loops are indicated by thick blue lines. The 1%- and 20%-gappyness cases require two and 16 outer loops for convergence, respectively. The final errors upon convergence are $E = 9 \times 10^{-6}$, and 3×10^{-2}, respectively. As can be anticipated from the very low error for the 1% case, the reconstructed velocity fields are visually indistinguishable from the original DNS data, and we hence refrain from showing the reconstructions.

Figure 3.4.7 shows the side-by-side comparison for the most severe case with 20% of gappyness and a final error of 3%. While the instantaneous flow fields are shown here, note that the gaps extend over significant time periods, as can be seen in figure 3.4.2(c). Similar to figure 3.4.4, the first column corresponds to the snapshot that exhibits the largest reconstruction error. The remaining three time instants are arbitrarily selected. The spatial gaps in these four

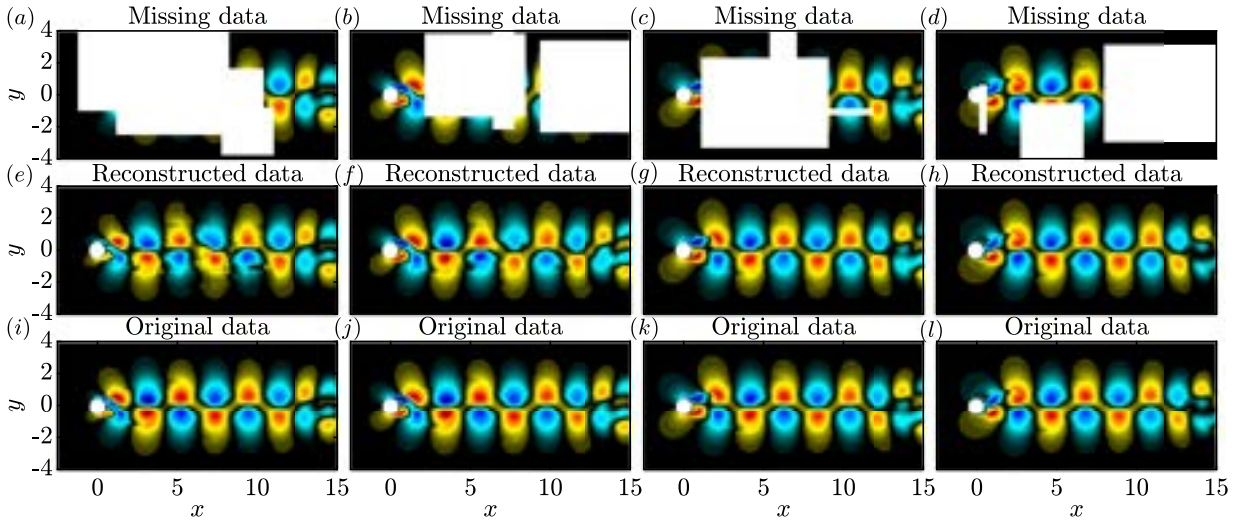

Figure 3.4.7: Same as figure 3.4.4, but for 20% gappyness.

snapshots correspond to 50%, 46%, 33%, and 40% of missing data, respectively. A comparison of the reconstructed and original fields reveals some local discrepancies at the fringes of the gaps, in particular where multiple gaps overlap. This is most notable in figure 3.4.7(e, f). These local discrepancies aside, the wake flow is accurately reconstructed terms of structure, phase and amplitude. The reconstructions are almost indistinguishable from the original data for the snapshots with 33% and 40% of missing data shown in figures 3.4.7(c,g,k) and 3.4.7(d,h,l), respectively. Results for the transverse velocity component are very similar and omitted for brevity. The relative errors are $e_i = 7.9 \times 10^{-2}$, 1.7×10^{-2}, 2.5×10^{-3}, and 1.3×10^{-3}, respectively. Considering that a large fraction of 20% of the data was missing, these errors are, arguably, low and the overall flow dynamics are accurately recovered. A quantitative comparison with other methods, later presented in §3.5, confirms this conjecture.

3.4.2 Example 2: PIV of turbulent cavity flow by Zhang et al. (2017, 2020)

Next, we consider the much more relevant and challenging example of experimental turbulent flow over an open cavity. The Reynolds number based on the cavity depth is $Re = \rho U_\infty D/\mu = 3.3 \times 10^5$, and the Mach number is $M = U_\infty/c_\infty = 0.6$. Here, c_∞ is the speed of sound.

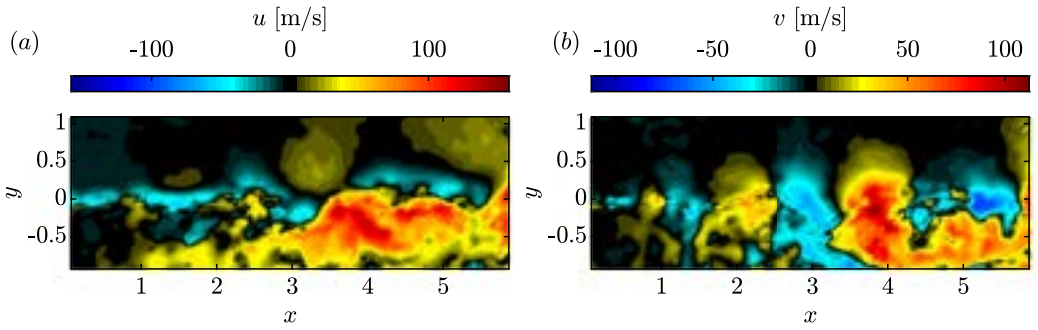

Figure 3.4.8: Instantaneous fluctuating flow field of the turbulent flow over an open cavity at $Re = 3.3\times10^5$ measured by Zhang et al. (2017, 2020): (*a*) streamwise velocity, u; (*b*) transverse velocity, v. The x- and y-coordinates are non-dimensionalized by cavity depth D.

Time-resolved particle image velocimetry (TR-PIV) was performed to obtain the velocity field in the center plane of an open cavity with a length-to-depth ratio of $L/D = 6$ and a width-to-depth ratio of $W/D = 3.85$. A total number of 16,000 snapshots was obtained at a sampling rate of 16kHz. The coordinates are non-dimensionalized by depth D, but the velocity components are reported in SI units. We refer to Zhang et al. (2019, 2017) and Zhang et al. (2020) for more details on the measurement campaign and the experimental setup, respectively. The instantaneous velocity field shown in figure 3.4.8 exemplifies, in stark contrast to the previous example, the chaotic nature of the flow. This example also tests the algorithm's performance in the presence of measurement noise that is not easily distinguished from physical turbulence.

As for the cylinder flow example in §3.4.1, we consider three cases with 1%, 5%, and 20% of missing data. The gaps are shown in figure 3.4.9 and were randomly generated in the same way as for the previous example. Taking into account the significantly larger length of the data sequence, the maximum temporal extent of the gaps was increased to 600 snapshots. As before, we choose $n_{\text{fft}} = 256$ and 50% overlap, resulting in a total number of 124 blocks. The dependence of the results on n_{fft} is investigated in 3.A. In the extreme example of 20% gappyness, every block is affected by gaps.

As in figure 3.4.3, the inner workings of the algorithm for the cavity flow with 5% of

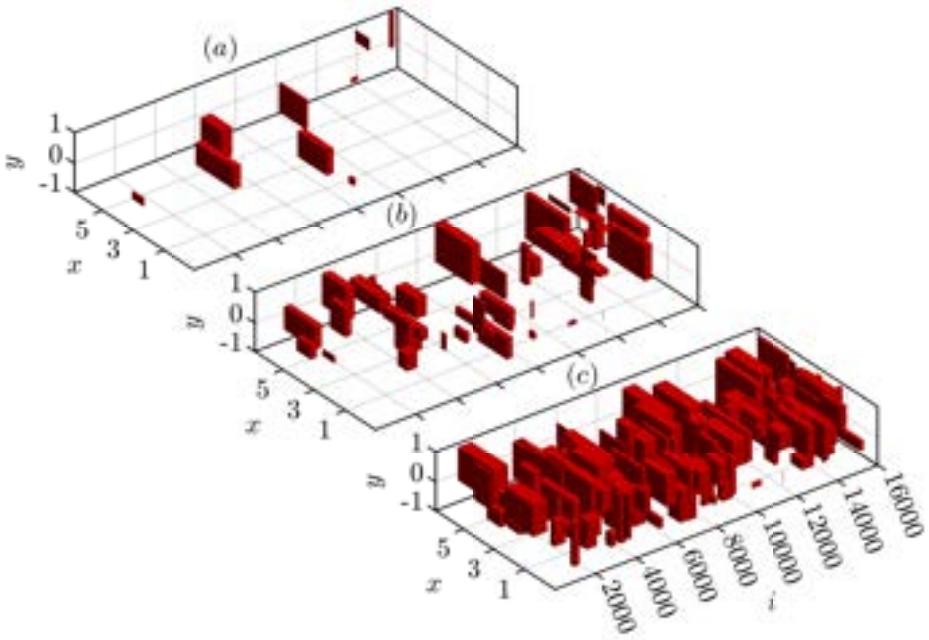

Figure 3.4.9: Randomly generated gaps for the turbulent flow over an open cavity: (*a*) 1% gappyness; (*b*) 5% gappyness; (*c*) 20% gappyness. Red blocks indicate gaps. The streamwise (*x*-*y*) plane is plotted over the snapshot index, *i*.

missing data are best understood from the relative errors and gap-wise convergence shown in figure 3.4.10. Figure 3.4.10(*a*) shows that the algorithm requires two outer iteration loops to satisfy the convergence criterion of $tol = 10^{-8}$. The first outer iteration reduces the global relative error by 81%. The second outer loop does not further reduce the error by an appreciable amount, and its final value remains at $E = 19\%$. In §3.5, we confirm that this value is lower than what is achieved by other established methods. A notable difference to the laminar case, shown in figure 3.4.3, is that the global relative error does not decay monotonically. The local relative error and convergence for three representative gaps during the first outer loop are shown in figure 3.4.10(*b*-*d*). The relative error for all gaps decays to about 20%. An important observation is that the gap-wise relative error always saturates before the convergence criterion of $tol = 10^{-8}$ is met. This observation, again, serves as an *a posteriori* justification for this choice of tolerance.

Figures 3.4.11 and 3.4.12 show the instantaneous streamwise and transverse velocity

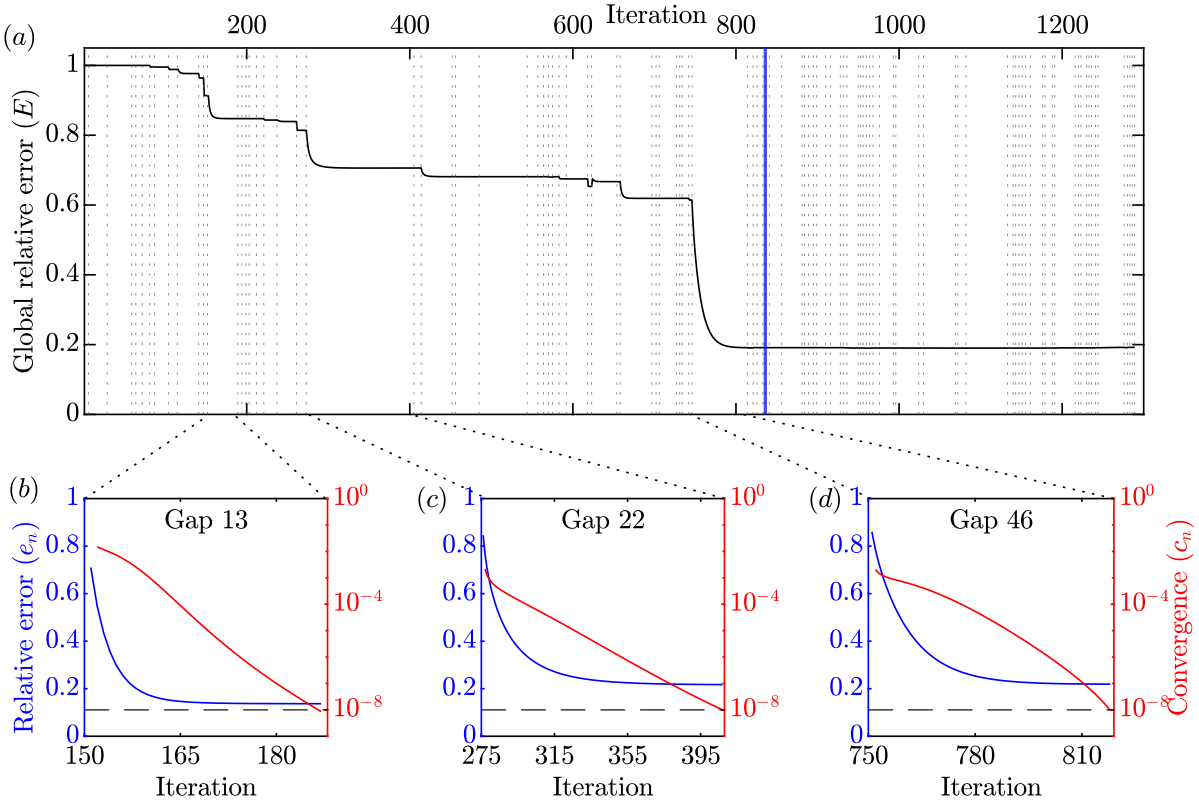

Figure 3.4.10: Errors and convergence for 5% gappyness, see figure 3.4.9(*b*). The global relative error is shown in (*a*). Inner (gap-wise) iterations are denoted by grey dotted lines and outer iterations as blue solid lines. Panels (*b-d*) show the gap-wise error and convergence for three randomly selected gaps within the first outer loop.

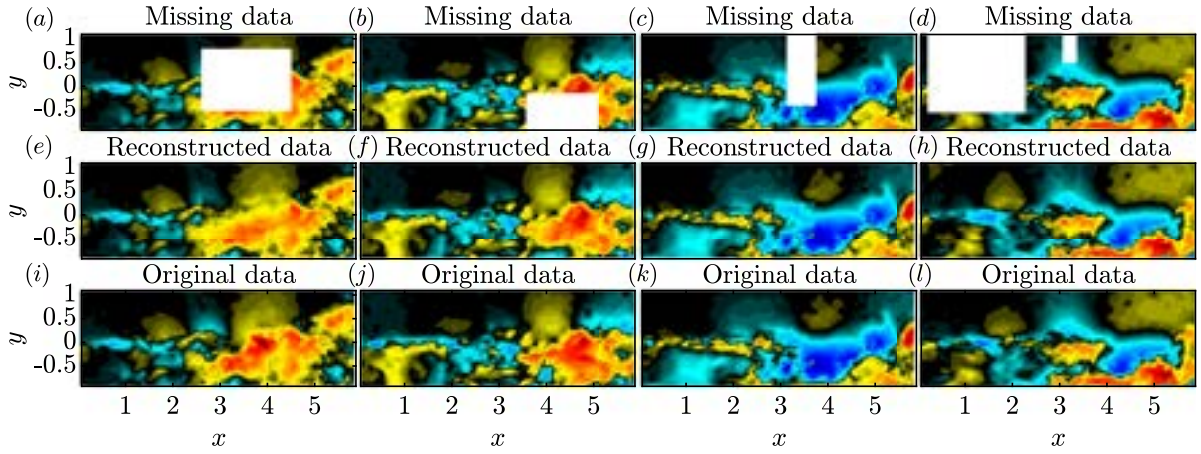

Figure 3.4.11: Reconstruction for the turbulent cavity flow with 5% gappyness at four time instances: (*a-d*) gappy data; (*e-h*) reconstructed data; (*i-l*) original data. False colors of the streamwise velocity fluctuations, u, are on the same scale in all plots.

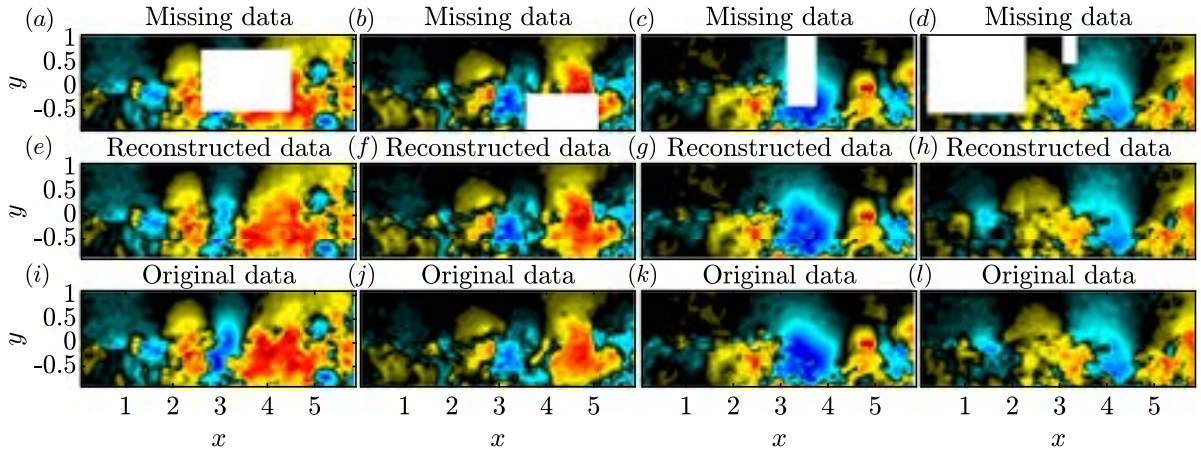

Figure 3.4.12: Same as figure 3.4.11, but for the transverse velocity fluctuations.

components for the gappy, reconstructed and original flow fields. Again, the first column is the snapshot with the largest reconstruction error, and the other three are arbitrarily selected. We observe that the reconstructions are very similar to the original flow field for all four time instances. The corresponding relative errors are e_i = 29%, 17%, 8%, and 22%, respectively. The comparison of panels (*e*) and (*i*) in figures 3.4.11 and 3.4.12 shows that the salient flow features are recovered by the algorithm, that is, despite the remaining error of 29%.

We next address the reconstruction of the two remaining cases with 1% and 20% of gappyness. Figure 3.4.13 shows the global relative errors for these cases. Two and five outer loops are required for convergence, and the final global relative errors are $E = 20.3\%$ and 19.4%, respectively. These values are very similar to that of the 5% case. This indicates that the reconstruction is not sensitive to the percentage of missing data within the range considered here. In each case, the reconstructions recover approximately 80% of the energy. This result is found in contrast to the laminar cylinder flow case, where the global relative error proportionally increases with the amount of missing data. As before we next inspect representative time instances for a qualitative assessment of the performance.

The reconstructions are compared to the gappy and original flow fields for 1% and 20% of missing data in figures 3.4.14 and 3.4.15, respectively. The reconstructions of the 1% case

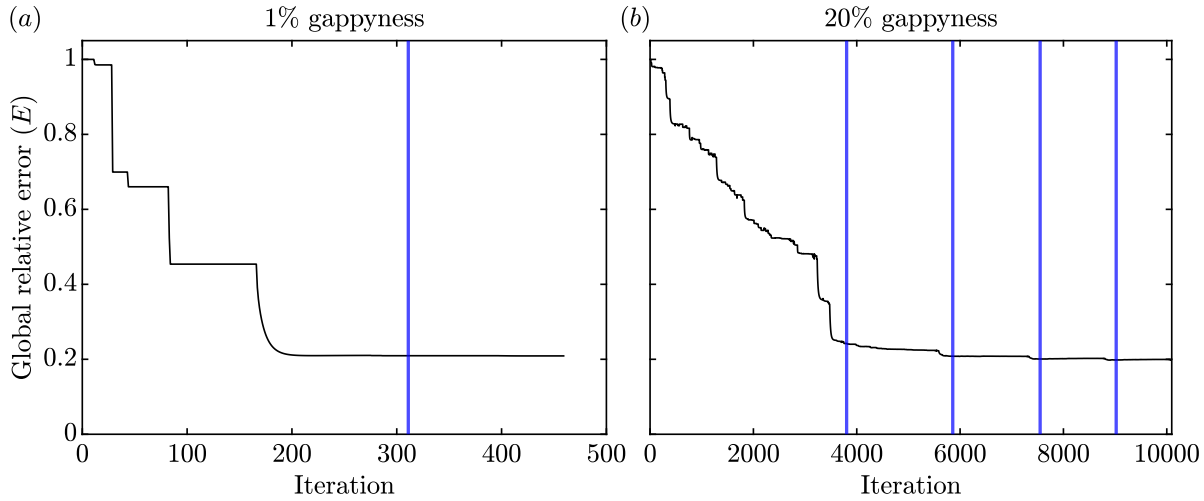

Figure 3.4.13: Global relative error of the gappy SPOD algorithm: (*a*) 1% gappyness; (*b*) 20% gappyness. The blue solid lines indicate the outer iterations.

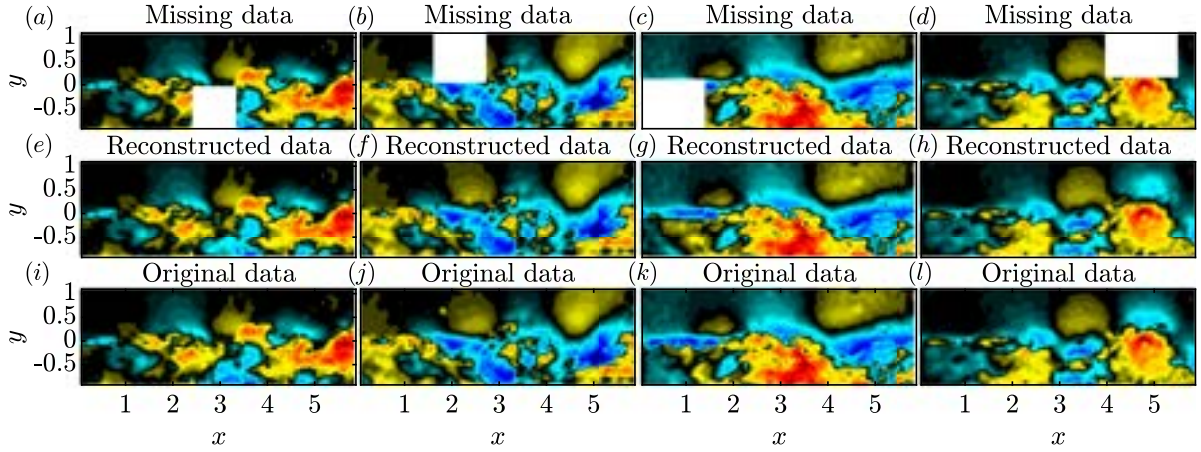

Figure 3.4.14: Reconstruction for the turbulent cavity flow with 1% gappyness at four time instances: (*a-d*) gappy data; (*e-h*) reconstructed data; (*i-l*) original data. False colors of the streamwise velocity fluctuations, u, are on the same scale in all plots.

are in very good agreement with the original data. For the 20% case shown in figure 3.4.15, large parts of the field-of-view are missing. An animation of the snapshots in the vicinity of the gaps (see supplemental material) further confirms that the gaps persist for a long time. The percentages of missing data for the four time instances are 58%, 48%, 28%, and 23%, and the corresponding relative errors are e_i = 43.2%, 26.4%, 13.2%, and 16.6%. A comparison between the reconstructed field-of-view in figure 3.4.15(*e*) and the reconstructed data in 3.4.15(*i*) shows

that the gappy SPOD algorithm was able to reconstruct large parts of the flow field. This puts into perspective the reconstruction error of $E = 19.4\%$ that might be perceived as large without this qualitative assessment. Note that correlation-based reconstruction is always limited by the physical length and time scales of the turbulent flow beyond which a reconstruction is not feasible. Comparing the reconstructed to the original data for the three remaining time instances confirms that the algorithm is capable of estimating many of the intricate details of the flow.

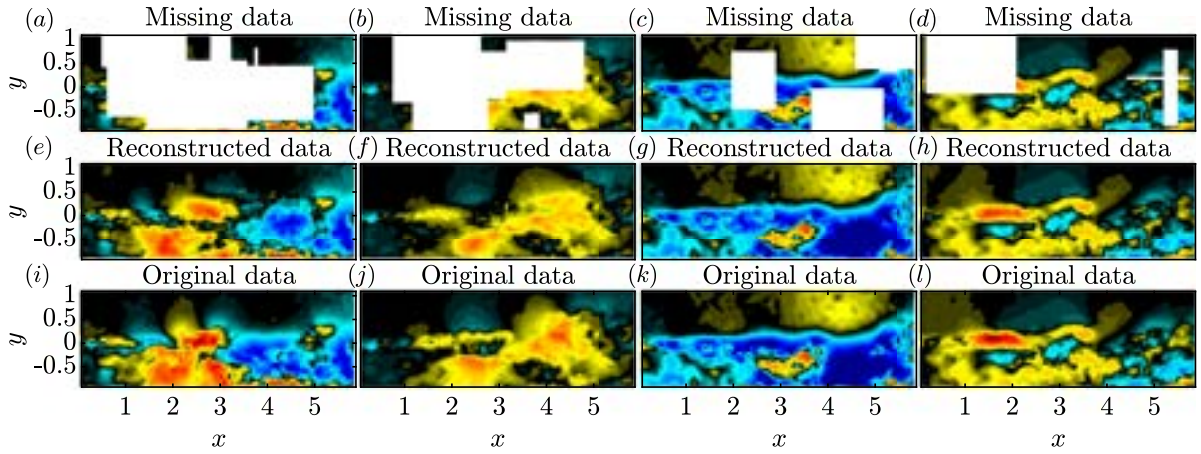

Figure 3.4.15: Reconstruction for the turbulent cavity flow with 20% gappyness at four time instances: (*a-d*) gappy data; (*e-h*) reconstructed data; (*i-l*) original data. False colors of the streamwise velocity fluctuations, u, are on the same scale in all plots.

3.4.3 Reconstruction of the turbulence statistics

After assessing the method's performance in terms of the global reconstruction error and with direct comparisons of original and reconstructed flow fields, we next focus on turbulence quantities. In particular, we consider the turbulent kinetic energy (TKE), TKE = $\frac{1}{2}(\overline{(u')^2} + \overline{(v')^2})$, and the Reynolds shear stress, $\tau_{xy} = \overline{u'v'}$. The comparison of the original, gappy, and reconstructed TKE fields for the 1%, 5%, and 20% cases are presented in figure 3.4.16. The cylinder and cavity flows are shown in figure 3.4.16(*a-g*) and 3.4.16(*h-n*), respectively. For 1% and 5%, moderate

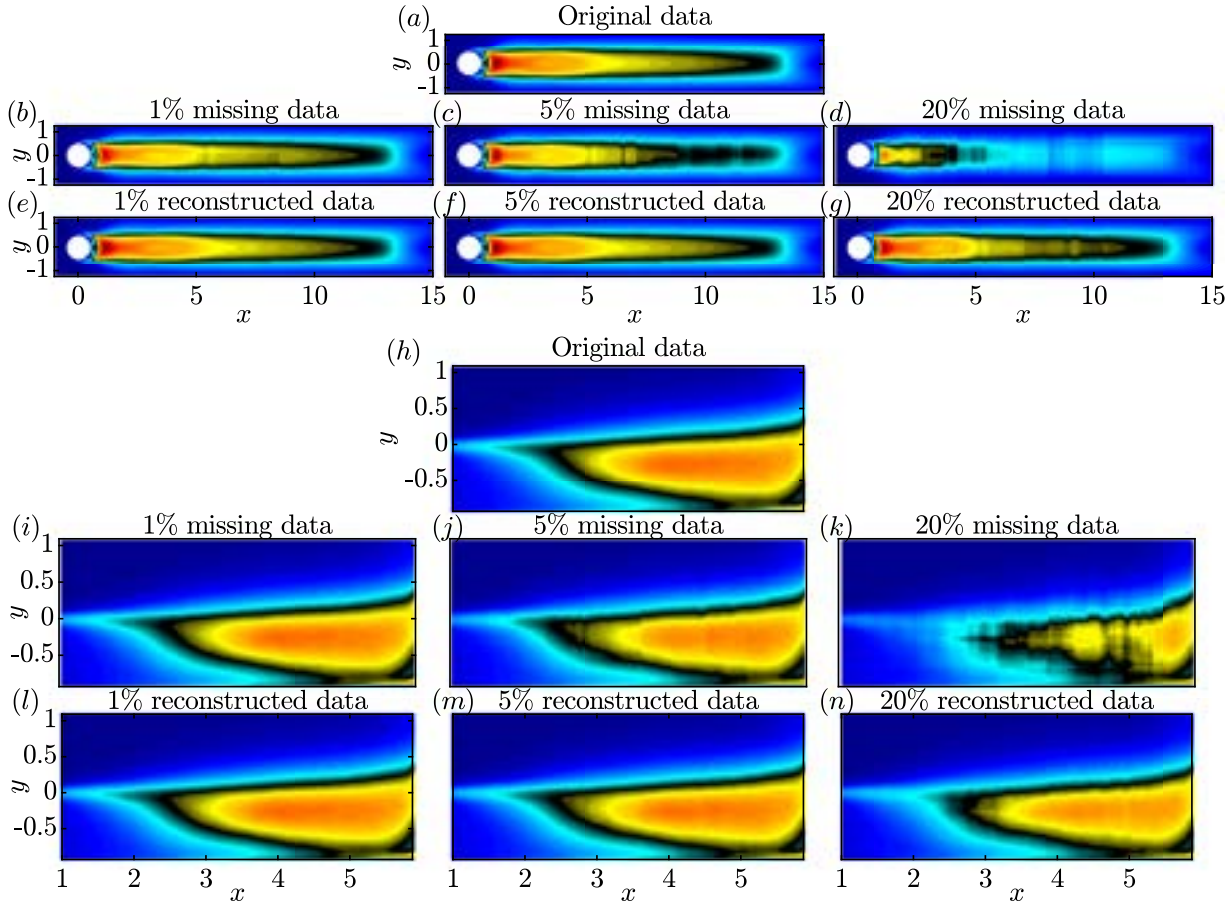

Figure 3.4.16: Turbulent kinetic energy fields for the gappy, reconstructed and original data: (*a-g*) cylinder flow; (*h-n*) the cavity flow. Contour levels are consistent between subplots (*a-g*) and (*h-n*).

distortions are observed in the gappy data for both cases, and the reconstructed TKE fields are almost indistinguishable from the original data. For 20%, a large fraction of TKE has been removed, and the flow field is heavily distorted. The reconstructions shown in panels (*g*) and (*n*), on the contrary, are smoother, recover large parts of the TKE, and compare well with the original data.

For a more quantitative assessment, the area-integrated TKE error is presented in table 3.4.2. In accordance with figure 3.4.16, the TKE error after reconstruction is almost negligible for 1% and 5% of missing data for the cylinder flow. The TKE error is also substantially lower for the cavity flow. For 20% of missing data, the TKE error reduces from 34.7% to 4.5%, and

Table 3.4.2: Area integrated TKE and Reynolds stress errors for the gappy and reconstructed flow fields.

Gappyness	TKE error (%)				Reynolds shear stress error (%)			
	Cylinder flow		Cavity flow		Cylinder flow		Cavity flow	
	Before	After	Before	After	Before	After	Before	After
1%	1.18%	3.40×10^{-3} %	0.65%	0.19%	1.67%	0.02 %	0.65%	0.14%
5%	8.23%	3.49×10^{-2} %	4.05%	1.3%	5.74%	0.18%	4.27%	1.02%
20%	34.72%	4.51%	21.96%	6.35%	25.25%	5.92%	24.59%	5.56%

from 22% to 6.4% for the two examples, respectively. These percentages correspond to $\approx$ 7- and 4-fold reductions. The qualitative counterparts to these numbers are the TKE field comparisons previously shown in figure 3.4.16(d,g) and 3.4.16(k,n), respectively. Also listed in table 3.4.2 is the area-integrated Reynolds shear stress error. Similar to the TKE error, the Reynolds shear stress error has been reduced significantly by a factor of $\approx$ 4 in both cases.

3.5 Comparison with other methods

Finally, we compare the performance of the gappy SPOD method to the established methods of gappy POD by Everson and Sirovich (1995) and Venturi and Karniadakis (2004) (referred to as gappy POD-ES and -VK in the following), and Kriging. For local Kriging, the exponential correlation model results, in agreement with Saini et al. (2016), in lower errors than the more standard Gaussian model. The more successful model is implemented in the MATLAB toolbox DACE (Lophaven et al., 2002) that was used for our comparisons. The same tool was used by Venturi and Karniadakis (2004), Raben et al. (2012), and Saini et al. (2016) for the same purpose.

Figure 3.5.1 compares the global relative errors for gappy SPOD, the two gappy POD algorithms, and Kriging. Both cases and all three levels of gappyness are considered. Both gappy POD methods have the number of modes as a free parameter that needs to be varied to identify the best-possible reconstruction. Kriging relies on interpolants instead of modes and

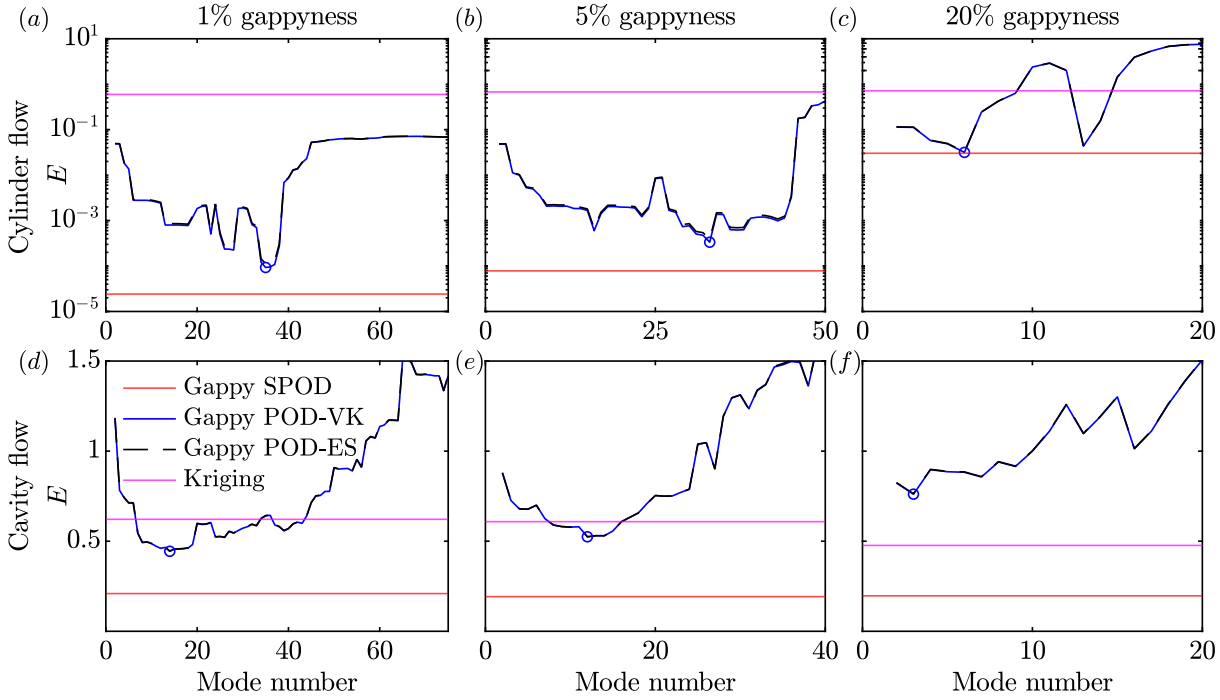

Figure 3.5.1: Global relative error for different reconstruction methods: (*a*-*c*) cylinder flow; (*d*-*f*) cavity flow; (*a*,*d*) 1%, (*b*,*e*) 5% and (*c*,*f*) 20% of missing data. The ordinate in (*a*-*c*)is on a logarithmic scale for clarity.

gappy SPOD does not truncate the modal basis. The reconstruction errors of these methods are therefore constant in figure 3.5.1. The gappy POD-ES and -VK methods produce almost identical errors (see also Raben et al., 2012, Saini et al., 2016), and we hence do not distinguish between them. The mode numbers were varied until candidates for the global minima, marked by circles, were identified as minima by observing the general trend of the errors. As the number of modes in classical POD is equal to the number of snapshots (4096 and 16000 for the data at hand), gappy POD becomes computationally intractable due to increasingly high compute times (see table 3 below). Therefore, there is no guarantee that the reconstruction corresponds to the actual global optimum. A few common trends are observed in all six cases in figure 3.5.1. In general, gappy POD outperforms Kriging and gappy SPOD outperforms gappy POD. For the cylinder flow and 1% and 5% of gappyness in figure 3.5.1(*a*,*b*), final reconstruction errors for gappy SPOD are 3.8 and 4.3 times below those of gappy POD and multiple orders of magnitude lower than those of Kriging. For 20% gappyness, gappy SPOD and gappy POD yield very similar results with only a marginal advantage of 2% for gappy SPOD, but both outperform Kriging by about one order of magnitude. For the turbulent cavity flow in figure 3.5.1(*d*-*f*), at all missing data percentages, gappy SPOD reduces the global relative error by about 80%, which is at least 20% lower than for other methods in all cases. In direct comparison with gappy POD, gappy SPOD achieves 2.1, 2.7, and 3.8 fold reductions in error for the three gappyness ratios, respectively. As in section §§3.4.1 and 3.4.2, we observe that the gappyness has a significant impact on the achievable error reduction for the periodic laminar flow. In contrast, the final error is almost independent of the percentage gappyness for the turbulent, noisy experimental data.

We next compare the compute times for Kriging, gappy POD, and gappy SPOD in table 3.5.1. With the exception of the cylinder flow at the two lower percentages (where gappy SPOD has an advantage), Kriging and gappy SPOD have similar computational times. A direct comparison with gappy POD is not possible as the optimal number of modes is not known a priori, and its computation becomes quickly intractable as the mode number is increased. The mode

Table 3.5.1: Comparison of computational time. The computations were performed on a high-performance workstation with 192GB of memory and two 3.0 GHz 48-core Intel Xeon Gold CPUs. The spatial degrees of freedom times the number of variables for the cylinder and cavity flows are 62500, and 16500, respectively. The corresponding number of snapshots are 4096 and 16000.

Gappy-ness	Cylinder flow (in hr)			Cavity flow (in hr)		
	Kriging	gappy POD	gappy SPOD	Kriging	gappy POD	gappy SPOD
1%	11.24	49.95 (75 modes)	1.63	2.79	27.88 (75 modes)	2.37
5%	28.91	64.69 (50 modes)	13.58	10.91	19.94 (40 modes)	7.28
20%	159.63	34.13 (20 modes)	139.86	46.84	26.30 (20 modes)	49.57

number shown in table 3.5.1 reflect the minimum number of modes required to guarantee that the global minimum was identified to the best of our ability. For the two examples at hand, we found that a decreasing number of modes was required for gappy POD as the gappyness increases. This gives gappy POD an advantage in terms of compute time for higher percentages of missing data. Note, however, that gappy SPOD yields a more accurate reconstruction, and does not require monitoring. In summary, gappy SPOD always outperforms Kriging and generally performs better (although in one case only marginally) than gappy POD in terms of the reconstruction error, but sometimes does so at a higher computational cost.

3.6 Missing snapshots

A common scenario not considered so far is that of missing snapshots, or even longer sequences of missing snapshots. Unlike the classical gappy POD methods (Everson and Sirovich, 1995, Venturi and Karniadakis, 2004), the gappy SPOD algorithm does not rely on a least-squares fit and hence does not become singular in this situation. Figure 3.6.1 shows the combination of gaps and missing snapshots investigated here, and which amounts to 5% of missing data. The gaps are randomly generated in the same way as in §§3.4.1 and 3.4.2. For isolated, non-consecutive missing snapshots, temporal interpolation can provide accurate reconstructions, and we hence do not consider this simpler scenario. Instead, we add for the cylinder and cavity flow,

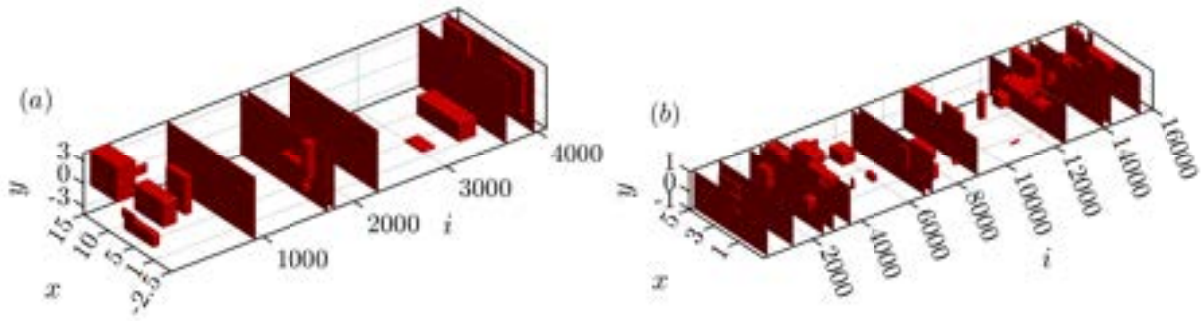

Figure 3.6.1: Randomly generated gaps with 5% of missing data and missing snapshots: (*a*) cylinder flow and (*b*) cavity flow.

respectively, five and ten sequences of ten to 25 consecutive missing snapshots. The start of the missing snapshot sequences and their duration are randomly selected within this interval. The main difference between localized gaps and missing snapshot sequences is that, in the latter, the algorithm solely relies on temporal correlation with previous and subsequent snapshots for the reconstruction.

The global relative errors for this scenario are shown in figure 3.6.2. As before, the tolerance is set to $tol = 10^{-8}$ and both cases require four outer loops for convergence. The final errors are $E = 28\%$, and 31%, respectively. For the cavity flow example, the final error, although higher, is still comparable to that of the 5% case shown in figure 3.4.10. For the cylinder flow example, on the other hand, the final error is comparable to that of the turbulent cavity flow, but significantly higher than the corresponding case shown in figure 3.4.3. A notable difference compared to cases without missing snapshots is that the converged solution does not necessarily yield the minimum global relative error. However, the converged values are within 4% of the global minimum, and about 70% of the missing energy is recovered for both examples. Missing snapshots apparently pose a special challenge to the algorithm, in particular for the laminar cylinder flow. An inspection of the reconstructed data before and after the largest jump occurring

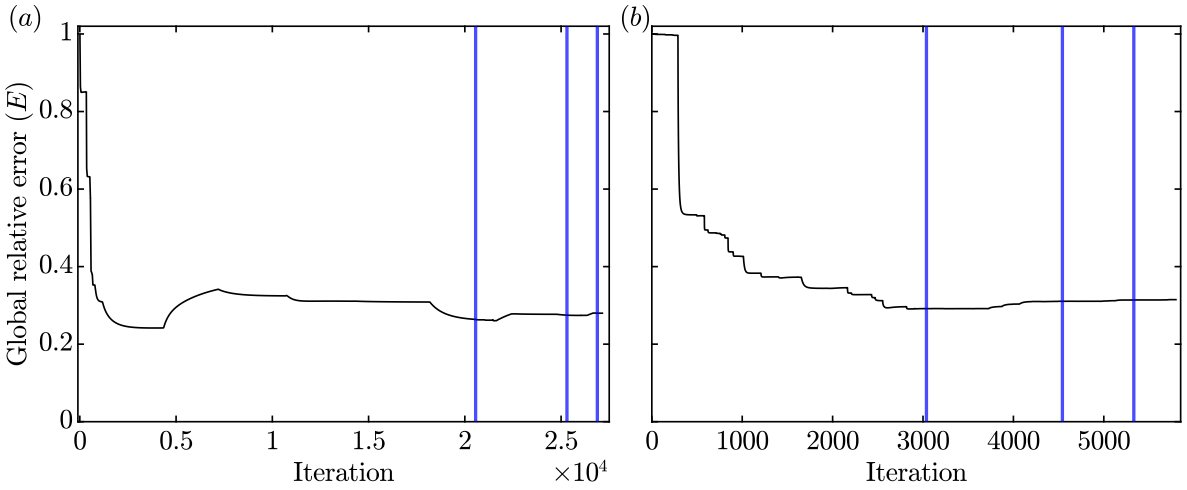

Figure 3.6.2: Global relative error for cases with missing snapshots shown in figure 3.6.1: (*a*) cylinder flow; (*b*) cavity flow.

at iteration 4340 in figure 3.6.2(*a*) reveals that the jump is caused by an inversion of the phase of the entire flow field, and that the jump occurs for the gap with the longest consecutive sequence of 25 missing snapshots. For simplicity, we refrain from introducing a special treatment of this very specific phase-inversion error and emphasize that the final error is comparable to its global minimum. A special treatment of this error type is a direction of future research.

3.7 Performance of the algorithm in the presence of noise and filtering

Experimental flow data such as the cavity flow data investigated in §4.2, inherently contains measurement noise. In Nekkanti and Schmidt (2021a), we have demonstrated the capability of SPOD for denoising by rank truncation. The underlying idea is that physical structures are coherent and therefore captured by the leading SPOD modes. Many sources of measurement noise, on the other hand, are incoherent and lead to additional low eigenvalues that can conveniently be truncated. This becomes clear in figure 3.7.1(*b*), where added Gaussian white noise with standard deviation, $\sigma = 0.1$ leads to the formation of a distinct noise floor in the

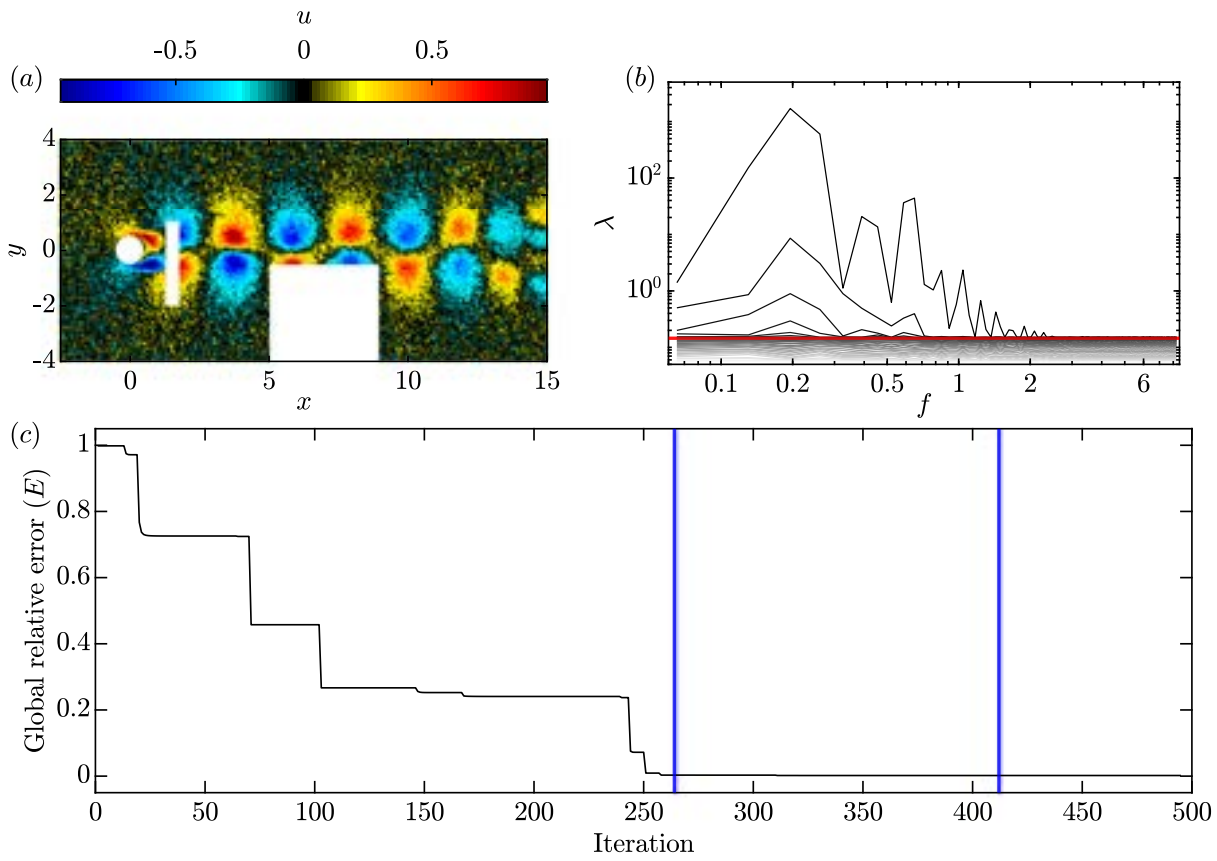

Figure 3.7.1: Gappy data reconstruction for flow with 5% gappyness subjected to random noise with standard deviation $\sigma = 0.1$: (*a*) instantaneous streamwise velocity field; (*b*) SPOD spectrum; (*c*) global relative error. The red line in (*b*) indicates the truncation threshold, chosen slightly above the noise floor.

otherwise noise-free numerical cylinder data with 5% gappyness. The same observation has been made for space-only POD by Venturi (2006) and Epps and Krivitzky (2019). A time instant of the streamwise velocity component, u, is shown in figure 3.7.1 (*a*). In the gappy SPOD algorithm, we use a truncation threshold slightly above the noise floor (red line in 3.7.1(*b*)) to remove noise in step (iii) before performing steps (iv)-(viii). The hard-thresholding leads to the truncation of 84% of the modes at the lowest non-zero frequency. Frequencies above $f = 2.6$ fall below the noise floor and are removed entirely. This significant truncation in terms of number of modes, however, only amounts to 2.3% of the total energy being removed. A positive by-product of the truncation is that the algorithm converges much faster and in fewer iterations. The total reconstruction error

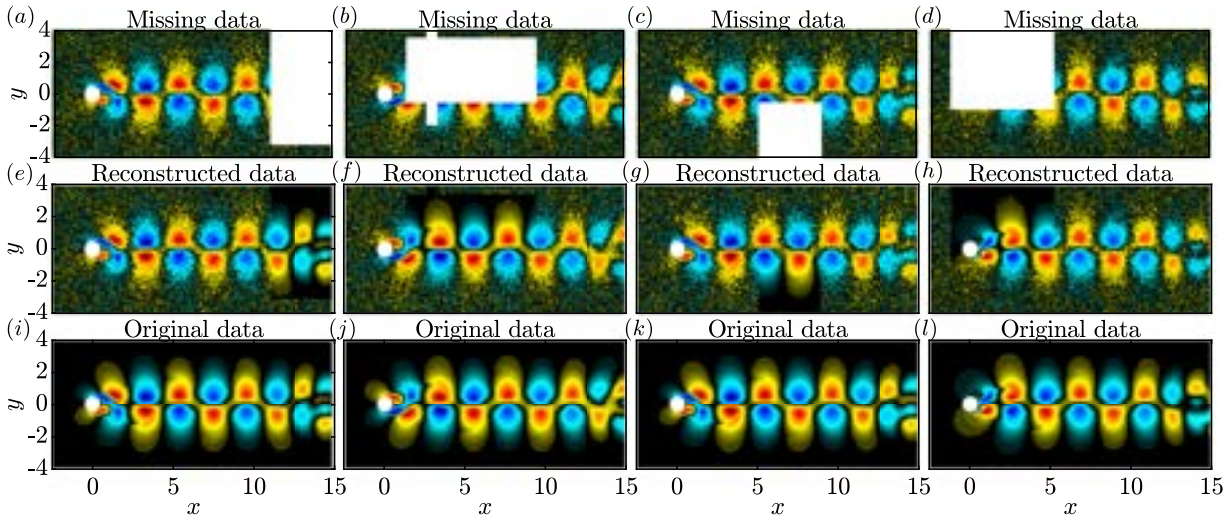

Figure 3.7.2: Same as figure 3.4.4 with added white noise.

upon convergence is 0.19% as compared to the 7.7×10^{-3}% of the original case in figure 3.4.3(b).

Figure 3.7.2 shows the instantaneous streamwise velocity component of the gappy data containing noise, reconstructed, and original flow fields, respectively. The same four time instances as in figure 3.4.4 are selected. A visual inspection revels that the reconstructions in the missing regions are almost identical to the original data, and that the noise has been removed in large parts. The relative errors for these four snapshots are $e_i = 0.3\%$, 0.2%, 0.15%, and 0.17%, respectively. Figures 3.7.1 and 3.7.2 show that the algorithm not only performs well in the presence of noise, but also removes it to a large degree.

3.8 Summary and discussion

A new algorithm is proposed that leverages the temporal correlation of SPOD modes with preceding and succeeding snapshots and their spatial correlation with the surrounding data to reconstruct partially missing or corrupted flow data. For demonstration purposes only, the reconstructed data are compared to the actual data in the corrupted regions. The algorithm itself exclusively relies on convergence metrics and fills in the gaps sequentially until the reconstruction

converges to a user-defined tolerance, both locally, that is for each gap, and globally. The method is demonstrated on simulation data of the flow around a cylinder and time-resolved PIV data of turbulent cavity flow; the first being a canonical benchmark example used in many previous studies and the latter a realistic scenario of turbulent flow data in the presence of measurement noise. For randomly seeded and sized gaps that amount to up to 20% of missing data and extend over large regions in space and many snapshots, the algorithm accurately recovers the missing instantaneous and mean flow fields as well as turbulence statistics. It generally outperforms the established methods, particularly for the turbulent flow, where it yields a significantly lower reconstruction error that translates into an at least two-fold reduction compared to gappy POD and Kriging. Notably, this comparably low reconstruction error appears largely unaffected by the percentage gappyness within the range tested here. Even though the different methods scale differently and the results are case-dependent, their computational costs are roughly comparable. A caveat to the strong performance of the new method is that it is strictly applicable to statistically stationary data only, and that it relies on a sufficiently well-converged SPOD of the data, which in turn requires a sufficiently long time series. The main limitation of the algorithm directly follows from the properties of the SPOD: accurate flow reconstruction is only possible within the physical correlation length and time scales of the flow. This limitation, however, applies to all correlation-based methods. A systematic study of the most important spectral estimation parameters shows that best practices for SPOD (Schmidt and Colonius, 2020) also lead to a good balance between the accuracy and computational cost of the gappy SPOD algorithm. In 3.7, we demonstrate that the algorithm not only performs well in the presence of noise, but also that mode truncation facilitates efficient denoising while reducing computational time. Contingent on further testing on more data sets, the present results suggest that the algorithm can be fully automated and applied to any sufficiently long stationary flow data.

Acknowledgements We gratefully acknowledge partial support from Office of Naval Research grant N00014-20-1-2311 and AFOSR Grant FA9550-22-1-0541. We thank Lou Cattafesta

and Yang Zhang for providing the TR-PIV data and fruitful discussions. The data was created with supported by the U.S. Air Force Office of Scientific Research award FA9550-17-1-0380. This chapter is a reprint of the material in the article: A. Nekkanti, and O. T. Schmidt. “Gappy spectral proper orthogonal decomposition”, Journal of Computational Physics, 478, 111950 (2023). The dissertation author was the primary investigator and author of this work.

Appendix

3.A Effect of spectral estimation parameters n_{fft} and n_{ovlp}

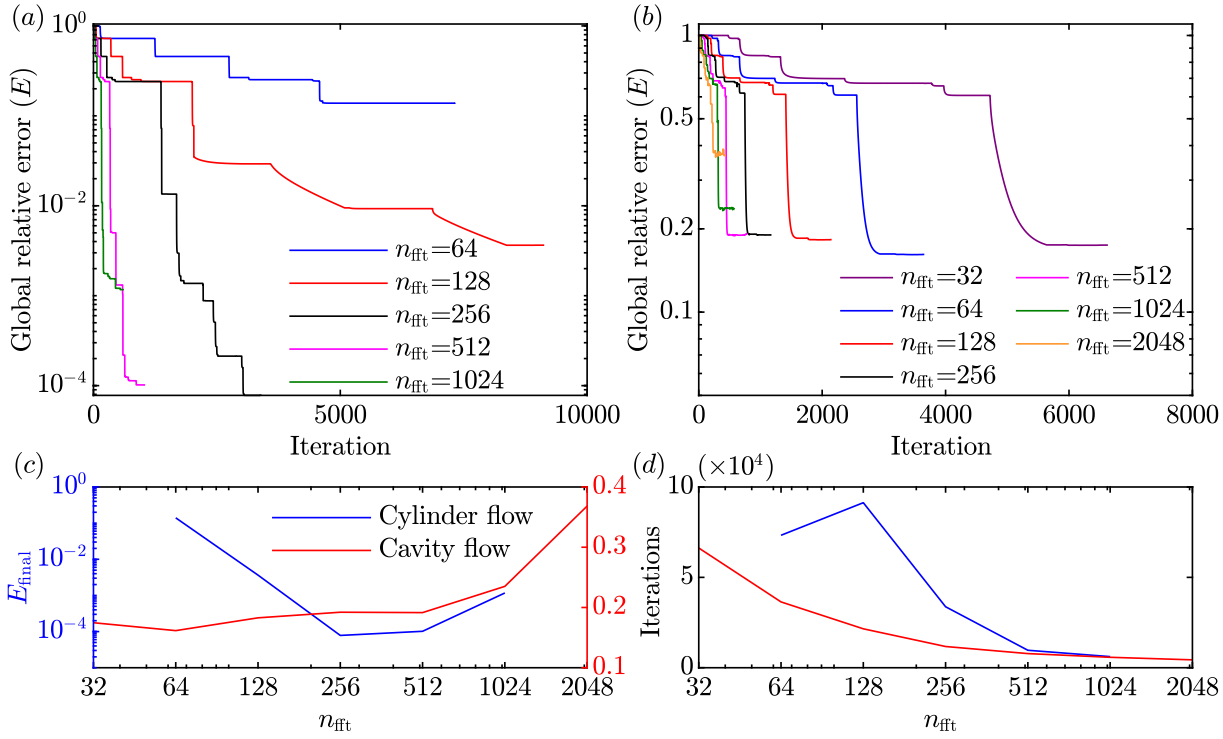

Figure 3.A.1: Effect of n_{fft} on the global relative error: (*a*) cylinder flow; (*b*) cavity flow; (*c*) final error, and (*d*), total number of iterations as a function of n_{fft}.

The arguably most crucial aspect of spectral estimation is the inevitable trade-off between variance and bias. In SPOD, this trade-off is mainly determined by the block size, n_{fft}. For low

n_{fft}, the frequency bin size, $\Delta f \propto 1/n_{\text{fft}}$, is large and the spectrum will be biased. For large n_{fft}, the total number of blocks, and therefore realizations of the Fourier transform, is low and the spectrum suffers from high variance. The number of blocks can be inflated by increasing the overlap, n_{ovlp}. However, values above 50% in practice do not yield lower-variance estimates as the information contained in neighbouring blocks becomes increasingly redundant (Schmidt and Colonius, 2020). Figure 3.A.1 summarizes a parameter study of n_{fft} for both test cases. As in figures 3.4.3 and 3.4.10, we show the global relative reconstruction errors for varying n_{fft} and 5% gappyness. Results for the cylinder and cavity flow cases are shown in figure 3.A.1(a) and 3.A.1(b), respectively. The final error is more sensitive for the laminar flow and is hence reported on a logarithmic scale. As before, all computations were converged to a tolerance of $tol = 10^{-8}$. The final errors, E_{final}, and total number of iterations, are extracted and reproduced in figure 3.A.1(c) and 3.A.1(d). In both cases, the global relative error first decreases and then increases with n_{fft}. The lowest errors are achieved for $n_{\text{fft}} = 256$, and $n_{\text{fft}} = 64$, respectively. With the exception of $n_{\text{fft}} = 64$ for the cylinder flow, the number of iterations decreases monotonically with n_{fft}. This can be seen in figure 3.A.1(d). The number of iterations, in turn, is directly indicative of the overall compute time. In the main text, we did not use this *a posteriori* knowledge of the optimal value of n_{fft}. For the cylinder, the best practise value of $n_{\text{fft}} = 256$ yields the minimum error. For the cavity flow this is not the case. However, the error for $32 \leqslant n_{\text{fft}} \leqslant 512$ only deviates within 3% from the optimal value. At the same time, using $n_{\text{fft}} = 256$ leads to a factor 3.5 savings in compute time as compared $n_{\text{fft}} = 64$. To summarize, the best practise of $n_{\text{fft}} = 256$ yielded the optimal value for one of the examples, and a very good compromise between reconstruction accuracy and compute time in the other.

The effect of the overlap, n_{ovlp}, is investigated in figure 3.A.2 for a fixed segment length of $n_{\text{fft}} = 256$ and 5% gappyness. The final reconstruction errors for $n_{\text{ovlp}} = 0\%$, 25%, 50% and 75% are shown in figure 3.A.2(a). For the turbulent cavity flow, the error decreases with increasing overlap. For the laminar cylinder wake, the error first decreases, but then increases again for the

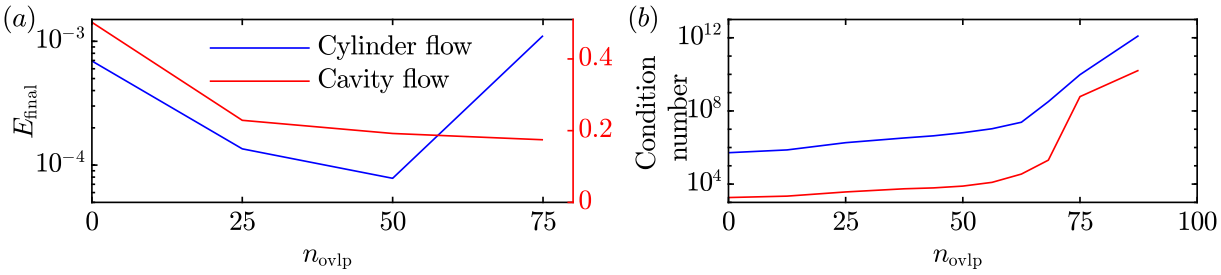

Figure 3.A.2: Effect of n_{ovlp} on the, (*a*), global relative error and, (*b*), condition number of the weighted CSD matrices for 5% missing data. The maximum condition number over all frequencies is shown.

largest overlap of $n_{\text{ovlp}} = 75\%$. Notably, the best-practice value of $n_{\text{ovlp}} = 50\%$ yields the lowest error for the cylinder flow and is within 2% of the optimum achieved for the cavity flow. The latter is achieved for $n_{\text{ovlp}} = 75\%$ and comes with an approximately 50% increase in computational cost. The increase of the error at $n_{\text{ovlp}} = 75\%$ for the laminar cylinder wake is unexpected at first. We speculate that it is related to the increasing redundancy of information in the overlapping blocks, which in turn results in increasing linear dependence. The latter can be gauged by the condition number. In figure 3.A.2(*b*), the maximum condition number over all frequencies, $\max_l(\lambda_l^{(1)}/\lambda_l^{(n_{\text{blk}})})$, is shown as a function of overlap. As the condition number is independent of the data reconstruction, more data points are computed and shown in figure 3.A.2(*b*). The trends for the two flows are similar, but the condition number of the cylinder flows is, indeed, significantly higher and elevated by about two orders of magnitude for $n_{\text{ovlp}} \lesssim 60\%$. For larger values, the condition numbers of both flows suddenly increase. These observations support the best-practice value of $n_{\text{ovlp}} = 50\%$, which stays well clear of ill-conditioning associated with high overlaps.

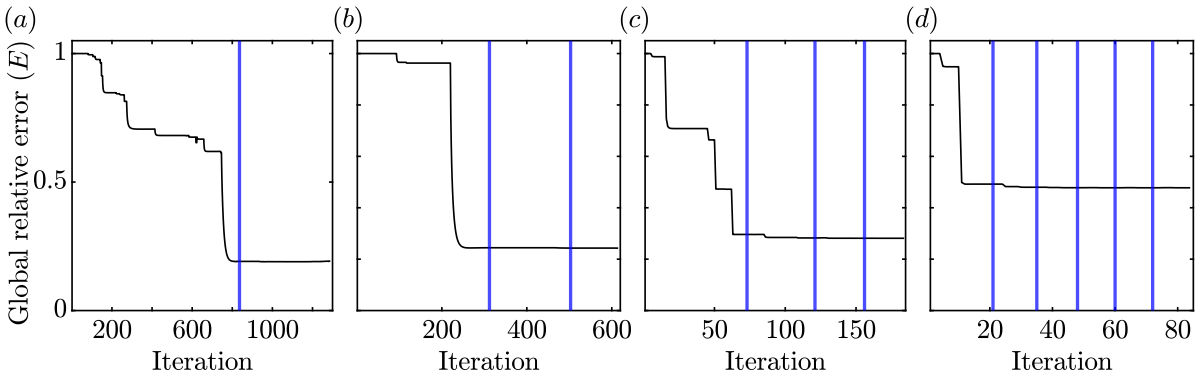

Figure 3.B.1: Global relative error for the cavity flow with 5% of missing data: (*a*) full data; (*b*) first half of the data; (*c*) first quarter of the data; (*d*) first 10% of the data. The total number of snapshots are 16000, 8000, 4000, and 1600, respectively.

3.B Effect of data length n_t

As a statistical method, SPOD relies on a large ensemble realizations of the Fourier transform to converge the modes and eigenvalues. We hence expect the quality of the reconstruction to be better for longer time series. The following study of increasingly truncated subsets of the 5% gappyness cavity data confirms this. The original example shown in figure 3.4.9(*b*) is truncated by 50%, 75%, and 90%. The convergence in terms of the global relative errors for the full and truncated datasets are shown in figure 3.B.1. For comparability, n_{fft} is fixed at 256. Upon convergence, the final global relative error increases with increasing truncation from $E = 19\%$ to 24.3%, 28.1%, and finally 47.8%, as anticipated. At the same time, we observe that the shorter datasets require a higher number of outer iterations for global convergence. The full and truncated datasets require two, three, four, and six outer iterations, respectively. These observations confirm the dependence of gappy SPOD algorithm on a sufficiently long time series and, therefore, sufficiently converged SPOD modes. As a rule of thumb, this suggests that gappy SPOD should only be applied to datasets that are suitable for SPOD analysis in the first place.

Part II

Investigating the flow physics of turbulent jets

Chapter 4

Modal analysis of the acoustic directivity in turbulent jets

4.1 Introduction

The reduction of jet noise is an important objective for the aviation community. The pioneering works by Crow and Champagne (1971) and Brown and Roshko (1974) were the earliest to report the presence of large-scale coherent structures in turbulent jets and shear layers, respectively. Here, large-scale refers to dimensions longer than or comparable to the jet diameter. Mollo-Christensen (1967) described them as intermittent spatial structures, or wavepackets, present in the mixing layer. Researchers (Crighton and Gaster, 1976, Crighton and Huerre, 1990, Michalke, 1977, Tam and Burton, 1984, Tam and Morris, 1980) have modeled the coherent structures as growing and decaying instability waves of the turbulent mean flow. These wavepackets were identified as the main source of aft-angle noise (Jordan and Colonius, 2013). The acoustic radiation of wavepackets is highly directive and concentrated in the downstream direction. The directive emission shows an exponential decay at high polar angles θ, or low jet inlet angle $\phi = 2\pi - \theta$, correspondingly. This pattern was termed superdirective radiation

by Crighton and Huerre (1990). In this work, we will use this word more loosely and refer to radiation patterns that are isolated and clearly directed downstream as superdirective. Cavalieri et al. (2012) have shown that the axisymmetric mode of the subsonic jets exhibit super-directivity. Readers can refer to Jordan and Colonius (2013) for a comprehensive review on wavepackets in turbulent jets.

Based on experimental observations and the author's physical interpretation of the source mechanisms, Tam et al. (1996) proposed a separation of the far-field spectrum into two empirical similarity spectra for the downstream and sideline radiation, respectively. This approach was later extended to subsonic jets by Viswanathan (2002, 2004) and Tam et al. (2008).

Modal decomposition techniques (Rowley and Dawson, 2017, Taira et al., 2017) facilitate the analysis of complex flows by extracting essential features. The most widely used approach, proper orthogonal decomposition (POD), was introduced by Lumley (Lumley, 1967, 2007) to educe coherent structures from turbulent flow fields. Space-only POD computed using the method of snapshots was later introduced by Sirovich (1987) and is the most commonly used form of POD. It decomposes the flow field into temporal coefficients and spatial modes that optimally represent the data in terms of energy. The temporal POD expansion coefficients contain, in general, a combination of different time scales and are only correlated at zero time lag. Spectral proper orthogonal decomposition (SPOD) is the frequency-domain variant of POD. It computes modes that oscillate at a single frequency from statistically stationary data. By construction, SPOD identifies structures that are coherent in both space and time (Towne et al., 2018) (in the strict mathematical sense). A number of studies showed that the dominant dynamics are often accurately captured by only a few modes (Citriniti and George, 2000, Glauser et al., 1987, Jung et al., 2004, Schmidt et al., 2018, Towne et al., 2018). Experimentally, Glauser et al. (1987), Citriniti and George (2000) and Jung et al. (2004) showed that a large fraction of the kinetic energy is contained in the first three SPOD modes. Recently, Schmidt et al. (2018) applied SPOD to high-fidelity simulation data of turbulent jets in the subsonic, transonic, and supersonic

regimes. The authors give a detailed account of the Kelvin-Helmholtz and the Orr-type instability mechanisms that dominate the initial shear-layer and the region downstream of the potential core, respectively. Towne et al. (2018) performed SPOD on Mach 0.4 turbulent jet and present a detailed account of the method and its relationship to space-only POD, resolvent analysis, and dynamic mode decomposition (DMD).

In this work, we perform SPOD of LES simulation data of jets at Mach 0.7, 0.9, and 1.5, and analyze radiation wave patterns with special emphasis on directivity. The methodology of SPOD is already explained in §2.2.1 and is hence omitted for brevity. §In section §4.2, the results are presented and the work is summarized in section §4.3.

4.2 Results and Discussions

We analyse the large-eddy simulations (LES) databases of turbulent jets at Mach numbers $M_j = 0.7$, 0.9 and 1.5 computed by Brès et al. (2017, 2018, 2019). The reader is referred to Brès et al. (2017, 2018), Brès and Lele (2019) for further details on the numerical method and meshing strategy. The flow is non-dimensionalized by the nozzle exit values, namely, velocity by U_j, pressure by $\rho_j U_j^2$, length by the nozzle diameter D, and time by D/U_j. Frequencies are reported in terms of the Strouhal number $St = fD/U_j$. A cylindrical domain Ω of size $x, r \in [0,30] \times [0,6]$ is used for the analysis. The LES data consists of 10,000 snapshots separated by a time step of $\Delta t c_\infty / D$. Important parameters are summarized in table 4.2.1.

Previous studies (Arndt et al., 1997, Cavalieri et al., 2011, 2012, Jordan and Colonius, 2013, Juve et al., 1979) have reported that most of the far-field sound energy is concentrated in the first three azimuthal wavenumbers, $m = 0, 1$ and 2. For the sound radiated in the downstream direction, the axisymmetric mode ($m = 0$) is most dominant, while the helical ($m = 1$) and the double-helical modes ($m = 2$) become more important in the sideline direction (Jordan and Colonius, 2013). In this study, we focus our attention on the noise emitted by these three azimuthal

Table 4.2.1: Parameters of the Large-Eddy Simulations

case	Re	M_j	T_j/T_∞	p_0/p_∞	$\Delta t c_\infty/D$	$St_{\max}$	Reference
Supersonic	1.55×10^5	1.5	1.74	3.67	0.1	1.0	case A2 Brès et al. (2017)
Transonic	1.01×10^6	0.9	1.0	1.7	0.2	1.6	Brès et al. (2018)
Subsonic	0.79×10^6	0.7	1.0	1.4	0.2	1.6	Brès and Lele (2019)

wavenumbers. The directivity of the radiation is expressed in terms of the jet inlet angle ϕ, defined with respect to the negative x-axis, such that 180° corresponds to the downstream direction and 90° to the sideline direction perpendicular to the jet axis.

The intensity of the sound radiated to different directions is computed by calculating the overall sound pressure level (OASPL) along the upper boundary at $r = 6$. At this radial distance, effects of the hydrodynamic pressure component are still partially present, in particular for low frequencies and downstream of the potential core (see also Bogey et al., 2007, Zaman, 1986). Acoustic analogies based on Kirchhoff's method (Lyrintzis and Mankbadi, 1996) or the Ffowcs-Williams Hawkings equations (Brès et al., 2017, Ffowcs Williams and Hawkings, 1969) may in principle be applied to extend the analysis to the true far-field, but this is beyond the scope of this study. Here, the noise at the radial distance $r = 6$ is used as a proxy of the far-field pressure. The power spectral density and the OASPL are defined as

$$\mathrm{PSD} = 10\log_{10}\left(\frac{2\hat{p}'(m,\phi,St)\hat{p}'^{*}(m,\phi,St)}{p_{\mathrm{ref}}^2 St_{\min}}\right), \quad \text{and} \tag{4.1}$$

$$\mathrm{OASPL} = 10\log_{10}\left(\sum_{St_{\min}}^{St_{\max}}\frac{2\hat{p}'(m,\phi,St)\hat{p}'^{*}(m,\phi,St)}{p_{\mathrm{ref}}^2}\right), \tag{4.2}$$

respectively. Here, p_{ref} is the reference pressure and $\hat{p}'$ is the Fourier transform of the pressure fluctuations in time.

The PSD is estimated using the Welch's method (1967) with 50% overlap and $n_{\mathrm{freq}} = 512$. Within the radial extent of the computational domain ($r \leqslant 6$) and at high jet inlet angles, the hydrodynamic component contributes a significant part of the energy associated with pressure

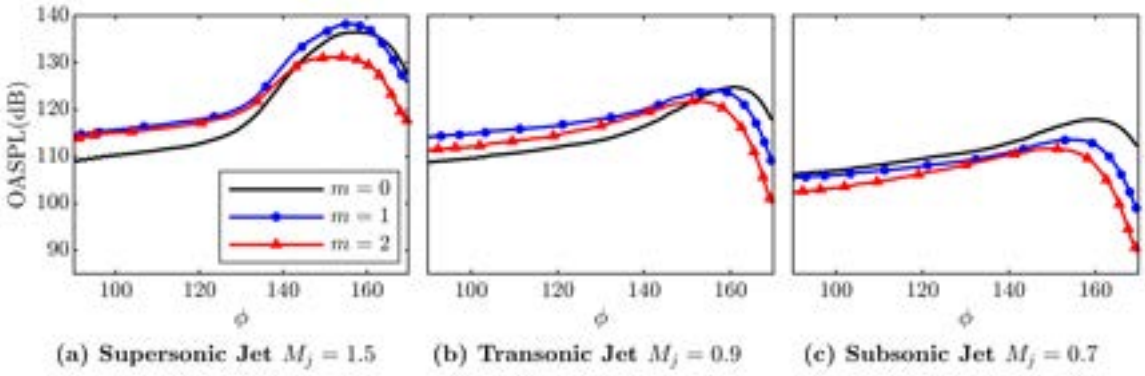

Figure 4.2.1: Overall sound pressure level at different jet inlet angles; OASPL for $m = 0$ (black solid lines), $m = 1$ (blue lines with circles) and $m = 2$ (red lines with triangles).

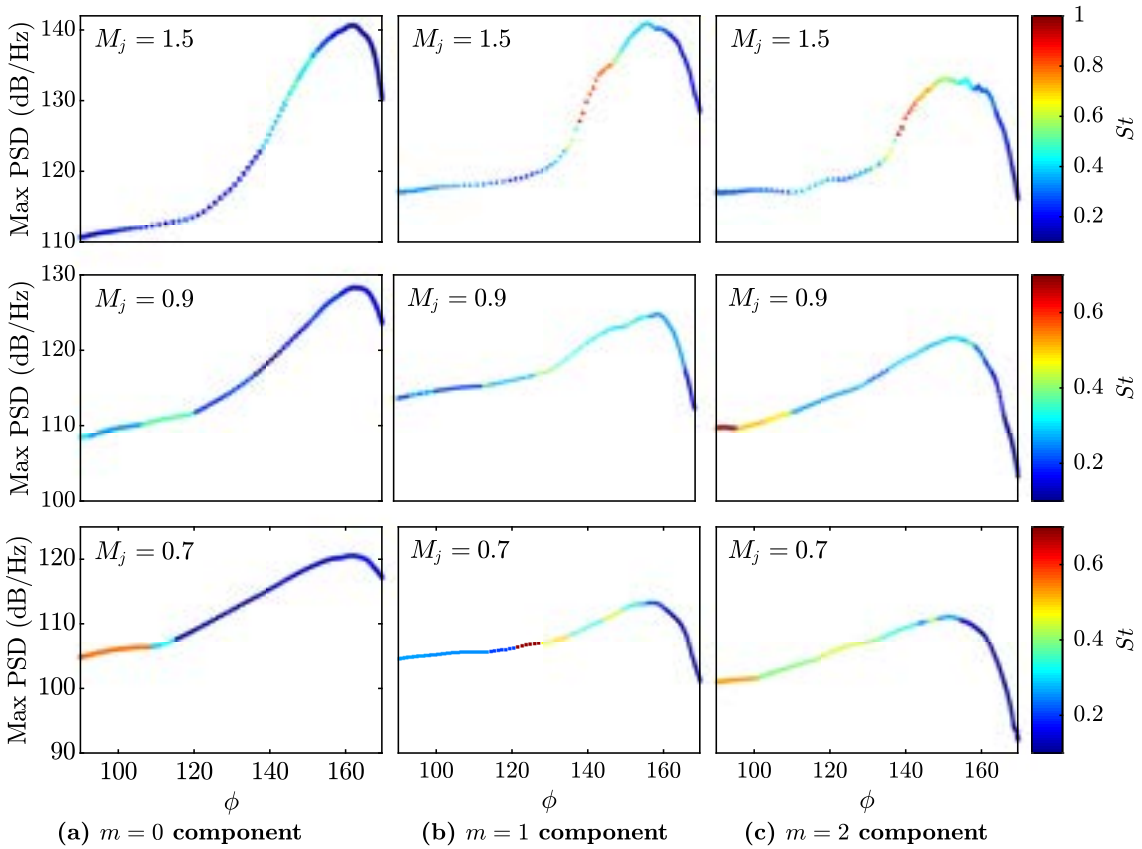

Figure 4.2.2: Maximum PSD as a function of jet inlet angle: $m = 0$, $m = 1$ and $m = 2$. False colors indicate corresponding peak frequency. The relative trends between different azimuthal components are identical to figure 2.2.

fluctuations (**?**). To eliminate the effect of the hydrodynamic component, a high-pass filter

($St \geqslant 0.1$) is used. The OASPL of the filtered signals for different azimuthal wavenumbers and different Mach numbers are presented are presented in figure 4.2.1. The overall sound pressure level at each ϕ is a measure of the total sound radiated in that particular direction. The OASPL of azimuthal mode $m = 1$ peaks at $\phi = 156^\circ$ for the supersonic jet, whereas the $m = 0$ component peaks at $\phi = 162^\circ$ for the transonic and subsonic jets. These angles are in agreement with the observations made by Jordan and Colonius (2013) and Tam et al. (2008). For the supersonic jet, the $m = 1$ component dominates at most angles. At lower inlet angles, $m = 2$ is the leading subdominant component. At higher angles, this component is replaced by $m = 0$. In the case of the transonic jet, $m = 1$ is the most dominant component in the range $90^\circ \leqslant \phi \leqslant 155^\circ$, whereas $m = 0$ is the most dominant component for $\phi \geqslant 155^\circ$. For subsonic jets, the OASPL curves in figure 4.2.1(c) show that, $m = 0$ is clearly the most dominant mode, followed by $m = 1$ and then $m = 2$. For all three jets, the $m = 1$ component is larger than the $m = 2$ contribution. With increasing azimuthal wavenumber, the peak OASPL shifts towards lower jet inlet angles.

The scatter plot in figure 4.2.2 shows the variation of the maximum PSD as a function of the jet inlet angle. False colors show the corresponding Strouhal number. Similar trends as for the OASPL are observed, see figure 4.2.1. The false color indicates the frequency with the largest contribution to the PSD at each angle. It can be seen that the frequency of the peak PSD is $St = 0.4$ for the supersonic case and $St = 0.2$ for the transonic and subsonic cases, respectively. In particular for the supersonic jet, it is observed that lobes in the PSD at high jet angle correspond to distinct frequency bands. In all three cases, the axisymmetric azimuthal component peaks at $\phi \approx 160^\circ$ and $St \approx 0.2$. The presence of discrete color bands in figure 4.2.2 suggests a clear relationship between radiation angle and frequency.

The SPOD eigenvalues and modes are computed for the pressure. The pressure 2-norm is used as a proxy of the acoustic energy in the far-field. To isolate contributions to the far-field, we

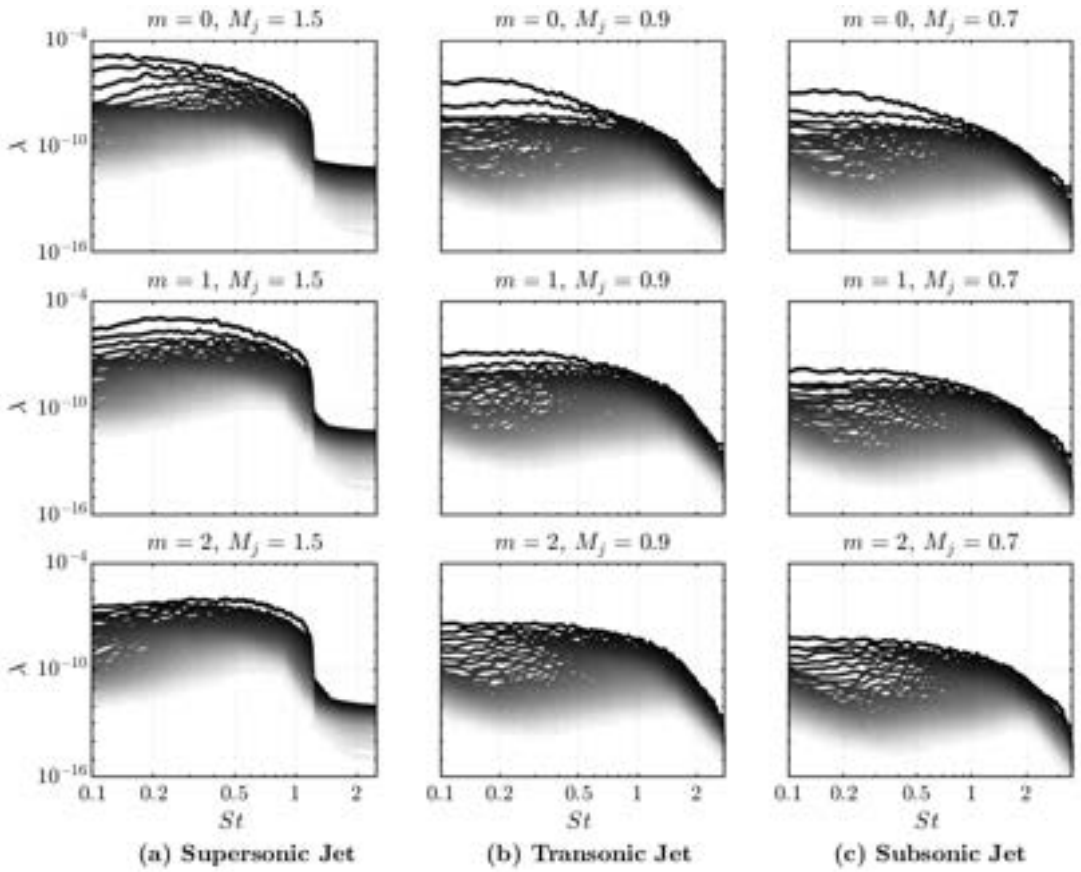

Figure 4.2.3: SPOD eigenvalue spectra for the far-field focus region as defined in Eq. (4.3).

choose a weighting function

$$W(x) = \begin{cases} 1 & \text{for } 5 \leqslant r \leqslant 6, \forall x \in \Omega \\ 0 & \text{otherwise.} \end{cases} \tag{4.3}$$

Figure 4.2.3 shows the SPOD spectra for all cases and azimuthal wavenumbers under consideration. Below $St = 0.1$, the far-field pressure partially consists of hydrodynamic fluctuations. As we are interested in acoustics, we omit this region for clarity. Parts of some of the spectra exhibit a large difference between the first (optimal, or leading) and second (first suboptimal) modes. This behavior is referred to as low-rank behavior (Schmidt et al., 2018) and indicates dominance of a physical mechanism associated with the first mode. It is most pronounced for the

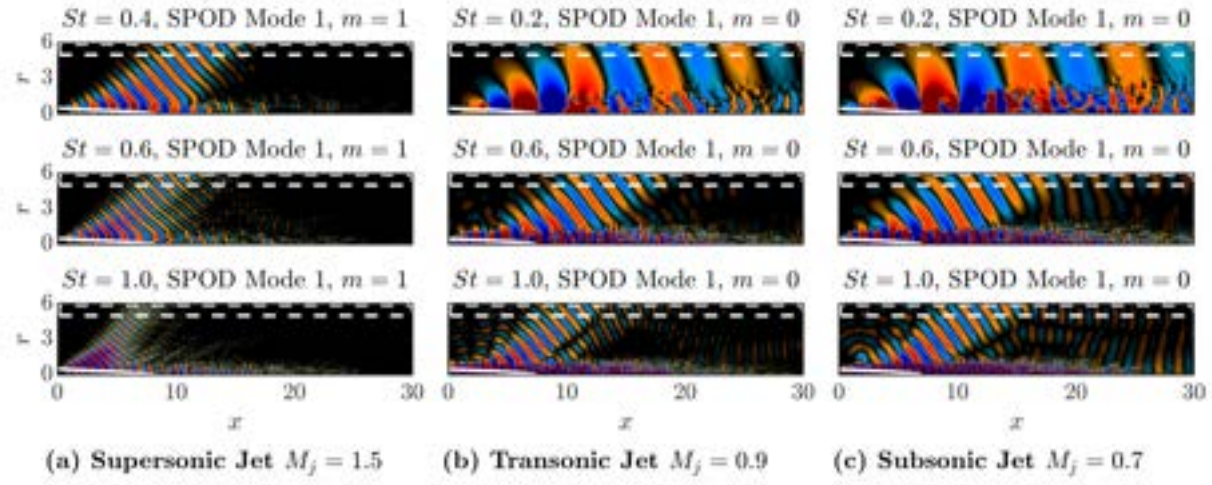

Figure 4.2.4: Leading SPOD modes at peak frequencies (top row), $St = 0.6$ (middle row) and for $St = 1.0$ (bottom row). The focus region is indicated by the dashed white box. White solid lines represent the edge of the potential core defined as $\bar{u}(x,r) = 0.95U_j$, where $\bar{u}$ is the mean axial velocity.

axisymmetric component within the ranges $0.1 \leqslant St \leqslant 0.6$ and $0.1 \leqslant St \leqslant 0.7$ for the transonic and subsonic jets, respectively. The prevalence of this behavior decreases as m increases. The frequency at which the low-rank behavior peaks is termed as the dominant frequency. Modes at representative frequencies and azimuthal wavenumbers are shown in figure 4.2.4. In particular, we pick the maximum OASPL azimuthal wavenumber, see figure 4.2.1. The SPOD modes clearly indicate the dominance of superdirective acoustic radiation emanating from the end of the potential core as the main source location of high inlet-angle jet noise. It is important to note that the patterns of the SPOD modes imply spatial correlation, but not causation. Due to the acoustic nature of the problem, the SPOD modes clearly reveal the source location, but not necessarily the source mechanism. In the particular case of turbulent jets, however, the primary source of the superdirective radiation has previously been identified as the Kelvin-Helmholtz-type (KH) annular instability of the jet shear-layer, using stability-theoretical tools (Nichols and Lele, 2011, Rigas et al., 2017, Schmidt et al., 2018). The pressure signature of a KH wavepacket is clearly visible in the supersonic jet for $m = 1$ (top panel of figure 4.2.4a).

The radiation patterns confirm the relationship between the jet inlet angle and frequency

previously discussed in the context of figure 4.2.2. Directive beams that propagate at steeper angles are observable at the higher frequencies of $St = 0.6$ and $St = 1.0$ (middle and bottom row figure 4.2.4). The first, second, and third sub-optimal modes at $St = 0.6$ are shown in figure 4.2.5. Multiple directive beams are observed for all the jets. The number of beams increases with mode number. The suboptimal mode of the transonic and subsonic jets exhibit two superdirective beams. These beams originate from either side of the end of the potential core. Rigas et al. (2017) suggest that these two beams originate from the KH wavepacket and the Orr-type waves, respectively (Schmidt et al., 2018, Tissot et al., 2017a). The higher suboptimal modes of the transonic and subsonic jets (middle and bottom row of figure 4.2.5 (b) and (c)) exhibit upstream and sideline propagating radiation. In section 4.2.2, this observation is addressed in more detail. Notably, very similar radiation patterns have been predicted by Jeun et al. (2016) using resolvent analysis and global modes by Schmidt et al. (2016).

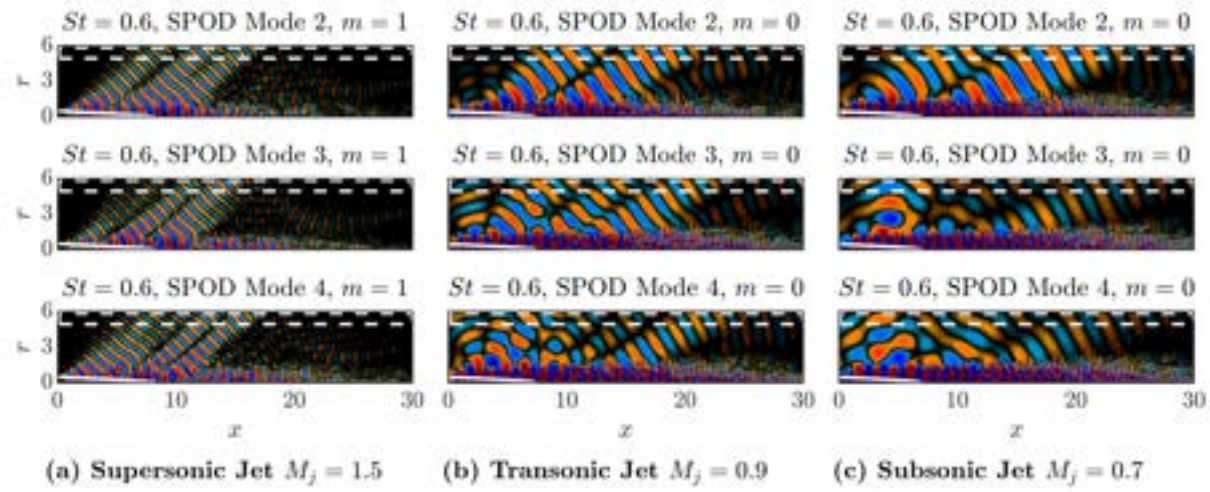

Figure 4.2.5: First, second and third suboptimal SPOD modes at $St = 0.60$. The focus region is indicated by the dashed white box. White solid lines represent the edge of the potential core defined as $\bar{u}(x,r) = 0.95U_j$, where $\bar{u}$ is the mean axial velocity.

The distinct radiation patterns identified by the leading SPOD modes may be leveraged to locate their origin. We obtain an estimate of this location by finding the absolute maximum of the pressure modes along the lipline, $r = 0.5$. This corresponds to the radial distance of

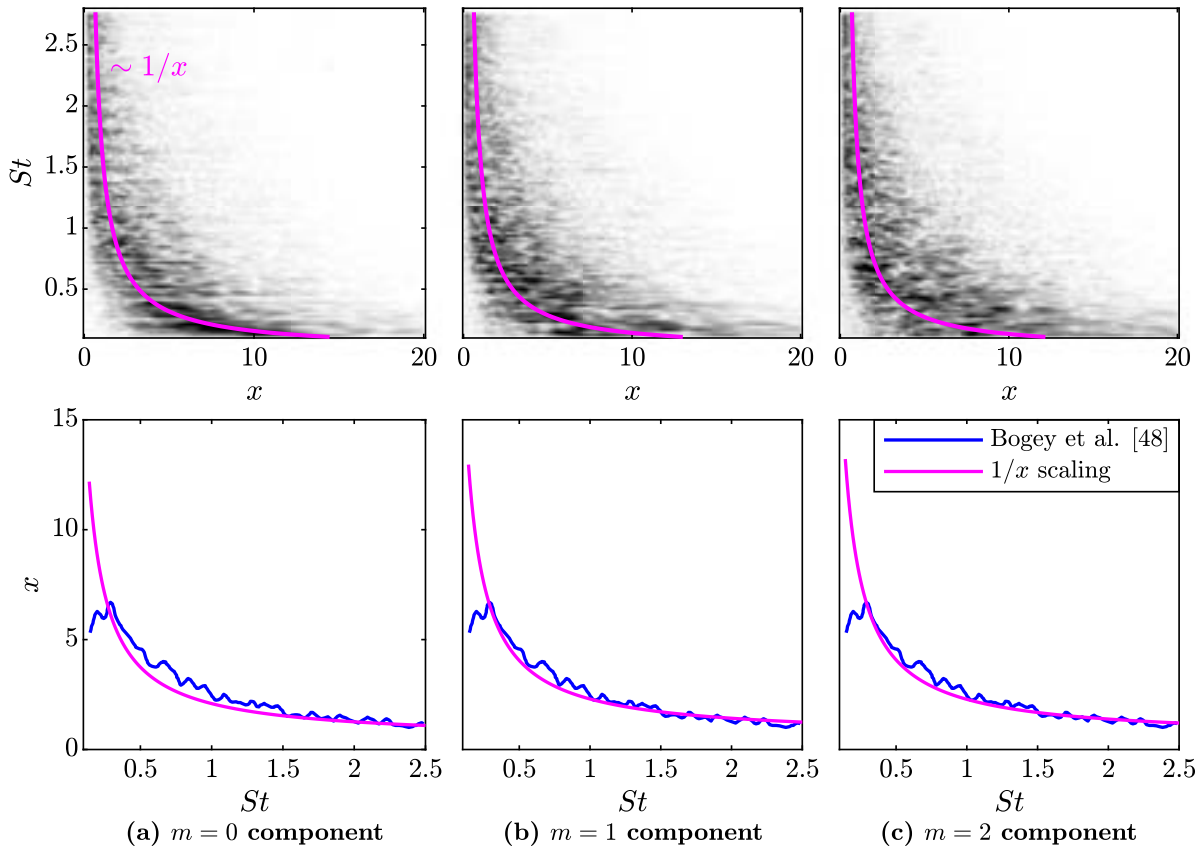

Figure 4.2.6: The source locations of the acoustic beams for the transonic jet $M_j = 0.9$ and azimuthal wavenumber (*a*) $m = 0$, (*b*) $m = 1$, and (*c*) $m = 2$. Top row denotes the normalized intensity of the SPOD modes (, black, gray, white, $0 \leqslant \psi/\|\psi\|_\infty \leqslant 1$) along the lipline $r = 0.5$. Least square fit of the scaling $St \sim 1/x$ is denoted by magenta lines. The location of the maximum intensity as a function of the St is shown in the bottom row. The scaling is compared to the experimental results by Bogey et al. (2007).

maximum turbulent activity close to the nozzle, but we note that the beam tracing does not depend on the exact radial location. Figure 4.2.6 shows the beam origin as a function of the Strouhal number for the transonic jet and different azimuthal wavenumbers. We focus on the transonic case for comparison with literature. In agreement with the findings of (Bogey et al., 2007, Narayanan et al., 2002, Zaman, 1986), high frequency radiation patterns originate near the nozzle exit, whereas the low frequency acoustic beams emanate from a location further downstream. Previous studies on acoustic source localization (Bishop et al., 1971, Schlinker et al., 2009, Zaman, 1986) and wavepacket modeling (Sasaki et al., 2017, Schmidt et al., 2018)

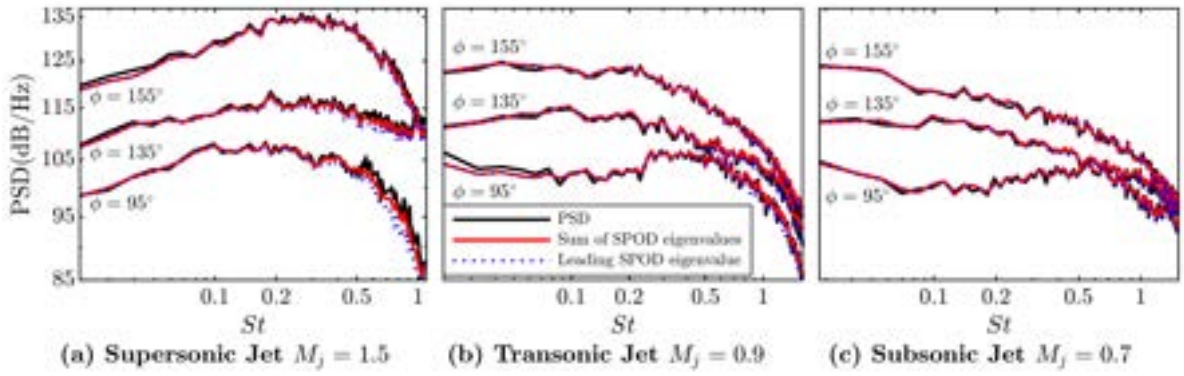

Figure 4.2.7: Comparison of PSD and SPOD spectra for the $m = 0$ component. Black lines represent the PSD, blue dotted lines represent the first SPOD mode and red lines represent the sum of all SPOD modes.

have shown that the frequency scales with $St \sim 1/x$ in the shear layer region. A least-square fit for this scaling is shown for the first three azimuthal wavenumbers. In the bottom row of figure 4.2.6, this curve fit is compared with the approximate source locations found experimentally by Bogey et al. (2007) for a comparable jet using the method of Zoppellari et al. (1997). Note that the full pressure signal used in the work of Bogey et al. (2007) is compared to different azimuthal components. A good match between the literature and the present results is observed.

Next, we examine the dominant radiation patterns for different angles by introducing a new weighting function $W_f(x)$ that focuses on small boxes that are representative of specific angles,

$$W_f(x) = \begin{cases} 1 & \text{for } 5 \leqslant r \leqslant 6, x_f - 0.5 < x < x_f + 0.5, \quad \text{where} \quad x_f \in [0.5, 29.5], \\ 0 & \text{otherwise.} \end{cases} \tag{4.4}$$

The center of each box of height and width $\Delta x = 1.0$ is used to calculate the angle. The PSD and SPOD spectrum for different jet inlet angles are compared in figure 4.2.7. This comparison is shown for $m = 0$. Similar trends are observed for higher azimuthal wavenumbers as well. To facilitate direct comparison with PSD, the SPOD spectrum is normalized by the area of the box. The leading SPOD mode (blue dotted line) is able to predict the PSD (black lines) accurately,

in particular at low frequencies. The total SPOD energy is obtained as the sum of all SPOD eigenvalues and shown as red lines. Only a marginal improvement of the comparison over the leading

account

to speci

approxi

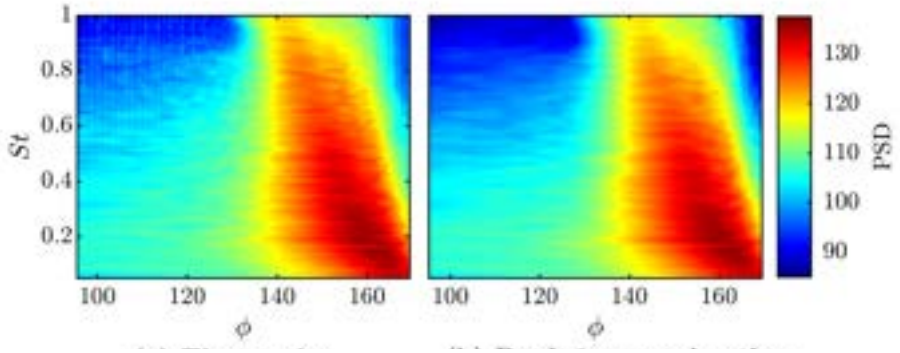

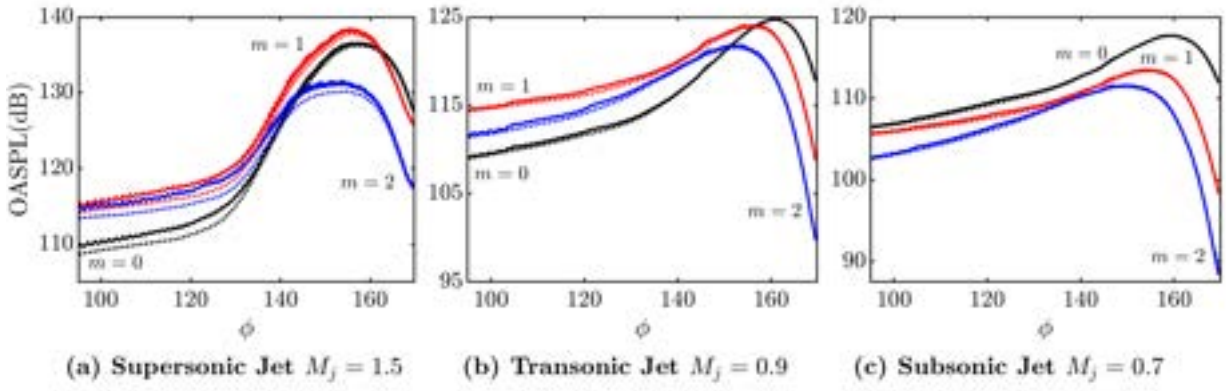

Figure 4.2.9: Comparison between OASPL of the LES pressure data (solid lines) and leading SPOD eigenvalue (dotted lines): $m = 0$ (black) , $m = 1$ (red) and $m = 2$ (blue).

Figure 4.2.8(b) shows the area-weighted eigenvalue of the leading SPOD mode as a function of frequency and inlet angle. The spectrum closely resembles the PSD of the raw pressure data shown in figure 4.2.8(a). For brevity, only the $m = 0$ component of the supersonic

jet is shown, but similar results are found for all other cases. The OASPL calculated from the data and the area-weighted SPOD energy of the first mode are compared in figure 4.2.9(a-c). The OASPL is calculated as in Eq. (4.2) using the spectrum shown in figure 4.2.8(b). The rank-1 SPOD approximation follows the trend of the OASPL well. Jeun and Nichols (2018b) made similar observations for a rank-1 approximation based on resolvent analysis. For the two lower Mach number jets, the OASPL curves predicted by the rank-1 approximation are more accurate than in the supersonic case.

4.2.1 Superdirective radiation

SPOD eigenvalue spectra for a focus region corresponding to the location of the peak OASPL (see Table 4.2.2) are shown in figure 4.2.10. All of these spectra exhibit low-rank behavior in the frequency range, $0.1 \leqslant St \leqslant 1.0$. The optimal and the suboptimal eigenvalues differ by up to three orders of magnitude in this band. This observation indicates that most of the energy is present in the first mode and is consistent with the results shown in figure 4.2.7. The leading SPOD modes at the peak frequencies are shown in the top row of figure 4.2.11. It is observed that the peak frequencies from the SPOD analysis and the peak PSD frequency coincide. This implies that the leading SPOD mode provides an accurate representation of the directive far-field radiation. Superdirective beams that encompass the region being investigated are observed. For the lower Mach number jets, the acoustic beams originate from the end of the potential core, whereas this location appears to be shifted slightly upstream in the supersonic case. The observations made for $M_j = 0.9$ are in agreement with the findings of Bogey and Bailly (2007). The superdirective radiation propagates at a steeper angle in the supersonic jet. The steeper propagation angle and upstream source location appear to cause a shift in the maximum directivity towards a lower jet inlet angle for the supersonic jet. Cavalieri et al. (2012) argue that the azimuthal interference of the helical mode and the smaller spatial extent of the helical wavepackets cause this difference. The leading SPOD modes at $St = 0.8$ are shown in the bottom

Table 4.2.2: Maximum OASPL and radiation angles for the different cases.

	Subsonic $M_j = 0.7$		Transonic $M_j = 0.9$		Supersonic $M_j = 1.5$	
	ϕ	$\text{OASPL}_{\text{max}}$ [dB]	ϕ	$\text{OASPL}_{\text{max}}$ [dB]	ϕ	$\text{OASPL}_{\text{max}}$ [dB]
$m = 0$	161.8°	117.7	162.0°	124.8	158.1°	136.6
$m = 1$	154.1°	113.5	157.0°	124.1	155.7°	138.5
$m = 2$	149.4°	111.6	151.4°	121.8	150.8°	131.5

row of Fig 4.2.11. Multiple beams emanating from different source locations are observed in

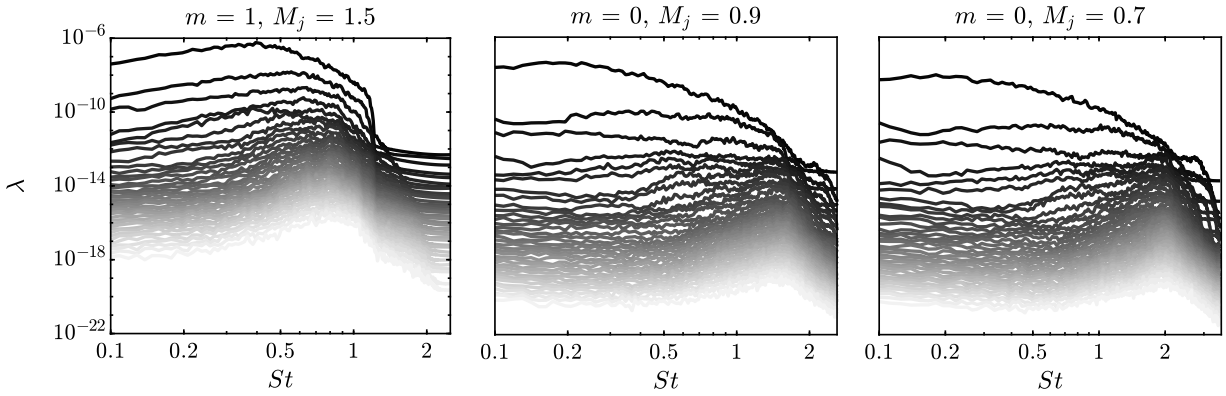

(a) Supersonic Jet $M_j = 1.5$ **(b) Transonic Jet** $M_j = 0.9$ **(c) Subsonic Jet** $M_j = 0.7$

Figure 4.2.10: SPOD eigenvalue spectra for the peak OASPL focus region. Spectra are shown for the dominant azimuthal wavenumber of each jet.

4.2.2 Noise generated in the sideline direction

To understand the generation of jet noise in the sideline direction, we focus our attention to the dominant radiation patterns to angles $\phi < 135^\circ$. These angles represent the region above the potential core. As before, we focus on the azimuthal wavenumber of the peak OASPL in that region (see figure 4.2.1). Figure 4.2.12 depicts the leading SPOD modes for $\phi = 95^\circ$. At the peak Strouhal numbers (top row of figure 4.2.12), upstream traveling radiation patterns are observed. The SPOD modes of the supersonic and transonic jets also reveal the presence of

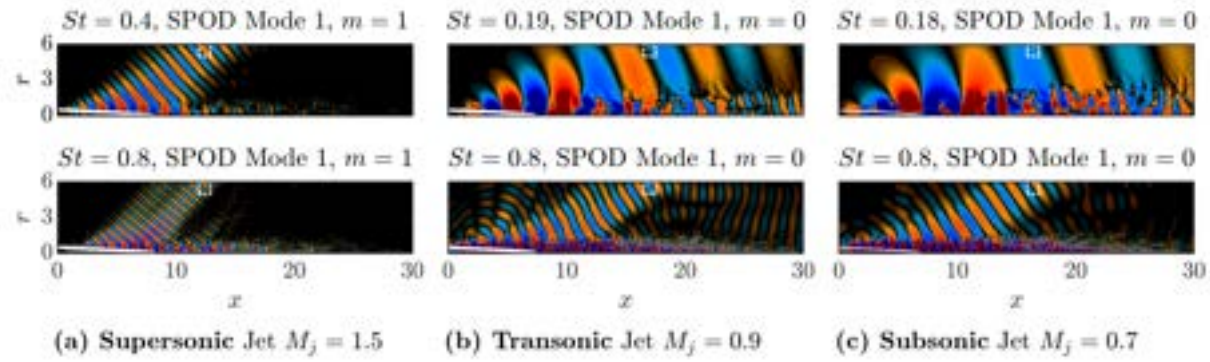

Figure 4.2.11: Leading SPOD modes at peak frequencies (top row) and for $St = 0.80$ (bottom row). The focus region is indicated by the dashed white box. White solid lines represent the edge of the potential core defined as $\bar{u}(x,r) = 0.95U_j$, where $\bar{u}$ is the mean axial velocity.

directive downstream radiation. Both the upstream and downstream radiation patterns originate from the same source location at the end of the potential core. The leading modes at $St = 0.8$ (bottom row of figure 4.2.12) exhibit multi-directive radiation patterns that include upstream,

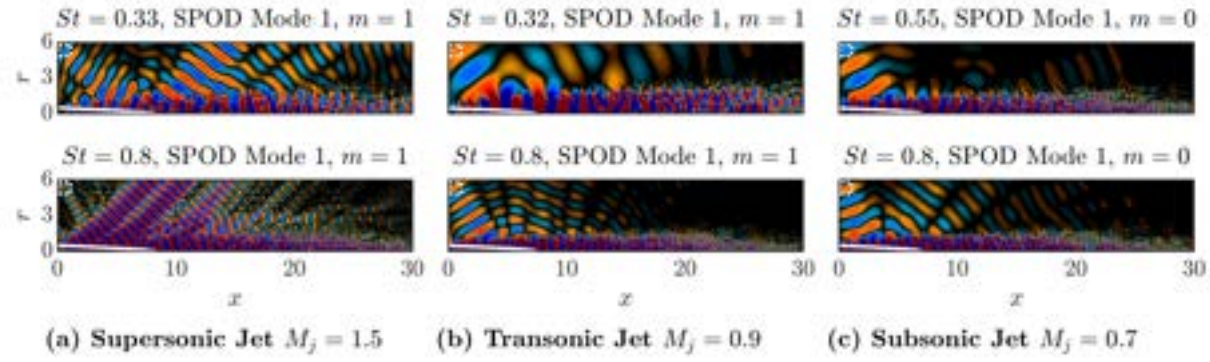

Figure 4.2.12: Leading SPOD modes at peak frequencies (top row) and for $St = 0.80$ (bottom row). The focus region is indicated by the dashed white box. White solid lines represent the edge of the potential core defined as $\bar{u}(x,r) = 0.95U_j$, where $\bar{u}$ is the mean axial velocity.

The sideline radiation perpendicular to the jet axis is investigated in figure 4.2.13. The SPOD was computed by translating the focus region along the upper boundary at an interval of $\Delta x = 0.1$. The angles for which perpendicular radiation patterns are observed were selected

manually. Notably, the identified angles of $\phi = 112^\circ$, $\phi = 129^\circ$ and $\phi = 131^\circ$ for the subsonic, transonic and supersonic jet, respectively, correspond to distinct frequency bands in figure 4.2.2. All modes also exhibit downstream radiation. For the supersonic jet, the downstream radiation is found considerably more energetic than the sideline beam. Similar to the findings of Freund (2001), these observations suggest that the sideline radiation is directly coupled with the dominant directive radiations, implying that both originate from the same source at the end of the potential core. For the higher frequency, $St = 0.8$, the source location is further upstream. This trend can be explained by the fact that the peak location of the KH wavepacket moves upstream with increasing

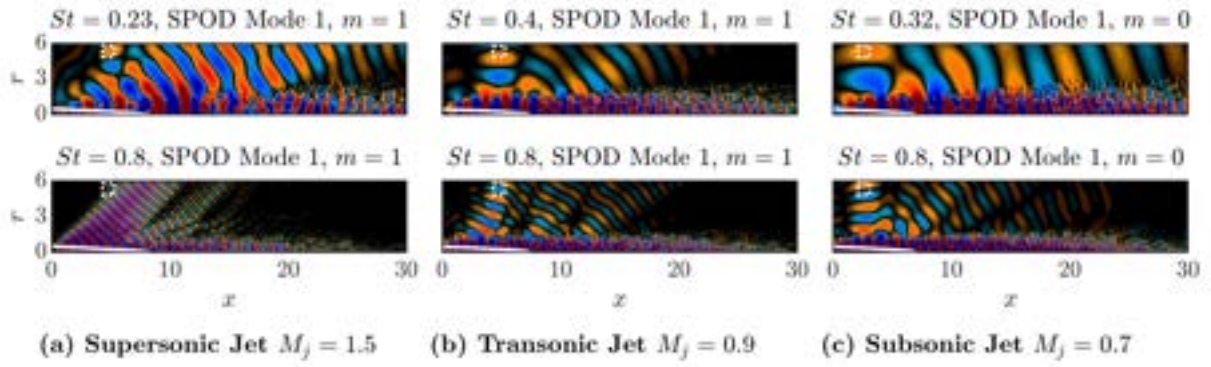

Figure 4.2.13: Leading SPOD modes at peak frequencies (top row) and for $St = 0.80$ (bottom row). The focus region is indicated by the dashed white box. White solid lines represent the edge of the potential core defined as $\bar{u}(x,r) = 0.95U_j$, where $\bar{u}$ is the mean axial velocity.

Next, we inspect the link between downstream and sideline radiation. In figure 4.2.14, the leading mode at $\phi = 156^\circ$ is compared with a higher mode (lower energy) at $\phi = 95^\circ$ and vice versa. The leading mode corresponding to the region of maximum directivity and the eighth mode at $\phi = 95^\circ$ are observed to resemble each other. Both of these modes exhibit superdirective beams that propagate at the same angle and originate from a similar location in the shear-layer. The bottom row of figure 4.2.14 shows the tenth mode at $\phi = 156^\circ$ and the leading mode at $\phi = 95^\circ$. As before, close correspondence is found. Note that the convergence of these higher SPOD modes

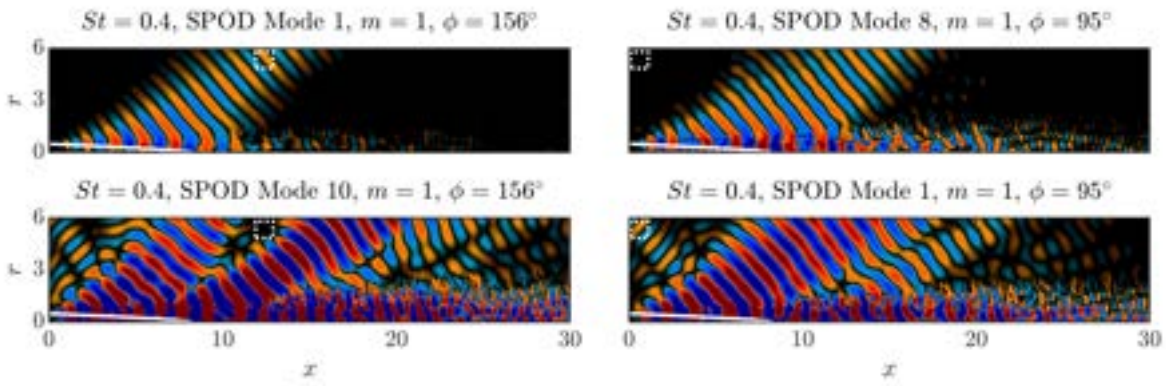

Figure 4.2.14: Comparison of leading and suboptimal SPOD modes for the supersonic jet $M_j = 1.5$ at $St = 0.40$: mode 1 (top left) and mode 10 (bottom left) for $\phi = 156°$; mode 8 (top right) and mode 1 (bottom right) for $\phi = 95°$. The most similar modes were identified by visual inspection.

is not guaranteed; see appendix 4.2.3. However, it was confirmed by manual inspection that the same flow features are consistently found within a narrow range of mode numbers if only a subset of the full data was used. This results clearly suggests that the sideline radiation is directly linked to the dominant downstream radiation pattern. Similar observations are found for the other cases. In summary, the observations made in Figs. 4.2.11-4.2.14 suggest that downstream and sideline emissions share the same location of origin. An important implication from a modeling perspective is that structures that are found to be dominant for a particular spatial weighting are recovered as suboptimal modes in the other. This means that, if a sufficient number of SPOD modes is retained, the two SPOD basis span a similar space.

Based on a comprehensive analysis of experimental data, Tam et al. (2008) suggest the use of two universal curves. The F-spectrum, which exhibits a distinct peak at lower frequencies, models radiation to downstream angles. Noise spectra of sideline radiation are generally more broadband and approximated by the so-called G-spectrum. The PSD for two angles representative of sideline radiation (at $\phi = 95°$) and downstream radiation (at $\phi = 160°$) are compared to the G and F spectra, respectively, in figure 4.2.15. The pressure PSD of the first three azimuthal wavenumbers contain most of the acoustic energy (Jordan and Colonius, 2013) and are summed

here. The PSD curves follow the similarity spectra for all the cases, with small deviations at higher frequencies. The peak frequency of the F-spectrum is around $St \approx 0.2$, in agreement with the experimental observations made by Tam et al. (1996), Viswanathan (2004), and Tam et al. (2008). The spectrum corresponding to the leading SPOD mode is also shown in figure 4.2.15;

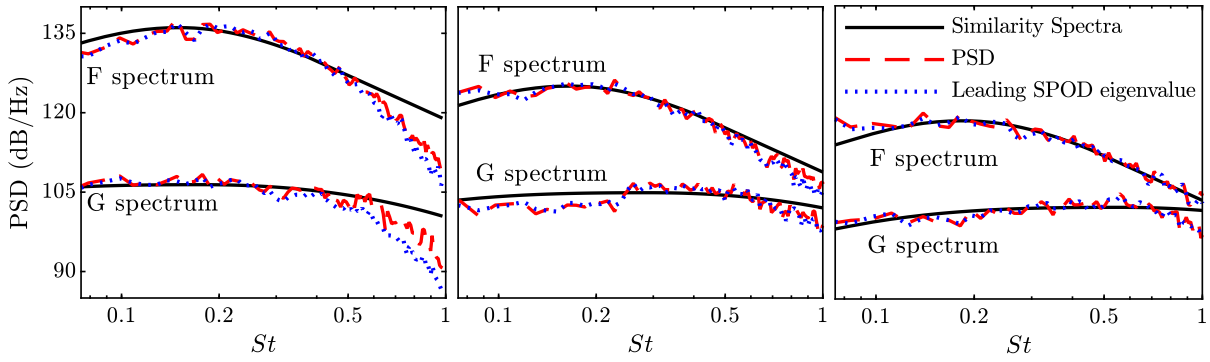

(a) Supersonic Jet $M_j = 1.5$ **(b) Transonic Jet** $M_j = 0.9$ **(c) Subsonic Jet** $M_j = 0.7$

Figure 4.2.15: Comparison of F and G spectra with PSD (red dashed lines) and the leading SPOD eigenvalues (blue dotted lines). The contributions from the first three azimuthal wavenumbers $m = 0, 1, 2$ are summed.

Figure 4.2.16 aims at summarizing our results in a compact and interpretable way by relating the origin of the acoustic beams, radiation angle and peak frequency. First, the peak Strouhal number of the leading SPOD mode is selected for each ϕ, or far-field location. Each line then connects the far-field location to the point corresponding to the absolute maximum of the mode $\left\|\psi^{(1)}_{St_{\text{peak}}}\right\|_\infty$. This point approximately tracks the origin of the beam and serves as a proxy for the source location (but not necessarily the source mechanism, as discussed in the context of figure 4.2.4 above). False colors indicate the corresponding peak frequency. A few trends are observed. The primary source location of the dominant downstream radiation appears to be located in the region surrounding the end of the potential core. Sideline radiation to low

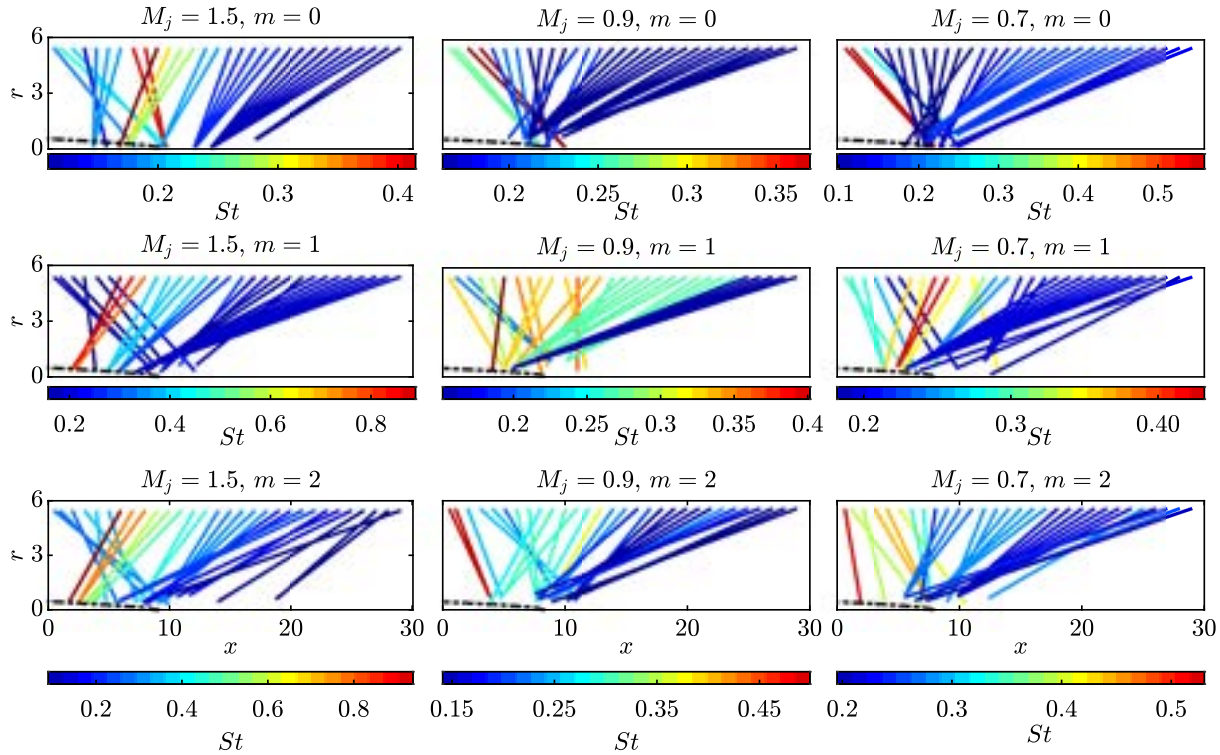

(a) Supersonic Jet $M_j = 1.5$ **(b) Transonic Jet** $M_j = 0.9$ **(c) Subsonic Jet** $M_j = 0.7$

Figure 4.2.16: Directivity plot obtained from directional SPOD analysis: straight lines connect far-field focus region to location of maximum absolute value of SPOD mode at peak frequency. Peak frequencies are indicated by false colors.

angles emanate from the jet shear-layer or the end of the potential core. In most cases, the sideline radiation appears to be slaved to the directive downstream radiation. In all cases the source location is in the vicinity of the jet axis ($r \approx 0$) or the lipline ($r \approx 0.5$), i.e., in the region where the Kelvin-Helmholtz wavepackets (inside the shear-layer) and Orr-type wavepackets (downstream of the potential core) dominate the dynamics of the jet. As observed earlier, the dominant superdirective radiation occurs at frequencies of $St \approx 0.2$, whereas higher frequencies are observed in the sideline direction.

4.2.3 Convergence of SPOD modes

Following Lesshafft et al. (2019) and Sano et al. (2019), the convergence of the SPOD modes is assessed by splitting the data into two parts containing 50% of the full data, each. The similarity of SPOD modes is quantified in terms of a normalized inner product,

$$\beta_{i;k} = \frac{\langle \psi_k, \psi_{i;k} \rangle_x}{\|\psi_k\|_x \cdot \|\psi_{i;k}\|_x}, \tag{4.5}$$

of the k-th mode $\psi_{i;k}$ from subset i with the k-th mode ψ_k from the full data. Here, $i = 1, 2$

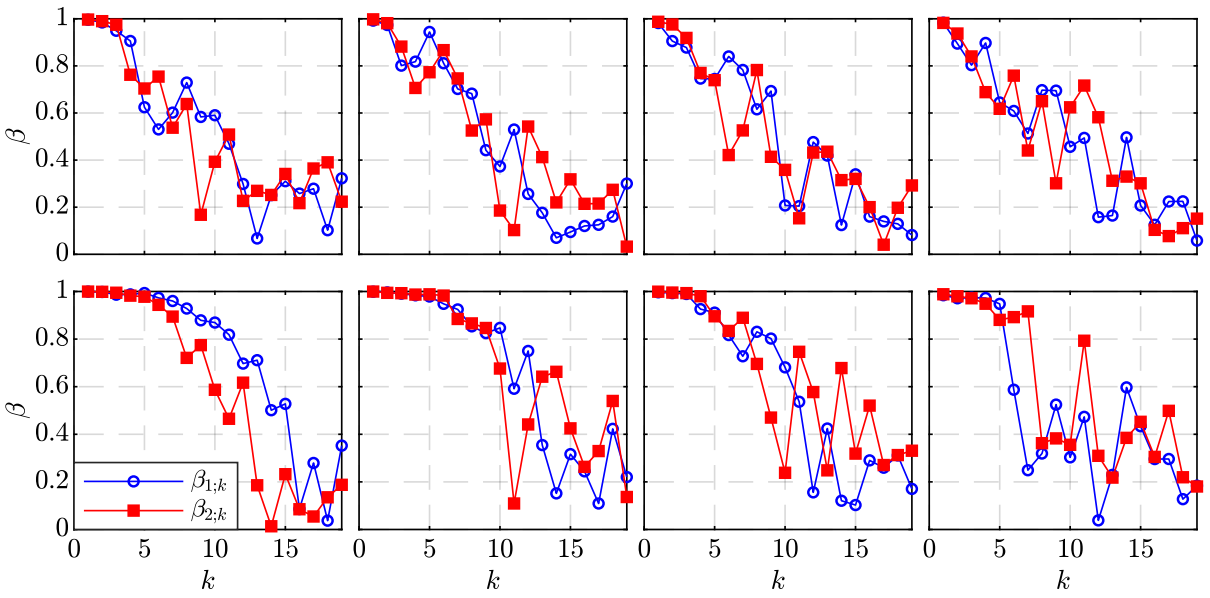

Figure 4.2.17: Convergence of SPOD modes for $M_j = 1.5$ and $m = 1$ at (a) $St = 0.2$ (b) $St = 0.4$ (c) $St = 0.60$ and (d) $St = 0.80$. The top and bottom row show the convergence of the SPOD modes computed using the weighting function of the full far-field (Eq. (5.10)), and the focus region of $\phi = 156^\circ$ (Eq. (2.22)), respectively.

Figure 4.2.17 shows this measure for $St = 0.2$, 0.4, 0.6, and 0.8. The two different weighting functions considered in this work, i.e., the full far-field (top row, see Eq. (4.3)), and

the focus region of $\phi = 156^\circ$ (bottom row, see Eq. (4.4) are considered for the supersonic jet and azimuthal wavenumber $m = 1$. Form the proximity of the values of $\beta_{i;k}$ for the two subsets and its high values of $\beta_{i;k} \gtrsim 0.8$, it can be concluded that at least the first three far-field modes are well converged. For the restricted focus region with $\phi = 156^\circ$, the first six modes are converged, following the same argument. Similar observations were found by Lesshafft et al. (2019), Sano et al. (2019).

4.3 Summary and conclusion

The first three azimuthal wavenumber components of supersonic, transonic, and subsonic jets are analyzed using spectral proper orthogonal decomposition with localized weighting. The dominant component is $m = 1$ for the supersonic jet and $m = 0$ for the subsonic case. In the transonic regime, $m = 1$ for $\phi \leqslant 150^\circ$ is surpassed by $m = 0$ for $\phi > 150^\circ$. In the sideline direction ($\phi \lesssim 130^\circ$), the $m = 1$ and $m = 2$ components are relatively more important. For all cases, the frequency of the peak PSD in the $m = 0$ component occurs for $St \approx 0.2$. The SPOD analysis identifies a single directive beam at $\phi \approx 160^\circ$ as the corresponding radiation pattern. The source of this superdirective beam is at the end of the potential core for low frequencies and in the shear-layer for higher frequencies. Suboptimal SPOD modes show multi-directive patterns that include radiation in the upstream and sideline directions. For the first few modes, a clear hierarchy is observed that directly relates the mode number to the number of beams. Additional data may further confirm this finding by improving convergence of the SPOD. Noise in the sideline direction is in most cases associated with higher frequencies. The SPOD modes reveal that the largest contributions to noise emissions in the sideline and downstream directions both take the form of acoustic beams that originate from the end of the potential core. The inspection of modes at different angles and suboptimal modes further underlines the notion that sideline and downstream radiation share the same source location. A comparison of the SPOD spectra with the

OASPL shows that the first SPOD eigenvalue accurately approximates the overall sound pressure over all angles. This implies that the corresponding mode structure is the single largest contributor to directional noise. Despite the limited radial extent of the domain, our observations strongly suggest that sideline and upstream radiation patterns are associated with the same large-scale coherent structures as the dominant downstream radiation. A possible source mechanism that was previously investigated in the context of wavepacket modeling by Cavalieri and Agarwal (2014), and that in line with this notion, is coherence decay. In particular, we propose a scenario in which the distortion of a coherent KH wavepacket gives rise to multi-directive burst events.

Acknowledgements

The authors thank Dr. Guillaume A. Brès for providing the jet LES data. The LES study was supported by the NAVAIR SBIR project, under the supervision of Dr John T. Spyropoulos. The main LES calculations were carried out on CRAY XE6 machines at DoD HPC facilities in ERDC DSRC.

Chapter 5

Triadic nonlinear interactions of forced versus unforced turbulent jets

5.1 Introduction

A potential strategy to reduce jet noise is to perform closed-loop control that attenuates the acoustic radiation from the wavepackets. With this objective in mind, first, we harmonically force the jet to gain an understanding of the alternation of dynamics in forced jets. The forcing increases the amplitude of the wavepackets above the background turbulence. Recently, the experimental closed-loop control of turbulent jets has demonstrated the attenuation of amplified wavepackets over a broad range of frequencies (Maia et al., 2022, 2021b, 2020). Once a strategy is designed to control the elevated wavepackets, it can be applied to a more realistic scenario of an unforced jet to reduce jet noise.

Following Crow and Champagne (1971), harmonically-forced jets has been the subject of numerous studies. The actuation of the jet has varied over a wide range of frequencies and forcing amplitudes. Most of these studies have focussed on two mechanisms that lead to the formation of coherent structures. One is the shear-layer mode or the Kelvin-Helmholtz instability,

the frequency at which the shear layer rolls up into vortices. The other is the preferred mode or the jet column mode (Hussain and Zaman, 1981), characterized by the frequency at which the jet exhibits the greatest response to external forcing. At low amplitudes of forcing, the jets exhibit a linear response. As the forcing amplitude increases, it triggers nonlinear interactions in jets. High levels of forcing and the resulting nonlinear interactions of coherent structures have rarely been explored. Broze and Hussain (1994), Husain and Hussain (1995), Raman and Rice (1991), Shaabani-Ardali et al. (2019) have investigated the nonlinear response to high amplitude forcing in jets, and most have focussed on initially-laminar jets. In this work, nonlinear interactions in unforced and forced jets are examined and compared for turbulent jets. Here, we perform LES of unforced and forced turbulent subsonic jets at a Reynolds number, $Re = \rho_j U_j D/\mu_j = 50,000$, and Mach number, $M = U_j/c_\infty = 0.4$, where ρ is the density, U the mean flow velocity, μ the dynamic viscosity, c the speed of sound, and the subscripts j and ∞ denote the jet and free-stream conditions. We validate our simulations with the experiments performed at Institut Pprime. Following the experiments, the jets are forced harmonically at a non-dimensional frequency of $St = fD/U_j = 0.4$, near the nozzle lip.

5.2 Bispectral mode decomposition

Bispectral mode decomposition (BMD) is a technique recently proposed by Schmidt (2020), to characterize the coherent structures associated with triadic interactions in statistically stationary flows. Here, we provide a brief overview of the method. The reader is referred to Schmidt (2020) for further details of the derivation and mathematical properties of the method. BMD is an extension of classical bispectral analysis to multidimensional data. The classical bispectrum is defined as the double Fourier transform of the third moment of a time signal. For a time series, $y(t)$ with zero mean, the bispectrum is

$$S_{yyy}(f_1, f_2) = \int\int R_{yyy}(\tau_1, \tau_2) e^{-i2\pi(f_1\tau_1 + f_2\tau_2)} d\tau_1 d\tau_2, \tag{5.1}$$

where $R_{yyy}(\tau_1, \tau_2) = E[y(t)y(t-\tau_1)y(t-\tau_2)]$ is the third moment of $y(t)$, and $E[\cdot]$ is the expectation operator. The bispectrum is a signal processing tool for one-dimensional time series that only measures the quadratic phase coupling at a single spatial point. In contrast, BMD identifies the intensity of the triadic interactions over the spatial domain of interest and extracts the corresponding spatially coherent structures.

BMD maximizes the spatial integral of the point-wise bispectrum,

$$b(f_k, f_l) = E\left[\int_\Omega \hat{\mathbf{q}}^*(x, f_k) \circ \hat{\mathbf{q}}^*(x, f_l) \circ \hat{\mathbf{q}}(x, f_k + f_l) dx\right]. \tag{5.2}$$

Here, $\hat{\mathbf{q}}$ is the temporal Fourier transform of $\mathbf{q}$ computed using the Welch approach (Welch, 1967) and $\circ$ denotes the Hadamard (or element-wise) product.

Next, as in equation (3.2), all the Fourier realizations at l-th frequency are arranged into the matrix, $\hat{\mathbf{Q}}_l$. The auto-bispectral matrix is then computed as

$$\mathbf{B} = \frac{1}{n_{\text{blk}}} \hat{\mathbf{Q}}_{k\circ l}^H \mathbf{W} \hat{\mathbf{Q}}_{k+l}, \tag{5.3}$$

where, $\hat{\mathbf{Q}}_{k\circ l}^H = \hat{\mathbf{Q}}_k^* \circ \hat{\mathbf{Q}}_l^*$.

To measure the interactions between different quantities, we construct the cross-bispectral matrix

$$\mathbf{B}_c = \frac{1}{n_{\text{blk}}} \left(\hat{\mathbf{Q}}_k^* \circ \hat{\mathbf{R}}_l^*\right) \mathbf{W} \hat{\mathbf{S}}_{k+l}. \tag{5.4}$$

Owing to the non-Hermitian nature of the bispectral matrix, the optimal expansion coefficients, $\mathbf{a}_1$ are obtained by maximising the absolute value of the Rayleigh quotient of $\mathbf{B}$ (or $\mathbf{B}_c$)

$$\mathbf{a}_1 = \arg\max_{\|\mathbf{a}\|=1} \left|\frac{\mathbf{a}^*\mathbf{B}\mathbf{a}}{\mathbf{a}^*\mathbf{a}}\right|. \tag{5.5}$$

The complex mode bispectrum is then obtained as

$$\lambda_1(f_k, f_l) = \frac{\mathbf{a}_1^* \mathbf{B} \mathbf{a}_1}{\mathbf{a}_1^* \mathbf{a}_1}. \tag{5.6}$$

Finally, the leading-order bispectral modes and the cross-frequency fields are recovered as

$$\phi_{k+l}^{(1)} = \hat{\mathbf{Q}}_{k+l} \mathbf{a}_1, \quad \text{and} \tag{5.7}$$

$$\phi_{k\circ l}^{(1)} = \hat{\mathbf{Q}}_{k\circ l} \mathbf{a}_1, \tag{5.8}$$

respectively. By construction, the bispectral modes and cross-frequency fields have the same set of expansion coefficients. This explicitly ensures the causal relation between the resonant frequency triad, (f_k, f_l, $f_k + f_l$), where $\hat{\mathbf{Q}}_{k\circ l}$ is the cause and $\hat{\mathbf{Q}}_{k+l}$ is the effect. The complex mode bispectrum, λ_1, measures the intensity of the triadic interaction and the bispectral mode, ϕ_{k+l}, represents the structures that results from the nonlinear triadic interaction.

5.3 Validation of LES

The experiments of the isothermal subsonic jets were performed at the "JET100" low Mach number jet facility at Institut PPRIME, Poitiers, France. The experiments were carried out for a jet Mach number M_j = 0.05, and Reynolds number of $Re = 50000$. The boundary layer is tripped inside the nozzle by a carborundum strip located $2.5D$ upstream from the nozzle exit. The turbulent jet is forced by eight loudspeakers that are equally distributed around the nozzle lipline ($r/D = 0.5$). The loudspeakers generate synthetic jets through an annular gap of width $0.01D$. For further details of the experimental setup, the reader is referred to Maia et al. (2022, 2021b, 2020).

We perform large-eddy simulations of subsonic jets using the compressible flow solver "Charles" developed at Cascade Technologies (Brès et al., 2017, 2018). Charles solves the spatially filtered compressible Navier–Stokes equations on unstructured grids using a density-

based finite-volume method. The LES combines the Vreman sub-grid model (Vreman, 2004) with the wall-model by Bodart and Larsson (Bodart and Larsson, 2012, Kawai and Larsson, 2012). The reader is referred to Brès et al. (2017, 2018) for further details on the numerical method and validation on jet flows.

The validation of the LES case for the present case follows the previous studies. In particular, the mesh used by Brès et al. (2018) is modified to accommodate the new nozzle geometry and refined in the vicinity of the synthetic jet actuators. The total grid size is 16.6 million control volumes. The LES is conducted for the experimental Reynolds number, whereas the Mach number is artificially increased to $M_j = 0.4$. Effects of compressibility are still small in this regime and the very small time steps associated with the incompressible limit are avoided.

The LES results for the unforced jet are compared to the experiments in figure 5.3.1. The mean and RMS streamwise velocities on the centerline and lipline are reported in figure 5.3.1(a,c) and 5.3.1(b,d), respectively. In figure 5.3.1(a), the mean streamwise velocities along the centerline of the experiment and the simulation are almost indistinguishable within the first ten jet diameters. The corresponding potential core length, indirectly defined as $\bar{u}(x = x_c) = 0.95U_j$ is $x_c \approx 6.2$. The RMS velocity along the centerline, shown in figure 5.3.1(c), matches well for the first six jet diameters and is underpredicted by about 10% further downstream. The lipline RMS velocity in figure 5.3.1(d) is slightly overpredicted near the nozzle and underpredicted with a maximum deviation of also about 10% further downstream. Clearly visible in the simulation results are grid transitions that were similarly observed by Brès et al. (2018). It was confirmed in the same work that increasing the resolution mitigates these transitions. More importantly, Brès et al. (2018) also showed that both nozzle-exit turbulent statistics and far-field noise predictions were accurate for the lower resolution simulations that exhibit grid transitions.

For the forced simulations, we follow Heidt et al. (2021) and model the effect of the loudspeaker actuators as an acoustic forcing in the annular region along the lip line, $0.50 \leqslant r \leqslant 0.51$, as

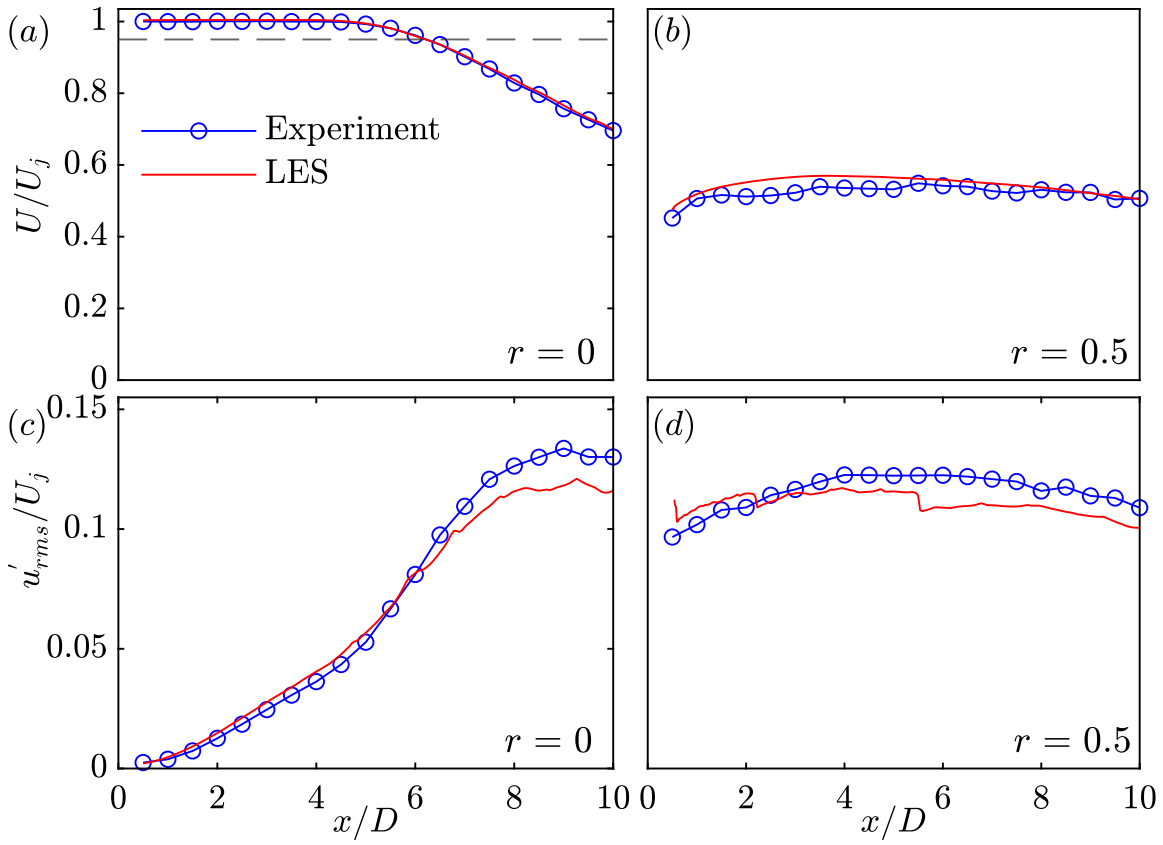

Figure 5.3.1: Comparison of the experiment with the LES simulations: centerline (a, c) and lipline (b, d). Profiles of the mean (a, b) and (c, d) RMS streamwise velocity. Black dashed line represents $U/U_i = 0.95$ and its intersection with the mean streamwise velocity indicates the

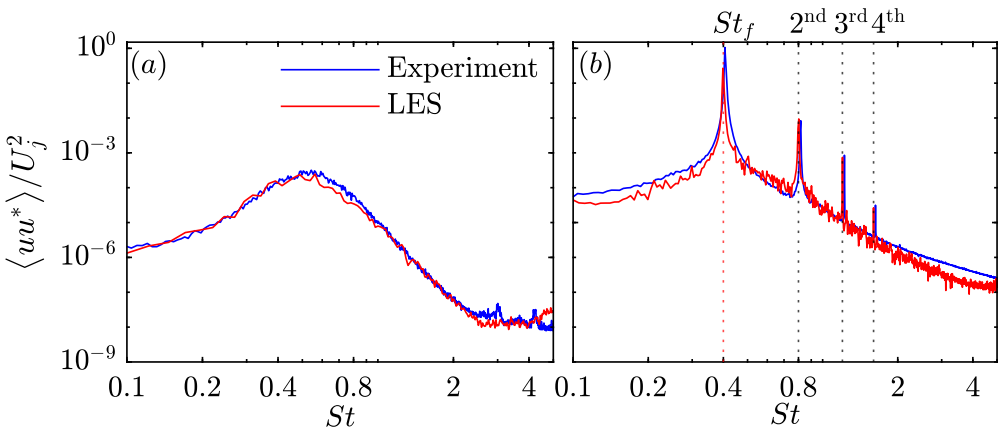

Figure 5.3.2: Power spectral density of the streamwise velocity at $x = 2$ and $r = 0$: (a) unforced jet; (b) forced jet. The experiment (blue line) is compared to the simulations (red line). $St = St_f = 0.4$ corresponds to the forcing frequency (red dotted line).

$$p(r) = 1 - 40000(r-0.505)^2, \tag{5.9a}$$

$$u_x(r,t) = Ap(r)\cos\left(m_f\theta\right)\sin\left(2\pi St_f t\right), \tag{5.9b}$$

$$u_r = u_\theta = 0, \tag{5.9c}$$

$$\rho = \rho_\infty + \rho_\infty u_x/c_\infty, \tag{5.9d}$$

$$p = p_\infty + \rho_\infty c_\infty u_x. \tag{5.9e}$$

The amplitude, A, was manually adjusted to match the experimental observations. Here, $St_f = 0.4$ is the forcing frequency. Figure 5.3.1(c,d) shows the power spectral densities of the centerline streamwise velocity at $x = 2$ for the unforced and axisymmetrically forced jets. The comparison between experiment and simulation are excellent for the unforced jet seen in figure 5.3.1(c). The best agreement for the forced case was obtained for $A = 0.4$ and is shown in figure 5.3.1(d). Both the peaks at the forcing frequency and its harmonics, as well as the number of active harmonics and the underlying broadband spectrum, are well predicted.

5.4 Triadic interactions in unforced and forced jets

Figure 5.4.1 shows the area-integrated power spectral densities (PSD) for the five most energetic azimuthal wavenumbers $m = 0, 1, 2, 3, 4$. The PSDs are integrated over the compressible energy norm. The azimuthal wavenumber $m = 1$ contains most of the energy for the unforced jet. For the axisymmetrically forced jet, we observe large peaks at the forcing frequency and its harmonics in the wavenumber $m = 0$. The peaks at these harmonic frequencies indicate the presence of triadic sum interactions. For the $m = \pm 1$-, $m = \pm 2$-, and $m = \pm 6$- forced jets, peaks are observed at the odd harmonics $St = St_f$, $3St_f$, $\cdots$, in the actuated azimuthal components, i.e., $m = 1$,$m = 2$ and $m = 6$, respectively. Peaks exist at the even harmonics ($St = 2St_f$, $4St_f$, $6St_f$,

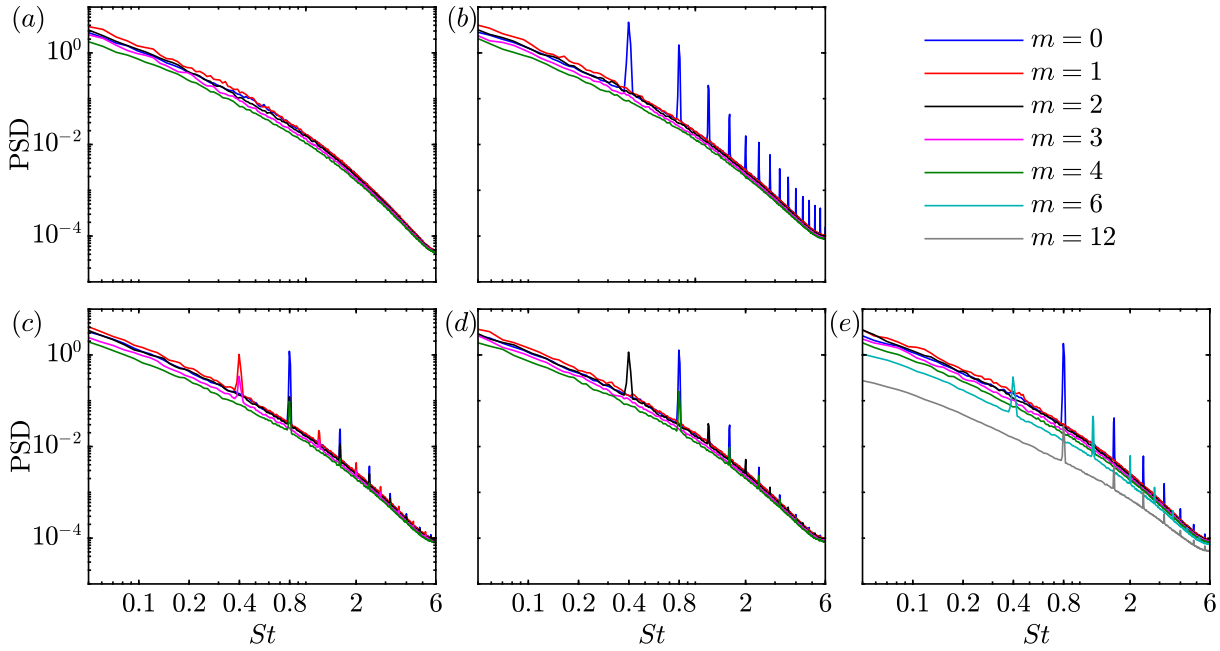

Figure 5.4.1: Integrated PSD of first five azimuthal wavenumbers, $m = 0, 1, 2, 3, 4$ for the four jets: (a) unforced; (b) axisymmetrically forced; (c) $m = \pm 1$-forced; (d) $m = \pm 2$-forced; (e) $m = \pm 6$-forced jet. In (e) $m = 6, 12$ are also shown. PSD is integrated over the compressible energy norm.

$\cdots$) in $m = 0$, 2, 4 for the $m = \pm 1$-forced jet, in $m = 0$, 4, 8 for the $m = \pm 2$-forced jet, and in $m = 0$, 12, 24 for the $m = \pm 6$-forced jet. These observations indicate that the triadic interactions occur in both the frequency and azimuthal wavenumber space for non-axisymmetrically forced jets.

5.4.1 Axisymmetrically forced jet

The mode bispectra for the unforced and forced jets are shown in figure 5.4.2. The high-intensity regions (false red color) in the mode bispectra signify the dominant triads that arise from the interactions of two frequencies. Different combinations of frequencies (St_1,St_2) interact to generate the same frequency ($St_1 + St_2$ = constant) along the diagonals of slope -1 in the mode bispectrum. For the forced jet (figure 5.4.2 (b)), a grid-like pattern is observed with vertical, horizontal, and diagonal lines at the forcing frequency and its harmonics with local

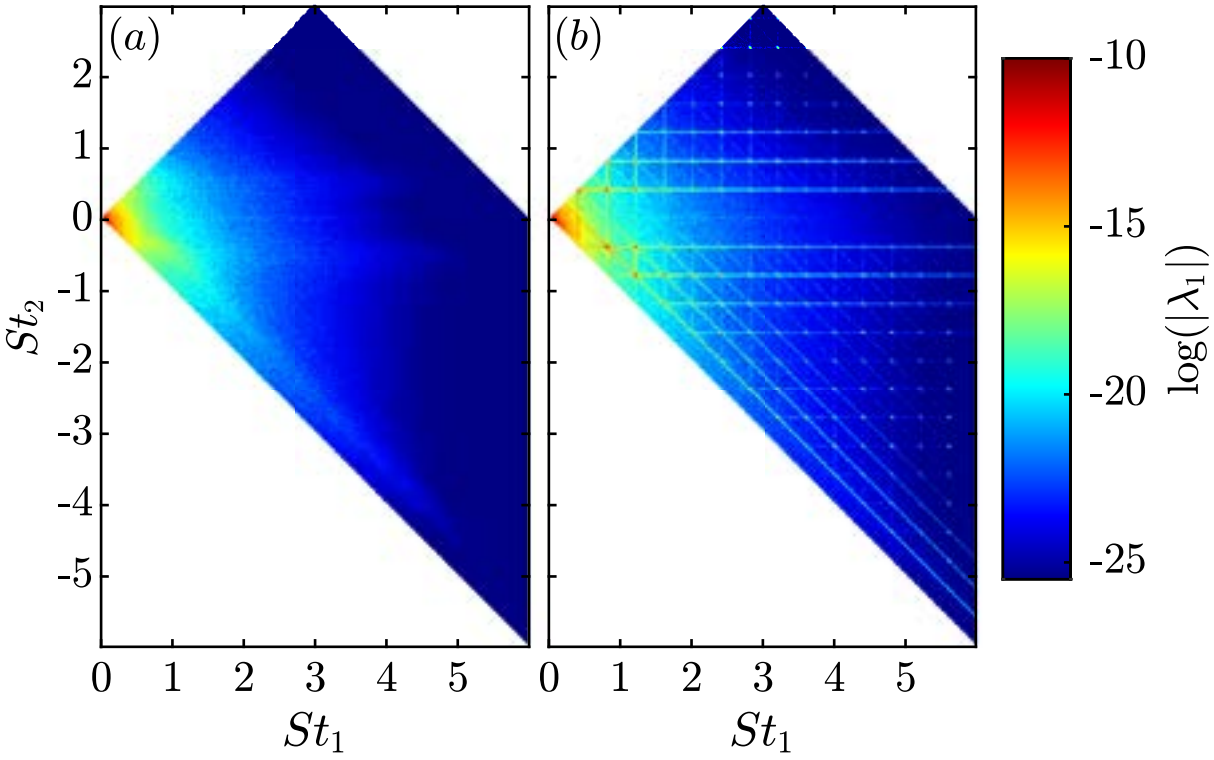

Figure 5.4.2: BMD spectra: (*a*) unforced turbulent; (*b*) forced turbulent jet.

maxima at the intersection of these lines. These local maxima represent the prominent triadic interactions. In particular the two most dominant triads are (0.4,0.4,0.8) and (0.8,-0.4,0.4). The latter triad indicates a back-scatter effect where energy is supplied to the fundamental by the second harmonic. In the case of unforced jets, a broadband behavior is observed, with the highest values concentrated at lower frequencies.

Next, we examine the mode bispectrum along different diagonals with $St_3 = \text{const}$ to identify the strongest non-linear interaction that result in a triad at each frequency. Figure 5.4.3 shows the mode bispectrum along the constant frequencies of St_3 = 0.0, 0.4, 0.8, and 1.2 for the two cases. The spectrum of the unforced jet is broadband for all St_3. The forced jet exhibits distinct peaks at the forcing frequency and its harmonics. The two most dominant triads are observed for $St_3 = 0.4$ in figure 5.4.3(*b*) and $St_3 = 0.8$ in 5.4.3(*c*). The first of these two triads is the difference interaction between $St_1 = 2St_f$ and $St_2 = -St_f$, i.e., between the

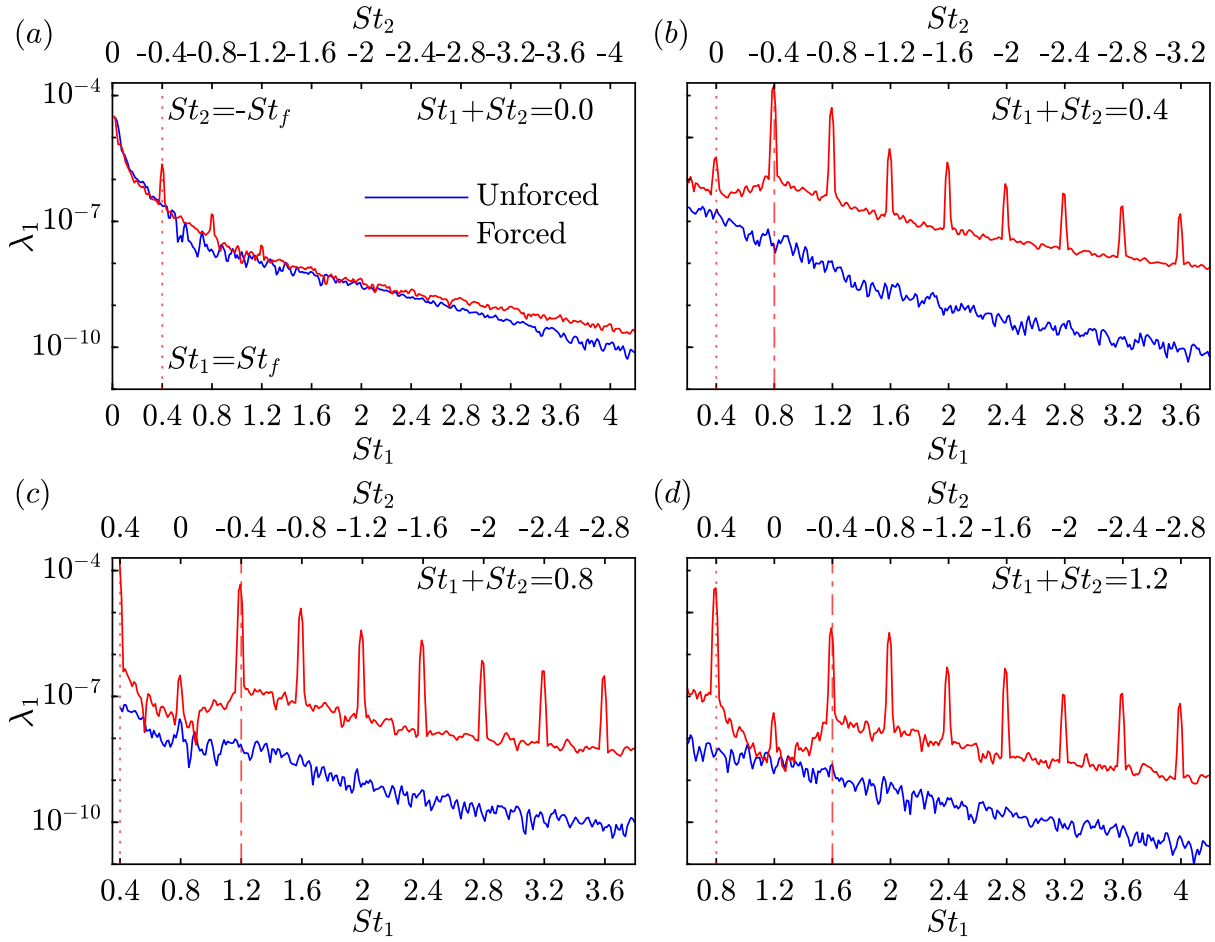

Figure 5.4.3: Mode bispectrum along diagonal of constant frequency: (*a*) $St_3 = St_1 + St_2 = 0.0$; (*b*) $St_3 = St_1 + St_2 = 0.4$; (*c*) $St_3 = St_1 + St_2 = 0.8$; (*d*) $St_3 = St_1 + St_2 = 1.2$. The red dotted and dash-dotted lines denote the forcing, and conjugate forcing frequency, respectively.

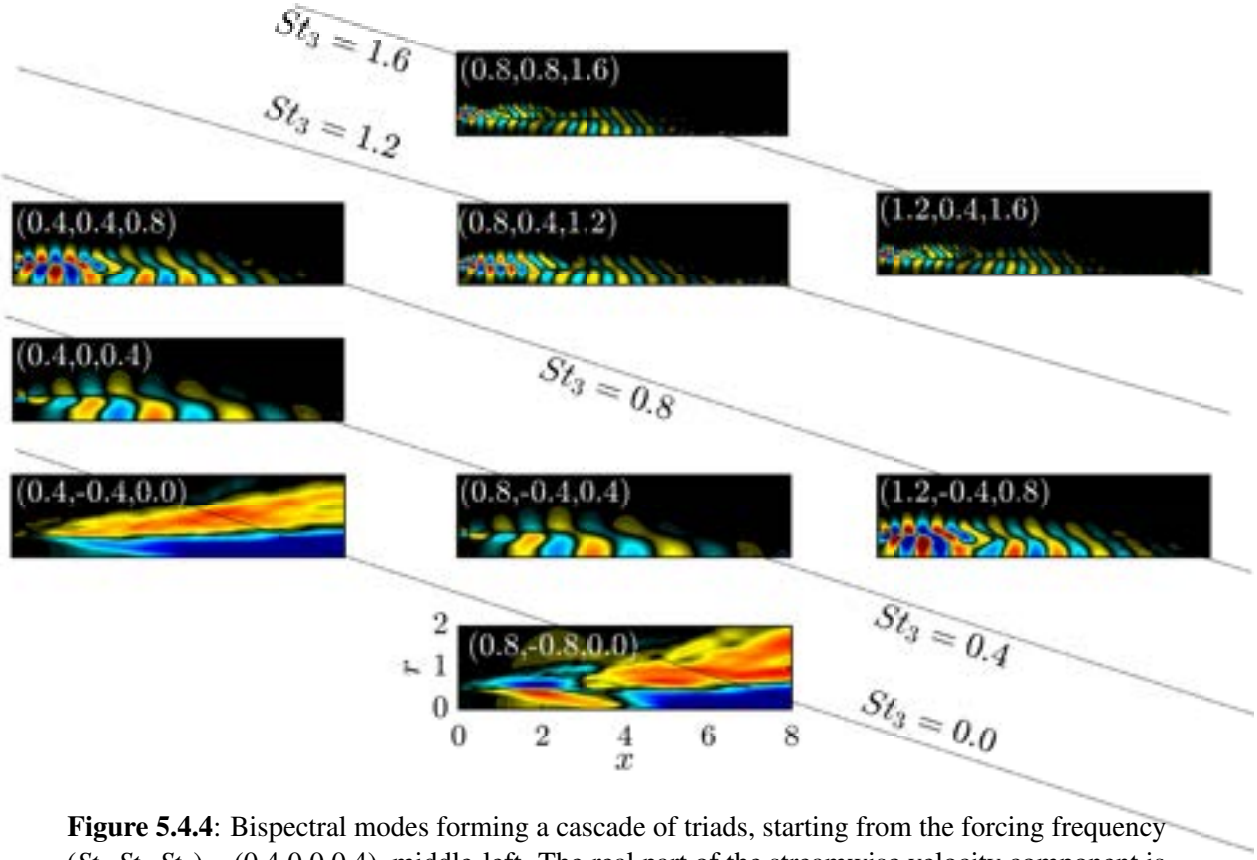

Figure 5.4.4: Bispectral modes forming a cascade of triads, starting from the forcing frequency (St_1,St_2,St_3) = (0.4,0.0,0.4), middle-left. The real part of the streamwise velocity component is shown.

second harmonic and the conjugate forcing frequency. The second triad is the fundamental self-interaction, (St_f,St_f,$2St_f$), that creates the second harmonic. The dips of the forced mode bispectrum observed for $St_2 = 0$ in figure 5.4.3(b), (c), and (d) correspond to the relative lower values of the mode bispectrum previously seen along the abscissa in figure 5.4.2(b). Note that the zero-frequency bin contains unresolved low frequency components due to the finite sampling frequency, and the non-zero mode bispectrum should not be interpreted along $St_2 = 0$.

The BMD modes of the triad cascade including the most significant interactions up to $St_1 \leqslant 2St_f$ are visualized in figure 5.4.4. The cascade starts with the mode at the forcing frequency, ϕ_{St_f+0} (left column middle row). The modes associated with the sum interactions are shown in the first and second row, and those associated with the difference interactions are shown in the fourth and fifth row. The mode ϕ_{St_f+0} self-interacts to generate the second harmonic, $\phi_{St_f+St_f}$.

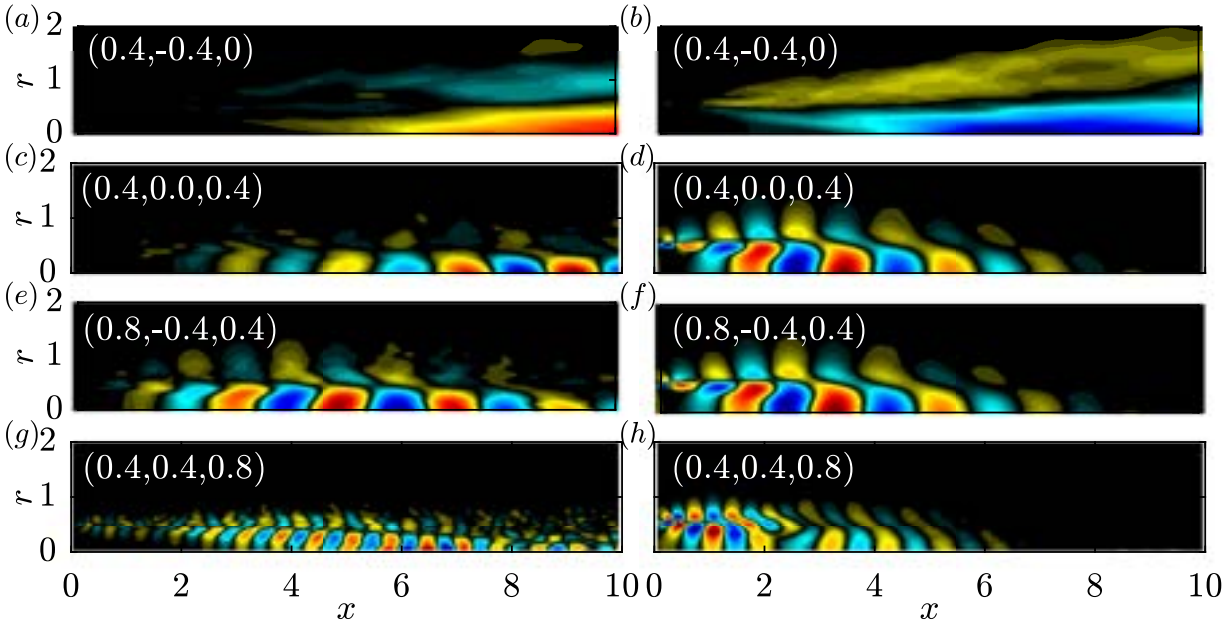

Figure 5.4.5: Streamwise velocity component of the BMD modes for the turbulent unforced (*a*,*c*,*e*,*g*) and forced jets (*b*,*d*,*f*,*h*) for different frequency triads: (*a*,*b*) (St_f,-St_f,0); (*c*,*d*) (St_f,0,St_f); (*e*,*f*) ($2St_f$,$-St_f$,St_f); (*g*,*h*) (St_f,St_f,$2St_f$).

The fundamental forcing mode and its second harmonic then interact to create the third harmonic, $\phi_{2St_f+St_f}$, and so on. In the negative St_2 plane, the destructive self interaction of the forcing mode creates a mean flow distortion mode, $\phi_{St_f+-St_f}$, with $St_3 = 0$. Inspecting the modes reveals that sum-interactions create modes with high wavenumbers and difference-interactions create modes with lower streamwise wavenumbers. This behaviour is in agreement with the linear dispersion relation of these Kelvin-Helmholtz (KH) type instability waves.

Another interesting observation is that the spatial structures of the modes along the diagonals of constant frequencies $St_3 = 0.4$, 0.8, 1.2 and 1.6 are very similar. As shown for the companion experiment by Maia et al. (2021a), these similar bispectral modes at constant $St_3 \neq 0$ resemble the leading SPOD modes at each frequency. This indicates that the spatial structures created by the triadic interactions are also the most energetic coherent structures. Along $St_3 = 0$, on the contrary, the streak-like structures with an increasing number of streamwise lobes are created by the destructive self-interactions of the forcing mode and its harmonics.

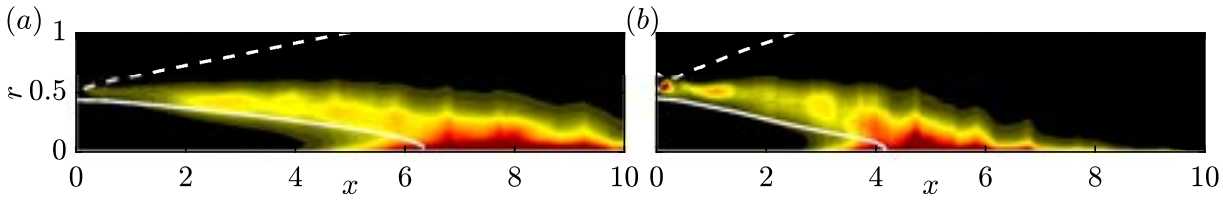

Figure 5.4.6: Integral interaction maps, $\sum_{k,l} \lambda_1(St_k, St_l)|\phi_{k\circ l} \circ \phi_{k+l}|$: (*a*) unforced turbulent jet; (*b*) forced turbulent jet. White solid and dashed lines outline the potential core and the jet width defined as lines of constant $u_x = 0.95U_j$ and $0.05U_j$, respectively.

Next, we compare the spatial structures of the BMD modes associated with the triadic interactions for unforced and forced turbulent jets. Figure 5.4.5 shows the streamwise velocity components for the dominant triads at (St_f,-St_f,0), (St_f,0,St_f), ($2St_f$,$-St_f$,St_f), and (St_f,St_f,$2St_f$), which correspond to the mean flow deformation, fundamental instability mode, a harmonic-fundamental difference interaction and fundamental self-interaction, respectively. The BMD modes reveal that the structures contributing to the triadic interactions are localized to the region near the end of the potential core for the unforced jet, whereas, for the forced jet, they are located at a more upstream location and are concentrated in the shear layer. This effect is more pronounced for the BMD mode of the fundamental self-interaction triad (St_f,St_f,$2St_f$), which exhibits a KH type wavepacket near the nozzle exit in the forced jet.

We next seek to identify the regions where triadic interactions are most active. This is achieved by summing the weighted interaction maps over all frequency triads as $\sum_{k,l} \lambda_1(St_k, St_l)|\phi_{k\circ l} \circ \phi_{k+l}|$. The resulting integral interaction maps are presented in figure 5.4.6 and indicate the regions where the triadic interactions are most active. Both jets exhibit strong triadic nonlinear interactions downstream of the potential core near the centerline. This observation is in agreement with previous findings by Cavalieri et al. (2013) and Tissot et al. (2017b), who, in the same region, observed that linear wavepacket models differ significantly from experiments. In addition to this 'natural' occurrence of nonlinear effects, the forced jet interaction map also reveals the presence of strong nonlinearity in the shear layer near the nozzle exit that is directly associated with the forcing. Also observed is a shortening of the potential core and a thickening of the shear layer.

This is in agreement with the previous works by Crow and Champagne (1971), Samimy et al. (2007b), who argue that the enhanced entrainment due to forcing leads to a widening of the shear layer, and consequently, a contraction of the potential core.

To identify the link between the triadic interactions in the near-field and the acoustic far-field, we perform BMD on the pressure data using a weight matrix,

$$\mathbf{W}_{\mathrm{ac}}(x) = \begin{cases} 1 & \text{for } 5 \leqslant r \leqslant 6, \forall x \in \Omega \\ 0 & \text{otherwise,} \end{cases} \tag{5.10}$$

that focuses on the far-field. Figure 5.4.7 shows the BMD modes for the resultant frequencies (St_3) of St=0.4 (*a*,*b*), 0.8 (*c*,*d*), 1.2 (*e*,*f*) and 1.6 (*g*,*h*). The BMD mode corresponding to the most dominant triad at each resultant frequency (St_3) is selected. The pressure components for the unforced and forced turbulent jets are shown in figure 5.4.7 (*a*,*c*,*e*,*g*) and 5.4.7 (*b*,*d*,*f*,*h*) respectively. In case of the forced jet, ($2St_f$,$-St_f$,St_f) is the most significant triad identified from the BMD spectra (not shown here). This identifies as the difference-interaction between the first harmonic and the forcing frequency and is the most significant triad. This observation is in agreement with the findings of Sandham et al. (2006), who show that unstable waves with difference-interactions ($St_3 = St_1 - St_2$) are more efficient radiators of jet noise than the sum-interactions ($St_3 = St_1 + St_2$). For the forced jet, the BMD modes exhibit beams that propagate at a steeper angle as compared to the unforced jet. For the triads (0.8, 0.4, 1.2) and (1.2, 0.4, 1.6), the unforced jet exhibits directive downstream radiation, whereas for the forced jet, we observe actuation-induced sideline noise. These sideline radiation patterns are similar to those found by Jeun et al. (2016) and Nekkanti and Schmidt (2021b).

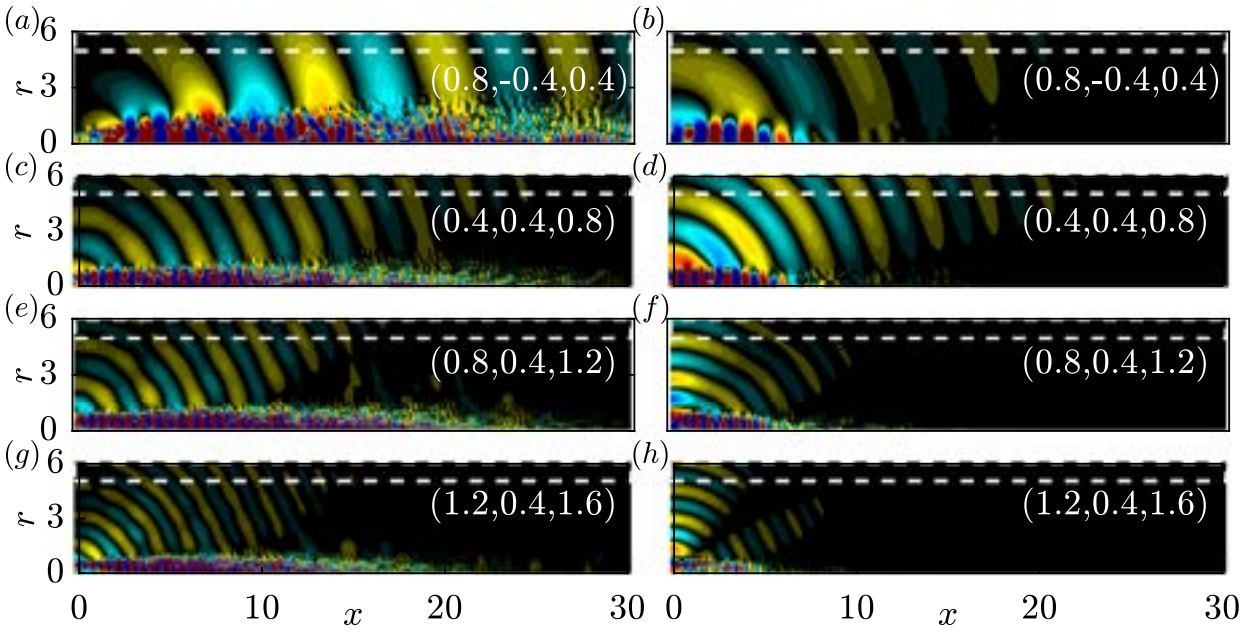

Figure 5.4.7: BMD modes of the pressure field for the turbulent unforced (*a*,*c*,*e*,*g*) and forced jets (*b*,*d*,*f*,*h*) for different frequency triads: (*a*,*b*) ($2St_f$,$-St_f$,St_f); (*c*,*d*) (St_f,St_f,$2St_f$); (*e*,*f*) ($2St_f$,St_f,$3St_f$); (*g*,*h*) ($3St_f$,St_f,$4St_f$).

5.4.2 Non-axisymmetrically forced jets

For non-axisymmetrically forced jets, peaks exist in multiple azimuthal wavenumbers, which indicates the interactions between different azimuthal wavenumbers. Hence, we compute the cross-BMD to characterize these triadic interactions. Figure 5.4.8 shows the cross-mode bispectra for the $m = \pm 1$ forced jet. Here, we show five azimuthal triplets, [m_1,m_2,m_3] = [1,-1,0], [1,1,2], [2,1,3], [2,2,4], and [3,1,4], where $m_1 + m_2 = m_3$. For the [1,-1,0] triplet, the cross-bispectra is symmetric about the lines, $St_1 = St_2$ and $St_1 = -St_2$. For the triplets, [1,1,2] and [2,2,4], the cross-bispectra is symmetric about the line $St_1 = St_2$, whereas there is no symmetry for the triplets, [2,1,3] and [3,1,4]. These symmetry lines are denoted using white dash-dotted lines. Figure 5.4.8(*a*) shows the interaction of helical component ($m = 1$) and its conjugate to generate the axisymmetric component. The most dominant frequency triads are (0.4,0.4,0.8), (1.2,-0.4,0.8), (0.4,-0.4,0.0) and their symmetric counterparts, for example, (-0.4,1.2,0.8), and (0.4,-1.2,-0.8). Similarly the self-interaction of the helical component generates peaks at the

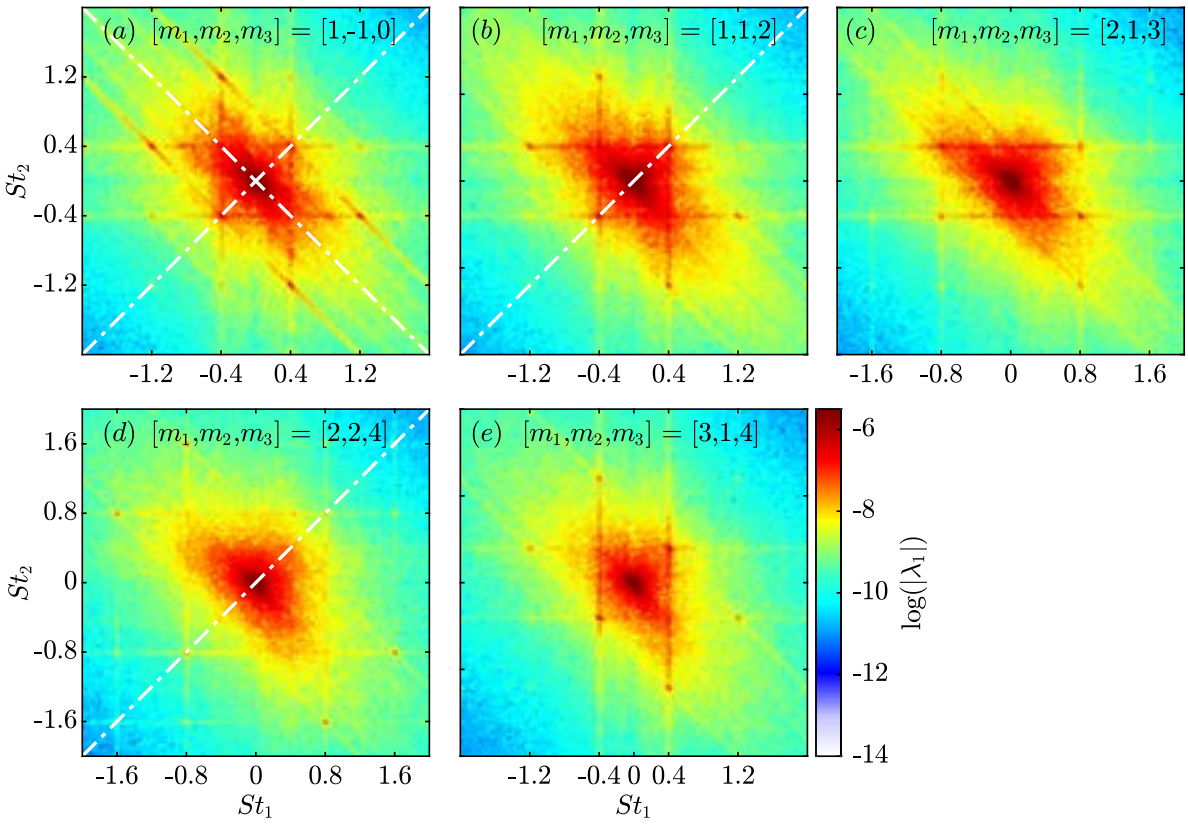

Figure 5.4.8: Cross-BMD spectra that shows the interaction of the azimuthal wavenumbers triads, [m_1, m_2, m_3], for the forced $m = \pm 1$ jet: (*a*) [1,-1,0]; (*b*) [1,1,2]; (*c*) [2,1,3]; (*d*) [2,2,4]; (*e*) [3,1,4]. The symmetry lines are denoted by white dash-dotted lines.

same frequency triads. For the azimuthal triplet, [2,1,3], the dominant frequency triads are (0.8,-0.4,0.4), (0.8,0.4,1.2), and (-0.8,1.2,0.4). As previously observed in figure 5.4.1, the odd azimuthal wavenumbers exhibit peaks at odd harmonics and the even azimuthal wavenumbers exhibit peaks at the even harmonics, and the different possible triadic interactions are

$$\text{if } m_1, m_2 \text{ are odd}, \quad (2n_1+1)St_f + (2n_2+1)St_f = 2(n_1+n_2+1)St_f \qquad m_3 \text{ is even}, \tag{5.11}$$

$$\text{if } m_1, m_2 \text{ are even}, \quad (2n_1)St_f + (2n_2)St_f = 2(n_1+n_2)St_f \qquad m_3 \text{ is even}, \tag{5.12}$$

$$\text{if } m_1 \text{ is odd}, m_2 \text{ is even}, \quad (2n_1+1)St_f + (2n_2)St_f = (2(n_1+n_2)+1)St_f \qquad m_3 \text{ is odd}, \tag{5.13}$$

where, $n_1,\ n_2 \in \mathbb{Z}$ are integers. Equations (5.11)-(5.13) show that the interaction of two odd or two even wavenumbers always generate peaks at the even harmonics, $\{2St_f, 4St_f, \cdots\}$, whereas the interaction of an odd and even wavenumber generate peaks at the odd harmonics, $\{St_f, 3St_f, 5St_f, \cdots\}$. The most significant frequency triads for the azimuthal triplets, [2,2,4], and [3,1,4] are (1.6,-0.8,0.8), and (0.4,0.4,0.8) which confirm this observation. Note that, the high intensity of the frequency (0,0,0) is ignored while considering the dominant triads because it is an artifact of the spectral leakage of BMD.

The back-scatter phenomenon is not limited to axisymmetrically forced jets but is also present in non-axisymmetrically forced ones. In the case of $m = \pm 1$ forced jets, the back-scatter effect is observed in the azimuthal triplet [2,-1,1] at the frequency triad (0.8,-0.4,0.4), which is not shown here for brevity. In this phenomenon, the second harmonic frequency $2St_f$ of the azimuthal wavenumber $2m_f$ supplies energy back to the fundamental mode, i.e., the mode corresponding to the frequency St_f and azimuthal wavenumber m_f.

Figures 5.4.9 and 5.4.10 show the cross-BMD spectra for the azimuthal triplets, [2,-2,0], [2,2,4] and [4,2,6] in the $m = \pm 2$-forced jet, and [6,-6,0], [6,6,12] and [12,6,18] in the $m = \pm 6$-forced jet, respectively. As shown in figure 5.4.1, the non-axisymmetric forcing affects only those azimuthal wavenumbers that are integer multiples of the forcing azimuthal wavenumber.

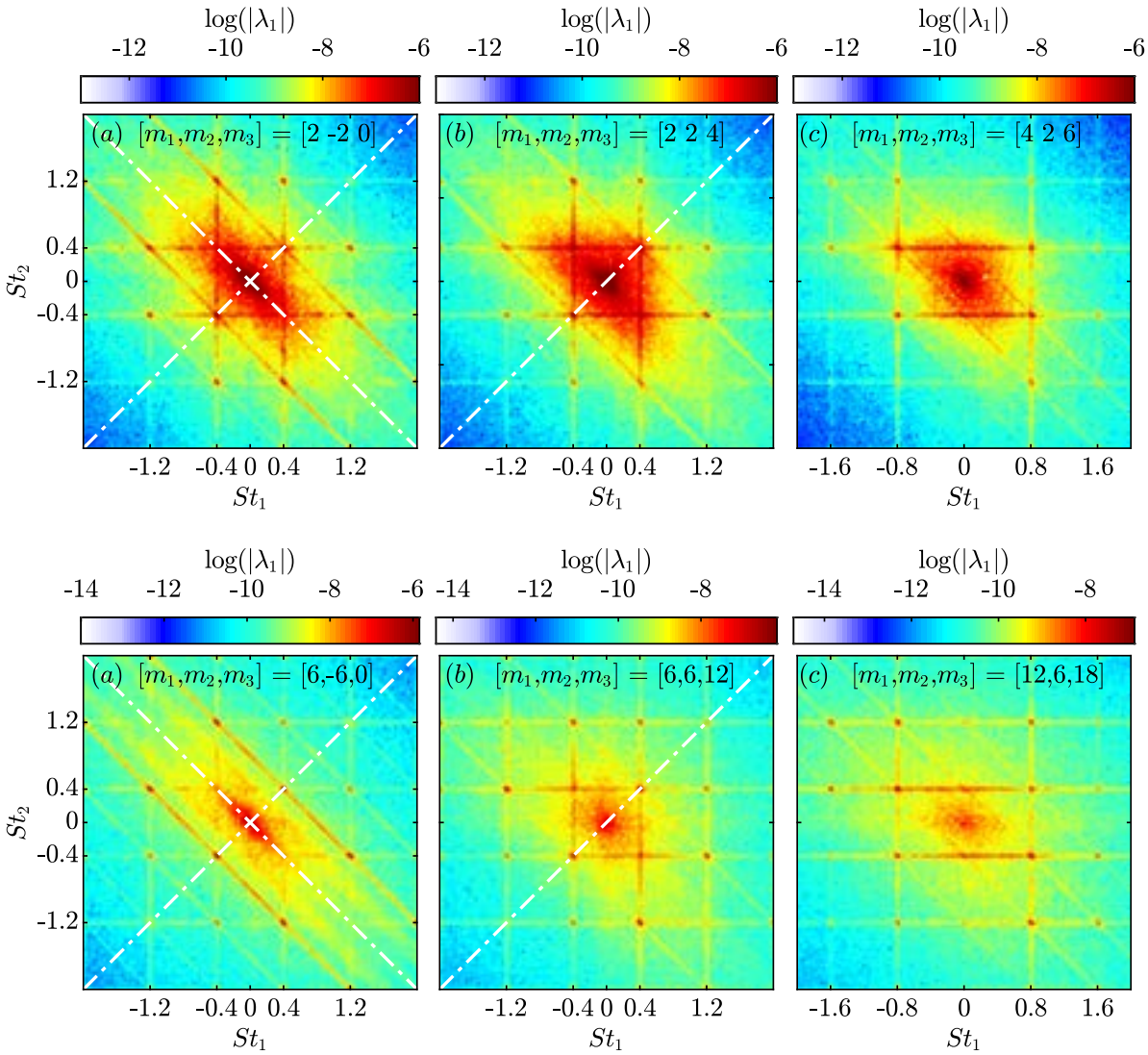

Figure 5.4.10: Cross-BMD spectra that shows the interaction of the azimuthal wavenumbers triads, [m_1,m_2,m_3], for the forced $m = \pm 6$ jet: (*a*) [6,-6,0]; (*b*) [6,6,12]; (*c*) [12,6,18].

Specifically, the $m = \pm 2$-forced jet excites the azimuthal wavenumbers, $\{\cdots, -4, -2, 0, 2, 4, \cdots\}$, while the $m = \pm 6$-forced jet excites the azimuhtal wavenumbers, $\{\cdots, -12, -6, 0, 6, 12, \cdots\}$. In the $m = \pm 2$ forced case, the peaks (0.4,0.4,0.8), (0.4,-0.4,0.0), and (1.2,-0.4,0.8) in $m = 0$ arise from the interactions between $m = 2$ and $m = -2$ at the forcing frequency and its odd harmonics. Local maxima at the same triads are observed for the self-interaction of $m = 2$ to generate the $m = 4$ component. In the [4,2,6] triplet, even harmonics in $m = 4$ interact with odd harmonics in $m = 2$ to generate odd harmonics in the $m = 6$ component. Similarly, for the $m = \pm 6$ forced

jet, the dominant azimuthal triplets are [6,-6,0], [6,6,12], and [12,6,18]. The first two triplets generate even harmonics, $\{0, 0.8, 1.6, \cdots, \}$, while the third triplet exhibits peaks at odd harmonics, $\{0.4, 1.2, 2.0, \cdots\}$. The spectra in figures 5.4.9(a) and 5.4.10(a) are symmetric about the lines $St_1 = \pm St_2$, and the spectra in 5.4.9(b) and 5.4.10(b) are symmetric about the line $St_1 = St_2$. The spectra in the 5.4.9(c) and 5.4.10(c), on the other hand, are asymmetric.

The observations of figures 5.4.8, 5.4.9, and 5.4.10 suggest the following trends for a general $m = \pm m_f$-forcing:

1. Even harmonics $\{0, 2St_f, 4St_f, \cdots\}$ are generated from azimuthal triplets of the form $[(2k_1)m_f, (2k_2)m_f, 2(k_1+k_2)m_f]$ and $[(2k_1+1)m_f, (2k_2+1)m_f, 2(k_1+k_2+1)m_f]$, where $k_1, k_2 \in \mathbb{Z}$.

2. Odd harmonics $\{St_f, 3St_f, 5St_f, \cdots\}$ arise from azimuthal triads of the form $[(2k_1+1)m_f, (2k_2)m_f, (2(k_1+k_2)+1)m_f]$.

3. The cross-BMD spectrum of the triads $[m_f, -m_f, 0]$ exhibits four-fold symmetry about the lines $St_1 = \pm St_2$.

4. The cross-BMD spectrum of the triads $[m_f, m_f, 2m_f]$ exhibits two-fold symmetry about the line $St_1 = St_2$.

5. The spectra of other triads, such as $[2m_f, m_f, 3m_f]$, are asymmetric.

Next, we will understand how the actuation of the jet results in the abovementioned triads. To begin, we express the Navier-Stokes equation in the following form:

$$\frac{\mathrm{d}\mathbf{q}}{\mathrm{d}t} = \mathcal{L}\mathbf{q} + Q(\mathbf{q}, \mathbf{q}). \tag{5.14}$$

Here, $\mathcal{L}$ represents the linear operator, and Q denotes the quadratic nonlinearities. By taking the Reynolds decomposition, $\mathbf{q}(\mathbf{x}, t) = \bar{\mathbf{q}}(\mathbf{x}) + \mathbf{q}'(\mathbf{x}, t)$, and substituting it into equation (5.14), we

obtain:

$$\frac{\mathrm{d}\mathbf{q}'}{\mathrm{d}t} = \mathcal{L}_{\bar{\mathbf{q}}}\mathbf{q}' + Q(\mathbf{q}', \mathbf{q}') \tag{5.15}$$

where, $\mathcal{L}_{\bar{\mathbf{q}}} = \mathcal{L} + Q(\bar{\mathbf{q}}, \cdot) + Q(\cdot, \bar{\mathbf{q}})$. When the jet is forced at an angular frequency of ω_f and azimuthal wavenumbers $\pm m_f$, the complex representation of the boundary forcing in equation (5.9b) is expressed as:

$$\mathbf{q}'_f \propto \left(e^{-i(\omega_f t - m_f \theta)} + e^{-i(\omega_f t + m_f \theta)} \right) + \text{c.c.} \tag{5.16}$$

At the n-th harmonic angular frequency, $n\omega_f$, the temporal Fourier decomposition of the equation can be written as

$$in\omega_f \hat{\mathbf{q}}_{n,m} = \mathcal{L}_{\bar{\mathbf{q}}}\hat{\mathbf{q}}_{n,m} + Q_{n,m}, \tag{5.17}$$

where,

$$Q_{n,m} = \begin{cases} \sum_l \sum_p Q(\hat{\mathbf{q}}_{l,p}, \hat{\mathbf{q}}_{n-l,m-p}) & \text{if } n,m \text{ are even or } n,m \text{ are odd} \\ 0 & \text{otherwise,} \end{cases} \tag{5.18}$$

denotes the non-linear interactions that result in the n-th harmonic angular frequency and the m-th azimuthal wavenumber. Here, in $\hat{\mathbf{q}}_{l,p}$, the first subscript denotes the l-th harmonic frequency index, and the second subscript denotes the p-th multiple of azimuthal wavenumber forcing.

For example, the triadic interactions that result in the second harmonic frequency can be written as:

$$Q_{2,0} = Q(\hat{\mathbf{q}}_{1,\pm1}, \hat{\mathbf{q}}_{1,\mp1}) + Q(\hat{\mathbf{q}}_{3,\pm1}, \hat{\mathbf{q}}_{-1,\mp1}) + Q(\hat{\mathbf{q}}_{4,\pm2}, \hat{\mathbf{q}}_{-2,\mp2}) + \cdots, \tag{5.19}$$

$$Q_{2,\pm1} = 0, \tag{5.20}$$

$$Q_{2,\pm2} = Q(\hat{\mathbf{q}}_{1,\pm1}, \hat{\mathbf{q}}_{1,\pm1}) + Q(\hat{\mathbf{q}}_{3,\pm3}, \hat{\mathbf{q}}_{-1,\mp1}) + Q(\hat{\mathbf{q}}_{4,\pm4}, \hat{\mathbf{q}}_{-2,\mp2}) + \cdots, \tag{5.21}$$

$$Q_{2,\pm3} = 0. \tag{5.22}$$

Similarly for the third harmonic frequency,

$$Q_{3,0} = 0, \tag{5.23}$$

$$Q_{3,\pm1} = Q(\hat{\mathbf{q}}_{1,\mp1}, \hat{\mathbf{q}}_{2,\pm2}) + Q(\hat{\mathbf{q}}_{2,\pm2}, \hat{\mathbf{q}}_{1,\mp1}) + Q(\hat{\mathbf{q}}_{4,\pm4}, \hat{\mathbf{q}}_{-1,\mp3}) + \cdots, \tag{5.24}$$

$$Q_{3,\pm2} = 0, \tag{5.25}$$

$$Q_{3,\pm3} = Q(\hat{\mathbf{q}}_{2,\pm2}, \hat{\mathbf{q}}_{1,\pm1}) + Q(\hat{\mathbf{q}}_{4,\pm4}, \hat{\mathbf{q}}_{-1,\mp1}) + Q\big(\hat{\mathbf{q}}_{5,\pm5}, \hat{\mathbf{q}}_{-2,\mp2}\big) + \cdots. \tag{5.26}$$

Equations (5.19 - 5.26) re-emphasize that the odd harmonic frequencies are present in the odd multiples of azimuthal wavenumber forcing, while even harmonic frequencies are present in the even multiples of m_f. These equations elucidate how the external forcing triggers the nonlinear interactions.

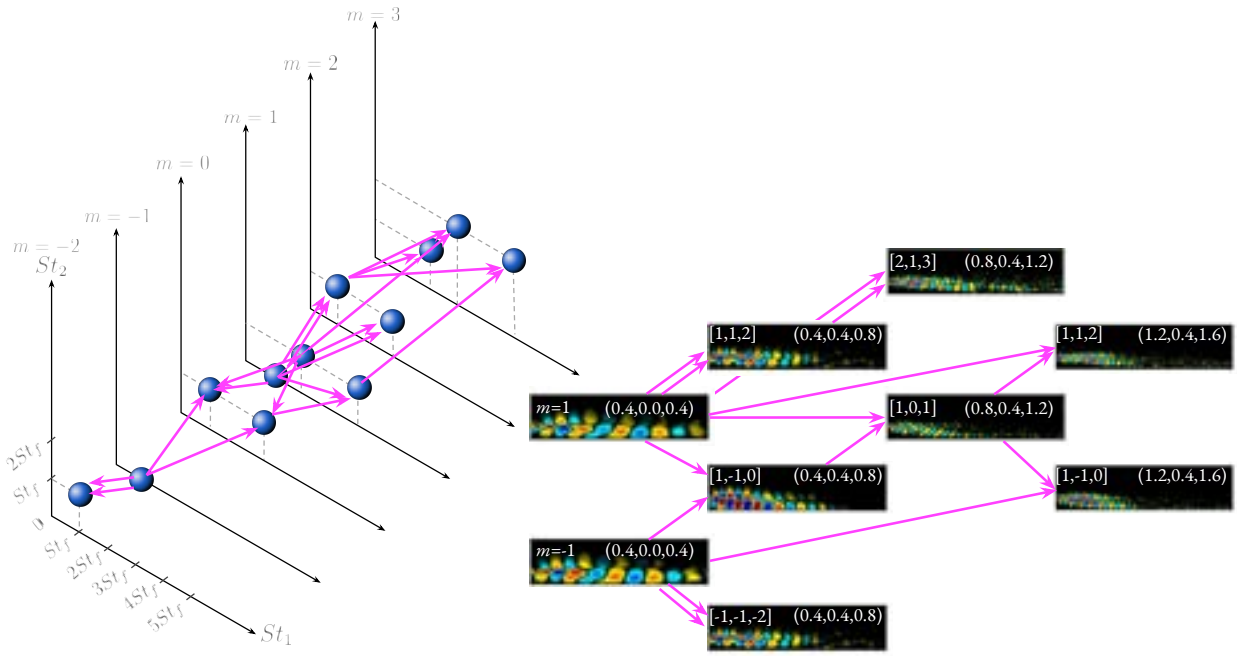

Figure 5.4.11: Example of a forward cascade of triads for the $m = \pm1$-forced jet.

Figure 5.4.11 shows the spatial structures involved in the cascade of triads for the $m = \pm1$-forced jet. The BMD modes in the frequency range $St_f \leqslant St_1 \leqslant 3St_f$ and the azimuthal wavenumber range $-1 \leqslant m_1 \leqslant 2$ are visualized here. The forcing initiates the cascade, where

$m = 1, St = 0.4$ and $m = -1, St = 0.4$ can undergo two possible interactions: (i) they can interact with each other to generate the $m = 0, St = 0.8$ mode through the wavenumber triad $[m_1, m_2, m_3] = [-1, 1, 0]$ and the frequency triad $(St_1, St_2, St_3) = (0.4, 0.4, 0.8)$; (ii) each of them can self-interact to result in $m = 2, St = 0.8$ or $m = -2, St = 0.8$. The generated modes (second column from the left) then interact with fundamental forcing modes to produce higher harmonics, such as the triad $[2, 1, 3]$, (0.8, 0.4, 1.2). Similarly, the cascade can be extended to higher frequencies and azimuthal wavenumbers. The cascade for $m_3 < 0$ is symmetric to $m_3 > 0$ and is not shown for brevity. Inspecting the modes reveals that the sum interactions in the frequency space create spatial structures with smaller wavelengths, while the sum interactions in the azimuthal wavenumber space result in modes with a larger swirl. An illustration of the cascade in the form of a directed acyclic graph is shown on the left in figure 5.4.11. Note that the cascade of triads shown in figure 5.4.11 is one of the many possible pathways of energy transfer.

Figure 5.4.12 depicts the cascade of triads generated by the $m = \pm 6$-forcing, similar to figure 5.4.11. The major difference is that the azimuthal wavenumbers $\{\cdots, -2, -1, 0, 1, 2, \cdots\}$ are replaced by $\{\cdots, -12, -6, 0, 6, 12, \cdots\}$, i.e., the odd and even integers are replaced by the odd and even integer multiples of 6. The higher azimuthal forcing actuates the spatial structures that are near the nozzle's exit. The BMD mode resulting from the self-interaction of the forcing, [6,6,12] and (0.4,0.4,0.8), is also localized to the vicinity of the nozzle's lip. Though the overall trends are similar, the BMD modes corresponding to the $m = \pm 6$ forcing exhibit greater swirl compared to the modes of the $m = \pm 1$ forcing. An interesting observation is that the BMD modes associated with the frequency triads (0.4, 0.4, 0.8) and (1.2, 0.4, 1.6) in the wavenumber triplet [6, -6, 0] resemble the modes associated with the same frequency triads in the wavenumber triplet [1, -1, 0] for the $m = \pm 1$-forced jet. This indicates that the different $m = \pm m_f$ forcings generate the same spatial structures in the wavenumber triplet $[m_f, -m_f, 0]$.

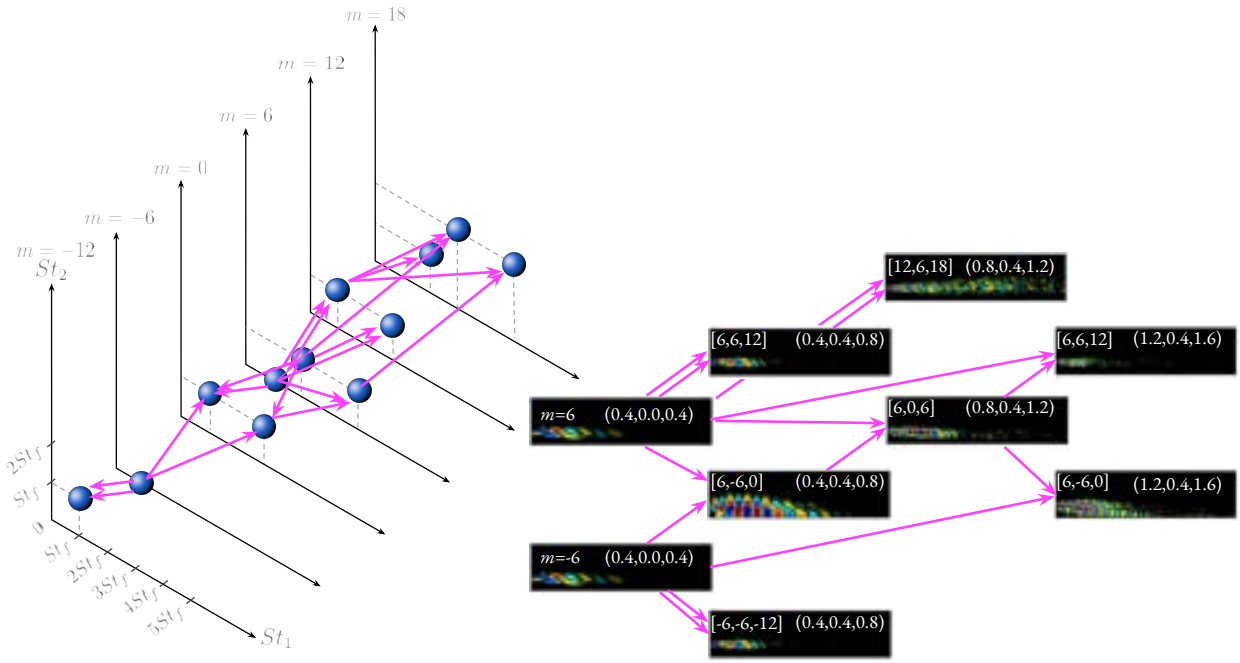

Figure 5.4.12: Example of a forward cascade of triads for the $m = \pm 6$-forced jet.

5.5 Mean flow distortion due to non-axisymmetric forcing

The non-axisymmetric forcing results in a distortion of the jet cross-section. Previous studies (Cohen and Wygnanski, 1987, Long and Petersen, 1992) demonstrate that the jet loses its axial symmetry when excited by the two different azimuthal modes of the same frequency, in particular, $m = \pm m_f$-forcing results in a $\cos\left(2m_f\theta\right)$ distortion, where θ is the azimuth angle. Figures 5.5.1, 5.5.2, 5.5.3 and 5.5.4 report similar observations.

Figures 5.5.1 and 5.5.2 show the contours of the mean streamwise velocity at various axial cross-sections. At the nozzle's exit, the cross-section is circular for all 5 jets. As the flow evolves downstream, the distortion of the mean flow is observed for non-axisymmetrically forced jets. For the $m = \pm 1$ forced jet, the cross-section is initially circular, and from $x = 2$ it undergoes distortion to an elliptical shape. The elliptical shape of the mean streamwise velocity persists till $x = 16$. The $m = \pm 2$-forced jet exhibits a square cross-section at $x = 1$ and 2, while a four-lobed structure is observed between $3 \leqslant x \leqslant 6$. The cross-section reverts back to a circular shape by

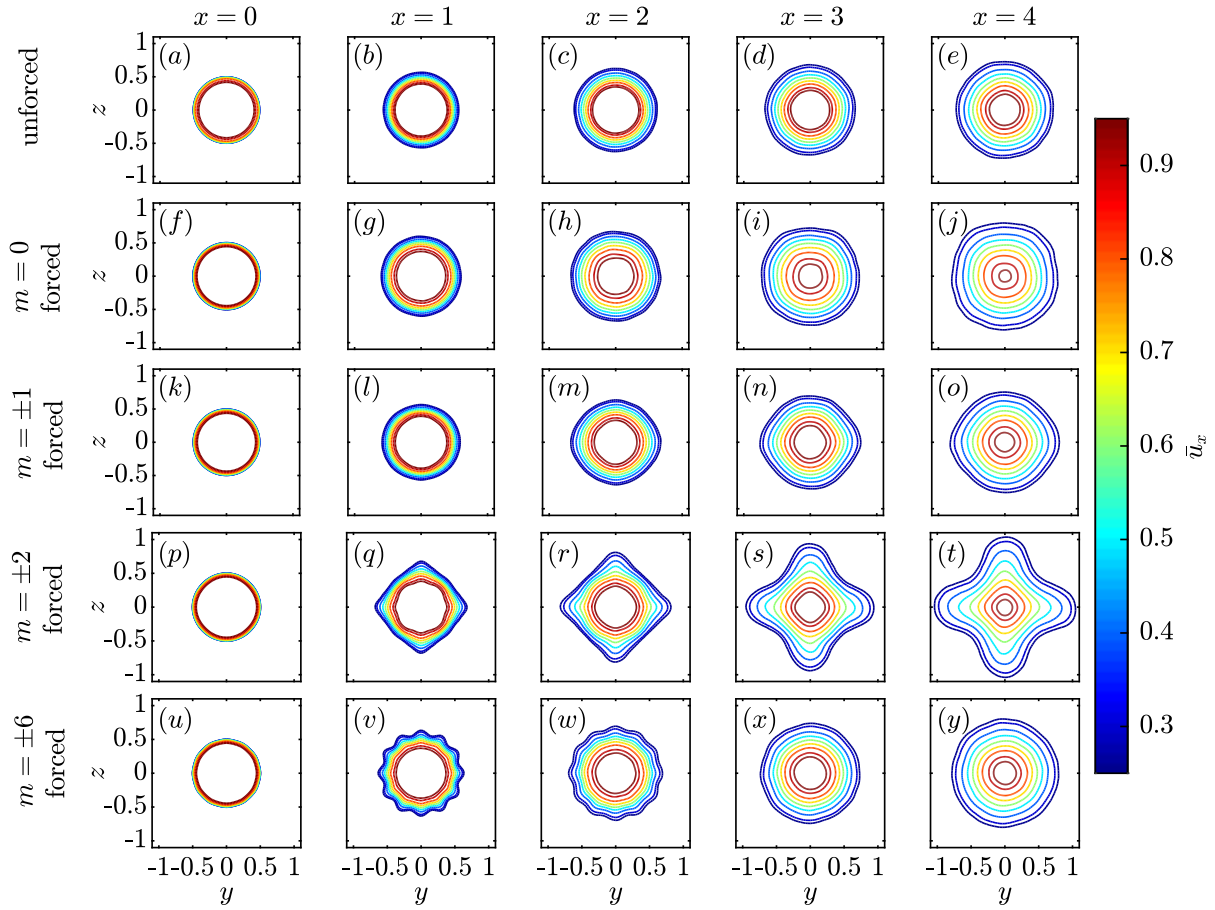

Figure 5.5.1: Mean streamwise velocity contours at five different streamwise cross-sections $x = 0, 1, 2, 3$, and 4: (*a-e*) unforced; (*f-j*) $m = 0$-forced; (*k-o*) $m = \pm 1$-forced; (*p-t*) $m = \pm 2$-forced; (*u-y*) $m = \pm 6$-forced.

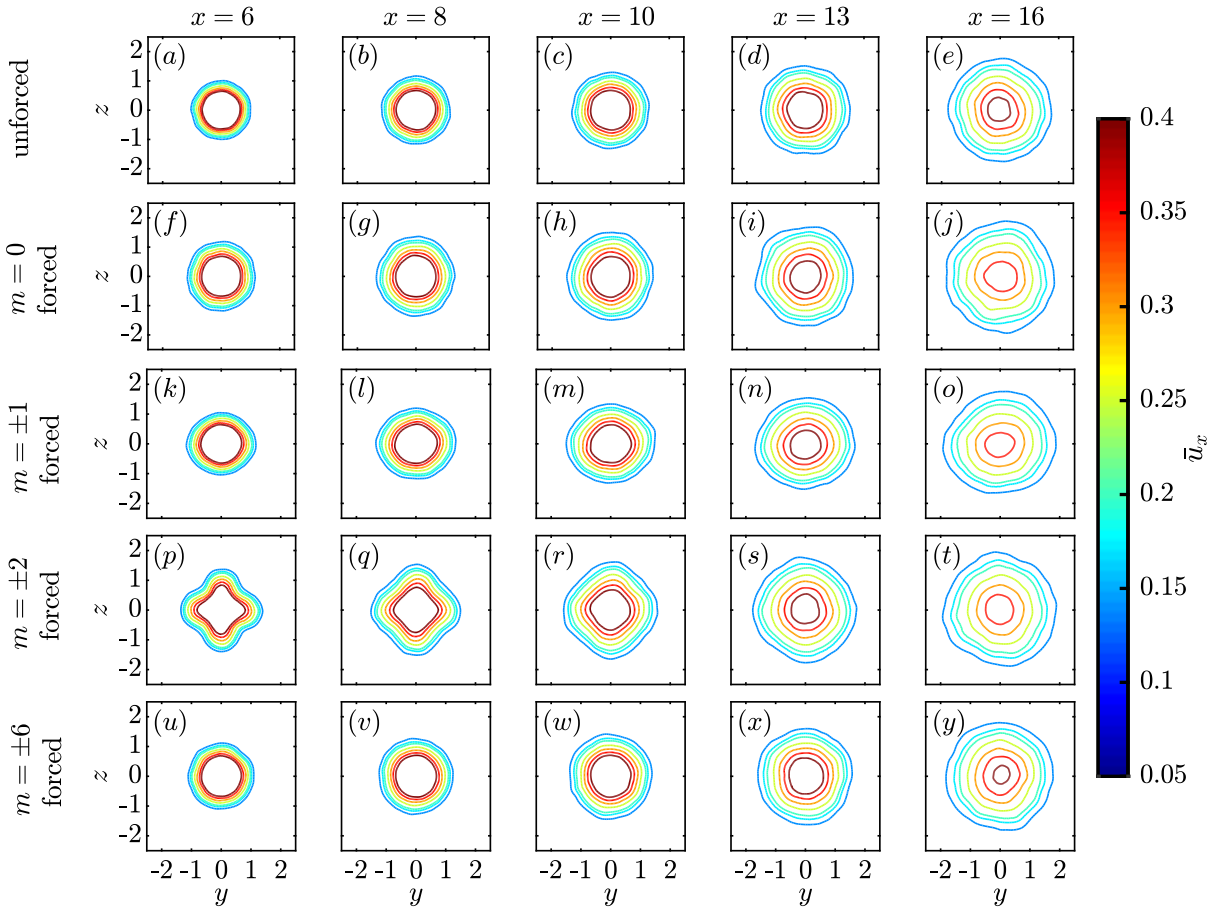

Figure 5.5.2: Mean streamwise velocity contours at five different streamwise cross-sections $x = 6, 8, 10, 13$, and 16: (*a-e*) unforced; (*f-j*) $m = 0$-forced; (*k-o*) $m = \pm 1$-forced; (*p-t*) $m = \pm 2$-forced; (*u-y*) $m = \pm 6$-forced.

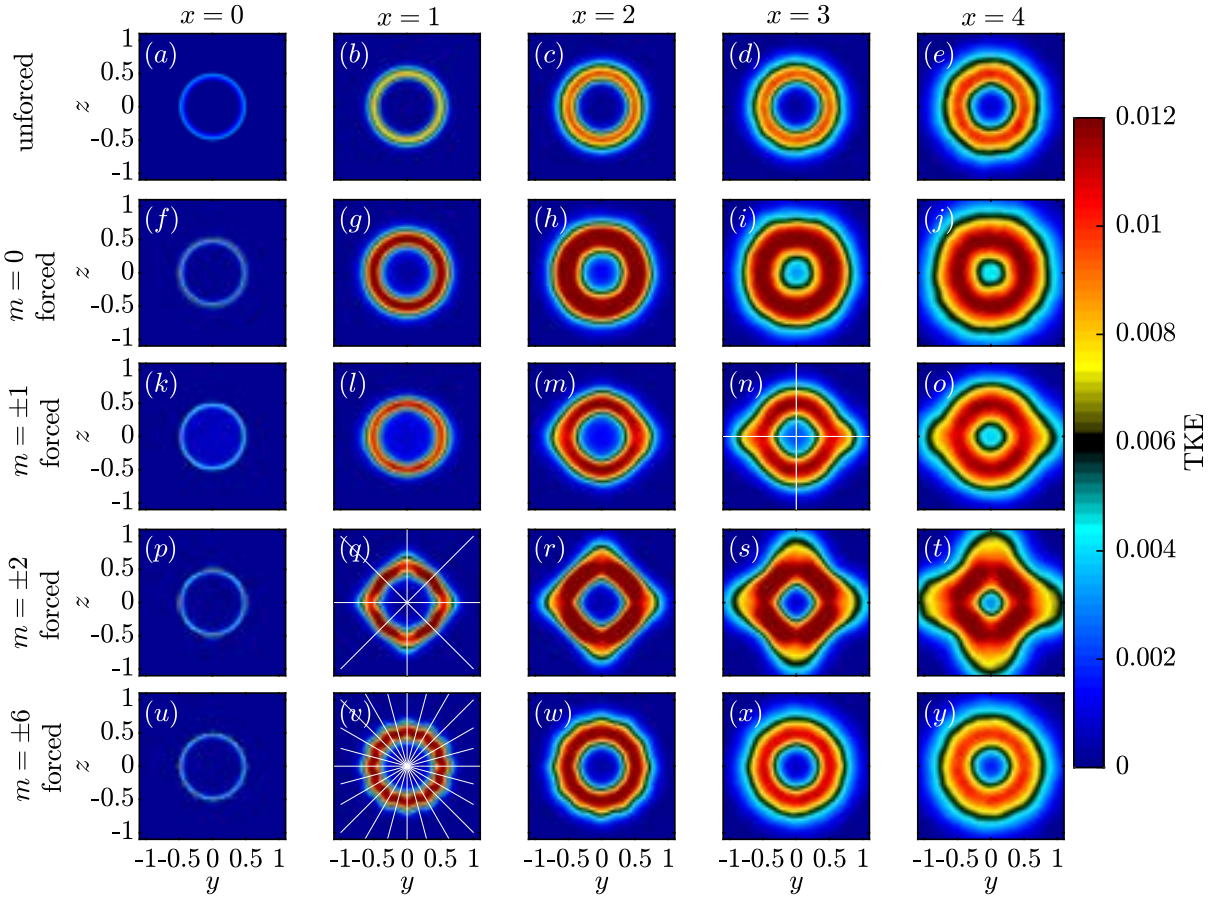

Figure 5.5.3: TKE at five different streamwise cross-sections $x = 0, 1, 2, 3$, and 4: (*a-e*) unforced; (*f-j*) $m = 0$-forced; (*k-o*) $m = \pm 1$-forced; (*p-t*) $m = \pm 2$-forced; (*u-y*) $m = \pm 6$-forced. The D_2, D_4, and D_{12} symmetries associated with the non-axisymmetric forcing are shown in panels (*n*), (*q*), and (*v*), respectively.

$x = 13$. The cross-section of the $m = \pm 6$ forced jet demonstrates a 12-lobed pattern, with each lobe placed at every 30 degrees. The degree of mean-flow distortion decreases quickly, and the cross-section regains its axisymmetric nature by $x = 3$. On the other hand, cross-section of the unforced and axisymmetrically forced jets remains circular throughout the entire domain. Slight deviations from a circular shape are seen at larger downstream distances, primarily due to a lack of convergence. Overall, these observations suggest that higher azimuthal wavenumber forcing results in mean flow distortion at a more upstream location, but its effect fades earlier. In contrast, lower azimuthal forcing causes delayed mean flow distortion but is more persistent.

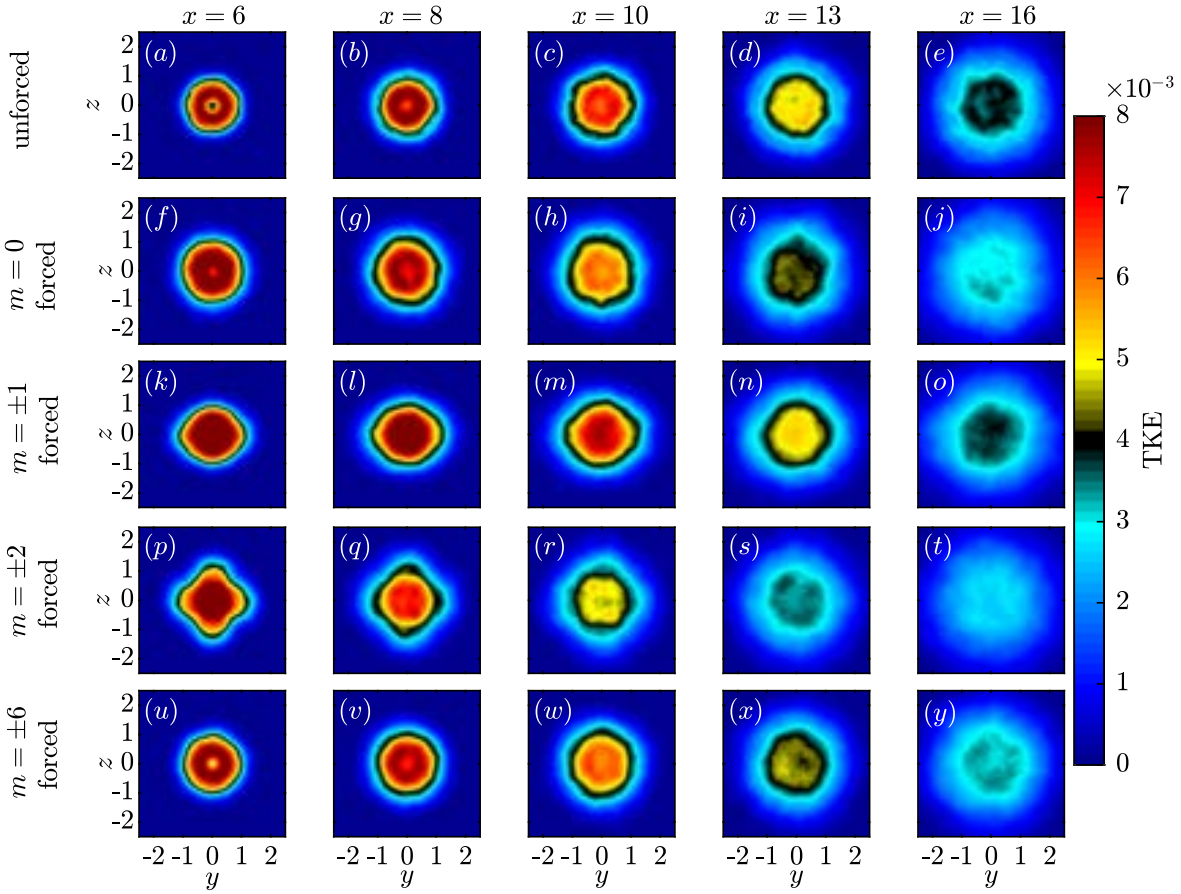

Figure 5.5.4: TKE at five different streamwise cross-sections $x = 6, 8, 10, 13$, and 16: (*a*-*e*) unforced; (*f*-*j*) $m = 0$-forced; (*k*-*o*) $m = \pm 1$-forced; (*p*-*t*) $m = \pm 2$-forced; (*u*-*y*) $m = \pm 6$-forced.

The turbulent kinetic energy (TKE), $K = \langle u_i' u_i' \rangle / 2$, for the 5 jets at different axial cross-sections, is shown in figures 5.5.3 and 5.5.4. Similar to figures 5.5.1 and 5.5.2, a $m = \pm m_f$ forcing results in patterns with $2m_f$ lobes. The TKE fields for the $m = \pm 1$ and $m = \pm 2$-forced jets, display elliptical and square cross-sections, respectively, while a dodecagon cross-section is observed at the nozzle's exit for the $m = \pm 6$-forced jet. The TKE fields exhibit trends similar to those of the mean flow, suggesting that non-axisymmetric forcing breaks the azimuthal symmetry of both the mean quantities and the turbulent statistics. Upon closer examination, the jets exhibit distinct symmetries: the $m = \pm 1$ forced jet is symmetric about the lines $y = 0$ and $z = 0$; the $m = \pm 2$ forced jet is symmetric about $y = 0$, $z = 0$, $y = z$, and $y = -z$; the $m = \pm 6$ forced jet is symmetric about the lines $z = \tan(n\pi/12)y$, where $n = 0, 1, 2, \ldots, 11$. The corresponding symmetric lines are shown in panels (*n*), (*q*), and (*v*) of figure 5.5.3. These findings indicate that the $m = \pm 1$, $m = \pm 2$, and $m = \pm 6$ cases display D_2, D_4, and D_{12} symmetries, respectively, where D represents the dihedral group. A complete decomposition into the components of the dihedral groups is beyond the scope of this work and we defer it to our future works.

For a quantitative measure of the cross-section distortions, we introduce two metrics:

$$U_x^{\text{dist}}(x) = \frac{\|U(x,r,\theta) - \langle U(x,r,\theta)\rangle_\theta\|_r}{\|\langle U(x,r,\theta)\rangle_\theta\|_r}, \tag{5.27}$$

$$K^{\text{dist}}(x) = \frac{\|K(x,r,\theta) - \langle K(x,r,\theta)\rangle_\theta\|_r}{\|\langle K(x,r,\theta)\rangle_\theta\|_r}, \tag{5.28}$$

where $\langle\cdot\rangle_\theta$ denotes the azimuthal mean and $\|\mathbf{q}\|_r^2 = \int_r \mathbf{q}^* \mathbf{W} \mathbf{q} \mathrm{d}r$. The equations (5.27), and (5.28), quantify the distortions of the mean streamwise velocity, and TKE, respectively. The corresponding results are presented in Figure 5.5.5(*a*) and (*b*). The $m = \pm 2$ forcing produces the largest distortion of both the mean streamwise velocity and TKE. A significant distortion is observed near the nozzle's exit for the $m = \pm 6$-forced jet, which diminishes rapidly within the first three diameters. The $m = \pm 1$ case exhibits the largest mean flow distortion beyond $x = 10$, emphasizing its persistence. However, its impact on TKE distortion is weaker than that of the

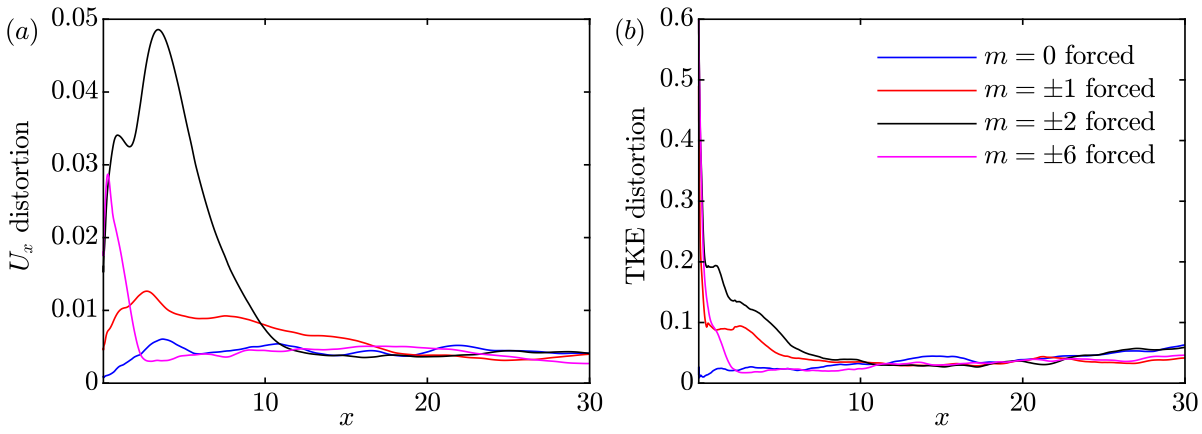

Figure 5.5.5: Cross-section distortion of the jet due to different forcing: (a) mean streamwise velocity; (b) TKE.

$m = \pm 2$ forcing. These findings suggest that the $m = \pm 1$ forcing is more effective in distorting the cross-section of mean flow rather than the TKE.

Next, the structures at $St \to 0$ for different forcings are visualized in figure 5.5.6. To obtain these structures, we use the D_2, D_4, and D_{12} symmetries and select the component that corresponds to the identity mapping. We then compute the FFT using the Welch approach and average the Fourier realizations at $St \to 0$. The streamwise velocity component u_x of the $m = \pm 1$-, $m = \pm 2$-, and $m = \pm 6$-forced jet is shown in figure 5.5.6. These structures are elongated regions of streamwise velocity and are reminiscent of streaks. For the $m = \pm 1$-forced jet, we observe two streaks with $u_x > 0$, and for a $\pm m_f$-forcing, we observe $2m_f$ streaks. We also show the TKE contours and find that the streaks are located in the regions of cross-section distortions. The spatial extent of streaks increases for lower m_f forcing, and the streaks originate at a more upstream location for higher m_f forcing. These observations suggest that the mean-flow distortion is caused by the streaky structures, and the characteristics of streaks determine the strength and persistence of cross-section distortion.

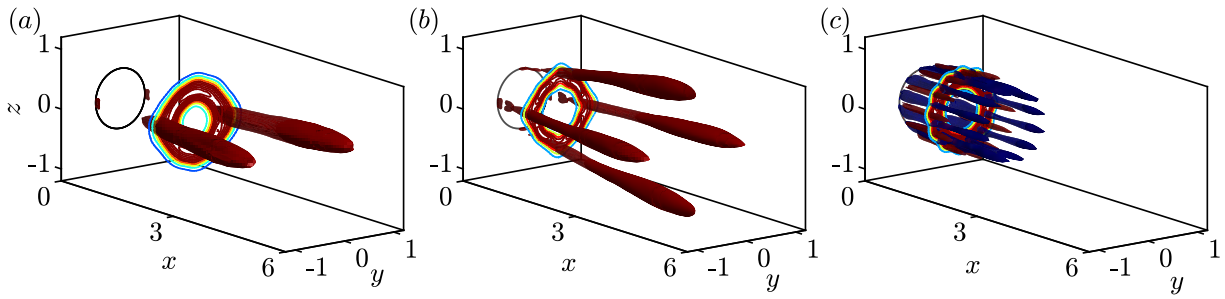

Figure 5.5.6: Large-scale streaky structures at $St = 0$ for the three non-axisymmetrically forced jets: (*a*) $m \pm 1$-forced jet; (*b*) $m = \pm 2$-forced jet; (*c*) $m = \pm 6$-forced jet. The D_2, D_4, and D_{12} symmetries are used to compute these structures. Isosurfaces of streamwise velocity ($u_x > 0$: red, $u_x < 0$; blue) at $\pm 50\%$ of their maximum value.

5.6 Summary and conclusions

LES of unforced and forced turbulent jets were performed and validated with companion experiments. The jet is axisymmetrically forced by blowing and suction at a frequency of $St = 0.4$ and with an amplitude that correspond to the jet velocity, triggering strong nonlinear interactions. The axisymmetric forcing produces a purely axisymmetric response and entails significant thickening of the shear layer and shortening of the potential core. The axisymmetric component, $m = 0$, exhibits peaks at the forcing frequency and its harmonics due to triadic interactions. BMD is employed to investigate the structures associated with these triads and their relative significance. The prominent azimuthal wavenumber triplet is [0, 0, 0] and the two most dominant triads arise due to the self-interaction of the forcing frequency, $[St_f, St_f, 2St_f]$, and due to harmonic-fundamental difference interaction, $(2St_f, -St_f, St_f)$, that scatters energy back into the fundamental. Integral interaction maps are defined to identify regions of activity of triadic interactions. Both unforced and forced jets exhibit strong interactions in the closure region of the potential core. This 'natural' region of nonlinear activity extends over ~ 6 jet diameters in the unforced case and over ~ 4 in the forced case, respectively. We speculate that the nonlinear activity in that region is the reason for the discrepancy of SPOD modes and linear resolvent (Schmidt et al., 2018) and global modes (Schmidt et al., 2017b), and similarly the discrepancy between

linear wavepacket models and experimental data, also attested to nonlinearity by Cavalieri et al. (2013) and Tissot et al. (2017b). In the forced jet, strong interactions that are associated with the large-amplitude forcing are identified in the vicinity of the actuator near the lip line. Additionally, BMD was applied to the far-field pressure and identified the difference-interaction between the first harmonic and the forcing frequency as the most significant triad. This observation is in agreement with the findings of Sandham et al. (2006).

For the non-axisymmetrically forced jet, the triadic interactions occur across different azimuthal wavenumbers. For a $m = \pm m_f$ forced jet, different wavenumber triplets are important, such as, $[m_f, -m_f, 0]$, $[m_f, m_f, 2m_f]$, and $[2m_f, m_f, 3m_f]$. The cascade of triads is initiated by the self-interaction of the fundamental frequency, $(St_f, St_f, 2St_f)$ in the wavenumber triplets $[m_f, -m_f, 0]$, $[m_f, m_f, 2m_f]$. The resulting triads then interact with the forcing modes to generate the odd harmonic frequencies in the odd integer multiples of the wavenumber forcing. For instance, the odd harmonic frequency $3St_f$ at $3m_f$ is created through the frequency triad $(2St_f, St_f, 3St_f)$ and the wavenumber triad $[2m_f, m_f, 3m_f]$. The cascade proceeds in a similar way to generate the even harmonics in the even integer multiples of the wavenumber forcing. As an example, the $3St_f$ at $3m_f$ interacts with St_f at m_f to generate the fourth harmonic frequency, $4St_f$, in the fourth integer multiple of the forcing wavenumber, $4m_f$.

Acknowledgements AN and OTS gratefully acknowledge support from Office of Naval Research grant N00014-20-1-2311 and National Science Foundation grant CBET 2046311. Parts of this chapter, with modifications, appear in two conference proceedings titled: 1) A. Nekkanti, O. T. Schmidt, I. Maia, P. Jordan, L. Heidt, & T. Colonius. "Bispectral mode decomposition of axisymmetrically and non-axisymmetrically forced turbulent jets", *AIAA Aviation 2023 Forum*; 2) A. Nekkanti, I. Maia, P. Jordan, L. Heidt, T. Colonius, & O. T. Schmidt. "Triadic nonlinear interactions and acoustics of forced versus unforced turbulent jets", *Twelfth International Symposium on Turbulence and Shear Flow Phenomena (TSFP), 2022*. The dissertation author is the primary investigator and author of this work.

Chapter 6

Nonlinear energy transfer in vortex-pairing of initially-laminar jets

6.1 Introduction

The seminal work by Brown and Roshko (1974) demonstrated the presence of large-scale coherent vortical structures in turbulent mixing layers. Winant and Browand (1974) showed that the pairing of these vortical structures significantly influences the growth of the mixing layers. Evidence of a similar process has been reported in axisymmetric jets. For initially-laminar or transitional jets, the fluid emerging from the nozzle forms an unstable laminar shear layer that grows very rapidly, forming ring vortices that further pair up (Moore, 1977). The pairing of vortex rings in jets was first described by Becker and Massaro (1968). They performed jet experiments at a moderate Reynolds number and forced the jet at a single frequency to illustrate the formation of vortices and subsequent pairing. Zaman and Hussain (1980) and Hussain and Zaman (1980) investigated the vortex pairing process in more detail by forcing a wide range of frequencies. In particular, they identified the vortex dynamics, the trajectories of vortices, and the role they play in the transition to turbulence. The process of vortex pairing not only provides us insights into

the transition to turbulence but also enables us to control turbulence by finding strategies that enhance or suppress turbulent mixing.

Vortex pairing is also a source of jet noise, especially in initially-laminar jets (Bridges and Hussain, 1987, Zaman, 1985a,b, 2012). In this regard, Bridges and Hussain (1987) showed that vortex-pairing events are acoustically unimportant for turbulent jets but play a significant role in the emitted noise for initially-laminar jets. Bogey and Bailly (2010) also investigated the influence of vortex pairing on the radiated noise in initially-laminar jets. They found that jets with larger momentum thickness exhibit stronger vortex pairing and consequently radiate more sound to the far-field. These results were further confirmed by Zaman (2012). Hence, understanding vortex pairing will provide us additional insights into the generation of jet noise, which is another motivation for this study.

Vortex pairing is also observed in plane shear layers, for example, Ho and Huang (1982) and Hajj et al. (1992). Ho and Huang (1982) compared the development of the fundamental and subharmonic modes in the vortex-pairing mechanism and found that the vortex rollup process is associated with the saturation of the fundamental frequency, while the vortex pairing process corresponds to the saturation of the subharmonic frequency. In a two-dimensional shear layer, Pierrehumbert and Widnall (1982) demonstrated that the emergence of the subharmonic frequency is linked to the pairing of vortices. The existing literature reports two possible routes for the growth of the subharmonic frequency. Monkewitz (1988) hypothesizes that a parametric resonance mechanism between the fundamental and the subharmonic modes leads to a pronounced growth of the subharmonic. Later, Hajj et al. (1992) demonstrated that this occurs due to nonlinear energy transfer. On the other hand, Mankbadi (1985) argued that pairing arises when the subharmonic component acquires sufficient energy from both the fundamental wave and the mean flow to become the largest-amplitude perturbation in the jet. Experimental investigations by Paschereit et al. (1995) show that most of the energy for the resonant growth of the subharmonic comes directly from the mean flow, and the fundamental-subharmonic interaction only acts as a catalyst.

In this study, we use spectral turbulent kinetic energy equations to shed light on the energy transfer that occurs during the vortex pairing process. In this study, we will use spectral turbulent kinetic energy equations to shed light on the energy transfer that occurs during the vortex pairing process.

The chapter is organized as follows: In §6.2, we discuss the methodology of the local linear stability theory. In §6.3, we identify and characterize the vortex pairing process using visualization, turbulent statistics, and SPOD. In §6.4, we revisit the spectral TKE equations and customize them based on the leading SPOD modes. In §6.5, we analyze the triadic interactions using BMD, and finally, in §6.6, we summarize the work.

6.2 Local linear stability theory

To identify the most unstable spatial waves, we will perform a local linear stability analysis. The flow will be linearized around the mean flow, assuming a locally parallel flow. This means that the streamwise derivatives of the mean flow in the streamwise direction are negligible. Firstly, we will use the Reynolds decomposition

$$\mathbf{q}(x,r,\theta,t) = \bar{\mathbf{q}}(x,r) + \mathbf{q}'(x,r,\theta,t), \tag{6.1}$$

where, $\mathbf{q} = [\rho, \mathbf{u}_x, \mathbf{u_r}, \mathbf{u}_\theta, \mathbf{T}]^T$. In local analysis, the base flow is considered to be homogeneous in the streamwise and azimuthal directions and in time, which leads to fluctuations of the form,

$$\mathbf{q}'(x,r,\theta,t) = \hat{\mathbf{q}}(r) e^{i(\alpha x + m\theta - 2\pi f t)}, \tag{6.2}$$

where α and m are streamwise and azimuthal wavenumbers, respectively, and f is the frequency. As the objective is to obtain the most unstable streamwise wavenumbers, i.e., α, we will specify the frequency f and solve the eigenvalue problem for $\alpha(f)$. Linearizing the Navier-Stokes

equations results in the following eigenvalue problem:

$$(i\omega I + \mathcal{L}_{\alpha,m})\hat{\mathbf{q}}_{\alpha,m} = 0. \tag{6.3}$$

Here, $\mathcal{L}$ is the linearized compressible Navier–Stokes operator. Following the approach of Rodríguez et al. (2015), we neglect the viscous terms of order α^2 and solve the resulting eigenvalue problem using the methodology of Maia et al. (2022, 2021b). Further details on the boundary conditions, domain extension, and domain mapping can be found in Maia et al. (2022, 2021b). At each frequency f, the growth or decay of disturbances in the jet is governed by the sign of the imaginary part of the streamwise wavenumber, $\alpha_i = \mathrm{Im}(\alpha)$: if $\alpha_i < 0$, the disturbances will grow exponentially downstream; if $\alpha_i > 0$, they will decay downstream.

6.3 Vortex-pairing and the formation of subharmoncis

We perform large-eddy simulation of an initially-laminar subsonic jet using the compressible flow solver "Charles" developed at Cascade Technologies Brès et al. (2017, 2018). Charles solves the spatially filtered compressible Navier–Stokes equations on unstructured grids using a density-based finite-volume method. The LES combines the Vreman sub-grid model (Vreman, 2004) with the wall-model by Bordat and Larsson (Bodart and Larsson, 2012, Kawai and Larsson, 2012). The reader is referred to Brès et al. (2017, 2018) for further details on the numerical method and validation on jet flows. The validation of the LES case for the present case follows the previous studies. In particular, the mesh used by Brès et al. (2018) is modified to accommodate the new nozzle geometry. The total grid size is 16.6 million control volumes. The LES is conducted for the experimental Reynolds number, whereas the Mach number is artificially increased to $M_j = 0.4$. Effects of compressibility are still small in this regime and the very small-time steps associated with the incompressible limit are avoided. The LES of a turbulent jet with the same Re and M_j was validated in the previous chapter §5.

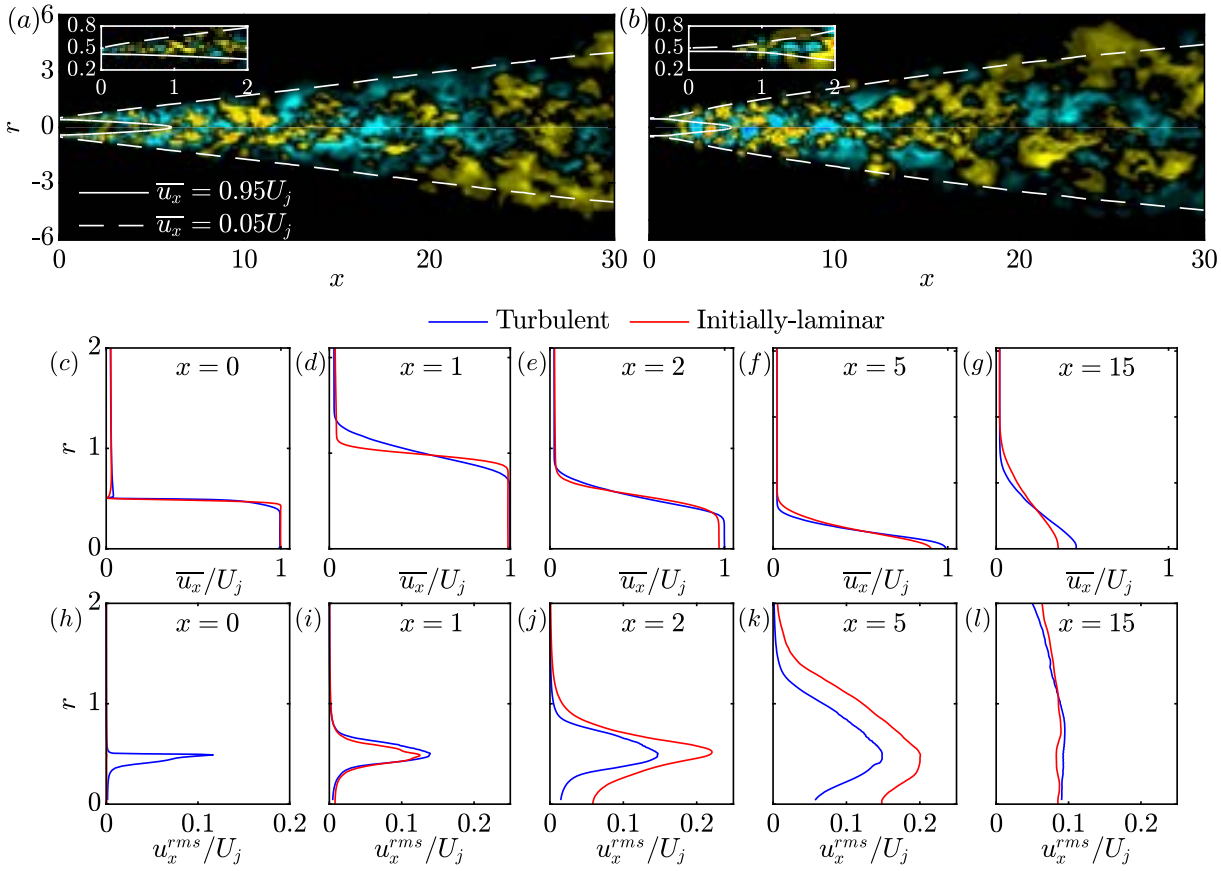

Figure 6.3.1: Development of the shear-layer in the turbulent and initially laminar jet. The instantaneous flow field of the turbulent, and initially-laminar jet are shown in (*a*), and (*b*), respectively. Mean (*c*-*g*) and RMS streamwise velocities (*h*-*k*) at different axial locations: (*c*,*h*) $x = 0$; (*d*,*i*) $x = 1$; (*e*,*j*) $x = 2$; (*f*,*k*) $x = 5$; (*g*,*l*) $x = 15$.

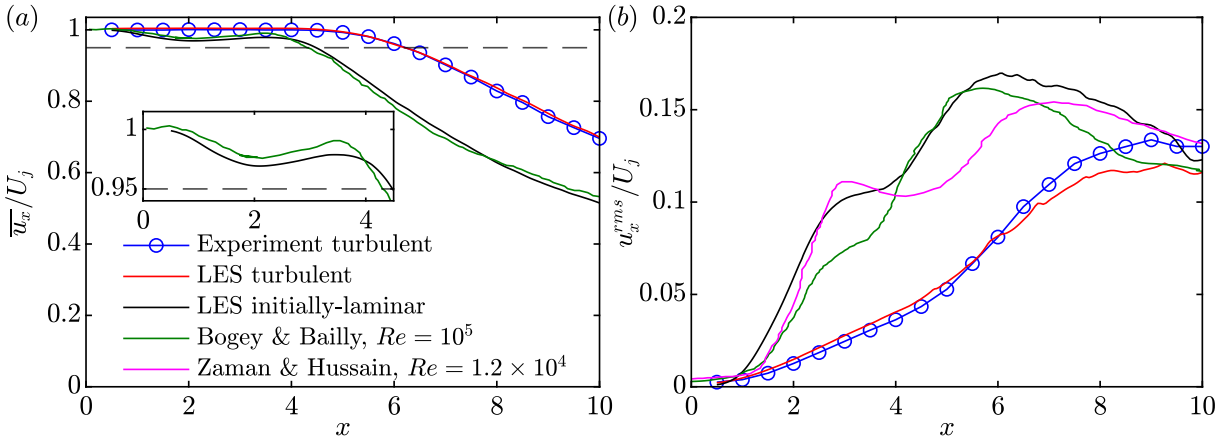

Figure 6.3.2: Comparison of the experiment with the LES simulations for the initially-laminar jet: (*a*) mean and (*b*) RMS streamwise velocity on the centerline. Black dashed line represents $\overline{u_x}/U_j = 0.95$ and its intersection with the mean streamwise velocity indicates the length of the potential core.

Figure 6.3.1 shows the evolution of an initially-laminar jet through visualizations and mean and RMS streamwise velocity. For comparison, the turbulent jet (tripped boundary-layer inside the nozzle) at the same Reynolds number is also shown. Panels (*a*,*b*) show instantaneous streamwise velocity fields for the two jets, revealing that the initially-laminar jet has a shorter potential core. The insets in panels (*a*,*b*) indicate that the initially-laminar jet starts to develop much later than the turbulent jet, around $x \approx 0.8$. This observation is further supported by the mean flow profiles in panels (*c*-*g*), which show that the turbulent jet transitions to a bell-shaped curved earlier than the initially-laminar jet. Additionally, in the region $0 \leqslant x \leqslant 1$, the gradient $\partial\bar{u}_x/\partial r$ is larger for the initially-laminar jet. The laminar jet experiences faster diffusion, eventually leading to a larger velocity gradient in the turbulent jet. Panels (*h*-*l*) depict the RMS streamwise velocity profiles. At the nozzle's exit, the turbulence intensity of the initially-laminar jet is almost zero, but it grows rapidly downstream and eventually exceeds the intensity of the turbulent jet. These observations suggest that although the initially-laminar jet starts to develop later, it grows much faster than the turbulent jet. Later we will demonstrate that this is a result of vortex-pairing, which is significantly stronger for initially-laminar jets (Bogey and Bailly, 2010, Kim and Choi, 2009).

We compare the LES of the initially-laminar jet to the turbulent jet (both LES and experimental), and two previous studies for the initially-laminar jet. Figure 6.3.2 shows the mean and RMS streamwise velocities on the centerline. For the turbulent jet, a good agreement was obtained between the numerical simulations and the experiments. On the other hand, the mean and RMS profiles of initially-laminar jet exhibits notable differences. Along the centerline, the mean flow predicted by the LES shows a dip at $x \approx 2$ (inset in figure 6.3.2(a)), which decays rapidly beyond the end of the potential core. For comparison, the mean flow velocity profile of Bogey and Bailly (2010) is shown, which exhibits a similar trend to our LES. Figure 6.3.2(b) shows that the LES of the initially-laminar jet overpredicts the RMS of streamwise velocity on the centerline. The most observable discrepancy is the hump at $x \approx 2.8$. These differences are due to the stronger vortex pairing in the case of the initially-laminar jet. The initially-laminar jet is sensitive to the shear-layer thickness and this effect has been explored in detail by Bogey and Bailly (2010), Bogey et al. (2012), Kim and Choi (2009). These studies demonstrated that for initially-laminar jets, a thicker shear layer grows faster and exhibits stronger vortex pairing, whereas a thinner shear layer develops earlier but at a slower rate, resulting in lower u_x^{rms} on the centerline (Bogey and Bailly, 2010). Figure 6.3.2 also includes the RMS of the streamwise velocity curves from previous works such as the experiments of Zaman and Hussain (1980) and the simulations of Bogey and Bailly (2010) for comparison. These curves showed a similar hump in the RMS of the streamwise velocity, and the Reynolds number of these studies were $Re = 1.2 \times 10^4$ and 10^5, respectively. These comparisons with the literature indicate that the tripping of the boundary layer inside the nozzle of the jet significantly influences the shear layer, causing the initially-laminar jet to behave differently from the turbulent jet. Our focus is on analyzing the nonlinear interactions that cause these discrepancies.

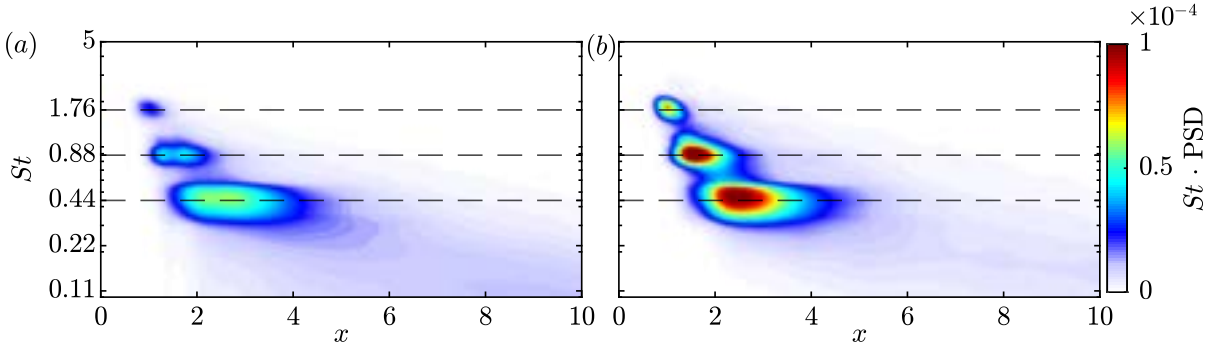

Figure 6.3.3: Pre-multiplied power spectral density along x: (a) streamwise velocity, u_x; (b) radial velocity, u_r. The PSD is integrated along the radial direction at each streamwise location.

6.3.1 Shear-layer instability

Figure 6.3.3 shows the premultiplied PSD for the streamwise and radial velocities, u_x and u_r, respectively. The PSD is computed at each spatial location and then integrated radially for each streamwise location. The PSD of both u_x and u_r show the prominence of three frequency components, $St = 1.76, 0.88$, and 0.44. The frequency $St = 1.76$ occurs at $x \approx 1$ and precedes $St = 0.88$, which in turn precedes $St = 0.44$. The occurrence of the subharmonic frequencies at a more downstream location, suggests the possibility of vortex-pairing that result in the formation of these subhamonics. The PSDs reveal that the frequencies $St = 1.76$, 0.88, and 0.44 are more significant in the radial velocity than the streamwise velocity component.

Figure 6.3.4(a) shows the contribution of frequencies $St = 1.76$, 0.88, 0.44, 0.22, and 0.11 to the total RMS of the streamwise and radial velocity on the centerline in (a) and on the lipline in (b) and (c), respectively. The total RMS is shown on the left ordinate whereas the RMS of five frequencies and their sum (denoted by a red line) are shown on the right ordinate. For the streamwise velocity on the centerline in (a), the curve corresponding to the sum of the five frequencies, though lower in magnitude, has a similar shape to that of the total RMS, which indicates that these five frequencies are sufficient to capture the trend of streamwise velocity on the centerline. The RMS of the frequency, $St = 0.44$, peaks at the same location as that of the hump at $x \approx 2.8$. The subharmonic of this frequency, $St = 0.22$, peaks at the location of the global

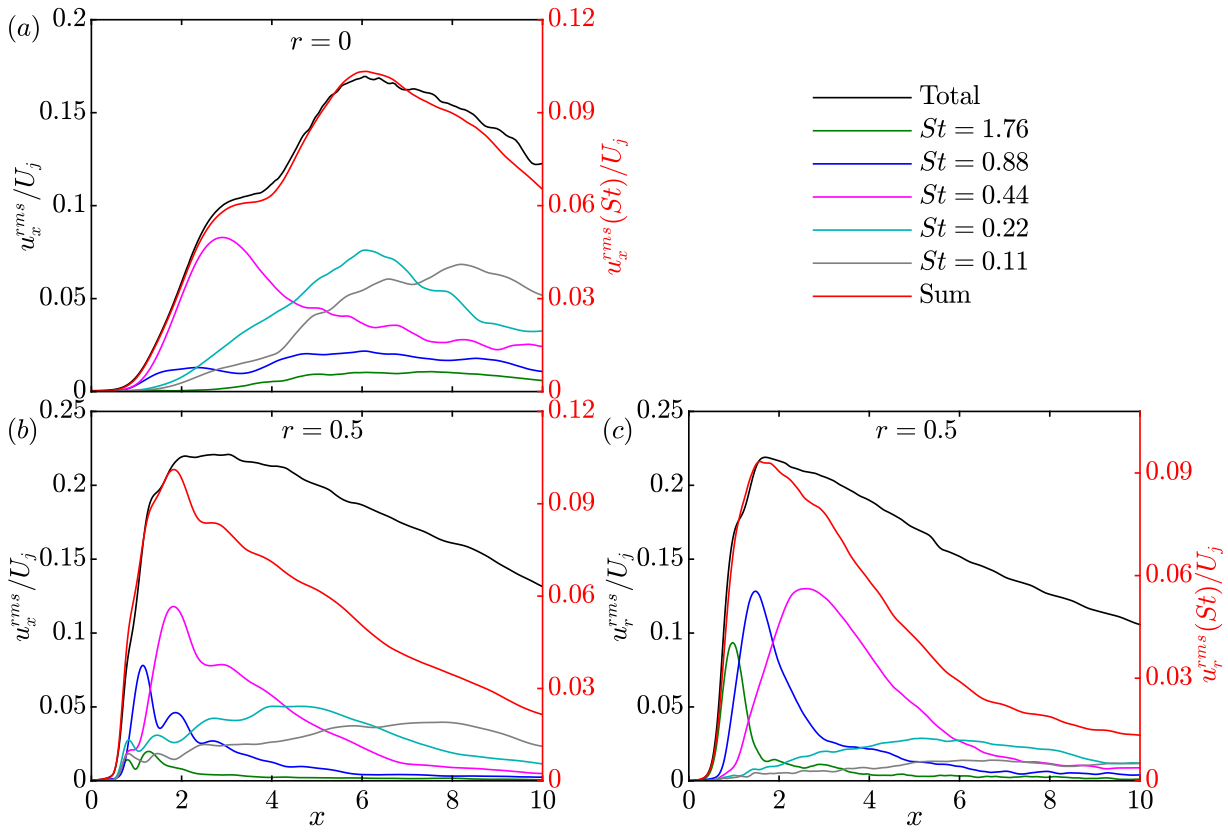

Figure 6.3.4: Development of the RMS velocities of total and individual frequencies along x: (a) u_x^{rms} on the centerline, $r = 0$; (b) u_x^{rms} on the lipline, $r = 0.5$;(c) u_r^{rms} on the lipline, $r = 0.5$. The total RMS (black curve) is plotted on the left ordinate and the remaining curves are plotted on the right ordinate.

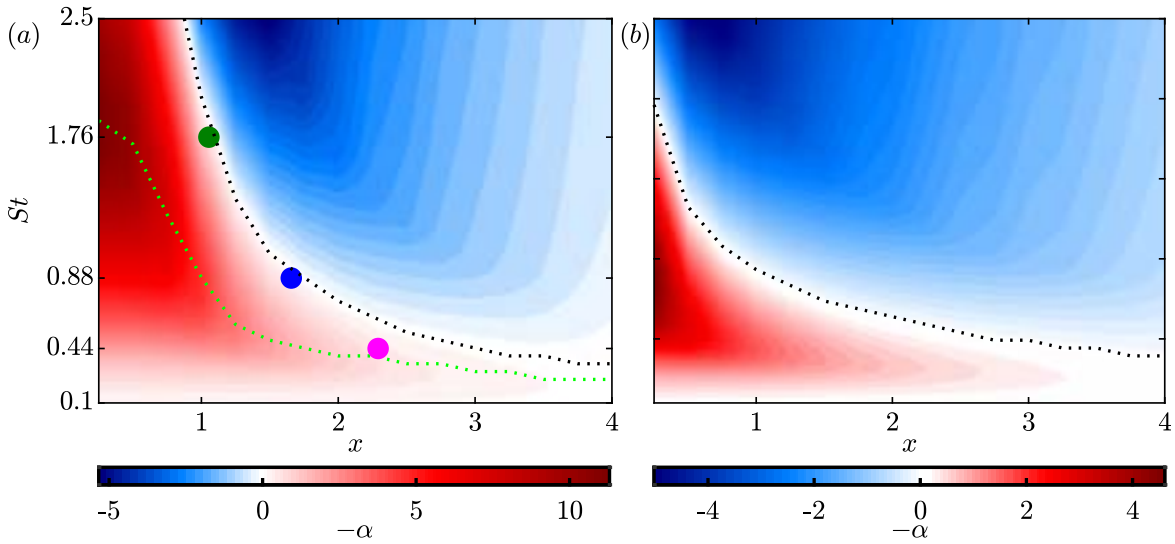

Figure 6.3.5: Most unstable eigenvalue obtained from local stability theory at various streamwise locations: (*a*) initially-laminar jet; (*b*) turbulent jet.

maximum of $x \approx 6$. The frequency $St = 0.11$ reaches its maximum further downstream at $x \approx 8$.

Along the lipline the total RMS of the streamwise and radial velocity exhibit a global maximum at $x \approx 1.8$. In both the velocity components $St = 0.44$ achieves the largest value of RMS among these five frequencies. In the radial velocity component, initially, $St = 1.76$ grows rapidly achieves its global maximum, and then decays. As $St = 1.76$ starts to decay, its subharmonic frequency $St = 0.88$, grows rapidly and overtakes $St = 1.76$. Similarly, the same trend is present for $St = 0.44$ which overtakes $St = 0.88$. In the streamwise velocity component, $St = 0.88$ is the first frequency that grows, saturates, and decays followed by $St = 0.44$. Note that, for u_x the $St = 1.76$ is not significant as previously observed in figure 6.3.3. These observations indicate that along the lipline, the subharmonic frequencies begin to grow as their harmonic frequencies start to decay. Our findings are in agreement with the findings of Hajj et al. (1992) and Shaabani-Ardali et al. (2019). These studies show that the simultaneous decay of the fundamental and growth of the subharmonic is due to the energy transfer from the fundamental to the subharmonic through a parametric resonance mechanism (Hajj et al., 1992, Monkewitz, 1988).

Next, we perform local linear stability analysis at different streamwise locations to

identify the fundamental frequency. Figure 6.3.5 shows the most unstable eigenvalues at different streamwise locations for the initially-laminar and turbulent jets. For both jets, the most unstable eigenvalues occur near the nozzle exit. For the initially-laminar jet, the frequency corresponding to the most unstable eigenvalue is $St \approx 1.76$, whereas it is $St \approx 0.81$ for the turbulent jet. This suggests that the spatially most unstable frequency is $St \approx 1.76$ for the initially-laminar jet, which occurs at the most upstream location. Therefore, we will identify this frequency as the fundamental frequency in the initially-laminar jet.

The green-dotted line represents the frequency corresponding to the most unstable eigenvalue, while the black-dotted line denotes the frequency corresponding to the neutrally stable eigenvalue. Additionally, the streamwise locations corresponding to the maximum PSD of the frequencies $St = 1.76$, 0.88, and 0.44 are shown, and they lie close to the neutrally stable curve. This suggests that the frequency is spatially most unstable at a more upstream position but attains its maximum amplitude more downstream. At this location, the wave is neutrally stable and starts to decay. The fundamental distinction between local stability theory and maximum PSD is that the former pinpoints the location where the frequency initially starts to grow spatially, while the latter reveals the location where the frequency attains its highest global amplitude.

The leading SPOD modes associated with $St = 1.76, 0.88, 0.44, 0.22$, and 0.11, are shown in figure 6.3.6. The modes exhibit structures in the shear-layer, which are shifted downstream at lower frequencies. For example, at $St = 1.76$ the structure is concentrated in the region $0.8 \leqslant x \leqslant 1.2$ around the lipline. At a lower frequency of $St = 0.44$, the leading SPOD mode has larger spatial support that peaks in $2 \leqslant x \leqslant 3$. Here, the streamwise velocity, u_x, is more concentrated on the centerline and the radial velocity, u_r on the lipline. Furthermore, the presence of this Kelvin-Helmhotlz-type wavepacket is directly correlated to the formation of hump in the RMS streamwise velocity on the centerline at $x \approx 3$. The structures of the modes at other frequencies are also associated with the peaks of the RMS velocities in figure 6.3.6. In the following, we will show that the process of vortex pairing leads to the formation of these

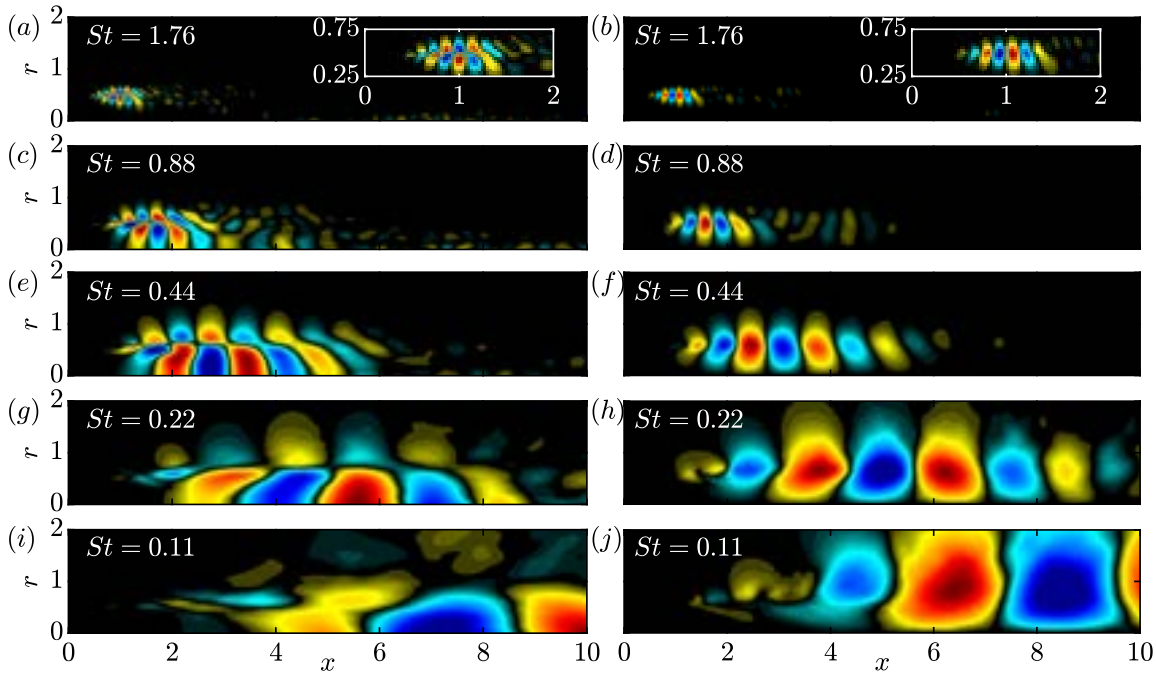

Figure 6.3.6: Leading SPOD modes at five representative frequencies: (*a*,*b*) $St = 1.76$;(*c*,*d*) $St = 0.88$; (*e*,*f*) $St = 0.44$; (*g*,*h*) $St = 0.22$; (*i*, *j*) $St = 0.11$. The left column represents the streamwise velocity component, u_x and the right column represents the radial velocity, u_r.

structures.

6.3.2 Vortex-pairing

The vortex pairing process is illustrated in figure 6.3.7, which shows eight different time instances of the vorticity ω_θ for the axisymmetric component $m = 0$. The first snapshot shows two vortices that form due to the roll-up of the shear layer. The roll-up and vortices are denoted by four red rectangles. These vortices are associated with a frequency of $St = 1.76$. The next three snapshots demonstrate the pairing of these vortices in the region between $1.2 \leqslant x \leqslant 2.1$. This proces is demonstrated using two blue rectangles in figure 6.3.7 (*b*-*d*). The first vortex pairing results in the formation of a vortex with a frequency of $St = 0.88$, which can also be observed in figure 6.3.7 (*c*-*e*). Then, the two $St = 0.88$ vortices, denoted by blue rectangles in (*e*), undergo pairing to form a vortex with a frequency of $St = 0.44$, as shown in figure 6.3.7 (*e*-*f*). During

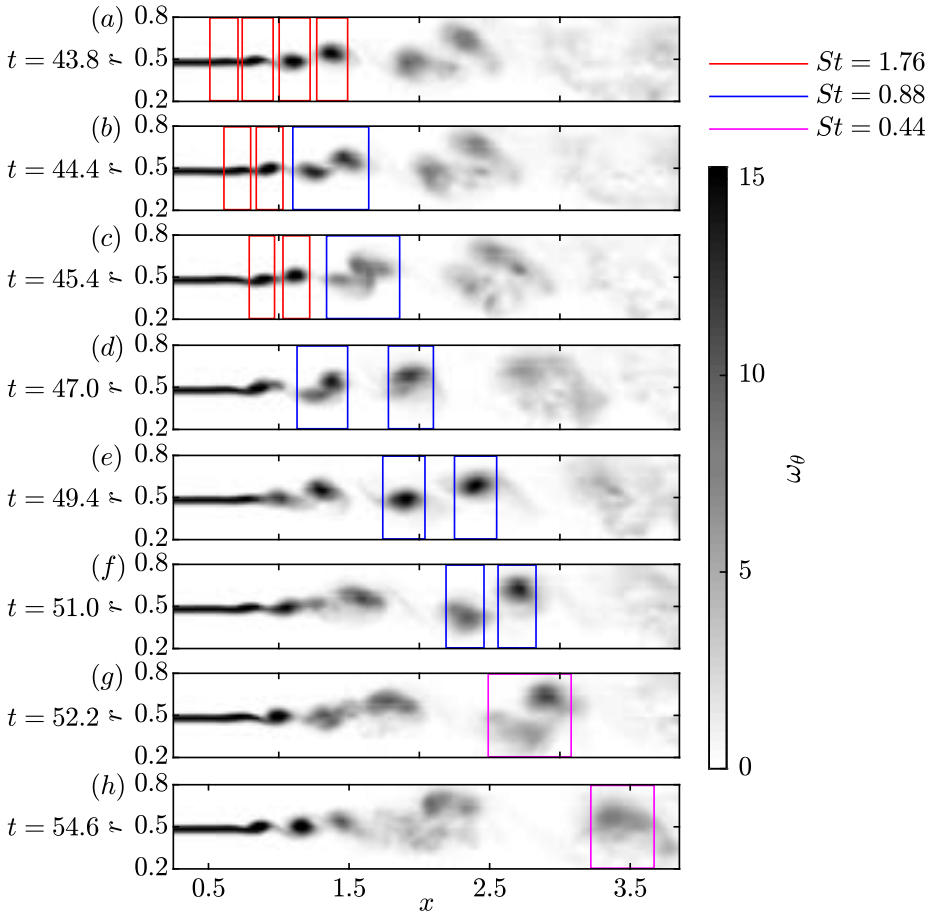

Figure 6.3.7: Visualization showing the pairing of vortices.

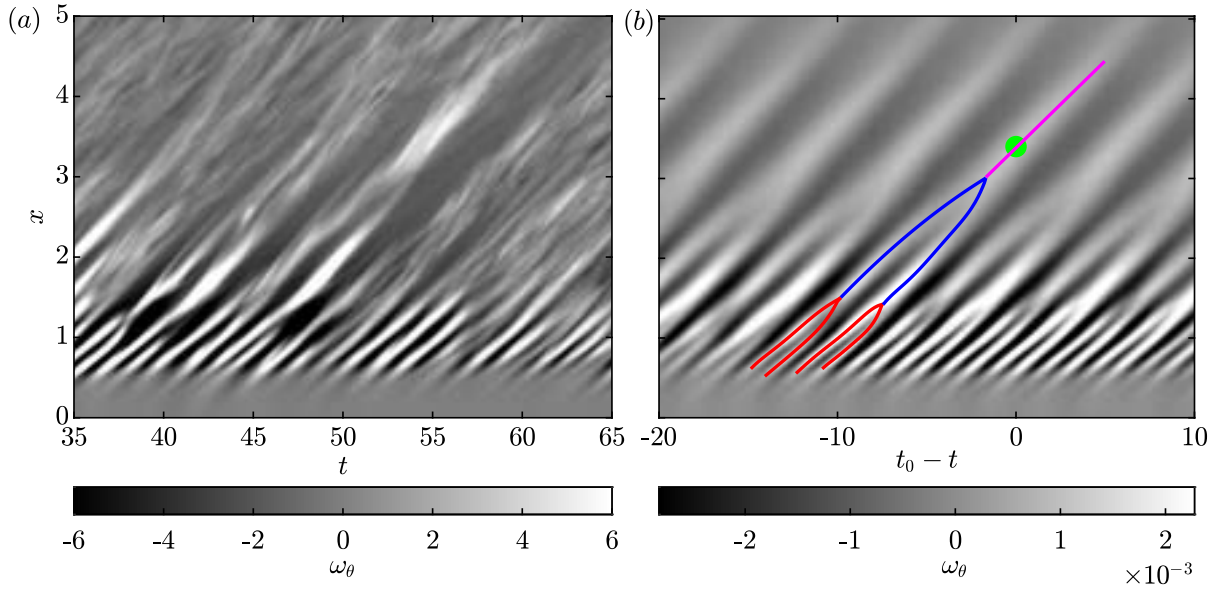

Figure 6.3.8: (*a*) *x*-*t* plots along the lipline showing the pairing of vortices. (*b*) The maximum frequency at the corresponding streamwise locations. The contour levels in (*a*) represent the vorticity fluctuations, ω'_θ.

this process, the vortex that is at a more upstream location accelerates and catches up with the decelerating downstream vortex. Eventually, they wrap around each other and form a single vortex at $x \approx 3.5$. The pairing of two vortices results in the formation of a larger vortex that is associated with half the frequency of the previous vortices. Our observations are in agreement with previous works by Zaman and Hussain (1980) and Shaabani-Ardali et al. (2019).

The vortex pairing is investigated in terms of the $x-t$ plots in figure 6.3.8. Figure 6.3.8(*a*) shows the vorticity fluctuations, ω'_θ, of the $m = 0$ component along the lipline in the time interval $35 \leqslant t \leqslant 65$. This interval encompasses the time instances shown in figure 6.3.7. Diagonal lines with slopes greater than zero represent the convective nature of the vortices, and these lines unite downstream to form a single line. For example, the vortex pairing process shown in figure 6.3.7 can be observed in the range $40 \leqslant t \leqslant 55$, $0.5 \leqslant x \leqslant 3.5$. The false color in white at $x \approx 3.5$, $t \approx 55$ corresponds to the $St = 0.44$ vortex. Note, however, that this is a single event of the vortex pairing. The objective here is to obtain a statistical representation of this event. To achieve this, we perform the following steps:

1. Reconstruct the flow field using the leading SPOD modes associated with the frequencies $St = 0.44, 0.88, 1.76$.

2. Select the point $x = 3.5, r = 0.5$ in the reconstructed field.

3. Identify the local maxima in the time series of this point as t_0, which is representative of the vortex pairing event.

4. Obtain the realization of each vortex-pairing event as $t \in [t_0^i - 20, t_0^i + 10]$, where i is the i-th local maxima at the chosen point

5. Average over all the realizations.

The $x-t$ plots along the lipline obtained from the aforementioned conditionally averaging is shown in figure 6.3.8(b). The first and second vortex-pairing events at $x \approx 1.5$ and $x \approx 3$, respectively, are evident here. We use polynomial curve fitting to illustrate this process. As in Figure 6.3.7, the red, blue, and magenta lines correspond to the frequencies of $St = 1.76$, 0.88, and 0.44, respectively.

6.4 Spectral Energy Budget

We investigate the spectral energy balance of kinetic energy. The motivation behind this analysis is to identify the nonlinear energy transfer between different frequencies and the net production of TKE associated with certain frequencies during the vortex pairing process. In the following, we will revisit the derivation of the spectral-TKE equation and then tailor it to compute the individual terms based on the leading SPOD modes. The readers are referred to refer to the work of Towne et al. (Reference Towne, Schmidt and Colonius2018) for a details of the derivation

We start by writing the Reynolds averaged Navier-Stokes equations for the turbulent fluctuations,

$$\frac{\partial u'_j}{\partial t} + \bar{u}_i \frac{\partial u'_j}{\partial x_i} + u'_i \frac{\partial u'_j}{\partial x_i} = -u'_i \frac{\partial \bar{u}_j}{\partial x_i} + \frac{\partial}{\partial x_i} \overline{u'_i u'_j} - \frac{\partial p'}{\partial x_j} + \frac{2}{Re} \frac{\partial s'_{ij}}{\partial x_i}, \tag{6.4}$$

where $s'_{ij} = 1/2\left(\partial u'_i/\partial x_j + \partial u'_j/\partial x_i\right)$ is the strain rate.

The next step is to compute the FFT of the equation (6.4) in time and azimuthal direction such that, $u'(x,r,\theta,t) = \sum_{\omega}\sum_{m} \hat{u}(x,r)e^{i(m\theta - 2\pi f t)}$ and then left multiply it with $\hat{u}^*_j(m,f)$,

$$\hat{u}^*_j(m,\omega)\left[\frac{\partial \hat{u}_j}{\partial t} + \bar{u}_i \frac{\partial \hat{u}_j}{\partial x_i} + \widehat{u_i \frac{\partial u_j}{\partial x_i}} = -\hat{u}_i \frac{\partial \bar{u}_j}{\partial x_i} - \frac{\partial \hat{p}}{\partial x_j} + \frac{2}{Re}\frac{\partial \hat{s}_{ij}}{\partial x_i}\right]_{m,f}. \tag{6.5}$$

Using continuity and taking the temporal mean, we get the following equation at an azimuthal wavenumber of m and frequency f:

$$\frac{\partial \hat{K}}{\partial t} = \mathcal{R}\left[-\bar{u}_i \frac{\partial \hat{K}}{\partial x_i} - \overline{\hat{u}^*_j \widehat{u_i \frac{\partial u_j}{\partial x_i}}} - \overline{\hat{u}^*_j \hat{u}_i \frac{\partial \bar{u}_j}{\partial x_i}} - \frac{2}{Re}\overline{\hat{s}^*_{ij}\hat{s}_{ij}} - \frac{\partial}{\partial x_j}\left(\overline{\hat{u}^*_j \hat{p}}\right) + \frac{2}{Re}\frac{\partial}{\partial x_i}\left(\overline{\hat{u}^*_j \hat{s}_{ij}}\right)\right], \tag{6.6}$$

where $\mathcal{R}$ denotes the real part and $\hat{K}(m,f) = \overline{\hat{u}^*_i(m,f)\hat{u}_i(m,f)}/2$. For statistical stationary flows, the left-hand side goes to zero. The most important terms for the current study are the nonlinear transfer term and the production, the second and third terms on the right-hand side, respectively.

The scale-specific production term is

$$\mathcal{P}(m,f) = -\mathcal{R}\left[\overline{\hat{u}^*_j(m,f)\hat{u}_i(m,f)\frac{\partial \bar{u}_j}{\partial x_i}}\right] \tag{6.7}$$

The scale-specific nonlinear transfer is

$$\mathcal{T}_{nl}(m,f) = -\mathcal{R}\left[\overline{\hat{u}^*_j(f,m)\widehat{u_i \frac{\partial u_j}{\partial x_i}}(f,m)}\right] \tag{6.8}$$

This term represents the total nonlinear transfer interactions that generate the frequency f and

wavenumber m. To identify the energy transfer of individual triads, i.e. $m_1 + m_2 = m_3$ and $f_1 + f_2 = f_3$, following Cho et al. (2018), this term is written in the discretized convolution:

$$\mathcal{T}_{nl}(m_3, f_3) = -\mathcal{R}\left[\overline{\hat{u}_j^*(m_3, f_3) \sum_{\substack{f_1+f_2=f_3 \\ m_1+m_2=m_3}} \hat{u}_i(m_1, f_1) \frac{\partial \hat{u}_j}{\partial x_i}(m_2, f_2)}\right] \tag{6.9}$$

For a single triad $[m_1, m_2, m_3]$, (f_1, f_2, f_3) this is expanded as follows:

$$\mathcal{T}_{nl}[(m_1, m_2, m_3), (f_1, f_2, f_3)] = -\mathcal{R}\left[\overline{\hat{u}_j^*(m_3, f_3)\hat{u}_i(m_1, f_1)\frac{\partial \hat{u}_j}{\partial x_i}(m_2, f_2)}\right] \tag{6.10}$$

The velocity field can be expanded in terms of the SPOD modal basis as

$$\mathbf{u}(f,t) \approx \sum_i a^{(i)}(f,t)\phi^{(i)}(x,f),. \tag{6.11}$$

where, a is the time-continuous expansion coefficients, obtained using the convolution approach described in §. We focus on kinetic energy production and nonlinear transfer of the most energetic structures so the modal basis is truncated after the leading mode at each frequency, i.e $i = 1$. Here, we are interested in the energy transfer only in the axisymmetic component, i.e., $m_1 = m_2 = m_3 = 0$, and we omit the azimuthal index with the understanding that the following equations are evaluated at $m = 0$,

$$\mathcal{T}_{nl}[(f_1, f_2, f_3)] = -\mathcal{R}\left(\overline{a^*(f_3)a(f_1)a(f_2)}\phi_j^*(f_3)\phi_i(f_1)\frac{\partial \phi_j}{\partial x_i}(f_2)\right), \tag{6.12}$$

$$\sum_{f_1+f_2=f_3} \mathcal{T}_{nl} = -\mathcal{R}\left(\sum_{f_1+f_2=f_3} \overline{a^*(f_3)a(f_1)a(f_2)}\phi_j^*(f_3)\phi_i(f_1)\frac{\partial \phi_j}{\partial x_i}(f_2)\right), \tag{6.13}$$

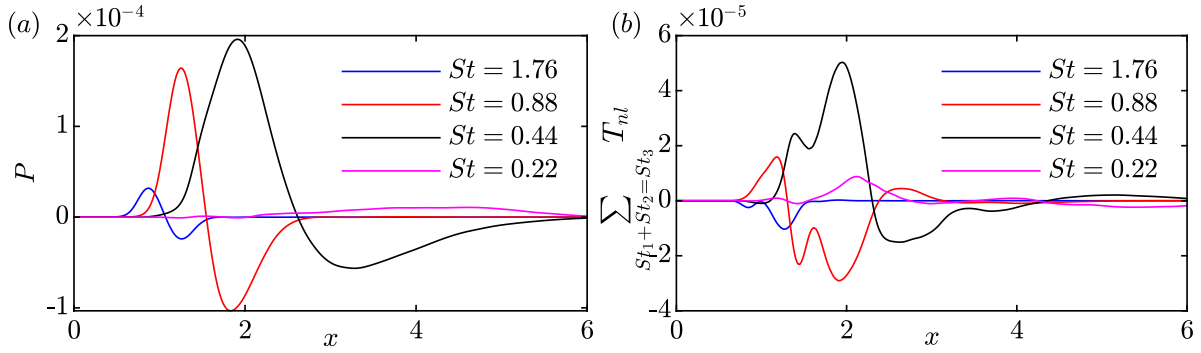

Figure 6.4.1: Production and nonlinear energy transfer terms for $St = 1.76, 0.88, 0.44$, and 0.22 integrated in r and as a function of streamwise locations.

$$\mathcal{P}(f_1) = -\overline{a^*(f_1)a(f_1)}\phi_j^*(f_1)\phi_i(f_1)\frac{\partial \bar{u}_j}{\partial x_i}, \tag{6.14}$$

$$\mathcal{P}(f_1) = -\lambda^{(1)}(f_1)\phi_j^*(f_1)\phi_i(f_1)\frac{\partial \bar{u}_j}{\partial x_i}. \tag{6.15}$$

Figure 6.4.1 shows the production and nonlinear energy transfer at frequencies $St = 1.76, 0.88$, 0.44, and 0.22. These terms are radially integrated and plotted as a function of the streamwise location. Positive production indicates energy gain from the mean flow, while negative production represents energy loss to the mean flow. Figure 6.4.1(a) shows that $St = 1.76$ is the earliest to gain energy from the mean flow and as it saturates, $St = 0.88$ begins to growth. Subsequently, $St = 0.88$ attains its global maximum at $x = 1.25$, which also corresponds to the location of global minimum of $St = 1.76$. Similarly, the global maximum of $St = 0.44$ and the global minimum $St = 0.88$ are in close proximity. The saturation of the subharmonic frequency has been related to the onset of vortex-pairing by Ho and Huang (1982) and was confirmed by Hajj et al. (1992, 1993). The production curves also suggest this and further reveal that at the beginning of vortex pairing the fundamental losses maximum energy to mean flow and the subharmonic gains its most energy from the mean flow. Another intersting observation is that the production of $St = 1.76, 0.88$, and 0.44 becomes negative at $x = 1.07$, 1.64 and 2.64, respectively, which correspond to the locations where the frequencies $St = 1.76, 0.88$, and 0.44 become neutrally stable.

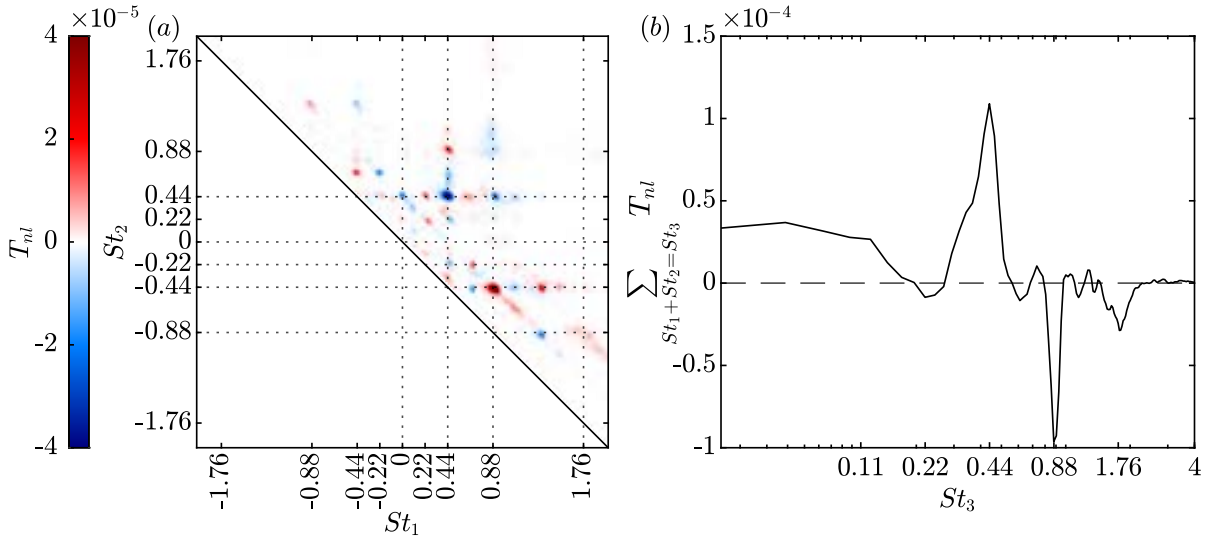

Figure 6.4.2: Spatial fields of production, dissipation, and nonlinear transfer terms integrated.

The net nonlinear energy transfer, computed using equation (6.13), is shown in Figure 6.4.1(b). The net nonlinear energy transfer is always $\mathcal{T}_{nl} \leqslant 0$ for $St = 1.76$. On the other hand, for $St = 0.88$ and 0.44, the energy is initially transferred into these frequencies, and as the flow evolves downstream, energy is extracted from these frequencies. The red and black curves in the region $1.3 \leqslant x \leqslant 2.3$ have a similar shape but are opposite in sign, which reveals that nonlinear interaction results in an energy loss for $St = 0.88$ and an energy gain for $St = 0.44$. This suggests the possibility of the energy being transferred from $St = 0.88$ to its subharmonic, $St = 0.44$. Later, in Figure 6.4.2, we will explore the energy transfer for each triadic interaction.

Figure 6.4.2 shows the energy transfer for each triadic interaction. The energy transfer for each triad is computed by integrating $T_{nl}[f_1, f_2, f_3]$, equation (6.12), over the spatial domain of interest. In figure 6.4.2(a), positive values (red color) denote the energy transfer to the frequency St_3 from frequencies St_1 and St_2, whereas negative values (blue color) indicate the extraction of energy from St_3 to St_1 and St_2. The two triads with the highest intensity are (0.88,-0.44,0.44) and (0.44,0.44,0.88). These triads exhibit positive and negative energy transfer, respectively. However, both triads convey the same information. The triad (0.88,-0.44,0.44) has a T_{nl} value greater than zero, indicating that energy is transferred from $St = 0.88$, and -0.44 to $St = 0.44$.

On the other hand, $T_{nl} < 0$ for the triad (0.44,0.44,0.88), which indicates that $St = 0.44$ extracts energy from $St = 0.88$. Additionally, even though the triads (1.76,-0.88,0.88) and (0.88,0.88,1.76) have lower amplitudes, they exhibit similar energy transfer behavior. These two triads reveal that energy is transferred from 1.76 to 0.88. These findings, in combination with observations from Figures 6.3.5, 6.3.7, and 6.3.8, suggest that during the vortex pairing process, energy is initially transferred from the fundamental ($St = 1.76$) to its first subharmonic ($St = 0.88$), and then from the first subharmonic to the second subharmonic ($St = 0.44$). Our results support the hypothesis of a parametric resonance mechanism proposed by Monkewitz (1988).

Figure 6.4.2(b) shows the net nonlinear energy transfer, obtained from equation (6.13) . At $St = 1.76$, and 0.88 the net nonlinear energy transfer is negative, whereas for $St = 0.44$ it is positive. This is not surprising as $T_{nl} < 0$ for the triads (0.44,0.44,0.88) and (0.88,0.88,1.76), which are the most significant contributors along $St_3 = 0.88$, and 1.76, respectively. Overall, the nonlinear interactions interaction results in an energy influx for $St = 0.44$ and an energy outflux at $St = 0.88$, and 1.76. This suggests that the second vortex-pairing event, occurring between the first and second subharmonic, is stronger than the first vortex-pairing event, occurring between the fundamental and the first subharmonic.

6.5 BMD analysis

Next, we perform the BMD to identify the spatial structures associated with the triads and further, we will try to construct a cascade of triads.

The mode bispectrum is shown in figure 6.5.1. The high-intensity regions (false red color) in the mode bispectra signify the dominant triads that arise from the interactions of two frequencies. Different combinations of frequencies (St_1,St_2) interact to generate the same frequency ($St_1 + St_2$ = constant) along the diagonals of slope -1 in the mode bispectrum. All the significant triads occur in the frequency range $0 \leqslant St_1 \leqslant 2$, $-1 \leqslant St_2 \leqslant 1$. The insert in figure

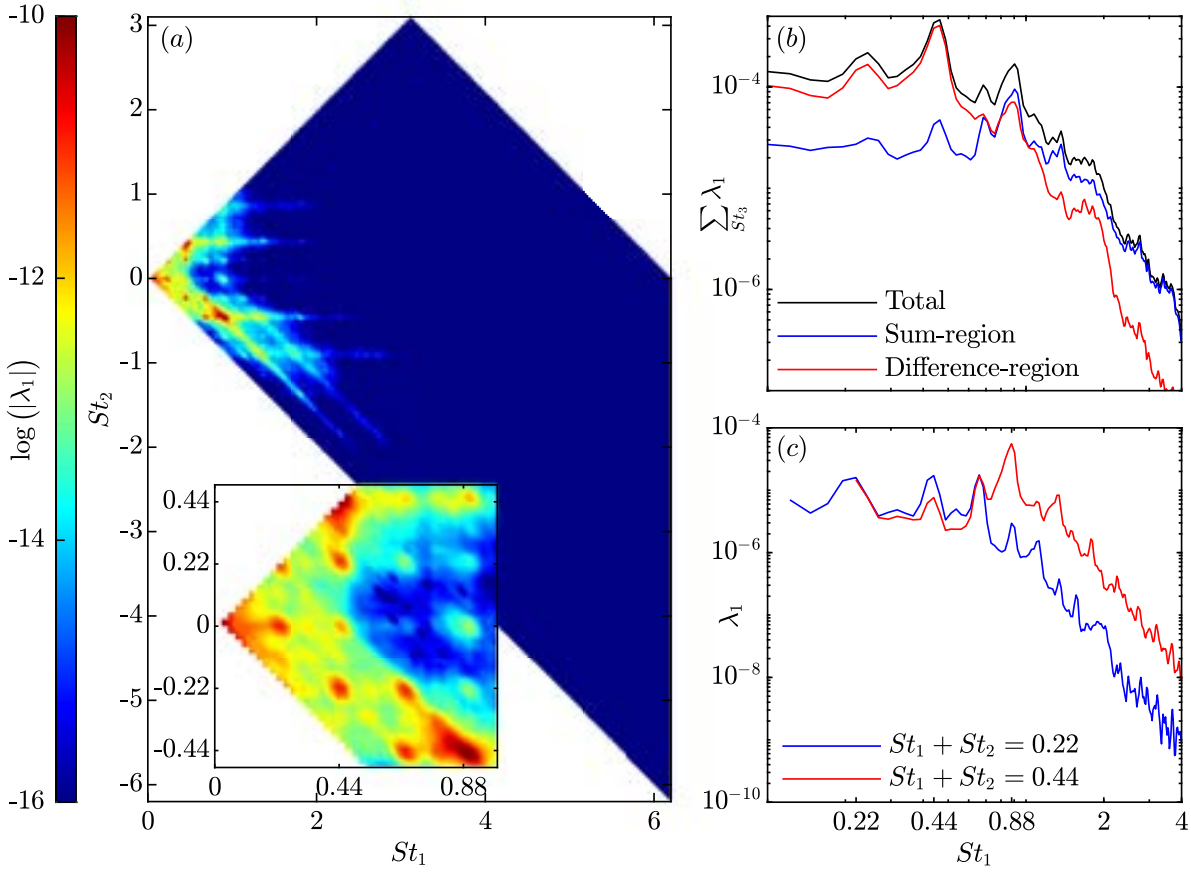

Figure 6.5.1: The mode bispectra of the laminar jet is shown in (*a*). The summed (along diagonals) mode bispectra: (*a*) unforced turbulent; (*b*) forced turbulent jet; (*c*) unforced initially-laminar; (*d*) forced initially-laminar. The inset shows a zoomed-in visualization of the BMD spectra in the range $0 \leqslant St_1 \leqslant 1.0$, $-0.5 \leqslant St_2 \leqslant 0.5$.

6.5.1(a) shows a zoomed-in view of the mode spectra highlighting the most dominant triads. The two most dominant triads are (0.44,0.44,0.88) and (0.88,-0.44,0.44). The latter corresponds to one of the vortex pairing processes, where the energy scatters back from 0.88 to 0.44. Furthermore, local maxima at (0.44.-0.22,0.22), (0.22,0.22,0.44), (0.22,0.0,0.22), and (0.44,0.22,0.66) represent the other prominent triadic interactions.

Figure 6.5.1(b) shows the mode bispectrum summed along the diagonals of frequency, St_3. The summed mode bispectrum, denoted by the black line, exhibits peaks at frequencies $St = 0.22$, 0.44, 0.66, 0.88, 1.32, and 1.76, and the global maximum at $St = 0.44$. This implies that the triadic interactions that result in the frequency of $St_3 = 0.44$ are the most significant. Figure 6.5.1(b) also shows the summed mode bispectrum in the sum- and difference-regions, i.e., $St_1, St_2 > 0$ and $St_1 > 0, St_2 < 0$, denoted by blue and red lines, respectively. The contribution of the difference-region is greater than the sum-region for $St_3 \leqslant 0.78$ and vice-versa for $St_3 > 0.78$. This indicates that the lower frequencies are a result of destructive interference between higher frequencies ,and the higher frequencies are an outcome of the constructive interference between lower frequencies. This implies an inverse cascade at lower frequencies and a (regular) energy cascade at higher frequencies.

The mode bispectum along the diagonals, $St_3 = 0.22$, and 0.44 are shown in figure 6.5.1(c). The line curves illustrate the most dominant frequency triads along the respective diagonals. For example, along $St_3 = 0.44$, it is clear that the most dominant triad is at $St_1 = 0.88$ and $St_2 = -0.44$, which reemphasizes the presence of vortex pairing. Along $St_3 = 0.22$, we find that three triads are of almost equal importance, (St_1,St_2,St_3) = (0.22,0.0,0.22), (0.44,-0.22,0.22), and (0.66,-0.44,0.22). These triads respectively denote the interaction of $St = 0.22$ with the mean flow, harmonic-fundamental difference interaction of $St = 0.22$, ultra harmonic-harmonic difference interaction (the latter two are analogous to vortex pairing). This suggests that the $St = 0.22$ can be generated through the vortex-pairing mechanism or by a resonant growth due to interaction with the mean flow. Paschereit et al. (1995) demonstrate that most of the energy to a subharmonic

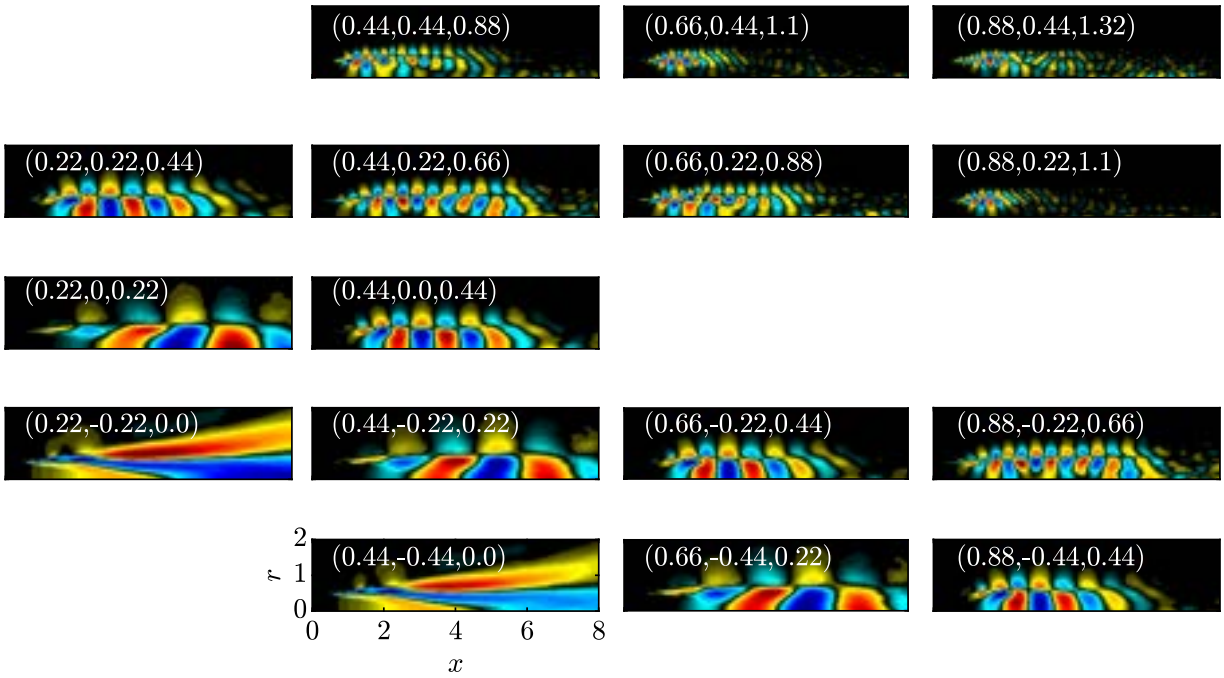

Figure 6.5.2: Bispectral modes forming a cascade of triads for the unforced initially-laminar jet, starting from the fundamental instability mode (St_1,St_2,St_3) = (0.44,0.0,0.44), middle-centre. The real part of the streamwise velocity component is shown.

comes directly from the mean flow.

The BMD modes of the triad cascade including the most significant interactions up to $St_1 \leqslant 0.88$ are visualized in figure 6.5.2. The cascade starts with the mode at the $St = 0.22$, $\phi_{0.22+0}$ (left column middle row). The modes associated with the sum interactions are shown in the first and second row, and those associated with the difference interactions are shown in the fourth and fifth row. The mode $\phi_{0.22+0}$ self-interacts to generate the $St = 0.44$, $\phi_{0.22+0.22}$. Next, the latter interacts with the former to create the $\phi_{0.44+0.22}$, and so on. In the negative St_2 plane, the destructive self interactions creates a mean flow distortion mode, $\phi_{0.22+-0.22}$, with $St_3 = 0$. Inspecting the modes reveals that sum-interactions create modes with high wavenumbers and difference-interactions create modes with lower streamwise wavenumbers. This behaviour is in agreement with the linear dispersion relation of these Kelvin-Helmholtz (KH) type instability waves.

Figure 6.5.3 shows the interaction maps and compares them with the spatial fields of

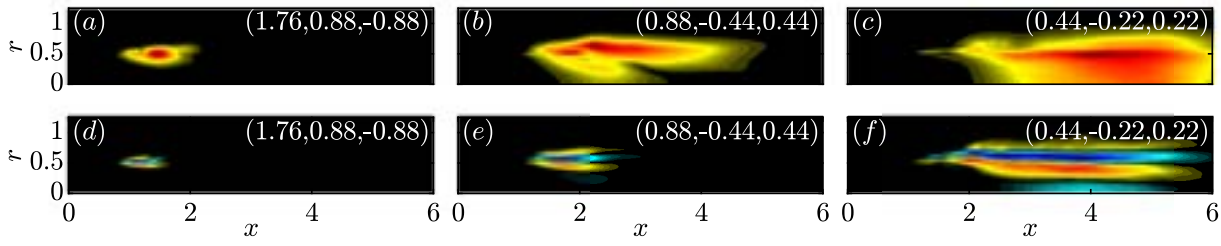

Figure 6.5.3: Interactive maps showing the spatial regions of nonlinear interactions of three triads corresponding to vortex pairing: (*a*) (1.76,-0.88,0.88); (*b*) (0.88,-0.44,0.44); (*c*) (0.44,-0.22,0.22).

the nonlinear transfer term. The interaction maps are obtained by taking the Hadamard product of the cross-frequency modes and the bispectral modes, i.e. $|\phi_{k\circ l} \circ \phi_{k+l}|$. The three triads that correspond to the vortex pairing, (1.76,-0.88,0.88), (0.88,-0.44,0.44), and (0.44,-0.22,0.22), are chosen. The figures demonstrate that the interaction maps obtained from the BMD can effectively highlight the precise regions of nonlinear interaction, which are also revealed by the spatial fields of the nonlinear transfer term. This indicates that the BMD can serve as a useful proxy for identifying the regions of nonlinear interactions.

6.6 Summary and concluding remarks

The large eddy simulation of an initially-laminar jet at $Re = 50,000$ is investigated and compared with a turbulent jet at the same Reynolds number. The difference between these two simulations is that the boundary layer is tripped for the turbulent jet, whereas it isn't for the initially-laminar jet. Compared to the turbulent jet, the initially-laminar jet develops later but at a faster rate, resulting in a shorter potential core length and a hump in the RMS velocity along the centerline. The centerline mean streamwise velocity also exhibits a dip at $x \approx 2$, and the turbulence intensity of the laminar jet is significantly higher than that of the turbulent jet for the first ten diameters. Similar observations have been reported in the works of Zaman and Hussain (1980) and Bogey and Bailly (2010). These are caused by the vortex-pairing in the shear layer,

which is significantly stronger for the untripped boundary layer.

This study aims to characterize the vortex-pairing and associated energy transfer. Two sets of vortex pairing occur during this process: (i) two vortices of $St = 1.76$ pair to form an $St = 0.88$ vortex, and (ii) two $St = 0.88$ vortices pair to form an $St = 0.44$ vortex. Using local stability theory, we identify the fundamental as the most unstable frequency, which is $St = 1.76$. We estimate different terms in the spectral-TKE equation using the leading modes of the spectral proper orthogonal decomposition, and two important terms are the non-linear transfer and the production. The non-linear transfer term reveals that energy is transferred from the fundamental to its subharmonic, resulting in the growth of the subharmonic. This transfer is caused by the most dominant triads of (St_1, St_2, St_3) = (1.76, -0.88, 0.88) and (0.88, -0.44, 0.44). Our results provide evidence for the hypothesis by Monkewitz (1988) that the energy transfer from the fundamental to the subharmonic is due to a parametric resonance mechanism. The production term in the spectral-TKE equation suggests that, at the start of the vortex pairing process, the fundamental loses maximum energy to mean flow, and the subharmonic gains its most energy from the mean flow. In addition to explaining the physics of energy transfer during vortex pairing, this study provides a framework for identifying the transfer of kinetic energy between the most energetic coherent structures at different scales.

Acknowledgments

This work has been supported by Office of Naval Research under grant N00014-20-1-2311 and National Science Foundation under grant CBET 2046311. This chapter is being prepared for publication titled: A. Nekkanti, and O. T. Schmidt, “Nonlinear energy transfer in vortex-pairing of initially-laminar jets”.

Chapter 7

Conclusions and Future work

Finally, we conclude by summarizing the contributions of this thesis and suggest potential future directions that can be explored.

7.1 Summary of contributions

In chapter 2 we extend SPOD for four different applications: low-rank reconstruction, denoising, prewhitening, and frequency-time analysis. Two approaches, frequency-domain, and time-domain, are proposed for low-rank reconstruction. The former conserves the orthogonality property and the frequency-mode correspondence of the SPOD modal basis, while the latter optimally reconstructs the instantaneous flow field using the least number of modes. These approaches are especially useful in reconstructing the flow field with the dominant dynamic and also have useful applications for low-order modeling. After establishing the advantages and disadvantages of these two approaches, we demonstrate SPOD-based denoising as an application of the frequency-domain approach. Significant noise reduction is achieved and at the same time, a substantial amount of energy of the original flow field is retained. Compared to a standard low-pass filter, SPOD-based denoising has the additional advantage of significant storage savings. Further, we develop a convolution strategy that computes time-continuous expansion coefficients

of the SPOD modes. Similar to the frequency-domain approach, this retains the orthogonality and mode-frequency correspondence of the SPOD. The spectrograms are able to identify the intermittent nature of the high-energy events. The occurrence of these events is directly linked to the presence of flow structures resembling the leading SPOD modes. The use of SPOD-based frequency–time analysis, provides additional physical insight by indicating time intervals during which a particular mechanism is active.

In chapter 3 we propose a gappy-SPOD algorithm to reconstruct the missing data in a flow field. The algorithm leverages the temporal correlation of SPOD modes with preceding and succeeding snapshots and their spatial correlation with the surrounding data to reconstruct partially missing or corrupted flow data. We demonstrate this method on simulation data of the flow around a cylinder and time-resolved PIV data of turbulent cavity flow. For randomly seeded and sized gaps that amount to up to 20% of missing data and extend over large regions in space and many snapshots, the algorithm accurately recovers the missing instantaneous and mean flow fields as well as turbulence statistics. It generally outperforms the established methods such as gappy-POD and Kriging. In particular, our method, gappy-SPOD, yields a significantly lower reconstruction error that translates to a two-fold reduction.

In chapter 4, we analyze three LES of turbulent jets in subsonic, transonic, and supersonic regimes. We identify the sources of the acoustic beams in different directions. In the downstream direction, the dominant radiations are super-directive. These emanate from the large-scale structures located at the end of the potential core, which are associated with lower frequencies ($St \leqslant 0.5$). We find that the radiation in the sideline and upstream directions also originates from the vicinity of the end of the potential core, and the sources of these beams are also large-scale coherent structures. Based on our results, we conclude that the upstream, sideline, and downstream radiation all originate from the same source.

In chapters 5 and 6, we perform large eddy simulations of six jets: two unforced and four forced jets. The unforced cases comprise an initially-laminar and a turbulent jet, with the former

referring to the case where the boundary layer inside the nozzle isn't tripped. All the forced jets are turbulent and forced at the azimuthal wavenumbers $m = 0$, $m = \pm 1$, $m = \pm 2$, and $m = \pm 6$. Chapter 5 investigates the nonlinear triadic interactions that are instigated due to the forcing. For a general $m = \pm m_f$-forcing, we observe that even harmonic frequencies are present in even multiples of m_f, and similarly, odd harmonic frequencies are present in odd multiples of m_f, i.e., $(2k+1)m_f$, for any integer k. Additionally, we found that difference-interactions are more efficient radiators of jet noise than sum-interactions. In chapter 6, we explored vortex-pairing, which is stronger in initially-laminar jets. Our emphasis was on the nonlinear energy transfer during this process. We approximated the spectral TKE equations using the leading SPOD modes to evaluate the production and nonlinear transfer terms. Our analysis revealed an inverse-energy cascade during the vortex-pairing process, where energy transfers from the fundamental to its first subharmonic and then from the first subharmonic to its second subharmonic.

7.2 Future work

7.2.1 Extension of the Modal techniques for turbulent flows

The application of SPOD-based reconstruction extends beyond denoising and frequency-time analysis. It is especially useful in reduced-order modeling, where the convolution expansion coefficients can be employed to construct a SPOD-based Koopman reduced-order model that is entirely data-driven and can provide valuable insights into different turbulent flows. By employing machine learning techniques such as LSTM, one can also propagate the expansion coefficients in time and obtain data over longer time series. Additionally, the convolution approach can provide time-continuous expansion coefficients of the coherent structures associated with turbulent flows. These coefficients can be used to compute the probability density function (PDF) of the structures and quantify their intermittency. Previous research, for example, Onorato et al. (2000), has computed PDF at specific locations and classified PDF with long tails as intermittent. However,

our approach enables the quantification of the intermittency of the entire spatial structure rather than just a single location.

Gappy SPOD has potential for future extensions, including customization of the algorithm to handle non-stationary data such as cyclo-stationary processes, and incorporation of trends for transient, non-stationary data. Improvements to the algorithm could also be made to fill in missing snapshots or data containing regions with missing data throughout the entire time series. One approach to this could involve using gappy-SPOD to fill in partially missing regions, followed by Kriging all the SPOD modes to fill in the missing regions in the modes. Finally, the Kriged-SPOD modes could be used with the expansion coefficients to fill in all the missing regions. A potentially relevant application for gappy-SPOD is optimal sensor placement for oceanic measurements.

7.2.2 Physical phenomenon in turbulent jets

Our findings suggest that the downstream and upstream acoustic beams originate from the same source, and this could be verified at farther radial distances, around $r \approx 50$, instead of the limited radial distance of $r = 6$ that we investigated. To achieve this, we propose the use of the Ffowcs-Williams Hawkings equations (Brès et al., 2017, Ffowcs Williams and Hawkings, 1969) to extend the current domain. Furthermore, investigating the source mechanism that generates sound in different directions is important. A possible source mechanism is coherence decay (Cavalieri and Agarwal, 2014), In particular, we propose a scenario in which the distortion of a coherent KH wavepacket gives rise to multi-directive burst events. Future SPOD-based jet noise models may further benefit from the observation that both the dominant downstream and sideline radiation patterns are part of a single SPOD basis.

There are a few potential avenues for future research based on the findings of the study. One direction is to investigate the mean flow distortion resulting from forcing the jet at different azimuthal wavenumbers. Another possible direction is to characterize the effect of the forcing on the far-field noise. It has been hypothesized by Wu and Huerre (2009) that the interaction of a

helical conjugate pair with $m = \pm 1$ generates a slowly modulating mean-flow distortion, which radiates low-frequency sound to jet angles between 45°-60°. Therefore, it could be beneficial to investigate this hypothesis and its potential implications for jet noise. Moreover, it would be valuable to understand the cascade of triads from a causality perspective, potentially using information theory metrics such as Shannon entropy. Lozano-Durán et al. (2020) have successfully employed Shannon entropy to identify causal interactions of energy-eddies in turbulent channel flows, and a similar approach may yield insights into the causal dynamics of triads in forced jets. Another long-term objective is to understand the direction of energy transfer during triadic interaction. Underpinning the direction of energy transfer during triadic interaction is another long-term objective.

In chapter 6, we characterized the vortex-pairing and energy transfer that occurs during this process. A future direction is to look into the nonlinear dynamics of this process. In particular, if the vortex-paring corresponds to a limit-cycle oscillator or chaotic attractor? Furthermore, our work lays out a framework for identifying nonlinear energy transfer, which can be used in different turbulent flows.

The techniques developed in this dissertation have the potential to be adapted for the analysis of different types of flows. For instance, in geophysical flows, they can be used to quantify the intermittency of submesoscales. Moreover, recent studies have provided evidence of energy transfers between mesoscales and submesoscales, and their seasonal reversal, which can be analyzed using the energy transfer approximated through the BMD. Additionally, some coherent structures, such as streaks, are found in various turbulent flows, including wall-bounded flows, jets, and wakes (Nekkanti et al., 2023). Future research could investigate the effects of factors such as angle of attack (Ortiz-Tarin et al., 2021) and stratification (Ortiz-Tarin et al., 2023) on these structures. Comparing the characteristics of streaks in jets with those in channel flows and wakes could help to reveal potential universal behavior of these low-frequency structures.

Bibliography

Adrian, R. J. and Westerweel, J. (2011). Particle image velocimetry. Number 30. Cambridge University Press.

Alvera-Azcárate, A., Barth, A., Beckers, J.-M., and Weisberg, R. H. (2007). Multivariate reconstruction of missing data in sea surface temperature, chlorophyll, and wind satellite fields. Journal of Geophysical Research: Oceans, 112(C3).

Alvera-Azcárate, A., Barth, A., Rixen, M., and Beckers, J.-M. (2005). Reconstruction of incomplete oceanographic data sets using empirical orthogonal functions: application to the Adriatic sea surface temperature. Ocean Modelling, 9(4):325–346.

Arndt, R. E. A., Long, D. F., and Glauser, M. N. (1997). The proper orthogonal decomposition of pressure fluctuations surrounding a turbulent jet. Journal of Fluid Mechanics, 340:1–33.

Aubry, N. (1991). On the hidden beauty of the proper orthogonal decomposition. Theoretical and Computational Fluid Dynamics, 2(5-6):339–352.

Aubry, N., Holmes, P., Lumley, J. L., and Stone, E. (1988). The dynamics of coherent structures in the wall region of a turbulent boundary layer. Journal of Fluid Mechanics, 192:115–173.

Bale, S. D., Kellogg, P. J., Mozer, F. S., Horbury, T. S., and Reme, H. (2005). Measurement of the electric fluctuation spectrum of magnetohydrodynamic turbulence. Physical Review Letters, 94(21):215002.

Beaudoin, J. F. and Aider, J. L. (2008). Drag and lift reduction of a 3D bluff body using flaps. Experiments in Fluids, 44(4):491–501.

Becker, H. A. and Massaro, T. A. (1968). Vortex evolution in a round jet. Journal of Fluid Mechanics, 31(3):435–448.

Beckers, J.-M., Barth, A., and Alvera-Azcárate, A. (2006). DINEOF reconstruction of clouded images including error maps? application to the sea-surface temperature around Corsican island.

Beckers, J.-M. and Rixen, M. (2003). EOF calculations and data filling from incomplete oceanographic datasets. Journal of Atmospheric and oceanic technology, 20(12):1839–1856.

Benner, P., Gugercin, S., and Willcox, K. (2015). A survey of projection-based model reduction methods for parametric dynamical systems. SIAM Review, 57(4):483–531.

Bishop, K. A., Williams, J. E. F., and Smith, W. (1971). On the noise sources of the unsuppressed high-speed jet. Journal of Fluid Mechanics, 50(1):21–31.

Boashash, B. (1988). Note on the use of the Wigner distribution for time-frequency signal analysis. IEEE Transactions on Acoustics, Speech, and Signal Processing, 36(9):1518–1521.

Bodart, J. and Larsson, J. (2012). Wall-modeling in large eddy simulation: length scales, grid resolution, and accuracy. Annual research briefs, pages 229–240.

Bogey, C. and Bailly, C. (2007). An analysis of the correlations between the turbulent flow and the sound pressure fields of subsonic jets. Journal of Fluid Mechanics, 583:71–97.

Bogey, C. and Bailly, C. (2010). Influence of nozzle-exit boundary-layer conditions on the flow and acoustic fields of initially laminar jets. Journal of Fluid Mechanics, 663:507–538.

Bogey, C., Barré, S., Fleury, V., Bailly, C., and Juvé, D. (2007). Experimental study of the spectral properties of near-field and far-field jet noise. International Journal of Aeroacoustics, 6(2):73–92.

Bogey, C., Marsden, O., and Bailly, C. (2012). Influence of initial turbulence level on the flow and sound fields of a subsonic jet at a diameter-based reynolds number of 105. Journal of Fluid Mechanics, 701:352–385.

Bowes, W., Rumpf, D., Bowler, D., Carnes, R., Fratarangelo, P., Heiser, W., Hu, D., Moin, P., and Voorhees, W. (2009). Report on jet engine noise reduction. Tech. Rep.

Brès, G. A., Ham, F. E., Nichols, J. W., and Lele, S. K. (2017). Unstructured large-eddy simulations of supersonic jets. AIAA Journal, pages 1164–1184.

Brès, G. A., Jordan, P., Jaunet, V., Le Rallic, M., Cavalieri, A. V. G., Towne, A., Lele, S. K., Colonius, T., and Schmidt, O. T. (2018). Importance of the nozzle-exit boundary-layer state in subsonic turbulent jets. Journal of Fluid Mechanics, 851:83–124.

Brès, G. A. and Lele, S. K. (2019). Modelling of jet noise: a perspective from large-eddy simulations. Philosophical Transactions of the Royal Society A, 377(2159):20190081.

Bridges, J. and Hussain, A. (1987). Roles of initial condition and vortex pairing in jet noise. Journal of Sound and Vibration, 117(2):289–311.

Brindise, M. C., Chiastra, C., Burzotta, F., Migliavacca, F., and Vlachos, P. P. (2017). Hemodynamics of stent implantation procedures in coronary bifurcations: An in vitro study. Annals of biomedical engineering, 45(3):542–553.

Brindise, M. C. and Vlachos, P. P. (2017). Proper orthogonal decomposition truncation method for data denoising and order reduction. Experiments in Fluids, 58(4):28.

Brown, E. D., Buchsbaum, S. B., Hall, R. E., Penhune, J. P., Schmitt, K. F., Watson, K. M., and Wyatt, D. C. (1989). Observations of a nonlinear solitary wave packet in the kelvin wake of a ship. Journal of Fluid Mechanics, 204:263–293.

Brown, G. L. and Roshko, A. (1974). On density effects and large structure in turbulent mixing layers. Journal of Fluid Mechanics, 64(4):775–816.

Broze, G. and Hussain, F. (1994). Nonlinear dynamics of forced transitional jets: periodic and chaotic attractors. Journal of Fluid Mechanics, 263:93–132.

Bui-Thanh, T., Damodaran, M., and Willcox, K. E. (2004). Aerodynamic data reconstruction and inverse design using proper orthogonal decomposition. AIAA Journal, 42(8):1505–1516.

Camussi, R. (2002). Coherent structure identification from wavelet analysis of particle image velocimetry data. Experiments in Fluids, 32(1):76–86.

Camussi, R. and Guj, G. (1997). Orthonormal wavelet decomposition of turbulent flows: intermittency and coherent structures. Journal of Fluid Mechanics, 348:177–199.

Cavalieri, A. V. G. and Agarwal, A. (2014). Coherence decay and its impact on sound radiation by wavepackets. Journal of Fluid Mechanics, 748:399–415.

Cavalieri, A. V. G., Jordan, P., Agarwal, A., and Gervais, Y. (2011). Jittering wave-packet models for subsonic jet noise. Journal of Sound and Vibration, 330(18-19):4474–4492.

Cavalieri, A. V. G., Jordan, P., Colonius, T., and Gervais, Y. (2012). Axisymmetric superdirectivity in subsonic jets. Journal of Fluid Mechanics, 704:388–420.

Cavalieri, A. V. G., Rodríguez, D., Jordan, P., Colonius, T., and Gervais, Y. (2013). Wavepackets in the velocity field of turbulent jets. Journal of Fluid Mechanics, 730:559–592.

Charonko, J., Karri, S., Schmieg, J., Prabhu, S., and Vlachos, P. (2010). In vitro comparison of the effect of stent configuration on wall shear stress using time-resolved particle image velocimetry. Annals of biomedical engineering, 38(3):889–902.

Chaturantabut, S. and Sorensen, D. C. (2010). Nonlinear model reduction via discrete empirical interpolation. SIAM Journal on Scientific Computing, 32(5):2737–2764.

Cho, M., Hwang, Y., and Choi, H. (2018). Scale interactions and spectral energy transfer in turbulent channel flow. Journal of Fluid Mechanics, 854:474–504.

Chu, T. and Schmidt, O. T. (2021). A stochastic SPOD-Galerkin model for broadband turbulent flows. Theoretical and Computational Fluid Dynamics, 35(6):759–782.

Citriniti, J. H. and George, W. K. (2000). Reconstruction of the global velocity field in the axisymmetric mixing layer utilizing the proper orthogonal decomposition. Journal of Fluid Mechanics, 418:137–166.

Cohen, J. and Wygnanski, I. (1987). The evolution of instabilities in the axisymmetric jet. part 2. the flow resulting from the interaction between two waves. Journal of Fluid Mechanics, 176:221–235.

Cohen, L. (1995). Time-frequency analysis, volume 778. Prentice hall.

Conan, B., Anthoine, J., and Planquart, P. (2011). Experimental aerodynamic study of a car-type bluff body. Experiments in Fluids, 50(5):1273–1284.

Crighton, D. and Gaster, M. (1976). Stability of slowly diverging jet flow. Journal of Fluid Mechanics, 77(2):397–413.

Crighton, D. and Huerre, P. (1990). Shear-layer pressure fluctuations and superdirective acoustic sources. Journal of Fluid Mechanics, 220:355–368.

Crow, S. C. and Champagne, F. H. (1971). Orderly structure in jet turbulence. Journal of Fluid Mechanics, 48(3):547–591.

Dawson, S. T., Hemati, M. S., Williams, M. O., and Rowley, C. W. (2016). Characterizing and correcting for the effect of sensor noise in the dynamic mode decomposition. Experiments in Fluids, 57:1–19.

Delville, J. (1994). Characterization of the organization in shear layers via the proper orthogonal decomposition. Applied Scientific Research, 53(3):263–281.

Discetti, S., Natale, A., and Astarita, T. (2013). Spatial filtering improved tomographic piv. Experiments in Fluids, 54(4):1505.

Doron, P., Bertuccioli, L., Katz, J., and Osborn, T. R. (2001). Turbulence characteristics and dissipation estimates in the coastal ocean bottom boundary layer from PIV data. Journal of Physical Oceanography, 31(8):2108–2134.

Edgington-Mitchell, D. (2019). Aeroacoustic resonance and self-excitation in screeching and impinging supersonic jets–a review. International Journal of Aeroacoustics, 18(2-3):118–188.

Epps, B. P. and Krivitzky, E. M. (2019). Singular value decomposition of noisy data: mode corruption. Experiments in Fluids, 60(8):1–30.

Everson, R. and Sirovich, L. (1995). Karhunen–loeve procedure for gappy data. JOSA A, 12(8):1657–1664.

Farge, M. (1992). Wavelet transforms and their applications to turbulence. Annual Review of Fluid Mechanics, 24(1):395–458.

Farge, M., Pellegrino, G., and Schneider, K. (2001). Coherent vortex extraction in 3d turbulent flows using orthogonal wavelets. Physical Review Letters, 87(5):054501.

Farge, M., Schneider, K., and Kevlahan, N. (1999). Non-Gaussianity and coherent vortex simulation for two-dimensional turbulence using an adaptive orthogonal wavelet basis. Physics of Fluids, 11(8):2187–2201.

Ffowcs Williams, J. E. and Hawkings, D. L. (1969). Sound generation by turbulence and surfaces in arbitrary motion. Philosophical Transactions of the Royal Society of London. Series A, Mathematical and Physical Sciences, 264(1151):321–342.

Fore, L. B., Tung, A. T., Buchanan, J. R., and Welch, J. W. (2005). Nonlinear temporal filtering of time-resolved digital particle image velocimetry data. Experiments in Fluids, 39(1):22–31.

Freund, J. B. (2001). Noise sources in a low-reynolds-number turbulent jet at mach 0.9. Journal of Fluid Mechanics, 438:277–305.

Freund, J. B. and Colonius, T. (2009). Turbulence and sound-field pod analysis of a turbulent jet. International Journal of Aeroacoustics, 8(4):337–354.

Gamard, S., George, W. K., Jung, D., and Woodward, S. (2002). Application of a "slice" proper orthogonal decomposition to the far field of an axisymmetric turbulent jet. Physics of Fluids, 14(7):2515–2522.

Gamard, S., Jung, D., and George, W. K. (2004). Downstream evolution of the most energetic modes in a turbulent axisymmetric jet at high reynolds number. Part 2. the far-field region. Journal of Fluid Mechanics, 514:205–230.

Ghate, A. S., Towne, A., and Lele, S. K. (2020). Broadband reconstruction of inhomogeneous turbulence using spectral proper orthogonal decomposition and gabor modes. Journal of Fluid Mechanics, 888.

Glauser, M. N. and George, W. K. (1992). Application of multipoint measurements for flow characterization. Experimental Thermal and Fluid Science, 5(5):617–632.

Glauser, M. N., Leib, S. J., and George, W. K. (1987). Coherent structures in the axisymmetric turbulent jet mixing layer. In Turbulent Shear Flows 5, pages 134–145. Springer.

Goparaju, H. and Gaitonde, D. V. (2022). Role of entropic instabilities in laminar-turbulent transition on a blunted flat plate. Physical Review Fluids, 7(10):103901.

Gordeyev, S. V. and Thomas, F. O. (2000). Coherent structure in the turbulent planar jet. Part 1. extraction of proper orthogonal decomposition eigenmodes and their self-similarity. Journal of Fluid Mechanics, 414:145–194.

Gordeyev, S. V. and Thomas, F. O. (2002). Coherent structure in the turbulent planar jet. Part 2. structural topology via pod eigenmode projection. Journal of Fluid Mechanics, 460:349–380.

Goza, A. and Colonius, T. (2017). A strongly-coupled immersed-boundary formulation for thin elastic structures. Journal of Computational Physics, 336:401–411.

Gu, D. and Philander, S. G. H. (1995). Secular changes of annual and interannual variability in the tropics during the past century. Journal of Climate, 8(4):864–876.

Gudmundsson, K. and Colonius, T. (2011). Instability wave models for the near-field fluctuations of turbulent jets. Journal of Fluid Mechanics, 689:97–128.

Gunes, H. and Rist, U. (2007). Spatial resolution enhancement/smoothing of stereo–particle-image-velocimetry data using proper-orthogonal-decomposition–based and Kriging interpolation methods. Physics of Fluids, 19(6):064101.

Gunes, H., Sirisup, S., and Karniadakis, G. E. (2006). Gappy data: To Krig or not to Krig? Journal of Computational Physics, 212(1):358–382.

Hajj, M., Miksad, R., and Powers, E. (1992). Subharmonic growth by parametric resonance. Journal of Fluid Mechanics, 236:385–413.

Hajj, M. R., Miksad, R. W., and Powers, E. J. (1993). Fundamental–subharmonic interaction: effect of phase relation. Journal of Fluid Mechanics, 256:403–426.

Harris, F. J. (1978). On the use of windows for harmonic analysis with the discrete Fourier transform. Proceedings of the IEEE, 66(1):51–83.

Hart, D. P. (2000). PIV error correction. Experiments in Fluids, 29(1):13–22.

Heidt, L., Colonius, T., Nekkanti, A., Schmdit, O., Maia, I., and Jordan, P. (2021). Analysis of forced subsonic jets using spectral proper orthogonal decomposition and resolvent analysis. In AIAA Aviation 2021 Forum, page 2108. American Institute of Aeronautics and Astronautics.

Hellström, L. H. O., Ganapathisubramani, B., and Smits, A. J. (2015). The evolution of large-scale motions in turbulent pipe flow. Journal of Fluid Mechanics, 779:701–715.

Hellström, L. H. O., Marusic, I., and Smits, A. J. (2016). Self-similarity of the large-scale motions in turbulent pipe flow. Journal of Fluid Mechanics, 792.

Hellström, L. H. O. and Smits, A. J. (2014). The energetic motions in turbulent pipe flow. Physics of Fluids, 26(12):125102.

Hellström, L. H. O. and Smits, A. J. (2017). Structure identification in pipe flow using proper orthogonal decomposition. Philosophical Transactions of the Royal Society A: Mathematical, Physical and Engineering Sciences, 375(2089):20160086.

Ho, C. M. and Huang, L. S. (1982). Subharmonics and vortex merging in mixing layers. Journal of Fluid Mechanics, 119:443–473.

Holmes, P., Lumley, J. L., Berkooz, G., and Rowley, C. W. (2012). Turbulence, coherent structures, dynamical systems and symmetry. Cambridge University press.

Huang, H., Dabiri, D., and Gharib, M. (1997). On errors of digital particle image velocimetry. Measurement Science and Technology, 8(12):1427.

Huang, N. E., Shen, Z., Long, S. R., Wu, M. C., Shih, H. H., Zheng, Q., Yen, N. C., Tung, C. C., and Liu, H. H. (1998). The empirical mode decomposition and the hilbert spectrum for nonlinear and non-stationary time series analysis. Proceedings of the Royal Society of London. Series A: mathematical, physical and engineering sciences, 454(1971):903–995.

Husain, H. and Hussain, F. (1995). Experiments on subharmonic resonance in a shear layer. Journal of Fluid Mechanics, 304:343–372.

Hussain, A. K. M. F. and Zaman, K. B. M. Q. (1980). Vortex pairing in a circular jet under controlled excitation. Part 2. Coherent structure dynamics. Journal of Fluid Mechanics, 101(3):493–544.

Hussain, A. K. M. F. and Zaman, K. B. M. Q. (1981). The 'preferred mode'of the axisymmetric jet. Journal of Fluid Mechanics, 110:39–71.

Iqbal, M. O. and Thomas, F. O. (2007). Coherent structure in a turbulent jet via a vector implementation of the proper orthogonal decomposition. Journal of Fluid Mechanics, 571:281–326.

Izatt, J. A., Kulkarni, M. D., Yazdanfar, S., Barton, J. K., and Welch, A. J. (1997). In vivo bidirectional color doppler flow imaging of picoliter blood volumes using optical coherence tomography. Optics letters, 22(18):1439–1441.

Jeun, J. and Nichols, J. W. (2018a). Input-output analysis of mach 0.9 jet noise. arXiv preprint arXiv:1806.09280.

Jeun, J. and Nichols, J. W. (2018b). Non-compact sources of sound in high-speed turbulent jets using input-output analysis. In 2018 AIAA/CEAS Aeroacoustics Conference, page 3467. American Institute of Aeronautics and Astronautics.

Jeun, J., Nichols, J. W., and Jovanović, M. R. (2016). Input-output analysis of high-speed axisymmetric isothermal jet noise. Physics of Fluids, 28(4):047101.

Jiménez, J. (2018). Coherent structures in wall-bounded turbulence. Journal of Fluid Mechanics, 842.

Jiménez-González, J. I. and Brancher, P. (2017). Transient energy growth of optimal streaks in parallel round jets. Physics of Fluids, 29(11):114101.

Johansson, P. B. V. and George, W. K. (2006a). The far downstream evolution of the high-Reynolds-number axisymmetric wake behind a disk. Part 1. Single-point statistics. Journal of Fluid Mechanics, 555:363–385.

Johansson, P. B. V. and George, W. K. (2006b). The far downstream evolution of the high-Reynolds-number axisymmetric wake behind a disk. Part 2. Slice proper orthogonal decomposition. Journal of Fluid Mechanics, 555:387–408.

Johansson, P. B. V., George, W. K., and Woodward, S. H. (2002). Proper orthogonal decomposition of an axisymmetric turbulent wake behind a disk. Physics of Fluids, 14(7):2508–2514.

Jordan, P. and Colonius, T. (2013). Wave packets and turbulent jet noise. Annual Review of Fluid Mechanics, 45:173–195.

Jung, D., Gamard, S., and George, W. K. (2004). Downstream evolution of the most energetic modes in a turbulent axisymmetric jet at high reynolds number. Part 1. the near-field region. Journal of Fluid Mechanics, 514:173–204.

Juve, D., Sunyach, M., and Comte-Bellot, G. (1979). Filtered azimuthal correlations in the acoustic far field of a subsonic jet. AIAA Journal, 17(1):112–113.

Kaplan, A., Cane, M. A., Kushnir, Y., Clement, A. C., Blumenthal, M. B., and Rajagopalan, B. (1998). Analyses of global sea surface temperature 1856–1991. Journal of Geophysical Research: Oceans, 103(C9):18567–18589.

Kawai, S. and Larsson, J. (2012). Wall-modeling in large eddy simulation: Length scales, grid resolution, and accuracy. Physics of Fluids, 24(1):015105.

Khaliq, M. N., Ouarda, T. B. M. J., Gachon, P., Sushama, L., and St-Hilaire, A. (2009). Identification of hydrological trends in the presence of serial and cross correlations: A review of selected methods and their application to annual flow regimes of canadian rivers. Journal of Hydrology, 368(1-4):117–130.

Kim, J. and Choi, H. (2009). Large eddy simulation of a circular jet: effect of inflow conditions on the near field. Journal of Fluid Mechanics, 620:383–411.

Kondrashov, D. and Ghil, M. (2006). Spatio-temporal filling of missing points in geophysical data sets. Nonlinear Processes in Geophysics, 13(2):151–159.

Kostas, J., Soria, J., and Chong, M. S. (2005). A comparison between snapshot POD analysis of PIV velocity and vorticity data. Experiments in Fluids, 38(2):146–160.

Lacombe, G., McCartney, M., and Forkuor, G. (2012). Drying climate in ghana over the period 1960–2005: evidence from the resampling-based mann-kendall test at local and regional levels. Hydrological Sciences Journal, 57(8):1594–1609.

Lesshafft, L., Semeraro, O., Jaunet, V., Cavalieri, A. V. G., and Jordan, P. (2019). Resolvent-based modeling of coherent wave packets in a turbulent jet. Physical Review Fluids, 4(6):063901.

Lighthill, M. J. (1954). On sound generated aerodynamically II. Turbulence as a source of sound. Proceedings of the Royal Society of London. Series A. Mathematical and Physical Sciences, 222(1148):1–32.

List, E. J. (1982). Turbulent jets and plumes. Annual Review of Fluid Mechanics, 14(1):189–212.

Long, T. A. and Petersen, R. A. (1992). Controlled interactions in a forced axisymmetric jet. Part 1. The distortion of the mean flow. Journal of Fluid Mechanics, 235:37–55.

Lophaven, S. N., Nielsen, H. B., and Søndergaard, J. (2002). DACE: a Matlab Kriging toolbox, volume 2. Citeseer.

Lozano-Durán, A., Bae, H. J., and Encinar, M. P. (2020). Causality of energy-containing eddies in wall turbulence. Journal of Fluid Mechanics, 882:A2.

Lumley, J. L. (1967). The structure of inhomogeneous turbulent flows. Atmospheric turbulence and radio wave propagation, pages 166–178.

Lumley, J. L. (1970). Stochastic tools in turbulence. Courier Corporation.

Lumley, J. L. (2007). Stochastic tools in turbulence. Courier Corporation.

Lyrintzis, A. and Mankbadi, R. (1996). Prediction of the far-field jet noise using kirchhoff's formulation. AIAA journal, 34(2):413–416.

Maia, I., Jordan, P., Heidt, L., Colonius, T., Nekkanti, A., and Schmidt, O. T. (2021a). Nonlinear dynamics of forced wavepackets in turbulent jets. In AIAA Aviation 2021 Forum, page 2277. American Institute of Aeronautics and Astronautics.

Maia, I. A., Jordan, P., and Cavalieri, A. V. G. (2022). Wave cancellation in jets with laminar and turbulent boundary layers: The effect of nonlinearity. Physical Review Fluids, 7(3):033903.

Maia, I. A., Jordan, P., Cavalieri, A. V. G., Martini, E., Sasaki, K., and Silvestre, F. J. (2021b). Real-time reactive control of stochastic disturbances in forced turbulent jets. Physical Review Fluids, 6(12):123901.

Maia, I. A., Jordan, P., Cavalieri, A. V. G., Martini, E., and Silvestre, F. (2020). Closed-loop control of forced turbulent jets. arXiv preprint arXiv:2009.09299.

Mankbadi, R. R. (1985). On the interaction between fundamental and subharmonic instability waves in a turbulent round jet. Journal of Fluid Mechanics, 160:385–419.

McKeon, B. J. and Sharma, A. S. (2010). A critical-layer framework for turbulent pipe flow. Journal of Fluid Mechanics, 658:336–382.

Meneveau, C., Lund, T. S., and Moin, P. (1992). Search for subgrid scale parameterization by projection pursuit regression. In Proceedings of Summer Program, pages 61–81. Stanford University.

Meyers, S. D., Kelly, B. G., and O'Brien, J. J. (1993). An introduction to wavelet analysis in oceanography and meteorology: With application to the dispersion of yanai waves. Monthly weather review, 121(10):2858–2866.

Michalke, A. (1977). Instability of a compressible circular free jet with consideration of the influence of the jet boundary layer thickness. NTRS, Washington, D.C. U.S. National Aeronautics and Space Administration.

Moczarski, L., Treleaven, N. C., Oberleithner, K., Schmidt, S., Fischer, A., and Kaiser, T. L. (2022). Interaction of multiple linear helical modes in the turbulent flow field of an industrial fuel injection system. In AIAA SciTech 2022 Forum, page 1061. American Institute of Aeronautics and Astronautics.

Mollo-Christensen, E. (1967). Jet noise and shear flow instability seen from an experimenter's viewpoint. Journal of Applied Mechanics, 34(1):1.

Monkewitz, P. A. (1988). Subharmonic resonance, pairing and shredding in the mixing layer. Journal of Fluid Mechanics, 188:223–252.

Moore, C. J. (1977). The role of shear-layer instability waves in jet exhaust noise. Journal of Fluid Mechanics, 80(2):321–367.

Muralidhar, S. D., Podvin, B., Mathelin, L., and Fraigneau, Y. (2019). Spatio-temporal proper orthogonal decomposition of turbulent channel flow. Journal of Fluid Mechanics, 864:614–639.

Murray, N. E. and Ukeiley, L. S. (2007). An application of Gappy POD. Experiments in Fluids, 42(1):79–91.

Narayanan, S., Barber, T. J., and Polak, D. R. (2002). High subsonic jet experiments: turbulence and noise generation studies. AIAA journal, 40(3):430–437.

Nekkanti, A., Maia, I., Jordan, P., Heidt, L., Colonius, T., , and Schmidt, O. T. (Osaka, Japan (Online), July 19-22, 2022). Triadic nonlinear interactions and acoustics of forced versus unforced turbulent jets. In Twelveth International Symposium on Turbulence and Shear Flow Phenomena (TSFP12).

Nekkanti, A., Nidhan, S., Schmidt, O. T., and Sarkar, S. (2023). Large-scale streaks in a turbulent bluff body wake. arXiv preprint arXiv:2304.08679.

Nekkanti, A. and Schmidt, O. T. (2021a). Frequency–time analysis, low-rank reconstruction and denoising of turbulent flows using SPOD. Journal of Fluid Mechanics, 926.

Nekkanti, A. and Schmidt, O. T. (2021b). Modal analysis of acoustic directivity in turbulent jets. AIAA Journal, 59(1):228–239.

Nekkanti, A. and Schmidt, O. T. (2023). Gappy spectral proper orthogonal decomposition. Journal of Computational Physics, 478:111950.

Nichols, J. W. and Lele, S. K. (2011). Global modes and transient response of a cold supersonic jet. Journal of Fluid Mechanics, 669:225–241.

Nidhan, S., Chongsiripinyo, K., Schmidt, O. T., and Sarkar, S. (2020). Spectral proper orthogonal decomposition analysis of the turbulent wake of a disk at Re= 50000. Physical Review Fluids, 5(12):124606.

Nidhan, S., Ortiz-Tarin, J. L., Chongsiripinyo, K., Sarkar, S., and Schmid, P. J. (2019). Dynamic mode decomposition of stratified wakes. In AIAA Aviation 2019 Forum, page 3330. American Institute of Aeronautics and Astronautics.

Nidhan, S., Schmidt, O. T., and Sarkar, S. (2022). Analysis of coherence in turbulent stratified wakes using spectral proper orthogonal decomposition. Journal of Fluid Mechanics, 934.

Noack, B. R., Afanasiev, K., Morzyński, M., Tadmor, G., and Thiele, F. (2003). A hierarchy of low-dimensional models for the transient and post-transient cylinder wake. Journal of Fluid Mechanics, 497:335–363.

Nogueira, P. A. S., Cavalieri, A. V. G., Jordan, P., and Jaunet, V. (2019). Large-scale streaky structures in turbulent jets. Journal of Fluid Mechanics, 873:211–237.

Ohh, C. Y. and Spedding, G. R. (2022). Wake identification of stratified flows using dynamic mode decomposition. Physical Review Fluids, 7(2):024801.

Oliver, M. A. and Webster, R. (1990). Kriging: a method of interpolation for geographical information systems. International Journal of Geographical Information System, 4(3):313–332.

Onorato, M., Camussi, R., and Iuso, G. (2000). Small scale intermittency and bursting in a turbulent channel flow. Physical Review E, 61(2):1447.

Ortiz-Tarin, J., Nidhan, S., and Sarkar, S. (2021). High-Reynolds-number wake of a slender body. Journal of Fluid Mechanics, 918:A30.

Ortiz-Tarin, J. L., Nidhan, S., and Sarkar, S. (2023). The high-Reynolds-number stratified wake of a slender body and its comparison with a bluff-body wake. Journal of Fluid Mechanics, 957:A7.

Papamoschou, D. (2018). Wavepacket modeling of the jet noise source. International Journal of Aeroacoustics, 17(1-2):52–69.

Paschereit, C., Wygnanski, I., and Fiedler, H. (1995). Experimental investigation of subharmonic resonance in an axisymmetric jet. Journal of Fluid Mechanics, 283:365–407.

Patel, H. D. and Yeh, C. A. (2023). Modal analysis for three-dimensional instability coupling mechanisms in turbulent wake flows over an airfoil. In AIAA SCITECH 2023 Forum, page 1987. American Institute of Aeronautics and Astronautics.

Picard, C. and Delville, J. (2000). Pressure velocity coupling in a subsonic round jet. International Journal of Heat and Fluid Flow, 21(3):359–364.

Pickering, E., Rigas, G., Nogueira, P. A., Cavalieri, A. V., Schmidt, O. T., and Colonius, T. (2020). Lift-up, Kelvin–Helmholtz and Orr mechanisms in turbulent jets. Journal of Fluid Mechanics, 896:A2.

Pierrehumbert, R. T. and Widnall, S. E. (1982). The two-and three-dimensional instabilities of a spatially periodic shear layer. Journal of Fluid Mechanics, 114:59–82.

Proctor, J. L., Brunton, S. L., and Kutz, J. N. (2016). Dynamic mode decomposition with control. SIAM Journal on Applied Dynamical Systems, 15(1):142–161.

Raben, S. G., Charonko, J. J., and Vlachos, P. P. (2012). Adaptive gappy proper orthogonal decomposition for particle image velocimetry data reconstruction. Measurement Science and Technology, 23(2):025303.

Raffel, M., Willert, C. E., Kompenhans, J., et al. (1998). Particle image velocimetry: a practical guide, volume 2. Springer.

Raiola, M., Discetti, S., and Ianiro, A. (2015). On PIV random error minimization with optimal POD-based low-order reconstruction. Experiments in Fluids, 56(4):75.

Raman, G. and Rice, E. (1991). Axisymmetric jet forced by fundamental and subharmonic tones. AIAA Journal, 29(7):1114–1122.

Reynolds, R. W. and Smith, T. M. (1994). Improved global sea surface temperature analyses using optimum interpolation. Journal of Climate, 7(6):929–948.

Rigas, G., Schmidt, O. T., Colonius, T., and Bres, G. A. (2017). One Way Navier-Stokes and resolvent analysis for modeling coherent structures in a supersonic turbulent jet. In 23rd AIAA/CEAS Aeroacoustics Conference, page 4046. American Institute of Aeronautics and Astronautics.

Rodionov, S. N. (2006). Use of prewhitening in climate regime shift detection. Geophysical Research Letters, 33(12).

Rodríguez, D., Cavalieri, A. V. G., Colonius, T., and Jordan, P. (2015). A study of linear wavepacket models for subsonic turbulent jets using local eigenmode decomposition of piv data. European Journal of Mechanics-B/Fluids, 49:308–321.

Rodriguez, D., Sinha, A., Bres, G. A., and Colonius, T. (2013). Acoustic field associated with parabolized stability equation models in turbulent jets. In 19th AIAA/CEAS Aeroacoustics Conference, page 2279. American Institute of Aeronautics and Astronautics.

Rodríguez, D., Sinha, A., Bres, G. A., and Colonius, T. (2013). Inlet conditions for wave packet models in turbulent jets based on eigenmode decomposition of large eddy simulation data. Physics of Fluids, 25(10):105107.

Rowley, C. W. and Dawson, S. T. M. (2017). Model reduction for flow analysis and control. Annual Review of Fluid Mechanics, 49:387–417.

Rowley, C. W., Mezić, I., Bagheri, S., Schlatter, P., Henningson, D., et al. (2009). Spectral analysis of nonlinear flows. Journal of Fluid Mechanics, 641(1):115–127.

Saini, P., Arndt, C. M., and Steinberg, A. M. (2016). Development and evaluation of gappy-POD as a data reconstruction technique for noisy PIV measurements in gas turbine combustors. Experiments in Fluids, 57(7):122.

Samimy, M., Debiasi, M., Caraballo, E., Serrani, A., Yuan, X., Little, J., and Myatt, J. H. (2007a). Feedback control of subsonic cavity flows using reduced-order models. Journal of Fluid Mechanics, 579:315.

Samimy, M., Kim, J. H., Kastner, J., Adamovich, I., and Utkin, Y. (2007b). Active control of high-speed and high-reynolds-number jets using plasma actuators. Journal of Fluid Mechanics, 578:305–330.

Sandham, N., Morfey, C., and Hu, Z. (2006). Sound radiation from exponentially growing and decaying surface waves. Journal of Sound and Vibration, 294(1-2):355–361.

Sano, A., Abreu, L. I., Cavalieri, A. V. G., and Wolf, W. R. (2019). Trailing-edge noise from the scattering of spanwise-coherent structures. Physical Review Fluids, 4(9):094602.

Sasaki, K., Cavalieri, A. V. G., Jordan, P., Schmidt, O. T., Colonius, T., and Brès, G. A. (2017). High-frequency wavepackets in turbulent jets. Journal of Fluid Mechanics, 830.

Schlinker, R., Simonich, J., Shannon, D., Reba, R., Colonius, T., Gudmundsson, K., and Ladeinde, F. (2009). Supersonic jet noise from round and chevron nozzles: experimental studies. In 15th AIAA/CEAS Aeroacoustics Conference (30th AIAA Aeroacoustics Conference), page 3257. American Institute of Aeronautics and Astronautics.

Schmid, P. J. (2010). Dynamic mode decomposition of numerical and experimental data. Journal of Fluid Mechanics, 656:5–28.

Schmid, P. J. (2011). Application of the dynamic mode decomposition to experimental data. Experiments in fluids, 50:1123–1130.

Schmid, P. J. (2022). Dynamic mode decomposition and its variants. Annual Review of Fluid Mechanics, 54:225–254.

Schmidt, O., Towne, A., Colonius, T., Jordan, P., Jaunet, V., Cavalieri, A. V. G., and Bres, G. A. (2016). Super-and multi-directive acoustic radiation by linear global modes of a turbulent jet. In 22nd AIAA/CEAS Aeroacoustics Conference, page 2808. American Institute of Aeronautics and Astronautics.

Schmidt, O. T. (2020). Bispectral mode decomposition of nonlinear flows. Nonlinear Dynamics, 102(4):2479–2501.

Schmidt, O. T. and Colonius, T. (2020). Guide to spectral proper orthogonal decomposition. AIAA Journal, 58(3):1023–1033.

Schmidt, O. T., Colonius, T., and Brés, G. A. (2017a). Wavepacket intermittency and its role in turbulent jet noise. In 55th AIAA Aerospace Sciences Meeting, page 0686. American Institute of Aeronautics and Astronautics.

Schmidt, O. T. and Schmid, P. J. (2019). A conditional space–time pod formalism for intermittent and rare events: example of acoustic bursts in turbulent jets. Journal of Fluid Mechanics, 867.

Schmidt, O. T., Towne, A., Colonius, T., Cavalieri, A. V. G., Jordan, P., and Brès, G. A. (2017b). Wavepackets and trapped acoustic modes in a turbulent jet: coherent structure eduction and global stability. Journal of Fluid Mechanics, 825:1153–1181.

Schmidt, O. T., Towne, A., Rigas, G., Colonius, T., and Brès, G. A. (2018). Spectral analysis of jet turbulence. Journal of Fluid Mechanics, 855:953–982.

Sciacchitano, A., Dwight, R. P., and Scarano, F. (2012). Navier–Stokes simulations in gappy PIV data. Experiments in Fluids, 53(5):1421–1435.

Sciacchitano, A. and Scarano, F. (2014). Elimination of PIV light reflections via a temporal high pass filter. Measurement Science and Technology, 25(8):084009.

Serinaldi, F. and Kilsby, C. G. (2015). Stationarity is undead: Uncertainty dominates the distribution of extremes. Advances in Water Resources, 77:17–36.

Shaabani-Ardali, L., Sipp, D., and Lesshafft, L. (2019). Vortex pairing in jets as a global floquet instability: modal and transient dynamics. Journal of Fluid Mechanics, 862:951–989.

Sinha, A., Rodríguez, D., Brès, G. A., and Colonius, T. (2014). Wavepacket models for supersonic jet noise. Journal of Fluid Mechanics, 742:71–95.

Sirovich, L. (1987). Turbulence and the dynamics of coherent structures. i. coherent structures. Quarterly of applied mathematics, 45(3):561–571.

Smith, T. M., Reynolds, R. W., Livezey, R. E., and Stokes, D. C. (1996). Reconstruction of historical sea surface temperatures using empirical orthogonal functions. Journal of Climate, 9(6):1403–1420.

Son, S. Y. and Kihm, K. D. (2001). Evaluation of transient turbulent flow fields using digital cinematographic particle image velocimetry. Experiments in Fluids, 30(5):537–550.

Stein, M. L. (1999). Interpolation of spatial data: some theory for Kriging. Springer Science & Business Media.

Stewart, K. C. and Vlachos, P. P. (2012). Vortex rings in radially confined domains. Experiments in Fluids, 53(4):1033–1044.

Stockwell, R. G., Mansinha, L., and Lowe, R. P. (1996). Localization of the complex spectrum: the S transform. IEEE transactions on signal processing, 44(4):998–1001.

Suzuki, T. and Colonius, T. (2006). Instability waves in a subsonic round jet detected using a near-field phased microphone array. Journal of Fluid Mechanics, 565:197–226.

Taira, K., Brunton, S. L., Dawson, S. T. M., Rowley, C. W., Colonius, T., McKeon, B. J., Schmidt, O. T., Gordeyev, S., Theofilis, V., and Ukeiley, L. S. (2017). Modal analysis of fluid flows: An overview. AIAA Journal, pages 4013–4041.

Tam, C., Golebiowski, M., and Seiner, J. (1996). On the two components of turbulent mixing noise from supersonic jets. In Aeroacoustics conference, page 1716. American Institute of Aeronautics and Astronautics.

Tam, C. K. and Burton, D. E. (1984). Sound generated by instability waves of supersonic flows. part 1. two-dimensional mixing layers. Journal of Fluid Mechanics, 138:249–271.

Tam, C. K. and Morris, P. J. (1980). The radiation of sound by the instability waves of a compressible plane turbulent shear layer. Journal of Fluid Mechanics, 98(2):349–381.

Tam, C. K. W., Viswanathan, K., Ahuja, K. K., and Panda, J. (2008). The sources of jet noise: experimental evidence. Journal of Fluid Mechanics, 615:253–292.

Taylor, M. H., Losch, M., Wenzel, M., and Schröter, J. (2013). On the sensitivity of field reconstruction and prediction using empirical orthogonal functions derived from gappy data. Journal of Climate, 26(22):9194–9205.

Tinney, C. E., Glauser, M. N., and Ukeiley, L. S. (2008a). Low-dimensional characteristics of a transonic jet. Part 1. proper orthogonal decomposition. Journal of Fluid Mechanics, 612:107–141.

Tinney, C. E., Ukeiley, L. S., and Glauser, M. N. (2008b). Low-dimensional characteristics of a transonic jet. Part 2. estimate and far-field prediction. Journal of Fluid Mechanics, 615:53–92.

Tissot, G., Lajús Jr, F. C., Cavalieri, A. V. G., and Jordan, P. (2017a). Wave packets and Orr mechanism in turbulent jets. Physical Review Fluids, 2(9):093901.

Tissot, G., Zhang, M., Lajús, F. C., Cavalieri, A. V. G., and Jordan, P. (2017b). Sensitivity of wavepackets in jets to nonlinear effects: the role of the critical layer. Journal of Fluid Mechanics, 811:95–137.

Towne, A., Cavalieri, A. V. G., Jordan, P., Colonius, T.and Schmidt, O., Jaunet, V., and Brès, G. A. (2017). Acoustic resonance in the potential core of subsonic jets. Journal of Fluid Mechanics, 825:1113–1152.

Towne, A. and Liu, P. (2019). Time-frequency analysis of intermittent coherent structures in turbulent flows. Bulletin of the American Physical Society, 64.

Towne, A., Schmidt, O. T., and Colonius, T. (2018). Spectral proper orthogonal decomposition and its relationship to dynamic mode decomposition and resolvent analysis. Journal of Fluid Mechanics, 847:821–867.

Tutkun, M., Johansson, P. B. V., and George, W. K. (2008). Three-component vectorial proper orthogonal decomposition of axisymmetric wake behind a disk. AIAA Journal, 46(5):1118–1134.

Venturi, D. (2006). On proper orthogonal decomposition of randomly perturbed fields with applications to flow past a cylinder and natural convection over a horizontal plate. Journal of Fluid Mechanics, 559:215–254.

Venturi, D. and Karniadakis, G. E. (2004). Gappy data and reconstruction procedures for flow past a cylinder. Journal of Fluid Mechanics, 519:315–336.

Vétel, J., Garon, A., and Pelletier, D. (2011). Denoising methods for time-resolved piv measurements. Experiments in Fluids, 51(4):893–916.

Viswanathan, K. (2002). Analysis of the two similarity components of turbulent mixing noise. AIAA journal, 40(9):1735–1744.

Viswanathan, K. (2004). Aeroacoustics of hot jets. Journal of Fluid Mechanics, 516:39–82.

von Storch, H. (1995). Misuses of statistical analysis in climate research. In: Analysis of Climate Variability. Springer, Berlin, Heidelberg. pages 11–26.

Vreman, A. (2004). An eddy-viscosity subgrid-scale model for turbulent shear flow: Algebraic theory and applications. Physics of Fluids, 16(10):3670–3681.

Welch, P. (1967). The use of fast Fourier transform for the estimation of power spectra: a method based on time averaging over short, modified periodograms. IEEE Transactions on audio and electroacoustics, 15(2):70–73.

Westerweel, J. (1994). Efficient detection of spurious vectors in Particle Image Velocimetry data. Experiments in Fluids, 16(3):236–247.

Westerweel, J., Elsinga, G. E., and Adrian, R. J. (2013). Particle image velocimetry for complex and turbulent flows. Annual Review of Fluid Mechanics, 45:409–436.

Willcox, K. (2006). Unsteady flow sensing and estimation via the gappy proper orthogonal decomposition. Computers & fluids, 35(2):208–226.

Willert, C. (1997). Stereoscopic digital particle image velocimetry for application in wind tunnel flows. Measurement Science and Technology, 8(12):1465.

Winant, C. D. and Browand, F. K. (1974). Vortex pairing: the mechanism of turbulent mixing-layer growth at moderate reynolds number. Journal of Fluid Mechanics, 63(2):237–255.

Wu, X. and Huerre, P. (2009). Low-frequency sound radiated by a nonlinearly modulated wavepacket of helical modes on a subsonic circular jet. Journal of Fluid Mechanics, 637:173–211.

Yakhot, A., Anor, T., and Karniadakis, G. E. (2007). A reconstruction method for gappy and noisy arterial flow data. IEEE transactions on medical imaging, 26(12):1681–1697.

Yildirim, B., Chryssostomidis, C., and Karniadakis, G. E. (2009). Efficient sensor placement for ocean measurements using low-dimensional concepts. Ocean Modelling, 27(3-4):160–173.

Zaman, K. (1985a). Effect of initial condition on subsonic jet noise. AIAA journal, 23(9):1370–1373.

Zaman, K. (1985b). Far-field noise of a subsonic jet under controlled excitation. Journal of Fluid Mechanics, 152:83–111.

Zaman, K. (1986). Flow field and near and far sound field of a subsonic jet. Journal of sound and vibration, 106(1):1–16.

Zaman, K. (2012). Effect of initial boundary-layer state on subsonic jet noise. AIAA journal, 50(8):1784–1795.

Zaman, K. B. M. Q. and Hussain, A. K. M. F. (1980). Vortex pairing in a circular jet under controlled excitation. Part 1. General jet response. Journal of Fluid Mechanics, 101(3):449–491.

Zhang, X., Harvey, K. D., Hogg, W. D., and Yuzyk, T. R. (2001). Trends in Canadian streamflow. Water Resources Research, 37(4):987–998.

Zhang, Y., Cattafesta, L., and Ukeiley, L. (2019). A spectral analysis modal method applied to cavity flow oscillations. In 11th International Symposium on Turbulence and Shear Flow Phenomena (TSFP11), UK.

Zhang, Y., Cattafesta, L. N., and Ukeiley, L. (2017). Identification of coherent structures in cavity flows using stochastic estimation and dynamic mode decomposition. In 10th International Symposium on Turbulence and Shear Flow Phenomena, TSFP 2017, page 3.

Zhang, Y., Cattafesta, L. N., and Ukeiley, L. (2020). Spectral analysis modal methods (SAMMs) using non-time-resolved PIV. Experiments in Fluids, 61(11):1–12.

Zhang, Y., Guo, Z., Wang, W., He, S., Lee, T., and Loew, M. (2003). A comparison of the wavelet and short-time fourier transforms for doppler spectral analysis. Medical engineering & physics, 25(7):547–557.

Zoppellari, E., Juve, D., Zoppellari, E., and Juve, D. (1997). Reduction of jet noise by water injection. In 3rd AIAA/CEAS Aeroacoustics Conference, page 1622.